

AD-A191 927

MICROMECHANICAL MODELING OF GRANULAR SOIL AT SMALL
STRAIN BY ARRAYS OF EL. (U) RENSSELAER POLYTECHNIC INST
TROY NY DEPT OF CIVIL ENGINEERING... E PETAKIS ET AL.

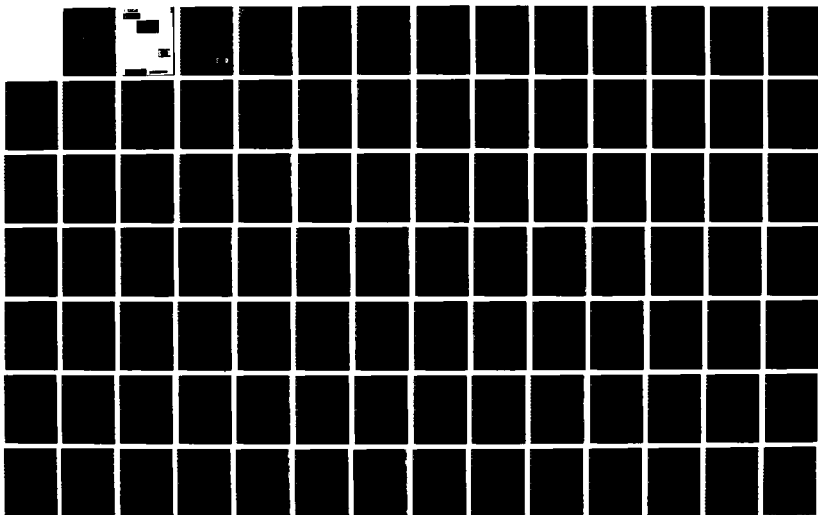
1/4

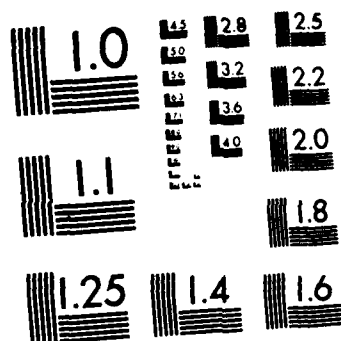
UNCLASSIFIED

28 SEP 87 RPI-CE-87-82 AFOSR-TR-88-8137

F/G 8/18

NL





MICROCOPY RESOLUTION TEST CHART
NATIONAL BUREAU OF STANDARDS 1963 A

Approved for public release;
distribution unlimited.

MICROMECHANICAL MODELING OF GRANULAR SOIL
AT SMALL STRAIN BY ARRAYS OF ELASTIC SPHERE

2
AFOSR-TR- 88 - 0 137

CE Report No. CE-87-02

Approved for public release;
distribution unlimited.

MICROMECHANICAL MODELING OF GRANULAR SOIL
AT SMALL STRAIN BY ARRAYS OF ELASTIC SPHERES

by

Emmanuel Petrakis and Ricardo Dobry

Prepared under Contract No. AFOSR-86-0135
United States Air Force
Office of Scientific Research
Bolling Air Force Base

Department of Civil Engineering
Rensselaer Polytechnic Institute
Troy, NY 12180-3590

September 1987

DTIC
ELECTE
FEB 29 1988
S H D

88 2 26 120

UNCLASSIFIED

SECURITY CLASSIFICATION OF THIS PAGE

A191 927

REPORT DOCUMENTATION PAGE

Form Approved
OMB No. 0704-0188

1a. REPORT SECURITY CLASSIFICATION UNCLASSIFIED			1b. RESTRICTIVE MARKINGS		
2a. SECURITY CLASSIFICATION AUTHORITY			3. DISTRIBUTION/AVAILABILITY OF REPORT Approved for Public Release; Distribution Unlimited		
2b. DECLASSIFICATION/DOWNGRADING SCHEDULE			5. MONITORING ORGANIZATION REPORT NUMBER(S) AFOSR-TR. 88-0137		
4. PERFORMING ORGANIZATION REPORT NUMBER(S) CE-87-02			7a. NAME OF MONITORING ORGANIZATION AFOSR/NA		
6a. NAME OF PERFORMING ORGANIZATION Rensselaer Polytechnic Institute		6b. OFFICE SYMBOL (if applicable)		7b. ADDRESS (City, State, and ZIP Code) Bldg. 410 Bolling AFB, DC 20332-6448	
6c. ADDRESS (City, State, and ZIP Code) Department of Civil Engineering Troy, N.Y. 12180-3580		9. PROCUREMENT INSTRUMENT IDENTIFICATION NUMBER SFR Contract AFOSR-86-0135			
8a. NAME OF FUNDING/SPONSORING ORGANIZATION AFOSR		8b. OFFICE SYMBOL (if applicable) NA		10. SOURCE OF FUNDING NUMBERS	
8c. ADDRESS (City, State, and ZIP Code) Bldg. 410 Bolling AFB, DC 20332-6448		PROGRAM ELEMENT NO. 6.1102F		PROJECT NO. 2302	TASK NO. C1
11. TITLE (Include Security Classification) (U) MICROMECHANICAL MODELING OF GRANULAR SOIL AT SMALL STRAIN BY ARRAYS OF ELASTIC SPHERES					
12. PERSONAL AUTHOR(S) Emmanuel Petrakis and Ricardo Dobry					
13a. TYPE OF REPORT Interim		13b. TIME COVERED FROM 86/05/06 TO 87/05/05		14. DATE OF REPORT (Year, Month, Day) September 28, 1987	
15. PAGE COUNT 270					
16. SUPPLEMENTARY NOTATION					
17. COSATI CODES			18. SUBJECT TERMS (Continue on reverse if necessary and identify by block number)		
FIELD	GROUP	SUB-GROUP	Particulate Mechanics, Stress-Strain Relationships, Regular Arrays of Spheres, Isotropy, Transverse Isotropy, Self Consistent Method, Small Strains, Threshold Strain, P-waves, shear modulus, σ_{max}		
19. ABSTRACT (Continue on reverse if necessary and identify by block number)					
<p>The need for a micromechanical approach to modeling the stress-strain response of granular soil is discussed and justified. This work focuses on the small shear strain ($\gamma < 0.01\%$) behavior, and investigates the validity of modeling analytically uniform, rounded-grained quartz sand by arrays of identical elastic, rough, quartz spheres. As a first step, the stress-strain properties of six regular arrays of spheres are studied in some detail, with focus on isotropic and and biaxial boundary loading.</p>					
(over)					
20. DISTRIBUTION/AVAILABILITY OF ABSTRACT <input checked="" type="checkbox"/> UNCLASSIFIED/UNLIMITED <input type="checkbox"/> SAME AS RPT <input type="checkbox"/> OTHER USERS			21. ABSTRACT SECURITY CLASSIFICATION UNCLASSIFIED		
22a. NAME OF RESPONSIBLE INDIVIDUAL Major Steven C. Boyce			22b. TELEPHONE (Include Area Code) (202) 767-6963		22c. OFFICE SYMBOL AFOSR/NA

19. ABSTRACT (Continued)

An analytical procedure is established for determining the elastic moduli of a random assemblage of equal, elastic, rough spheres of arbitrary mean porosity, subjected to isotropic confining pressure. The procedure uses the properties of the regular arrays already described, it accounts for the spatial distribution of porosity, and it calculates the macroscopic moduli through the Self Consistent Method. The procedure was applied to compute the shear and bulk moduli of assemblages of quartz spheres, which were then compared to static and dynamic measurements on uncycled and heavily precycled quartz sands reported in the literature. Although the theoretical sands are significantly stiffer than the actual soils, excellent agreement was found with resonant column measurements on heavily precycled Ottawa sand at small strains.

Finally, a new two-dimensional model of the stress-strain behavior of granular soil at small strains is presented. The model is based on an incremental solution to the contact problem of two equal, elastic, rough spheres and is implemented through nonlinear finite element techniques. The results of numerical experiments conducted on this idealized aggregate are compared to laboratory data on the static and cyclic small strain behavior of actual sand, as well as to recent compressional wave velocity measurements on anisotropically consolidated dry sands, with good agreement. These measurements, performed at the large cubic triaxial facility at the University of Texas, have shown that the P-wave velocity depends only on the principal stress parallel to the direction of wave propagation; this finding was also predicted by the simulation.

Concluding, the hypothesis that certain aspects of the behavior of granular soil are due to the particulate nature of the soil is justified. These aspects cannot be interpreted and reproduced analytically unless this particulate nature is taken into account.

TABLE OF CONTENTS

	Page
LIST OF TABLES.	iv
LIST OF FIGURES	v
LIST OF SYMBOLS	xviii
ACKNOWLEDGEMENTS.	xxiii
ABSTRACT.	xxv
1. INTRODUCTION.	1
2. LABORATORY MEASUREMENTS ON SANDS AT SMALL STRAINS	5
3. STRESS-STRAIN MATHEMATICAL MODELLING.	13
4. THE MICROMECHANICAL APPROACH.	17
4.1 General Solution of the Contact Problem.	23
4.1.1 Implementation of the Model and Sensitivity Analysis.	27
4.1.2 Verification of the Model	28
4.2 Studies in Crystals.	30
5. DIFFERENTIAL STRESS-STRAIN RELATIONS FOR REGULAR ARRAYS OF SPHERES.	34
5.1 Simple Cubic Array (sc).	35
5.2 Body Centered Cubic Array (bcc).	42
5.3 Face Centered Cubic Array (fcc).	45
5.4 Cubical-Tetrahedral (ct) and Tetragonal-Sphenoidal (ts).	48
5.5 Comparison of Different Cubic Arrays	50
6. AN ANALYTICAL MODEL OF GRANULAR SOIL OF ARBITRARY VOID RATIO UNDER ISOTROPIC PRESSURE	54
6.1 The Self Consistent Method	55 ^{or}
6.2 The Model.	60
6.3 Application to Quartz Sand	64



Justification	
By _____	
Distribution/	
Availability Codes	
Dist	Avail and/or Special
A-1	

TABLE OF CONTENTS (Continued)

	Page
7. A TWO-DIMENSIONAL NUMERICAL MICROMECHANICAL MODEL FOR THE STRESS-STRAIN BEHAVIOR OF A GRANULAR SOIL AT SMALL STRAINS	68
7.1 Aggregate Description.	69
7.2 The Element.	70
8. MONOTONIC LOADING SIMULATIONS OF THE AGGREGATE.	74
8.1 Isotropic Compression.	74
8.2 Isotropic Compression Followed by Pure Shear	74
8.3 Isotropic Compression Followed by Biaxial Compression.	75
8.4 Yielding and Failure Considerations.	76
8.5 Discussion of Results.	79
9. CYCLIC LOADING SIMULATIONS OF THE AGGREGATE	82
9.1 Cyclic Isotropic Compression	82
9.2 Isotropic Compression Followed by Cyclic Shear Loading.	82
9.3 Constrained Moduli of the Aggregate and P-Wave Velocities Under Biaxial Compression	82
10. CONCLUSION.	85
11. REFERENCES.	87
TABLES.	98
FIGURES	101
APPENDIX A: Stress-Strain Relations for a Body Centered Cubic Array.	166
APPENDIX B: Simulation of Triaxial and Pure Shear Loading in Cubic Arrays.	182
APPENDIX C: Program Listing of the Constitutive Law for the Simple Cubic Array	195
APPENDIX D: Media Configurations Used to Simulate the Aggregate.	216

TABLE OF CONTENTS (Continued)

	Page
APPENDIX E: Medium 2: Compression with Constant Mean Stress. Element Stress-Strain Behavior.	220
APPENDIX F: Medium 1: Biaxial Compression with Variable Mean Stress. Element Stress-Strain Behavior . .	237
APPENDIX G: Medium 2: Compression with Mean Stress Constant. Variation of Normalized Stress and Strain During Loading.	254

LIST OF TABLES

	Page
Table 1. Properties of Regular Arrays of Equal Spheres (Deresciewicz, 1958, Van Vlack, 1964).	99
Table 2. Feasible Regular Arrays or "Cells" (Shahinpoor, 1981). Coordination No. = N = No. of Contacts per Sphere. $[u, m, \ell]$ gives No. of Contacts of Spheres with Layer Above, Same Layer and Layer Below: $N = u + m + \ell$	100
Table 3. Properties of Quartz Used in this Report	100

LIST OF FIGURES

	Page
Figure 1. Variation of V_s with Principal Stress in (a) Direction of Wave Propagation, (b) Direction of Polarization (Particle Motion) and (c) Out-of-Plane Direction (Roesler, 1979)	102
Figure 2. Effect on V_p of Principal Stress, σ_c , Perpendicular to Wave Propagation for Biaxial Loading Case (Kopperman et al., 1982)	103
Figure 3. Stress-Strain Curves for Monotonic Loading of Dry Granular Soils.	104
Figure 4. Stress-Strain Hysteresis Loops for Reversed Loading (Hardin and Drnevich, 1972)	104
Figure 5. Plastic Potential Surfaces: (a) Drucker et al., (b) Lade and Duncan, (c) Original Cam-Clay, (d) Modified Cam-Clay, (e) DiMaggio and Sandler, (f) Zienkiewicz et al. (Hardin, 1978)	105
Figure 6. Isotropic Hardening Model (Chen, 1975).	106
Figure 7. Kinematic Hardening Model (Chen, 1975).	106
Figure 8. Finite Difference Simulation of a Triaxial Test on a 100-disc Model (Cundall and Strack, 1983.	107
Figure 9. Elastic Spheres Under Normal and Tangential Loads . .	108
Figure 10. Tangential Force-Displacement Relation for N Constant, T Increasing (Dobry et al, 1982).	108
Figure 11. Regular Arrays of Equal Spheres (Deresiewicz, 1958) .	109
Figure 12. Regular Array No. 2 (see Table 2) (1,0,3); $N=4$; $n=0.6599$; $e=1.9403$	110
Figure 13. Rod Wave Velocity Measurements in Regular Dense Array of Steel Spheres Isotropically Loaded (Duffy and Mindlin, 1957, figure presented by Richart et al., 1970)	110
Figure 14. Contact Force Space and Conical Yield Surfaces, Elastic-Plastic Incremental Solution of Mindlin's Problem (Seridi and Dobry, 1984).	111

LIST OF FIGURES

	Page
Figure 15. Force-Deformation Behavior of Two Elastic Rough Spheres in Contact: Analytical Solution for Oscillating Oblique Forces (a) $dT/dN > f$ and (b) $dT/dN < f$ (after Mindlin and Deresiewicz, 1953).	112
Figure 16. Force-Deformation Behavior of Two Elastic Rough Spheres in Contact: Analytical Solutions for (a) Normal Force Increasing, Tangential Force Increasing; (b) Normal Force Decreasing, Tangential Force Increasing; (c) Normal Force Increasing, Tangential Force Decreasing; (d) Normal Force Decreasing, Tangential Force Decreasing (after Mindlin and Deresiewicz, 1953) . . .	113
Figure 17. Numerical Simulation of the Force-Deformation Behavior for Two Equal, Elastic, Rough Spheres in Contact: Load-Displacement Relation for an Oscillating Oblique Force with $dT/dN > f$	114
Figure 18. Numerical Simulation of the Force-Deformation Behavior for Two Equal, Elastic, Rough Spheres in Contact: Load-Displacement Relation for an Oscillating Oblique Force with $dT/dN < f$	115
Figure 19. Numerical Simulation of the Force-Deformation Behavior for Two Equal, Elastic, Rough Spheres in Contact: Load-Displacement Relation for the Case in Which the Normal Force Increases and the Tangential Force Increases	116
Figure 20. Numerical Simulation of the Force-Deformation Behavior for Two Equal, Elastic, Rough Spheres in Contact: Load-Displacement Relation for the Case in Which the Normal Force Decreases and the Tangential Force Increases	117
Figure 21. Numerical Simulation of the Force-Deformation Behavior for Two Equal, Elastic, Rough Spheres in Contact: Load-Displacement Relation for the Case in Which the Normal Force Increases and the Tangential Force Decreases	118

LIST OF FIGURES

	Page
Figure 22. Numerical Simulation of the Force-Deformation Behavior for Two Equal, Elastic, Rough Spheres in Contact: Load-Displacement Relation for the Case in which the Normal Force Decreases and the Tangential Force Decreases	119
Figure 23. Repeating Six Crystal Aggregate in an Infinite Plane (Angle of Slip Shown in Each Crystal). (after Lin and Ito, 1965)	120
Figure 24. Regular Simple Cubic Array of Equal Spheres.	121
Figure 25. (a) Body-Centered Cubic Array of Equal Spheres; (b) Body-Centered Cubic Array (after Van Vlack, 1964).	122
Figure 26. (a) Face-Centered Cubic Array of Equal Spheres; (b) Face-Centered Cubic Array (after Van Vlack, 1964).	122
Figure 27. Threshold Strain for the Simple Cubic (sc), Body-Centered Cubic (bcc) and Face-Centered Cubic (fcc) Arrays of Quartz Spheres	123
Figure 28. Shear Stress-Strain Curves for Simple Cubic Array of Quartz Spheres	124
Figure 29. Secant Shear Modulus Versus Shear Strain: Comparison Between Calculated G/G_{\max} for the Simple Cubic Array and Experimental Range for Sand (Dobry et al., 1982).	125
Figure 30. Influence of Stress Ratio, $K = \sigma_1/\sigma_3$ on G_{\max} : Comparison Between Prediction From Simple Cubic Array and Experimental Range for Sand.	125
Figure 31. Triaxial Compression of Regular Arrays and Influence of the Value of Intergranular Friction, f : (a) Triaxial Compression of Body-Centered Cubic Array of Quartz Spheres and (b) Triaxial Compression of Face-Centered Cubic Array of Glass Spheres (Brauns, 1966).	126
Figure 32. Poisson's Ratio of Regular Cubic Arrays, ν , as a Function of the Poisson's Ratio of the Spheres, ν_s . .	127

LIST OF FIGURES

	Page
Figure 33. Triaxial Loading: Obliquity, σ_{22}/σ_0 , at Failure Versus the Coefficient of Intergranular Friction, f , for Three Regular Cubic Arrays.	128
Figure 34. Shear Wave Velocity, V_s , Versus Stress Ratio, K , for Biaxial Confinement and $\theta_z = 0$: Analytical and Experimental Results.	129
Figure 35. Shear Modulus Versus Coordination Number (= Number of Contacts per Sphere) for Regular Cubic Arrays of Quartz Spheres.	130
Figure 36. Shear Wave Velocity Versus Void Ratio. Comparison Between Predictions from Regular Cubic Arrays and Measurements in Quartz Sand	131
Figure 37. Histogram and Random Two-Dimensional Packing of Equal Sized Spherical Steel Balls (after Shahinpoor and Shahrpass, 1982).	132
Figure 38. Cut-Away Artistic View of a Space Filling Configuration of Voronoi Polyhedra Containing Regular Arrays of Spheres (finney, 1983)	133
Figure 39. Shear Strain Experienced by Each Inclusion, γ_i , as a Function of its Shear Stiffness, G_i . Comparison Between Finite Element (FEM) and Self Consistent Method Results.	134
Figure 40. Discretization of Probability Density Function of Porosity, $p(n)$, to Represent a Medium of Macroscopic Porosity, $\bar{n}=0.35$, by a Combination of Three Regular Cubic Arrays.	135
Figure 41. Shear Modulus, G_{max} , Versus Isotropic Confining Pressure Analytical and Experimental Results for $e=0.46$	136
Figure 42. Shear Modulus, G_{max} , Versus Isotropic Confining Pressure Analytical and Experimental Results for $e=0.54$	137
Figure 43. Shear Modulus, G_{max} , Versus Isotropic Confining Pressure Analytical and Experimental Results for $e=0.58$	138

LIST OF FIGURES

	Page
Figure 44. Confining Pressure Versus Volumetric Strain. Analytical and Experimental Results for $e=0.54$	139
Figure 45. Stress State on a Simple Cubic Array of Identical Spheres	140
Figure 46. 16-Element Media Used in the Simulation and Angle of Orientation of Each Element.	141
Figure 47. Stress-Strain Behavior, (c), of a Simple Cubic Array of Quartz Spheres Subjected to Biaxial Stress, $\sigma_{11}=1.61$, $\sigma_{22}=2.0$ Kg*/cm ² , Followed by Pure Shear, σ_{12} , to Failure. (a) and (b) Portray the Corresponding Force-Deformation Behavior of the "Weak" and "Strong" Contact, Respectively.	142
Figure 48. Medium 1: Stress-Strain Behavior for Hydrostatic Compression Loading starting from $\sigma_0^0=3.0$ Kg*/cm ² . . .	143
Figure 49. (a) Orientation of the Applied Principal Stresses During Pure Shear Loading with Mean Stress Constant, $\sigma_0^0=0.56(\sigma_1^0 + \sigma_2^0)=\text{Constant}$; (b) Orientation of an Element	144
Figure 50. Difference in Applied Principal Stresses, $\sigma_1^0 - \sigma_2^0$, Versus Shear Strain, $\gamma = \epsilon_1 - \epsilon_2$, Calculated for all Media (16 and 64 elements), and for Values of $\alpha=0^\circ$, 22.5° , 45° , 67.5° , and 90° (MX=medium X, AYY=inclination of σ_1 is YY degrees).	145
Figure 51. Medium 2: Compression with Constant Mean Stress ($\sigma_0^0=1.0$ Kg*/cm ²). Stress-Strain Behavior of Element E2 Oriented at $\beta=10^\circ$	146
Figure 52. Medium 2: Compression with Constant Mean Stress ($\sigma_0^0=1.0$ Kg*/cm ²). Stress-Strain Behavior of Element E4 Oriented at $\beta=50^\circ$	147
Figure 53. Medium 2: Compression with Constant Mean Stress ($\sigma_0^0=1.0$ Kg*/cm ²). Stress-Strain Behavior of Element E1 Oriented at $\beta=70^\circ$	148
Figure 54. Failure Surface of the Aggregate, Determined From Four Stress Paths.	149

LIST OF FIGURES

	Page
Figure 55. Medium 1: Stress-Strain Curve for the Aggregate for Compression Loading with Variable Mean Stress Following Isotropic Pressure, $\sigma_0^0 = 1 \text{ Kg */cm}^2$	150
Figure 56. Medium 1: Compression with Variable Mean Stress ($\sigma_0^0 = 1.0 \text{ Kg */cm}^2$) Stress-Strain Behavior of Element E1 Oriented at $\beta = 10^\circ$	151
Figure 57. Medium 1: Compression with Variable Mean Stress ($\sigma_0^0 = 1.0 \text{ Kg */cm}^2$) Stress-Strain Behavior of Element E2 Oriented at $\beta = 50^\circ$	152
Figure 58. Poisson's Ratio for the Aggregate Calculated from the Compression with Variable Mean Stress Simulation.	153
Figure 59. Medium 5: Compression with Constant Mean Stress. Stress-Strain Behavior for Element E50 oriented at $\beta = 45^\circ$	154
Figure 60. Medium 5: Compression with Constant Mean Stress. Stress-Strain Behavior for Element E44 oriented at $\beta = 45^\circ$	155
Figure 61. Medium 5: Compression with Constant Mean Stress. Stress-Strain Behavior for Element E36 oriented at $\beta = 0^\circ$	156
Figure 62. Medium 2: Compression with Constant Mean Stress ($\sigma_0^0 = 1.0 \text{ Kg */cm}^2$). Normalized Element Normal Stress, $\sigma_{11}/(\sigma_1 - \sigma_2)$ Versus Angle of Orientation β , of the Element for Three Inclinations of Principal Stress, $\alpha = 0, 45$ and 90 degrees.	157
Figure 63. Medium 2: Compression with Constant Mean Stress ($\sigma_0^0 = 1.0 \text{ Kg */cm}^2$). Normalized Element Normal Stress, $\sigma_{22}/(\sigma_1 - \sigma_2)$ Versus Angle of Orientation β , of the Element for Three Inclinations of Principal Stress, $\alpha = 0, 45$ and 90 degrees.	158
Figure 64. Medium 2: Compression with Constant Mean Stress ($\sigma_0^0 = 1.0 \text{ Kg */cm}^2$). Normalized Element Normal Stress, $\sigma_{12}/(\sigma_1 - \sigma_2)$ Versus Angle of Orientation β , of the Element for Three Inclinations of Principal Stress, $\alpha = 0, 45$ and 90 degrees.	159

LIST OF FIGURES

	Page
Figure 65. Medium 1: Stress-Strain Behavior for Cyclic Isotropic Loading, $\sigma_o^o \pm \Delta\sigma_o^o$, with $\sigma_o^o = 3 \text{ Kg}^*/\text{cm}^2$ and $\Delta\sigma_o^o = 2 \text{ Kg}^*/\text{cm}^2$	160
Figure 66. Medium 1: Stress-Strain Behavior for Cyclic Pure Shear Loading Following Isotropic Compression, $\sigma_o^o = 1.0 \text{ Kg}^*/\text{cm}^2$. (a) $\tau_c = 0.20 \text{ Kg}^*/\text{cm}^2$; (b) $\tau_c = 0.35 \text{ Kg}^*/\text{cm}^2$	161
Figure 67. Medium 1: Stress-Strain Behavior for Cyclic Pure Shear Loading Following Isotropic Compression, $\sigma_o^o = 1.0 \text{ Kg}^*/\text{cm}^2$. (a) $\tau_c = 0.420 \text{ Kg}^*/\text{cm}^2$; (b) $\tau_c = 0.43 \text{ Kg}^*/\text{cm}^2$	162
Figure 68. (a) Normalized Shear Modulus, G/G_{\max} ; (b) Damping Ratio, λ ; both Versus Shear Strain, γ . Comparison Between Values Measured in Sand, and Those Calculated with the Simulated Aggregate and the Simple Cubic Array in Pure Shear	163
Figure 69. Computation of Damping Ratio, λ , from a Stress-Strain Loop	164
Figure 70. Normalized Constrained Moduli, D_{11}/D_{11} Versus Stress Ratio, $K = \sigma_1/\sigma_2$. Comparison Between Analytical and Experimental Results. (a) in the Direction of σ_1^o ; and (b) in the Direction of σ_2^o (σ_2^o is kept constant)	165
Figure A1. Representative Unit Volume and Applied Incremental Forces.	181
Figure A2. Octant of Sphere with Center at Apex H of the Representative Unit Volume of a bcc Array, with Applied and Contact Forces Shown.	181
Figure B1. (a) Representative Unit Volume of an fcc Array with State of Stress (b) Sphere Centered a Apex A with Applied Stresses, Contact Forces and Displacements (Brauns and Leussink, 1970)	194
Figure B2. Triaxial Compression of an fcc Array of Glass Spheres: Analytical and Experimental Results (Brauns and Leussink, 1970)	194

LIST OF FIGURES

	Page
Figure 65. Medium 1: Stress-Strain Behavior for Cyclic Isotropic Loading, $\sigma_0^0 \pm \Delta\sigma_0^0$, with $\sigma_0^0 = 3 \text{ Kg */cm}^2$ and $\Delta\sigma_0^0 = 2 \text{ Kg */cm}^2$	160
Figure 66. Medium 1: Stress-Strain Behavior for Cyclic Pure Shear Loading Following Isotropic Compression, $\sigma_0^0 = 1.0 \text{ Kg */cm}^2$. (a) $\tau_c = 0.20 \text{ Kg */cm}^2$; (b) $\tau_c = 0.35 \text{ Kg */cm}^2$	161
Figure 67. Medium 1: Stress-Strain Behavior for Cyclic Pure Shear Loading Following Isotropic Compression, $\sigma_0^0 = 1.0 \text{ Kg */cm}^2$. (a) $\tau_c = 0.420 \text{ Kg */cm}^2$; (b) $\tau_c = 0.43 \text{ Kg */cm}^2$	162
Figure 68. (a) Normalized Shear Modulus, G/G_{\max} ; (b) Damping Ratio, λ Both Versus Shear Strain, γ . Comparison Between Values Measured in Sand, and Those Calculated with the Simulated Aggregate and the Simple Cubic Array in Pure Shear	163
Figure 69. Computation of Damping Ratio, λ , from a Stress-Strain Loop	164
Figure 70. Normalized Constrained Moduli, D_{11}/D_{11} Versus Stress Ratio, $K = \sigma_1^0/\sigma_2^0$. Comparison Between Analytical and Experimental Results. (a) in the Direction of σ_1^0 ; and (b) in the Direction of σ_2^0 (σ_2^0 is kept constant)	165
Figure A1. Representative Unit Volume and Applied Incremental Forces.	181
Figure A2. Octant of Sphere with Center at Apex H of the Representative Unit Volume of a bcc Array, with Applied and Contact Forces Shown.	181
Figure B1. (a) Representative Unit Volume of an fcc Array with State of Stress (b) Sphere Centered a Apex A with Applied Stresses, Contact Forces and Displacements (Brauns and Leussink, 1970)	194
Figure B2. Triaxial Compression of an fcc Array of Glass Spheres: Analytical and Experimental Results (Brauns and Leussink, 1970)	194

LIST OF FIGURES

	Page
Figure D1. Configuration of the Media Used in the Simulations and Orientation of Each Element	217
Figure D2. Configuration of the Media Used in the Simulations and Orientation of Each Element	218
Figure D3. Configuration of Medium 5 Used in the Simulations and Orientation of Each Element	219
Figure E1. Medium 2: Compression with Constant Mean Stress ($\sigma_0^0=1.0 \text{ Kg */cm}^2$). Stress-Strain Behavior of Element E1 Oriented at $\beta=70^\circ$	221
Figure E2. Medium 2: Compression with Constant Mean Stress ($\sigma_0^0=1.0 \text{ Kg */cm}^2$). Stress-Strain Behavior of Element E2 Oriented at $\beta=10^\circ$	222
Figure E3. Medium 2: Compression with Constant Mean Stress ($\sigma_0^0=1.0 \text{ Kg */cm}^2$). Stress-Strain Behavior of Element E3 Oriented at $\beta=40^\circ$	223
Figure E4. Medium 2: Compression with Constant Mean Stress ($\sigma_0^0=1.0 \text{ Kg */cm}^2$). Stress-Strain Behavior of Element E4 Oriented at $\beta=50^\circ$	224
Figure E5. Medium 2: Compression with Constant Mean Stress ($\sigma_0^0=1.0 \text{ Kg */cm}^2$). Stress-Strain Behavior of Element E5 Oriented at $\beta=20^\circ$	225
Figure E6. Medium 2: Compression with Constant Mean Stress ($\sigma_0^0=1.0 \text{ Kg */cm}^2$). Stress-Strain Behavior of Element E6 Oriented at $\beta=30^\circ$	226
Figure E7. Medium 2: Compression with Constant Mean Stress ($\sigma_0^0=1.0 \text{ Kg */cm}^2$). Stress-Strain Behavior of Element E7 Oriented at $\beta=60^\circ$	227
Figure E8. Medium 2: Compression with Constant Mean Stress ($\sigma_0^0=1.0 \text{ Kg */cm}^2$). Stress-Strain Behavior of Element E8 Oriented at $\beta=10^\circ$	228
Figure E9. Medium 2: Compression with Constant Mean Stress ($\sigma_0^0=1.0 \text{ Kg */cm}^2$). Stress-Strain Behavior of Element E9 Oriented at $\beta=40^\circ$	229

LIST OF FIGURES

	Page
Figure E10. Medium 2: Compression with Constant Mean Stress ($\sigma_0^0=1.0 \text{ Kg */cm}^2$). Stress-Strain Behavior of Element E10 Oriented at $\beta=80^\circ$	230
Figure E11. Medium 2: Compression with Constant Mean Stress ($\sigma_0^0=1.0 \text{ Kg */cm}^2$). Stress-Strain Behavior of Element E11 Oriented at $\beta=20^\circ$	231
Figure E12. Medium 2: Compression with Constant Mean Stress ($\sigma_0^0=1.0 \text{ Kg */cm}^2$). Stress-Strain Behavior of Element E12 Oriented at $\beta=80^\circ$	232
Figure E13. Medium 2: Compression with Constant Mean Stress ($\sigma_0^0=1.0 \text{ Kg */cm}^2$). Stress-Strain Behavior of Element E13 Oriented at $\beta=30^\circ$	233
Figure E14. Medium 2: Compression with Constant Mean Stress ($\sigma_0^0=1.0 \text{ Kg */cm}^2$). Stress-Strain Behavior of Element E14 Oriented at $\beta=60^\circ$	234
Figure E15. Medium 2: Compression with Constant Mean Stress ($\sigma_0^0=1.0 \text{ Kg */cm}^2$). Stress-Strain Behavior of Element E15 Oriented at $\beta=70^\circ$	235
Figure E16. Medium 2: Compression with Constant Mean Stress ($\sigma_0^0=1.0 \text{ Kg */cm}^2$). Stress-Strain Behavior of Element E16 Oriented at $\beta=50^\circ$	236
Figure F1. Medium 1: Compression with Variable Mean Stress ($\sigma_0^0=1.0 \text{ Kg */cm}^2$). Stress-Strain Behavior of Element 1 Oriented at $\beta=10^\circ$	238
Figure F2. Medium 1: Compression with Variable Mean Stress ($\sigma_0^0=1.0 \text{ Kg */cm}^2$). Stress-Strain Behavior of Element 2 Oriented at $\beta=50^\circ$	239
Figure F3. Medium 1: Compression with Variable Mean Stress ($\sigma_0^0=1.0 \text{ Kg */cm}^2$). Stress-Strain Behavior of Element 3 Oriented at $\beta=60^\circ$	240
Figure F4. Medium 1: Compression with Variable Mean Stress ($\sigma_0^0=1.0 \text{ Kg */cm}^2$). Stress-Strain Behavior of Element 4 Oriented at $\beta=20^\circ$	241

LIST OF FIGURES

	Page
Figure F5. Medium 1: Compression with Variable Mean Stress ($\sigma_0^0=1.0 \text{ Kg */cm}^2$). Stress-Strain Behavior of Element 5 Oriented at $\beta=80^\circ$	242
Figure F6. Medium 1: Compression with Variable Mean Stress ($\sigma_0^0=1.0 \text{ Kg */cm}^2$). Stress-Strain Behavior of Element 6 Oriented at $\beta=70^\circ$	243
Figure F7. Medium 1: Compression with Variable Mean Stress ($\sigma_0^0=1.0 \text{ Kg */cm}^2$). Stress-Strain Behavior of Element 7 Oriented at $\beta=10^\circ$	244
Figure F8. Medium 1: Compression with Variable Mean Stress ($\sigma_0^0=1.0 \text{ Kg */cm}^2$). Stress-Strain Behavior of Element 8 Oriented at $\beta=30^\circ$	245
Figure F9. Medium 1: Compression with Variable Mean Stress ($\sigma_0^0=1.0 \text{ Kg */cm}^2$). Stress-Strain Behavior of Element 9 Oriented at $\beta=20^\circ$	246
Figure F10. Medium 1: Compression with Variable Mean Stress ($\sigma_0^0=1.0 \text{ Kg */cm}^2$). Stress-Strain Behavior of Element 10 Oriented at $\beta=80^\circ$	247
Figure F11. Medium 1: Compression with Variable Mean Stress ($\sigma_0^0=1.0 \text{ Kg */cm}^2$). Stress-Strain Behavior of Element 11 Oriented at $\beta=70^\circ$	248
Figure F12. Medium 1: Compression with Variable Mean Stress ($\sigma_0^0=1.0 \text{ Kg */cm}^2$). Stress-Strain Behavior of Element 12 Oriented at $\beta=20^\circ$	249
Figure F13. Medium 1: Compression with Variable Mean Stress ($\sigma_0^0=1.0 \text{ Kg */cm}^2$). Stress-Strain Behavior of Element 13 Oriented at $\beta=60^\circ$	250
Figure F14. Medium 1: Compression with Variable Mean Stress ($\sigma_0^0=1.0 \text{ Kg */cm}^2$). Stress-Strain Behavior of Element 14 Oriented at $\beta=50^\circ$	251
Figure F15. Medium 1: Compression with Variable Mean Stress ($\sigma_0^0=1.0 \text{ Kg */cm}^2$). Stress-Strain Behavior of Element 15 Oriented at $\beta=30^\circ$	252

LIST OF FIGURES

	Page
Figure F16. Medium 1: Compression with Variable Mean Stress ($\sigma_0^0=1.0 \text{ Kg */cm}^2$). Stress-Strain Behavior of Element 16 Oriented at $\beta=40^\circ$	253
Figure G1. Medium 2: Compression with Constant Mean Stress $\sigma_0^0=1.0 \text{ Kg */cm}^2$. Normalized Element Stress Versus Applied Principal Strain Difference for All Elements Oriented 10°	255
Figure G2. Medium 2: Compression with Constant Mean Stress $\sigma_0^0=1.0 \text{ Kg */cm}^2$. Normalized Element Stress Versus Applied Principal Strain Difference for All Elements Oriented 20°	256
Figure G3. Medium 2: Compression with Constant Mean Stress $\sigma_0^0=1.0 \text{ Kg */cm}^2$. Normalized Element Stress Versus Applied Principal Strain Difference for All Elements Oriented 30°	257
Figure G4. Medium 2: Compression with Constant Mean Stress $\sigma_0^0=1.0 \text{ Kg */cm}^2$. Normalized Element Stress Versus Applied Principal Strain Difference for All Elements Oriented 40°	258
Figure G5. Medium 2: Compression with Constant Mean Stress $\sigma_0^0=1.0 \text{ Kg */cm}^2$. Normalized Element Stress Versus Applied Principal Strain Difference for All Elements Oriented 50°	259
Figure G6. Medium 2: Compression with Constant Mean Stress $\sigma_0^0=1.0 \text{ Kg */cm}^2$. Normalized Element Stress Versus Applied Principal Strain Difference for All Elements Oriented 60°	260
Figure G7. Medium 2: Compression with Constant Mean Stress $\sigma_0^0=1.0 \text{ Kg */cm}^2$. Normalized Element Stress Versus Applied Principal Strain Difference for All Elements Oriented 70°	261
Figure G8. Medium 2: Compression with Constant Mean Stress $\sigma_0^0=1.0 \text{ Kg */cm}^2$. Normalized Element Stress Versus Applied Principal Strain Difference for All Elements Oriented 80°	262

LIST OF FIGURES

	Page
Figure G9. Medium 2: Compression with Constant Mean Stress $\sigma_o^o=1.0 \text{ Kg}^*/\text{cm}^2$. Normalized Element Stress Versus Applied Principal Strain Difference for All Elements Oriented 10°	263
Figure G10. Medium 2: Compression with Constant Mean Stress $\sigma_o^o=1.0 \text{ Kg}^*/\text{cm}^2$. Normalized Element Stress Versus Applied Principal Strain Difference for All Elements Oriented 20°	264
Figure G11. Medium 2: Compression with Constant Mean Stress $\sigma_o^o=1.0 \text{ Kg}^*/\text{cm}^2$. Normalized Element Stress Versus Applied Principal Strain Difference for All Elements Oriented 30°	265
Figure G12. Medium 2: Compression with Constant Mean Stress $\sigma_o^o=1.0 \text{ Kg}^*/\text{cm}^2$. Normalized Element Stress Versus Applied Principal Strain Difference for All Elements Oriented 40°	266
Figure G13. Medium 2: Compression with Constant Mean Stress $\sigma_o^o=1.0 \text{ Kg}^*/\text{cm}^2$. Normalized Element Stress Versus Applied Principal Strain Difference for All Elements Oriented 50°	267
Figure G14. Medium 2: Compression with Constant Mean Stress $\sigma_o^o=1.0 \text{ Kg}^*/\text{cm}^2$. Normalized Element Stress Versus Applied Principal Strain Difference for All Elements Oriented 60°	268
Figure G15. Medium 2: Compression with Constant Mean Stress $\sigma_o^o=1.0 \text{ Kg}^*/\text{cm}^2$. Normalized Element Stress Versus Applied Principal Strain Difference for All Elements Oriented 70°	269
Figure G16. Medium 2: Compression with Constant Mean Stress $\sigma_o^o=1.0 \text{ Kg}^*/\text{cm}^2$. Normalized Element Stress Versus Applied Principal Strain Difference for All Elements Oriented 80°	270

List of Symbols

Greek Letters:

α^*	: constant; value of the Eshelby S-tensor
α	: relative vertical displacement between the centers of two spheres in contact
α	: angle of orientation of major principal stress
a_{sc}, a_{bcc}, a_{fcc}	: length of edge of representative volume of the sc, bcc and fcc arrays respectively
β	: constant ($= dT/dN$)
β	: angle of orientation of the element
β^*	: constant; value of the Eshelby S-tensor
γ	: engineering shear strain
$\bar{\gamma}_i$: average shear strain experienced by inclusion i
γ_t	: threshold strain
γ_{ij}	: engineering shear strains (components of the strain tensor)
δ_{ij}	: Kronecker delta
δ_{ij}	: displacement
δ	: horizontal displacement between the centers of two spheres in contact
ϵ_{ij}	: strain tensor
ϵ^e, ϵ^p	: elastic and plastic strains respectively
$\bar{\epsilon}_{v_i}$: average volumetric strain experienced by inclusion i
$\bar{\epsilon}_v$: average macroscopic volumetric strain
θ	: constant ($= f/\beta$)
θ_z	: angle of incidence of S-wave

λ : coefficient of proportionality in plastic flow rule
 λ : constant, parameter of the probability density function of the void ratio, $p(e)$
 ν : Poisson's ratio
 ν^* : macroscopic Poisson's ratio
 ν_s : Poisson's ratio of the spheres
 π : 3.14159
 ρ : mass density
 σ_{ii} ($i=1,2,3$) : normal stress applied to regular array
 σ_{ij} : stress tensor
 σ_{ij} ($i,j=1,2,3$): shear stress applied to regular array
 σ_{ij}^o : applied (macroscopic) state of stress
 σ_a : axial stress
 σ_a, σ_b : principal stresses in directions of propagation and polarization
 σ_c : principal stress in direction of no propagation/no polarization
 σ_o : isotropic confining pressure
 $\bar{\sigma}_o$: mean effective stress
 σ_i ($i=1,2,3$) : principal stress
 $\bar{\sigma}_i$ ($i=1,2,3$) : effective principal stress
 $\frac{1}{\sigma_o}$: isotropic stress experienced by inclusion i
 σ_o^o : applied isotropic stress
 τ^o : applied shear stress
 τ : shear stress

τ^*	: shear stress at failure ($=f\sigma_0$)
σ_v, σ_n	: vertical and horizontal stresses
Latin Letters :	
A	: area of face of elementary volume
a	: constant ($0.15 \leq a \leq 0.23$)
a	: radius of area of contact between two spheres in contact
C	: constant
C_{ijkl}	: Compliance Matrix
C_n, C_t	: Normal and Tangential Compliance respectively
C_n	: Uniformity Coefficient
c_1	: volume concentration
D, D_{ij}	: Constrained Modulus
\bar{D}, D	: Displacement between centers of two spheres in contact
D_{10}	: percent passing
$\bar{d}D, dD$: Displacement increment
E	: Young's Modulus
E_s	: Young's Modulus of the spheres
e	: void ratio
e_{min}, e_{max}	: minimum and maximum void ratio respectively
\bar{e}	: mean void ratio
F	: constant
$f(\sigma_{ij})$: yield function
f	: friction coefficient
FEM	: finite element method

G_i	: shear modulus of inclusion i ($i = 1, \dots, N$)
G^*	: macroscopic shear modulus
G	: secant shear modulus
G_s	: shear modulus of the spheres
\bar{G}	: normalized shear modulus
G_{\max}	: shear modulus at very small strains
$g(\sigma_{ij})$: plastic potential
H, H_o, H_p	: tangential elastoplastic and elastic moduli
I_1	: first invariant of the stress tensor
K_i	: Bulk Modulus of inclusion i ($i = 1, \dots, N$)
K^*	: macroscopic Bulk modulus
K	: stress ratio ($K = \sigma_z/\sigma_o$)
k	: constant ($k = (2-v_s)/2(1-v_s)$)
L	: constant ($= T/fN_o$)
L^*	: constant ($= T^*/fN_o$)
M	: constant
m	: constant
m_a, m_b, m_c	: constants
n	: constant
n	: porosity
\bar{n}	: mean porosity, macroscopic porosity
n_{\min}, n_{\max}	: minimum and maximum porosity respectively
N	: Number of cycles
N	: Number of phases or materials
N	: Normal force

N_{ij}	: Contact forces at local coordinate system
N_{ij}	: Contact forces
N_0	: Normal contact force due to application of σ_0
N	: constant
\bar{N}, N	: contact normal force
P	: constant
\bar{P}, P	: contact force
P_a	: atmospheric pressure
P_{ij}	: applied forces
$p(x)$: probability density function of x
R	: radius of spheres
S_x, S_y, S_z	: elastic constants
S_{ijkl}	: Stiffness matrix
T_x, T_y	: Tangential contact forces in x and y directions
dT_n, dT_t	: outward normal and tangential components to the yield surface of the applied tangential force increment
t, t_0, t_1	: time
x_i	: coordinate
\bar{T}, T	: tangential force
T^*	: tangential force at failure ($= fN_0$)
V_p, V_s	: P and S wave velocities
V_L	: rod wave velocity

ACKNOWLEDGEMENTS

The authors wish to acknowledge the following people and organizations for their valuable assistance in this project.

The Air Force Office of Scientific Research (AFOSR), Bolling Air Force Base, Washington, D.C. who sponsored the research. Colonel Lawrence Hokanson and Dr. Spencer Wu, project managers, for their warm support and encouragement.

The Dept. of Civil Engineering of the University of Texas at Austin, for the warm hospitality and support provided during their stay in Austin in 1985.

Professor Kenneth H. Stokoe, II of the University of Texas at Austin (UT), for his wholehearted support, hospitality, encouragement, cooperation and many stimulating discussions, and Dr. Shannon H.H. Lee, also of UT, for sharing with us some of his valuable experimental data.

Professor George Dvorak of Rensselaer Polytechnic Institute (RPI), for his suggestions, which were most valuable in developing the analytical model of Chapter 6.

Professor Mark S. Shephard, also of RPI, and the staff of RPI's Interactive Computer Graphics Center, for their ideas and work related to the use of computer graphics in modelling granular arrays, and for permitting the use of computer code ABAQUS.

Professors E.H. Lee of RPI and Y.A. Bahei-El-Din for their suggestions and stimulating discussions.

Mr. Percy Ng of RPI, currently working on a similar project, for his indispensable help and stimulating discussions through this work.

Finally, we wish to thank Mrs. Jo Ann Grega for the excellent and prompt typing of this text.

ABSTRACT

The need for a micromechanical approach to modeling the stress-strain response of granular soil is discussed and justified. This work focuses on the small shear strain ($\gamma \leq 0.01\%$) behavior, and investigates the validity of modeling analytically uniform, rounded-grained quartz sand by arrays of identical elastic, rough, quartz spheres. As a first step, the stress-strain properties of six regular arrays of spheres are studied in some detail, with focus on isotropic and and biaxial boundary loading.

An analytical procedure is established for determining the elastic moduli of a random assemblage of equal, elastic, rough spheres of arbitrary mean porosity, subjected to isotropic confining pressure. The procedure uses the properties of the regular arrays already described, it accounts for the spatial distribution of porosity, and it calculates the macroscopic moduli through the Self Consistent Method. The procedure was applied to compute the shear and bulk moduli of assemblages of quartz spheres, which were then compared to static and dynamic measurements on uncycled and heavily precycled quartz sands reported in the literature. Although the theoretical sands are significantly stiffer than the actual soils, excellent agreement was found with resonant column measurements on heavily precycled Ottawa sand at small strains.

Finally, a new two-dimensional model of the stress-strain behavior of granular soil at small strains is presented. The model is based on an incremental solution to the contact problem of two equal, elastic, rough spheres and is implemented through nonlinear finite element techniques.

The results of numerical experiments conducted on this idealized aggregate are compared to laboratory data on the static and cyclic small strain behavior of actual sand, as well as to recent compressional wave velocity measurements on anisotropically consolidated dry sands, with good agreement. These measurements, performed at the large cubic triaxial facility at the University of Texas, have shown that the P-wave velocity depends only on the principal stress parallel to the direction of wave propagation; this finding was also predicted by the simulation.

Concluding, the hypothesis that certain aspects of the behavior of granular soil are due to the particulate nature of the soil is justified. These aspects cannot be interpreted and reproduced analytically unless this particulate nature is taken into account.

CHAPTER 1

INTRODUCTION

The main objective of this work is to present a simple, yet rigorous, particulate mechanics model of the stress-strain response of granular soil under small shear strains, γ , of the order of $10^{-2}\%$ or less. The proposed model idealizes sand as a combination of regular arrays of elastic, rough spheres and uses Mindlin's formulation for the contacts.

"Elastic constants" of interest at very small strains(*) include the shear and bulk moduli and the Poisson's Ratio(s). Experimental results and basic considerations indicate that these "constants" depend on both the void ratio of the soil and the state of confining stresses. The variations of these moduli and of the damping of the soil with an applied shear strain up to the threshold are also of interest, as is the value of the threshold strain itself at which gross sliding occurs at the grains' contacts.

These small strain soil parameters are very important in geotechnical engineering problems involving cyclic loading or wave propagation in the soil, such as: ocean wave loading, soil structure interaction, site response, ground settlement and liquefaction during earthquakes. Due to this, a great number of experimental studies of small strain behavior

(*) The concepts of small and large shear strains as used here are consistent with usual Soil Dynamics terminology, but they do not coincide with that of traditional Soil Mechanics, where much greater strains of about 1% or larger are usually of interest.

have been performed, and correlations have been developed for practical use. Especially important are the equations for the shear modulus at very small strains, G_{\max} , in sands developed by Hardin and Richart (1963) and Seed and Idriss (1970), be used on the assumption that these soils can be treated as elastic isotropic solids. In both correlations, discussed in more detail in Section 2, $G_{\max} = A \cdot (\bar{\sigma}_0)^{0.5}$, with $\bar{\sigma}_1$, $\bar{\sigma}_2$, $\bar{\sigma}_3$ being the effective principal stresses, $\bar{\sigma}_0 = (\bar{\sigma}_1 + \bar{\sigma}_2 + \bar{\sigma}_3)/3$ is the mean effective stress and A is a soil constant which depends on void ratio or relative density. Both correlations assume that G_{\max} (and thus, also, the shear wave velocity, $V_s = (G_{\max}/\rho)^{1/2}$), is the same for isotropically or anisotropically loaded sand, provided that the mean stress $\bar{\sigma}_0$ is the same; also, both correlations assume that for the anisotropic loading case G_{\max} and V_s do not change with direction.

These assumptions for G_{\max} in sands have been challenged more recently by the experimental results obtained by Roesler (1979), Knox et al. (1982) and Yu and Richart (1984), as discussed in Section 2. Therefore, a main motivation for this work was the need, suggested by those experimental findings, for a fresh approach to our basic understanding of G_{\max} and other small-strain soil parameters. Some preliminary analytical results previously obtained by Dobry et al. (1982), had shown that a particulate mechanics approach was very well suited to this purpose, and should be the basis of this fresh approach.

The large strain ($0.01\% > \gamma$) behavior of granular soils is also very important in engineering problems involving cyclic loading, and especially those related to earthquakes. At these strains, the stress-strain

behavior becomes strongly nonlinear and hysteretic, and rearrangement of particles take place producing phenomena such as densification and pore water pressure build-up (Silver and Seed, 1971; Youd, 1972; Dobry et al., 1982; National Research Council, 1985). A number of continuum mechanics models, based mostly on the Incremental Theory of Plasticity, try to simulate this behavior and have been proposed for soils, as discussed in Chapter 3.

A summary literature review of previous relevant particulate mechanics studies is presented in Chapter 4. Many of these past investigations have focused on the very large strain ($\gamma > 1\%$) and strength behavior of granular soils; at those very large strains, gross sliding and rolling of the grains are main contributors to the overall strain, while the elasticity of the particles and contacts play a minor or negligible role. On the other hand, for the small to large strain ranges of interest of the proposed research, the elasticity of the particles and the details of the force-displacement response at the contacts are very significant factors. The discussion in Chapter 4 includes a general model recently proposed for the force-displacement response at the contact between two identical elastic spheres (Seridi and Dobry, 1984, Dobry et al., 1987).

The results of the present research are discussed in Chapters 5 through 9. Chapter 5 presents a detailed study of the differential stress-strain relations for various regular arrays of spheres. Chapter 6 describes an application of these findings, using the Self-Consistent Method, to a random arrangement of regular arrays subjected to isotropic

boundary loading, and with the arrangement having an arbitrary macroscopic void ratio. Chapter 7 presents the formulation of a two-dimensional simulation using nonlinear finite element techniques and the contact model of Chapter 4. The results of this simulation appear in Chapters 8 and 9, where an excellent agreement is noted between the simulation and laboratory measurements.

CHAPTER 2

LABORATORY MEASUREMENTS ON SANDS AT SMALL STRAINS

Starting around 1960, a number of cyclic and dynamic laboratory measurements have been performed to determine the stress-strain behavior of granular arrays and of natural sands at small strains. Properties studied have included: i) maximum shear modulus at very small strains, G_{\max} ; ii) the variation of secant modulus, G , with shear strain, γ ; iii) the Poisson's ratio of the soil; iv) the variation of shear damping ratio with strain; and v) the threshold shear strain, γ_t , at which densification and pore pressure buildup start. Many of these tests have been conducted in a triaxial cell, on sand specimens isotropically or anisotropically consolidated under a biaxial stress state ($\sigma_2 = \sigma_3$ or $\sigma_2 = \sigma_1$), with the small strain measurements performed using the pulse method, the resonant column or cyclic torsional techniques, and with particular emphasis on shear modulus determinations. Important results and state-of-the-art summaries of these modulus measurements have been presented by Duffy and Mindlin (1957), Hardin and Richart (1963), Lawrence (1965), Richart et al. (1970), Seed and Idriss (1970), Hardin and Drnevich (1972), Woods (1978), Iwasaki et al. (1978), and Tatsuoka et al. (1979).

As mentioned before, "small strains" are defined here by the condition $\gamma < \gamma_t$, as in this range the original geometry of the granular array or sand remains essentially unchanged, with very few or no particles experiencing gross sliding or rolling, and, thus, with the macroscopic strain of the array being controlled by the elastic deformations of the particles and by localized slips within the areas of contact areas

between particles. In many sands, $\gamma_t \approx 10^{-4} = 10^{-2}\%$; measurements and studies of γ_t have been presented by Drnevich and Richart (1970), Youd (1972), Pyke (1973), Dobry et al. (1980, 1981, 1981a, 1982), Dyvik et al. (1982), Oner (1984) and National Research Council (1985).

On the basis of laboratory measurements, Hardin and Richart (1963) proposed the following expression for G_{\max} :

$$G_{\max} = f(e)(\bar{\sigma}_0)^{0.5} \quad (1)$$

where e = void ratio, $f(e) = 2630(2.17-e)^2/(1+e)$ for round-grained sands, and $f(e) = 1230(2.97-e)^2/(1+e)$ for angular-grained sands; both G_{\max} and $\bar{\sigma}_0$ are in psi in Eq. 1.

Seed and Idriss (1970) proposed the alternative expression:

$$G_{\max} = 1,000 K_{2\max} (\bar{\sigma}_0)^{0.5} \quad (2)$$

where G_{\max} and $\bar{\sigma}_0$ are in psf, and $K_{2\max}$ is a function of relative density.

Eqs. 1-2 reflect the conclusion of these and other studies, that G_{\max} and V_s are mainly a function of void ratio or relative density, and of the mean effective normal stress $\bar{\sigma}_0$. Other variables, such as static shear stresses, stress history, stress path (compression versus extension loading), frequency of cyclic loading, degree of saturation, were found to have, either a small effect or no effect at all (Richart et al., 1970, Yu and Richart, 1984). One exception is that a large number of shear prestraining cycles at strains larger than the threshold was found to increase G_{\max} significantly (Drnevich and Richart, 1970).

It is useful to make explicit some of the implications of Eqs. 1-2 for anisotropically loaded dry sand, either for the general "triaxial" case in which $\sigma_1 \neq \sigma_2 \neq \sigma_3$ or, as is very usually the case in the field, the "biaxial" case, $\sigma_1 \neq \sigma_2 = \sigma_3$. (The bars have now been dropped from the stresses, as for a dry sand, $\bar{\sigma} = \sigma$). These implications are:

- i) G_{\max} and V_s depend equally on σ_1 , σ_2 and σ_3 .
- ii) For a shear wave propagating in the sand, the value of V_s is the same whatever the directions of propagation and polarization of the wave.

Implication ii) is equivalent to assume that, at very small strains, the anisotropically loaded sand can be modeled as an isotropically elastic material, defined by the two elastic constants G_{\max} and Poisson's Ratio, ν . Under the usual additional assumption that for a dry sand, $\nu \approx 0.3$ to 0.4 is a constant independent of confining stresses, a set of implications similar to i) and ii) can be obtained, but now for a dilational, P-wave, travelling in this dry sand. If we call D , V_p the constrained modulus and P-wave velocity, respectively, the corresponding implications are:

- iii) D and V_p depend equally on σ_1 , σ_2 and σ_3 , with $D \propto (\sigma_0)^{0.5}$ and $V_p \propto (\sigma_0)^{0.25}$.
- iv) The value of V_p is the same whatever the direction of propagation of the P-wave.

Five recent experimental studies have attempted to verify in detail this formulation by Hardin/Richart and Seed/Idriss, and specifically the validity of implications i) through iv) above for anisotropically loaded

dry sand.

Schmertmann (1978) measured V_p and V_s in several directions in a large dry sand specimen (4 ft diameter by 4 ft high). In these tests, a biaxial state of stress could be achieved, $\sigma_1 = \sigma_v \neq \sigma_2 = \sigma_3 = \sigma_h$, with σ_v, σ_h = vertical, horizontal stresses, with the stresses varying between 5 to 20 psi, and with a stress ratio, $\sigma_1/\sigma_3 = 1$ to 3. He found that there was a slight amount of inherent anisotropy (different wave velocities in the horizontal and vertical directions when $\sigma_v = \sigma_h$). He also found that for constant $\sigma_o = 1/3(\sigma_v + 2 \sigma_h)$ and variable σ_1/σ_3 , V_s varied less than 10%, thus verifying the basic Hardin/Richart assumption as a first approximation for V_s in this biaxial case. However, V_p was strongly affected by σ_1/σ_3 . The results suggested that, for P-waves propagating in the vertical direction, V_p depended more on σ_v than on σ_o .

Roesler (1979) measured V_s using a 1 ft³ cubical dry sand sample. In these tests, a true triaxial state of stresses was achieved. Test pressures ranged from 5.8 psi to 23 psi, with $\sigma_1/\sigma_3 = 1$ to 1.8. He propagated the shear waves along either of the principal stress directions (σ_a), with particle motions polarized in another principal direction (σ_b). The third principal direction, or out-of-plane direction, is neither a direction of propagation nor polarization (σ_c). Roesler found that his results followed the law:

$$V_s = B \sigma_a^{0.149} \sigma_b^{0.107} \sigma_c^0 \quad (3)$$

where $B = \text{constant}$. These results are illustrated in Fig. 1. For isotropic confinement ($\sigma_0 = \sigma_a = \sigma_b = \sigma_c$) they do confirm the Hardin-Richtart law that $G_{\max} \propto (\sigma_0)^{0.5}$ and $V_s \propto (\sigma_0)^{0.25}$, as $0.149 + 0.107 = 0.256$. However, for the general case, Eq. 3 contradicts Eqs. 1-2, in that now V_s is completely independent of σ_c . Also, Roesler's results for this case indicate that V_s is a function of direction and the sand cannot be treated as an isotropic elastic material; therefore, more than two elastic constants are necessary to define it.

Stokoe et al. (1980) developed at the University of Texas at Austin (U.T.) a large scale, 7 ft³ cubical triaxial facility, for the specific purpose of measuring V_s and V_p in dry sand. In this facility, a triaxial state of stress, $\sigma_1 \neq \sigma_2 \neq \sigma_3$ can be achieved. All tests performed to date at U.T. have used a local medium to fine, washed mortar sand classified as SP, with effective grain size, $D_{10} = 0.28$ mm and a uniformity coefficient $C_u = 1.7$. The sand is placed by the raining technique and is tested dry. Values of principal stresses used have ranged between 10 psi and 40 psi, with the stress ratio, $\sigma_1/\sigma_3 = 1$ to 4. Knox et al. (1982) used this facility to study V_s and, similarly to Roesler, they propagated the shear waves along one of the principal stresses (σ_a), and polarized parallel to another principal stress (σ_b). They expressed V_s as:

$$V_s = F \sigma_a^{ma} \sigma_b^{mb} \sigma_c^{mc} \quad (4)$$

where $F = \text{constant}$. They found values of $ma \approx mb \approx 0.09$ to 0.12 , and $mc \approx 0$ to 0.01 . Except for some minor differences, these results are

identical to those of Roesler, including the independence of V_s on σ_c . Kopperman et al. (1982) used the same U.T. facility and sand to study P-waves and concluded that:

$$V_p = L \sigma_a^{0.22} \quad (5)$$

where L = constant. The insensitivity of V_p to variations in the stresses σ_b and σ_c perpendicular to wave propagation is illustrated by Fig. 2. Again, and similar to Schmertmann's findings, these results indicate that V_p is strongly dependent on direction of propagation when the sand is anisotropically loaded.

Yu and Richart (1984) performed resonant column tests on three sands subjected to a biaxial state of stress. Their results essentially agreed with those of Roesler and Knox; however, they found some effect of the stress ratio on the results. They proposed for G_{max} the expression:

$$G_{max} = C P_a^{0.49} \sigma_v^{0.26} \sigma_h^{0.25} (1 - a K_n^2) \quad (6)$$

where C =constant, P_a =atmospheric pressure, a =0.15 to 0.23, with a mean value of 0.18, $K_n = (\sigma_1/\sigma_3 - 1) / [(\sigma_1/\sigma_3)_{max} - 1]$, and $(\sigma_1/\sigma_2)_{max}$ corresponds to shear failure of the sand. Except for the factor $1 - a K_n^2$, which is usually between 0.8 and 1, Eq. 6 is consistent with Eqs. 3 and 4 proposed by Roesler and Knox.

Therefore, all of these results clearly indicate that implications i) through iv) above, associated with the currently used correlations for V_p and V_s in sands, need to be revised and upgraded. In most cases of practical interest, sands are anisotropically loaded, and thus more than

two elastic constants may be needed to specify the behavior of the soil at very small strains. For the typical biaxial state of stresses existing in the field under geostatic conditions, for which all horizontal normal stresses are equal but different from the vertical stress, the sand will behave as a cross-anisotropic elastic solid and 5 elastic constants will be generally needed (Love, 1927, Sokolnikoff, 1956). In the more general case of $\sigma_1 \neq \sigma_2 \neq \sigma_3$, as it may happen in the soil under a structure, the sand can be described as an orthotropic elastic solid, with three planes of elastic symmetry, and a total of 9 elastic constants are needed (Sokolnikoff, 1956).

The previous discussion focused on the elastic properties of sand at very small strains, $\gamma \approx 10^{-4}\%$, and especially on V_p and V_s measurements. If larger loads and strains are applied to a dry granular soil, compression-wave type loading induces a nonlinear locking stress-strain response, while shear-wave type loading induces a yielding response (see Fig. 3). This behavior is obviously associated with the particulate nature of the soil (Seed and Idriss, 1970; Hardin and Drenvich, 1972). During cyclic shear loading in sand, stress-strain hysteresis loops are generated such as shown in Fig. 4; these loops are essentially strain-rate and frequency independent. For small strains, $\gamma < \gamma_t \approx 10^{-2}\%$, the hysteretic loop repeats itself cycle after cycle, and no permanent volumetric strain is observed, thus suggesting an essentially non-destructive though nonlinear behavior, controlled mainly by the response of the contacts between the grains, and with no coupling between shear and volumetric strains. At shear strains, $\gamma > \gamma_t$, although the overall behavior remains approximately

the same, densification occurs, and there is also some increase in stiffness, with the shear stress-strain curve and the tips of the loop going up a little as the number of cycles increases (see Fig. 4). For the strain range $0.01\% < \gamma < 0.1\%$ to 1% , the monotonic and cyclic behavior of the sand is always contractive, that is, shear strains generate exclusively compressive volumetric strains, independently of the density of the sand. However, for strains larger than about $\gamma \approx 1\%$, a mixture of contractive and dilative behavior is measured in dense sands, with expansion of the soil occurring during part of the cycle in cyclic shear loading (Youd, 1972). At all strains, and for both shear and compression-type cyclic loading, the stress-strain response of dry granular soil is strongly dependent on the level of normal stresses acting on it.

CHAPTER 3

STRESS-STRAIN MATHEMATICAL MODELLING

A significant amount of research has been directed to obtain stress-strain constitutive relations for cyclic and dynamic loading of soil. Most of these studies have modelled the soil as an elastic-plastic material, using as a basis tool the Incremental Theory of Plasticity. In this type of model, which is particularly appropriate for dry granular soil, the total strain increment is equal to the sum of elastic and plastic strain increments, $d\epsilon_{ij} = d\epsilon_{ij}^e + d\epsilon_{ij}^p$, with all $d\epsilon$ being strain rate independent (Drucker and Prager, 1952; Reyes, 1966; Chen, 1975; Lade and Duncan, 1975; Prevost, 1978; Hardin, 1978). Based on the V_p measurements by Roesler previously described in Section 2, Hardin (1980) suggested the following expressions for $d\epsilon_{ij}^e$ in dry granular soil:

$$d\epsilon_x^e = \frac{F(e)}{P_a^{1-n}} * \left(\frac{d\sigma_x}{S_x \sigma_x^n} - \nu \frac{d\sigma_y}{S_y \sigma_y^n} - \nu \frac{d\sigma_z}{S_z \sigma_z^n} \right)$$

$$d\gamma_{xy}^e = \frac{2(1 + \nu)F(e)}{P_a^{1-n} S_{xy}} * \frac{d\tau_{xy}}{(\sigma_x \sigma_y)^{n/2} - \frac{\tau_{xy}^{2+n}}{\sigma_x \sigma_y}} \quad (7)$$

where ϵ_x^e = normal strain, $\gamma_{xy}^e = 2\epsilon_{xy}^e$ = engineering shear strain, and four additional equations are obtained by permutation of subscripts. In these equations, σ_x , σ_y and σ_z = normal stresses; τ_{xy} = a shear stress; P_a = atmospheric pressure; and $F(e) = 0.3 + 0.7 e^2$, where e = void ratio. Eqs. 7 contain five elastic constants (S_x , S_y , S_z , S_{xy} and ν); based on

Roesler's experimental V_s results, a power of stress $n = 0.5$ was proposed.

A variety of associated and nonassociated flow rules have been proposed for the plastic strain increment, of the form:

$$d\epsilon_{ij}^p = \lambda \frac{\partial g}{\partial \sigma_{ij}} \quad (8)$$

where λ = coefficient of proportionality, and $g(\sigma_{ij})$ is the plastic potential function, which may or may not coincide with the yield function $f(\sigma_{ij})$ at which plastic strains develop. Figure 5 shows the shapes of a number of plastic potential surfaces proposed for soil by different authors.

In the simplest type of elastic-plastic model, there is only one yield (failure) surface. For stresses below that surface, the behavior is assumed to be perfectly elastic. However, granular and other soils develop plastic strains even at the small shear strains of interest to this report. To allow for this behavior, a wide variety of strain-hardening laws have been proposed, including families of yield surfaces and specific strain-hardening yield rules. In some of these models, the elastic region is completely eliminated, thus allowing for plastic flow at very low levels of stress and strain (Mroz, 1967; Prevost, 1977). One of the earliest developments included various cap models, based on the work done at Cambridge University by Roscoe and his co-workers (i.e., Roscoe, 1970). This includes the models proposed in several papers by DiMaggio and Sandler (1971), which have been widely used for dynamic analyses of soil response to explosions. Several capped

yield models are included in Fig. 5.

An important aspect of the development of elastic-plastic models is the definition of the strain-hardening law, which defines the modifications of the yield surface(s) in the course of the plastic flow. This is especially critical for cyclic loading, where the type of strain-hardening determines the stress-strain behavior after load reversals. In most of the models described above, which were originally developed for monotonic loading, isotropic strain-hardening is assumed (Hill, 1950), with the yield surfaces expanding as the stresses increase (Fig. 6). When isotropic hardening is assumed, a large amount of load reversal is required for additional yielding to occur, in contradiction with the observed behavior of experimental hysteresis loops such as shown in Fig. 4.

A better alternative for earthquake loading is provided by the kinematic strain-hardening law, sketched in Figure 7. The kinematic model was originally proposed by Ishlinsky (1954) and Prager (1955). Iwan (1967) proposed a rheological representation for the stress-strain model, constituted by infinite elasto-plastic elements placed in series or in parallel. This model is a non-frictional one, with all the nested yield surfaces being circular cylinders in principal stress space. Mroz (1967, 1969) proposed a general model for elastic-plastic materials, composed also of a field of yield surfaces, with a combination of kinematic and isotropic strain-hardening laws. Prevost (Prevost and Hoeg, 1975; Prevost, 1977, 1978), Mroz, Norris and Zienkiewicz (1978, 1979) and Vicente and Dobry (1983), have proposed to use this model to

predict static and cyclic behavior of soils. The model is flexible enough to allow its adaptation to the cases of drained and undrained loading, and to incorporate important large strain cyclic phenomena such as densification, liquefaction and stiffness degradation. Anisotropically loaded soils are represented by nonsymmetric nested surfaces in stress space. Under cyclic shear loading, the strain-hardening behavior is basically kinematic for the reasons described above. A simultaneous isotropic hardening (or softening) is allowed with the corresponding expansion or contraction of the yield surfaces as cyclic loading develops. This isotropic expansion (contraction) thus could simulate in dry granular soil the observed increase of stiffness caused by cyclic loading above $\gamma_t \approx 10^{-2}\%$.

CHAPTER 4

THE MICROMECHANICAL APPROACH

Eqs. 1-2 for G_{\max} and similar expressions for other small strain moduli in dry sands assume that the controlling normal stress parameter is the mean stress σ_0 : $G_{\max} = f(\sigma_0)$. As discussed in Chapter 2, more detailed measurements have revealed the elastic anisotropy of a dry sand subjected to different principal stresses, and they have also shown that the functional relationship between principal stresses $\sigma_1, \sigma_2, \sigma_3$, on one hand, and G_{\max} and other elastic constants on the other, is not $G_{\max} = f(\sigma_0)$ but rather $G_{\max} = f(\sigma_a, \sigma_b)$; similarly, for the constrained modulus, $D = f(\sigma_a)$. Derivations shown later in Section 5.1 for a simple cubic regular array of elastic rough spheres match very well with those recent experimental findings in sands. This strongly suggests that a micro-mechanical (particulate mechanics) approach should be used to analytically simulate and generalize the experimental observations.

A great number of studies have been performed using particulate models to understand and model the behavior of cohesionless soils and other granular materials. Most of these investigations have been analytical, but they have also included measurements in actual granular soils, as well as in regular or random arrays of spheres (3-D) or disks/rods (2-D); a number of them have dealt with the load-deformation characteristics at the contact between two elastic bodies possessing friction (Mindlin's problem). State-of-the-art summaries have been presented by Deresiewicz (1958, 1973), Mogami (1965), Scott and Ko (1969), Richart et al. (1970), White (1965), Harr (1977), and Dobry and Grivas (1978),

between others. The proceedings of two US/Japan seminars on the mechanics of granular materials contain excellent papers on the subject (Cowin and Satake, 1978; Jenkins and Satake, 1983).

A number of these studies have focused on the probabilistic aspects and statistical distributions of different parameters within the soil or granular medium, and their effect on the mechanical behavior of the array. These have included investigations of the orientations of the individual particles, of the spatial distribution of porosity, and of the distribution of number, orientation and levels of force transmitted by the contacts, conducted between others by Smith et al. (1929), Dantu (1957), Field (1963), Mogami (1965), Grivas and Harr (1974), Oda (1974), Yanagisawa (1978), Shahinpoor and Shahrpass (1982), Nemat-Nasser and Mehrabadi (1983), and Dobry and Petrakis (1984).

Many of those analytical investigations, computer simulations and observations have focused on the stress-strain behavior at very large strains and on the failure of dry granular media. Because of this very large strain nature of the phenomena, the load-deformation characteristics of the particles' contacts have played a minor or negligible role, and the emphasis has been on changes in the geometric arrangement of the grains due to their sliding and rolling. In some of these investigations the compliance of the contacts has been eliminated altogether by assuming perfectly rigid particles. Some important references here are Rowe (1962), Morgenstern (1963), Horne (1965), Konishi (1978), and Oda et al. (1983). Cundall and Strack (1983) performed numerical experiments of 2-D random arrays of disks using an explicit finite difference procedure

(see Fig. 8). In these, the authors successfully simulated "compression triaxial" loading to failure, and studied in detail the spatial distribution of contact forces and the distribution and relative contributions of sliding and rolling to macroscopic strain, during anisotropic deviatoric loading with constant σ_3 . One of their conclusions for this deviatoric loading is that the major principal stress σ_1 is transmitted mainly by a few "stiff chains" of particles having large contact forces, with the particles in between chains being lightly loaded; sliding and rolling occurs mainly in those lightly loaded regions. Oner (1984) worked with a similar numerical scheme to predict the observed threshold strain γ_t at which sliding and rolling starts, while Dobry et al. (1982) used a regular simple cubic array of spheres for the same purpose.

Of special interest are the investigations which have studied the stress-strain behavior of granular arrays considering the elasticity of the particles and the corresponding compliances at the contacts. Most of these studies have assumed spherical grain shapes and elastically isotropic grains characterized by three material constants (two elastic and one friction coefficient). All of these investigations have used the normal and tangential compliances at the contact between two elastic bodies, derived by Hertz (1882), Cattaneo (1938), and Mindlin and his co-workers (Mindlin, 1949, Mindlin et al. 1951, Mindlin and Deresiewicz, 1953). Figures 9 and 10 show, respectively, the distortion of two spheres subjected to normal (N) and tangential (T) contact loads, and the tangential load-displacement curve for constant N. As noted in the summary reviews of the contact theory by Deresiewicz (1958, 1973) and

Dobry and Grivas (1978), Mindlin and his co-workers developed the basic theoretical framework of the contact problem, and solved it for some special force time histories; however, the general problem of computing the displacements for a contact force $\vec{P} = \vec{N} + \vec{T}$, whose magnitude and direction change arbitrarily, remained unsolved. Only very recently, Seridi and Dobry (1984) provided a general and practical solution to this general problem, thus making it possible the use of direct stiffness and finite difference techniques to simulate the 3-D response of granular array at small strains. A more detailed discussion of this general solution is presented in Section 4.1.

The contact theory has been repeatedly used to predict the elastic stress-strain properties of granular arrays of spheres. Several authors calculated the influence of isotropic confining pressure on V_p and V_s for various arrays of smooth and rough spheres, and concluded that both velocities increase proportionally to $(\sigma_0)^{1/6}$ (Hara, 1935, Takahashi and Sato, 1950, Gassman, 1951, White and Sengbush, 1953, Brandt, 1955). Of special interest here are some detailed analytical and experimental investigations of regular arrays of equal spheres. Deresiewicz (1958) lists the five stable regular arrays included in Table 1 and sketched in Fig. 11, which range from the loosest simple cubic, (void ratio, $e = 0.91$) to the densest pyramidal (also called face centered cubic array) and tetrahedral (also called hexagonal close packed), both with $e = 0.35$. More complete lists and descriptions of feasible regular arrays have been presented by Filep (1936), Brown (1978) and Shahinpoor (1981). Table 2 reproduces one of these lists containing 31 arrays, while Fig. 12 presents elevation and

plane views for one of the loosest arrays of Table 2 (Cell No. 2 with $e = 1.94$). Deresiewicz (1958a) investigated in detail the simple cubic array subjected to an initial isotropic loading followed by an arbitrary stress history. He found that the array is statically determinate in this case, provided that the stress field is uniform, with a one-to-one correspondence between the nine components of the stress tensor and the nine independent components of the contact forces. Whitman et al. (1964) studied a 2-D version of the simple cubic array subjected to triaxial and confined compression. Duffy and Mindlin (1957), Duffy (1959) and Hendron (1963) investigated the densest arrays of Fig. 11 and Table 1, which are statically indeterminate, including some measurements of compressional (rod) wave velocity, V_L , in stainless steel granular bars loaded isotropically (see Fig. 13). As shown in the figure, the measured values of V_L are somewhat smaller than predicted, with the difference being greater at small values of σ_0 , and with this difference increasing for the low tolerance balls; at high pressures the measured V_L approach the predicted one. As a result, the observed $V_L \propto (\sigma_0)^m$, where $m > 1/6 = 0.167$ predicted by the theory. This difference is explained by Deresiewicz (1958), by the small differences in size between the actual spheres, which results in the number of actual, load-transmitting contacts being smaller than predicted; thus, the array is less stiff than calculated. When the tolerance becomes higher or the pressure increases, the number of these actual contacts also increases and approaches the theoretical value, and thus the measured velocity also approaches the prediction. As discussed in Chapter 2, values of $m \approx 0.25 > 0.167$ have also been measured for V_s

in isotropically loaded sands, most probably due to the same reason: an increase in the number of actual contacts as σ_0 increases.

Several approaches have been used to model the effect of deviations from regularity in arrays of equal or unequal spheres. Smith et al. (1929) proposed considering a random array as formed by clusters of loose and dense regular arrays, each present in such proportion as to yield the overall void ratio or porosity; this idea was generalized by Munro and Jowitt (1974) and Brown (1978), who used the concept of maximum entropy to find the contribution of each regular array. Ko and Scott (1967) used a similar procedure to investigate the stress-strain behavior under isotropic compression; in this study, "holey" models were used, in which some of the spheres in both the loose and the dense regular component array are slightly smaller than the other spheres. In this way the effect on the bulk modulus of the increased number of contacts caused by an increasing pressure, was incorporated into the model. Perry and Brown (1981) studied the influence of having different size spheres on the compliance of the array. Davis and Deresiewicz (1977) investigated the compressibility of a 3-D random array of smooth equal spheres subjected to isotropic loading. Walton (1987) derived a method for computing the effective elastic moduli of a random packing of identical elastic spheres subjected to hydrostatic or uniaxial compression. For simplicity, he assumed that the spheres are either infinitely rough or perfectly smooth. Serrano and Rodriguez-Ortiz (1973) suggested a method for generating random configurations of unequal disks or spheres having a prescribed grain size distribution; their work was continued by the 2-D numerical

simulations by Cundall and by Oner, previously discussed.

4.1 General Solution to the Contact Problem

The problem of the contact of two elastic, elliptical, semi-infinite bodies subjected to a normal force was first studied by Hertz (1882), who also solved the specialized case of the contact of two elastic spheres subjected to a normal force, N . This solution demonstrated for the first time that the force-deformation behavior at the contact is nonlinear elastic. Subsequently, all work on the same topic was concerned with the loading of bodies by normal forces, until Cattaneo (1938), Mindlin (1949), and Mindlin and Deresiewicz (1953) addressed the problem of the contact of two elastic, rough spheres subjected to a combination of normal and tangential forces, and presented a number of closed form solutions for each of the cases studied. Recently, Walton (1978) studied the problem of the oblique contact of two equal spheres for the case in which both the tangential normal forces are applied simultaneously; this is a different case from the work mentioned above and it will not be discussed here.

The general case of two elastic, rough spheres subjected to a normal force followed by a tangential force, (Fig. 9), solved by Cattaneo (1938) and Mindlin (1949), is a problem of the linear theory of elasticity; however, since the solution yields an infinite shear stress at the edge of the contact area, a slip needs to be prescribed at this edge, which transforms the formulation into a mixed boundary value problem where the stress and the displacement are known at the contact. This permanent set induces a nonlinear behavior, which is different from that computed by

Hertz, since it is accompanied by energy dissipation. As demonstrated by Mindlin and Deresiewicz (1953), due to the slip, the force-deformation relations depends now on the entire past history of the loading as well as the instantaneous rates of change of the normal and tangential forces. A typical force-deformation behavior of two spheres subjected to a constant normal force, N , and to a monotonically increasing tangential force, T , is shown in Fig. 10, where the nonlinear, yielding behavior can be clearly observed.

All of the above suggest that a phenomenological plasticity model could describe this nonlinear behavior. Such a formulation would provide the long awaited (Detesiewicz, 1958a) "general" solution to the problem of the contact of two elastic, rough spheres subjected to an arbitrary force history, which in turn, could be used in numerical simulations. This has been achieved recently through a constitutive law (Seridi and Dobry, 1984) for the force-deformation behavior of two identical elastic, rough spheres in contact under a combination of arbitrarily varying normal and tangential forces, which was implemented through the program CONTACT (Dobry et al., 1987). This model is an elastic-plastic incremental model with kinematic hardening, the main features of which are similar to those of the plasticity models described in Chapter 3, and are described below:

Yield Condition:

Since failure of the contact occurs when the tangential force, $T = (T_x^2 + T_y^2)^{1/2}$ exceeds fN , see Fig. 10, where f is the coefficient of friction, T_x and T_y the force components in the x and y directions and N

the normal force, the failure surface is defined as follows:

$$T^2 = T_x^2 + T_y^2 = f^2 N^2 \quad (9)$$

This is the equation for a cone in the three-dimensional force space, N , T_x , T_y (see Fig. 14).

Mindlin and Deresiewicz (1953) demonstrated that in the loading case where $0 < dT/dN < f$, no energy is dissipated, while for $dT/dN > f$ energy is dissipated. This indicates that the yield surfaces are also cones of semi-angle $\phi = \tan^{-1}f$ parallel to the failure cone, the positions of which are determined by the history of the loading, as shown in Fig. 14. Therefore, the equation of any yield surface is:

$$(T_x - x)^2 + (T_y - y)^2 = f^2 (N - N_1)^2 \quad (10)$$

where $\vec{X} = x \hat{i} + y \hat{j} + N_1 \hat{k}$ is the location vector of the apex of the conic surface, and $\vec{F} = T_x \hat{i} + T_y \hat{j} + N \hat{k}$ is the current force point (Fig. 14).

Since the two spheres subjected to a tangential force are constantly slipping, this implies that there is an infinite number of yield cones. The elastic region is the inside of the cone whose apex is at the current force point.

Flow Rule:

For a given force increment $d\vec{F} = dN \hat{k} - dT \hat{t}$, the increment of displacement between the centers of the two spheres is:

$$d\vec{D} = d\delta_x \hat{i} + d\delta_y \hat{j} + d\alpha \hat{k} = d\delta + d\alpha \hat{k} \quad (11)$$

The value of $d\vec{D}$ is given by:

$$d\vec{D} = \frac{dN}{2Ga} \frac{\hat{k}}{1-\nu} + \frac{fdN}{H_0} \hat{n} + \frac{dT_n - fdN}{H} \hat{n} + \frac{dT_t}{H_p} \hat{t} \quad (12)$$

where: \hat{n} : normal unit vector to the yield circle at the current force point,

\hat{t} : tangential unit vector tangent to the yield circle at the current force point

$$dT_n = d\vec{T} \cdot \hat{n} \quad (13)$$

$$dT_t = d\vec{T} \cdot \hat{t} = (dT^2 - dT_n^2)^{1/2} \quad (14)$$

$$d\vec{T} = dT_n \hat{n} + dT_t \hat{t} \quad (15a)$$

$$= d\vec{T}_n + d\vec{T}_t \quad (15b)$$

$H_0 = \frac{4G_a}{2-\nu}$ is the elastic modulus

$H = H_0 \left(1 - \frac{K}{fN}\right)^{1/3}$, elastoplastic modulus corresponding to the yield circle of radius K

$$H_p = \frac{8G_a}{2-\nu} \frac{K}{3fN} \left[1 - \left(1 - \frac{1}{fN}\right)^{2/3}\right] \quad (16)$$

is the tangential elastic modulus

f : coefficient of friction of the material of the spheres

$a = (BNR)^{1/3}$, with $B = \frac{3(2-\nu)}{8G}$

R = radius of the two spheres

Hardening Rule:

In the 3-D force space, the axis of any yield surface translates without rotation in such a way that it remains always parallel to the N-axis. This is clearly a kinematic hardening behavior, the mathematical expression of which is given by:

$$\vec{dX} = d\vec{T} - f dN \hat{n} + (K + fdN) d\hat{n} \quad (17)$$

where \vec{dX} is the translation in the π -plane of the center of the yield surface, K is the radius of the yield surface on the π -plane and $d\hat{n}$ is the change of the direction in the normal unit vector to the yield surface on the π -plane of the current force point.

A sketch depicting the rules described above appears in Fig. 14.

4.1.1 Implementation of the Model and Sensitivity Analysis

The above constitutive relation was implemented in the computer program CONTACT, as described in detail by Seridi and Dobry (1984) and Dobry et al. (1987). Subsequently, a sensitivity analysis was done in order to determine the range of the values of the force increment to be used in the incrementally linear analysis. This was done by varying the force increments in the case in which the normal force was kept constant and the tangential force increased monotonically, and by comparing the resulting displacements with those obtained using the analytical solution by Mindlin and Deresiewicz (1953). It was found that the value of the tangential displacement obtained was insensitive to the size of the force increment, if the ratio of the normal to the tangential force increment is less than 1/50; it was also found that the error is less than 2% if

this ratio is about $1/30$ (Dobry et al., 1987). In all cases described in the next section, as well as in the numerical simulations of Chapter 7, increments of similar size were used.

4.1.2 Verification of the Model

The above constitutive relation, implemented in the computer program CONTACT, was subsequently tested to verify that it reproduces accurately the analytical solutions obtained by Mindlin and Deresiewicz (1953). Six of the cases originally solved by Mindlin and Deresiewicz (1953) are presented here, but this time the force-deformation behavior of the two spheres in contact is computed using the program CONTACT and the elastic properties of quartz ($E_s = 295,182 \text{ Kg}^*/\text{cm}^2$, $\nu_s = 0.15$ and $f = 0.5$, White, 1964). Because of the complexity of some of the cases, only six of the most easily visualized cases will be presented herein. The force-deformation curves from the analytical results of Mindlin and Deresiewicz (1953) are reproduced separately in Figs. 15 and 16, while the corresponding numerical results obtained with program CONTACT are shown in Figs. 17 to 22.

1. Load-Displacement Relation for Oscillating Oblique Force,

$dT/dN > f$ (Fig. 17):

The normal force, N , is kept constant at 1.61 Kg^* , while the applied tangential force, T , oscillates between -0.8 Kg^* and $+0.8 \text{ Kg}^*$. The results are shown in Figure 17, where the data points stand for the analytical results, and the continuous curve for the values obtained using CONTACT.

2. Oscillating Oblique Force, $dT/dN < f$ (Fig. 18):

The normal force is increased to 1.61 Kg*, and then the tangential force increases to 0.3 Kg* while the normal force decreases so that $dT/dN = 0.3$, which is less than f . Subsequently, the shear force and the normal force oscillate so that dT/dN remain constant at 0.3. It can be seen that there is no loop after one cycle; this was also found by Mindlin and Deresiewicz (1953).

3. Normal Force Increasing, Tangential Force Increasing (Fig. 19):

The normal force increases from 1.61 Kg* to 2.01 Kg*, while the tangential force increases from 0.4 to 0.6 Kg*, and then to 1.0 Kg* (as shown in the loading path in the T-N space which appears in Fig. 19). The solid line corresponds to the case in which the tangential force increases from 0 to 1.0 Kg* while the normal force remains constant. The individual points correspond to the force path described above. This corresponds to Fig. 7 in the Mindlin and Deresiewicz (1953) paper, which is reproduced in Fig. 16a.

4. Normal Force Decreasing, Tangential Force Increasing (Fig. 20):

The normal force decreases from 2.01 Kg* to 1.61 Kg* while the tangential force decreases from 0.5 Kg* to 0.3 Kg* and then increases to 0.8 Kg* (as indicated by the load path in Fig. 20). The solid curve corresponds to the force path described above, and the individual points to the case in which the tangential force increases with the normal force remaining constant (this corresponds to Fig. 16b, which is Fig. 10 in Mindlin and Deresiewicz (1953)).

5. Normal Force Increasing, Tangential Force Decreasing (Fig. 21):

The normal force increases from 1.61 Kg* to 2.01 Kg*, while the tangential force is reduced from 0.4 to 0.2 Kg* (as indicated in Fig. 21). Again, the solid lines correspond to the stress path described above, and the individual points to the force path in which the tangential force increases from 0 to 1.0 Kg* while the normal force remains constant at 1.61 Kg* (this corresponds to Fig. 16c, which is Fig. 12 in Mindlin and Deresiewicz (1953)).

6. Normal Force Decreasing, Tangential Force Decreasing (Fig. 22):

This is a complicated loading path (shown in Fig. 22). The points, once more, correspond to the force path with the constant normal force. This reproduces Fig. 14 of Mindlin and Deresiewicz, which has been reproduced in Fig. 16d.

It can be seen that the computer program CONTACT, which is based on the constitutive law derived by Seridi and Dobry (1984), reproduces accurately all the solutions obtained by Mindlin and Deresiewicz. Therefore, it can be assumed with confidence that the program functions properly. On this basis it will be used in the numerical simulations of Chapter 7.

4.2 Studies in Crystals

The concept of Micromechanics, besides its obvious application to the behavior of granular media, has been applied over the years to predict the response of polycrystalline aggregates from the behavior of single crystals. It has been demonstrated that this micromechanical

modeling can adequately interpret most of the phenomena associated with the elastic and plastic macroscopic behavior of polycrystalline media such as metals.

For years, researchers have been simulating the elastoplastic behavior of polycrystalline aggregates through a variety of analytical, semianalytical and numerical techniques (Taylor, 1938, Hershey, 1954, Bishop and Hill, 1951, 1951a, Budiansky et al., 1960, Budiansky and Wu, 1962, Lin, 1964, Lin and Ito, 1966, 1967, Hill, 1967, Canova et al., 1984, 1985). One of the approaches most commonly used is to model the polycrystal as an assemblage of equal, isotropic crystals, with N slip systems, which are randomly oriented (Fig. 23). This results in an isotropic polycrystal when the distribution of the orientation of the crystals is statistically uniform; moreover this distributes randomly in all directions the orientations of the slip planes of the monocrystals. The yield surfaces of the resulting macroscopic medium are determined by these slip planes. Plastic strain in the aggregate starts when the first individual crystal slips; after sliding has occurred in a number of these monocrystals, the yield surface(s) change (harden) accordingly. As the aggregate is loaded farther beyond the elastic range, more and more crystals slip, and eventually the failure surface is reached (Lin and Ito, 1966).

In the early stages of that research, Taylor (1938), by considering an aggregate of randomly oriented rigid-plastic for crystals under uniaxial tension, computed the amounts of slip in each crystal by assuming that the strain experienced by each monocrystal was the same as

the applied, macroscopic, uniform strain. Then, by equating the sum of the work in the monocrystals to the work done on the aggregate, he was able to obtain a tensile stress-strain curve, and a value for the yield stress of the aggregate which later was proved to be the upper bound of the actual yield stress (Lin, 1964). Taylor also showed that the slip in the monocrystal depends on the resolved shear stress (the shear stress along the slip direction and on the slip plane), and that this slip is independent of the normal stress acting on that plane. Bishop and Hill (1951) derived a relationship between the stress and the plastic strain in a polycrystalline aggregate of fcc crystals, and obtained a more refined value of the limiting value of the yield stress which they found to be $1.536\sigma_y$, where σ_y is the yield stress of the single crystal. The same value was computed by Budiansky et al. (1960), who abandoned the assumption of strain uniformity throughout the polycrystal and computed instead the stress field inside each crystal. Using general results of the Eshelby (1957) solution for the elastic field inside an elliptical, elastic inclusion contained within an elastic medium, they solved the problem of an isolated, elastic-ideally plastic, spherical grain contained within an infinite, stressed elastic matrix, and they proved that the stress and strain fields inside the grain, while orientation dependent, were homogeneous. Later, Budiansky and Wu (1962) considered an "average" interaction between the different phases, that is the effect of the stress release due to a slip in one group of crystals on the corresponding average stress increase in another, and they calculated numerically macroscopic stress-strain curves in simple tension and pure shear.

The behavior of a random packing of identical spheres is similar in some respects to the polycrystalline medium just described, as it is well known that random assemblages of equal spheres tend to crystalize (see Chapter 6). Since the individual grains in a uniform, granular, rounded grained soil can be modelled by spheres, it is possible to consider, in first approximation, that the individual grain packings within the sand behave like randomly oriented crystals. However, a main difference is that the properties of these grain packings are now pressure dependent and the amount of slip in each of these packings, in contrast to the polycrystalline aggregates, depends now on the normal pressure acting on the slip plane. For example, it can be assumed that a simple cubic array of equal spheres (sand grains) is a pressure dependent monocrystal with three slip planes, with each slip plane containing two slip directions 90 degrees apart. Also, at large strains beyond the first slip (corresponding to the threshold strain of the soil), the sand may experience dilation under shear which is not necessarily present in polycrystalline aggregates.

CHAPTER 5

DIFFERENTIAL STRESS-STRAIN RELATIONS FOR REGULAR ARRAYS OF SPHERES

The general solution of the problem of the contact between two spheres can be used to derive incremental stress-strain relationships for regular arrays of spheres. These stress-strain relationships are discussed in this Chapter, with particular emphasis on the behavior under isotropic loading followed by very small but arbitrary stress and strain increments, and for the following regular arrays:

- i) simple cubic array (sc, see Figs. 11a and 24), discussed in Section 5.1
- ii) body centered cubic array (bcc, see Fig. 25); discussed in Section 5.2
- iii) face centered cubic or pyramidal array (fcc, see Figs. 11d and 26); discussed in Section 5.3
- iv) cubical tetrahedral (ct, see Fig. 11b) and tetragonal-sphenoidal arrays (ts, see Fig. 11c); discussed in Section 5.4.

Most of these incremental stress-strain relations were taken from Deresiewicz (1958a), Duffy and Mindlin (1957) and Maklhouf and Stewart (1967). However, some are new; in particular, the body centered cubic array is discussed here for the first time.

In addition to the five regular arrays listed above, a sixth regular array is the hexagonal closed packed or tetrahedral array (hcp, see Fig. 11e, see also Deresiewicz, 1958). Table 1 lists the most important parameters of all six arrays. A comparison of the behavior of the sc,

bcc and fcc cubic arrays is presented in Section 5.5.

5.1 Simple Cubic Array (sc)

The simple cubic array sketched in Figs. 11a and 24 is the simplest of all regular arrays of equal spheres. One sphere of radius R represents the whole array, and for a uniform stress field this is a statically determinate system with a one-to-one correspondence between the array's stresses and the contact forces (Deresiewicz, 1958a). If the normal stresses parallel to the axes of the array are σ_{ii} ($i = 1, 2, 3$, see Fig. 24), the normal contact forces N_i are: $N_i = 4R^2 \sigma_{ii}^{(*)}$. If the shear stresses parallel to the axes of the array are σ_{ij} ($i, j = 1, 2, 3$ and $i \neq j$), the corresponding tangential contact forces are $T_{ij} = 4R^2 \sigma_{ij}$. These relations occur due to equilibrium and are independent of the previous history of stresses. Therefore, they are also valid for any stress and force increments at any stage during the loading, provided that no gross sliding of the contact has taken place $dN_i = 4R^2 d\sigma_{ii}$, $dT_{ij} = 4R^2 d\sigma_{ij}$. Figure 24 illustrates the case in which an anisotropic state of stresses is applied first, with all $\sigma_{ij} = 0$, followed by small arbitrary increments $d\sigma_{ii}$ and $d\sigma_{ij}$.

A similar set of simple relations is valid in this case between the array strains and the displacements between spheres; these relations are obtained for a uniform strain field based on simple geometric considerations. If α_i = normal relative displacement of centers of the two

(*) Indicinal tensor notation is not used here, that is, σ_{ii} does not imply a sum of several terms.

adjacent spheres separated by contact i , and δ_{ij} , δ_{ik} = tangential relative displacements between the same two centers, then: $\epsilon_{ii} = \alpha_i/(2R)$; and $\gamma_{ij} = 2\epsilon_{ij} = (\delta_{ij} + \delta_{ji})/(2R)$, where ϵ_{ii} = normal strain, and γ_{ij} = engineering shear strain of the array. Again, all these relations are independent of the prior history of strains and are valid for incremental displacements and strains.

The elastic stiffnesses corresponding to small stress and strain increments applied to the array subsequent to an isotropic stress state, $\sigma_{11} = \sigma_{22} = \sigma_{33} = \sigma_0$, $\sigma_{ij} = 0$ are:

$$\begin{bmatrix} d\sigma_{11} \\ d\sigma_{22} \\ d\sigma_{33} \\ d\sigma_{12} \\ d\sigma_{13} \\ d\sigma_{23} \end{bmatrix} = \begin{bmatrix} S_{1111} & 0 & 0 & 0 & 0 & 0 \\ 0 & S_{2222} & 0 & 0 & 0 & 0 \\ 0 & 0 & S_{3333} & 0 & 0 & 0 \\ 0 & 0 & 0 & S_{1212} & 0 & 0 \\ 0 & 0 & 0 & 0 & S_{1313} & 0 \\ 0 & 0 & 0 & 0 & 0 & S_{2323} \end{bmatrix} \begin{bmatrix} d\epsilon_{11} \\ d\epsilon_{22} \\ d\epsilon_{33} \\ d\epsilon_{12} \\ d\epsilon_{13} \\ d\epsilon_{23} \end{bmatrix} \quad (18)$$

$$\text{where } S_{1111} = S_{2222} = S_{3333} = \left(\frac{3}{2}\right)^{1/3} (1-\nu_s)^{-2/3} (\sigma_0 G_s^2)^{1/3} \quad (19)$$

$$S_{1212} = S_{1313} = S_{2323} = \left(\frac{3}{2}\right)^{1/3} \frac{2(1-\nu_s)^{1/3}}{(2-\nu_s)} (\sigma_0 G_s^2)^{1/3}$$

Notice that the stiffness matrix is diagonal, and therefore the Poisson's ratio of the array, $\nu = |d\epsilon_{22}/d\epsilon_{11}| = 0$, for "triaxial" loading

corresponding to increasing σ_{11} and constant $\sigma_{22} = \sigma_{33} = \sigma_0$. The array has a $\nu = 0$ quite independently of the values of σ_0 and ν_s (see Fig. 29).

Note that, for a given σ_0 , Eqs. 18-19 describe a linearly elastic anisotropic medium. The necessary and sufficient conditions for this medium to be isotropic are of the type $S_{1111} - S_{1122} = S_{1212}$. These are satisfied only for a Poisson's ratio of the spheres, $\nu_s = 0$. This assumption results in an isotropic medium with $\nu = 0$.

For the case of an anisotropic state of stress, $\sigma_{11} \neq \sigma_{22} \neq \sigma_{33}$, $\sigma_{ij} = 0$, ($i \neq j$), the coefficients become:

$$\left. \begin{aligned} S_{1111} &= \left(\frac{3}{2}\right)^{1/3} (1-\nu_s)^{-2/3} (\sigma_{11} G_s^2)^{1/3} \\ S_{2222} &= \left(\frac{3}{2}\right)^{1/3} (1-\nu_s)^{-2/3} (\sigma_{22} G_s^2)^{1/3} \\ S_{3333} &= \left(\frac{3}{2}\right)^{1/3} (1-\nu_s)^{-2/3} (\sigma_{33} G_s^2)^{1/3} \end{aligned} \right\} \quad (20)$$

$$S_{1j1j} = 4\left(\frac{3}{2}\right)^{1/3} * \frac{(1-\nu_s)^{1/3}}{2-\nu_s} * \frac{G_s^{2/3}}{\left(\frac{1}{\sigma_{11}}\right)^{1/3} + \left(\frac{1}{\sigma_{jj}}\right)^{1/3}} ; \quad i \neq j \quad (21)$$

where G_s and ν_s are the shear modulus and Poisson's Ratio of the material of the spheres.

The array locks under "triaxial" conditions (σ_{11} increasing with $\sigma_{22} = \sigma_{33} = \sigma_0 = \text{constant}$), while it fails in pure shear (σ_{12} increasing with all other $d\sigma = 0$). Because the stiffness matrix, $[S]$, in Eq. 18 is

diagonal, the corresponding diagonal compliance matrix is $[C] = [S]^{-1}$, with each compliance being the reciprocal of the corresponding diagonal stiffness term. That is, $C_{iiii} = 1/S_{iiii}$ and $C_{ijij} = 1/S_{ijij}$, and $\{d\epsilon\} = [C] \{d\sigma\}$.

In this simple cubic array, and again for the case of isotropic loading, $\sigma_{ii} = \sigma_{jj} = \sigma_{kk} = \sigma_0$; for P- and S-waves propagating along principal axis i of the array (and, for the S-wave, polarized parallel to principal axis j), the wave propagation velocities V_p and V_s are proportional to $(\sigma_0)^{1/6}$, and thus, the corresponding constrained and shear moduli, $D = \rho V_p^2 = d\sigma_{ii}/d\epsilon_{ii}$ and, $G_{\max} = \rho V_s^2 = d\sigma_{ij}/d\gamma_{ij}$, are both proportional to $(\sigma_0)^{0.33}$. As discussed in Section 4, a similar dependence of modulus on $(\sigma_0)^{0.33}$ is also predicted for other regular arrays, while laboratory measurements on regular arrays and soils indicate that $G_{\max} \propto (\sigma_0)^{0.5}$.

For this same case of isotropic loading and for a cubic array of quartz spheres, and if the array is loaded in pure shear, $d\sigma_{ij} = d\sigma_{ji}$, then a threshold shear strain, $\gamma_t = 4.5 \times 10^{-3}$. $(\sigma_0)^{2/3}$ is predicted where γ_t is in inch/in and σ_0 is in psi (see Appendix B, Eq. B5). This expression was obtained using the properties of quartz listed in Table 3. At $\gamma = \gamma_t$, gross sliding occurs at contacts i and j , and there is a tendency for a change in the geometric arrangement of the spheres. This predicted relation between γ_t and σ_0 for a sc array of quartz spheres is plotted in Fig. 22 while Fig. 28 shows the detailed shear stress-strain plots up to the threshold (failure). In the range of most practical interest for soils, $5 \text{ psi} < \sigma_0 < 15 \text{ psi}$, the expression gives

$\gamma_t = 10^{-4}\% = 10^{-2}\%$, which agrees very well with the measured γ_t in sands as discussed in Section 2. Expressions for the secant modulus reduction, G/G_{\max} , and for the damping ratio of the array, versus strain increment $\gamma = d\gamma_{ij}$ were also obtained for a cubic array of quartz spheres (Dobry et al., 1982), and were compared with actual measurements in sands, with good agreement. The corresponding comparison for G/G_{\max} versus γ is reproduced in Fig. 29 for an assumed $\gamma_t = 1.5 \times 10^{-2}\%$.

The more general case of anisotropic loading of the cubic array, with $\sigma_{11} \neq \sigma_{22} \neq \sigma_{33}$, is very interesting, as this model crudely simulates the laboratory measurements of V_p and V_s on anisotropically loaded sands discussed in Chapter 2. For a P-wave propagating parallel to the i -axis of the array, the predicted expressions for $D = d\sigma_{ii}/d\epsilon_{ii}$ and V_p are:

$$\left. \begin{aligned} D &= [(3)^{1/3}/2] [E_s/(1-\nu_s)^{2/3}] (\sigma_{ii})^{1/3} \\ V_p &= (D/\rho)^{1/2} \end{aligned} \right\} \quad (22)$$

where E_s , ν_s = elastic constants of the spheres. Therefore, both D and V_p are functions only of the normal stress σ_{ii} in the direction of propagation, and do not depend on the other two array stresses σ_{jj} and σ_{kk} .

For an S-wave propagating parallel to the i -axis of the anisotropically loaded array and with motions polarized parallel to the j -axis of the array, the corresponding expressions for $G_{\max} = d\sigma_{ij}/d\gamma_{ij}$ and V_s are:

$$G_{\max} = \frac{[3(1-\nu_s)^2]^{1/3} (E_s)^{2/3}}{(2-\nu_s)(1+\nu_s)} \frac{\sigma_{ii}^{1/3} \sigma_{jj}^{1/3}}{\sigma_{ii}^{1/3} + \sigma_{jj}^{1/3}} \quad (23)$$

$$V_s = (G_{\max}/\rho)^{1/2}$$

G_{\max} and V_s are functions only of the normal stresses in the direction of propagation (σ_{ii}) and polarization (σ_{jj}), and do not depend on the third, out of plane array stress σ_{kk} . Furthermore, as Eqs. 23 are symmetric with respect to σ_{ii} and σ_{jj} , the values of V_s and G_{\max} do not change if the directions of propagation and polarization are interchanged.

These conclusions for the simple cubic array, that V_p depends only on σ_{ii} , and V_s depends only on σ_{ii} and σ_{jj} , are identical to the experimental findings of Roesler (1979), Knox et al. (1932), Kopperman et al. (1982), and Yu and Richart (1984) on anisotropically loaded sands, previously discussed in Section 2. The symmetry of σ_{ii} and σ_{jj} in Eq. 23 is also present as a symmetry of σ_a and σ_b in empirical Equation 4, obtained by Knox et al. (1982) from their sand measurements.

Of course, Eqs. 22 and 23 cannot be used directly for quantitative predictions in sands, as they give $D \propto \sigma_o^{1/3}$ and $G_{\max} \propto \sigma_o^{1/3}$ for the isotropic case, while D and $G_{\max} \propto (\sigma_o)^{1/2}$ in actual sands. It is interesting to modify Eq. 23 to make it consistent with this empirical fact, by replacing $\sigma_{ii}^{1/3}$, $\sigma_{jj}^{1/3}$ by $\sigma_{ii}^{1/2}$, $\sigma_{jj}^{1/2}$, and then to compare measurements and predictions. The new equation is $G_{\max} = M\sigma_{ii}^{0.5}\sigma_{jj}^{0.5}/(\sigma_{ii}^{0.5} + \sigma_{jj}^{0.5})$, where M = constant. It is useful to specialize this expression for the biaxial case, $\sigma_{ii} = \sigma_{11} = \sigma_v$, $\sigma_{jj} = \sigma_{kk} = \sigma_{33} = \sigma_h$, to be able to compare it with the empirical Eq. 6 obtained by Yu and Richart

for sand. If $K = \sigma_{11}/\sigma_{jj} = \sigma_{11}/\sigma_{33}$, the new equation becomes: $G_{\max} = N\sigma_v^{0.25}\sigma_h^{0.25}[2K^{0.25}/(1+K^{0.5})]$, where $N = 0.5M$. It is convenient to define the normalized parameter $\bar{G} = G_{\max}/(N\sigma_v^{0.25}\sigma_h^{0.25})$, where $\bar{G} = 1$ for $K = 1$. The theoretical expression $G = 2K^{0.25}/(1+K^{0.5})$ has been plotted in Fig. 30. The corresponding empirical expression $\bar{G} = 1 - 0.18 K_n^2$, obtained from Eq. 6, has also been superimposed on Fig. 30 for typical values $K_{\max} = 3$ and 4. The trends of the predicted and measured curves are the same in Fig. 30, with the laboratory results showing a somewhat faster decrease in G as K_n increases.

The fact that the crude particulate model used here is capable of predicting the lack of influence of the two stresses perpendicular to propagation on V_p (Eq. 22), and of the out-of-plane stress on V_s and G_{\max} (Eq. 23), as well as the general trend of the relationship between G_{\max} and the in-plane stresses (Fig. 30), is extremely encouraging. The main advantage of the cubic array used here is its simplicity, but of course this model is still far from representing real sand. One deficiency (which it shares with other regular arrays), is that in the general case the array itself is inherently anisotropic even when isotropically loaded (crystal-type behavior); that is, G_{\max} and other "elastic" stress-strain parameters are somewhat different for shear stresses corresponding to axes which are different from the structural axes (axes of symmetry of the array 1, 2, 3 selected in Fig. 24). However, when the material of the spheres has $\nu_s = 0$, the array is isotropic when isotropically loaded at very small increments. Also, the array locks when a "triaxial" test is conducted on it along any of its structural axes, instead of yielding

and eventually failing in shear as it happens with actual granular materials.

5.2 Body Centered Cubic Array (bcc)

The body centered cubic array, sketched in Fig. 25, was the next regular array studied. It is also represented by one sphere, and the relations between stress and contact forces can be easily determined for one uniform stress field of interest: isotropic loading followed by small stress increments. The coordination number (number of contacts/sphere) is now eight instead of six for the simple cubic array, and, thus, the computations are somewhat more involved. A procedure analogous to that used for analyzing the simple cubic array can be followed, except that it is now easier to work directly with the compliance matrix, C_{ijkl} , $[C] = [S]^{-1}$, instead of the stiffness matrix $[S]$ used before in Eq. 18.

For the case of isotropic loading, followed by small stress increments, $[C]$ has the following form:

$$\begin{bmatrix} d\epsilon_{11} \\ d\epsilon_{22} \\ d\epsilon_{33} \\ d\epsilon_{12} \\ d\epsilon_{13} \\ d\epsilon_{23} \end{bmatrix} = \begin{bmatrix} C_{1111} & C_{1122} & C_{1133} & 0 & 0 & 0 \\ C_{2211} & C_{2222} & C_{2233} & 0 & 0 & 0 \\ C_{3311} & C_{3322} & C_{3333} & 0 & 0 & 0 \\ 0 & 0 & 0 & C_{1212} & 0 & 0 \\ 0 & 0 & 0 & 0 & C_{1313} & 0 \\ 0 & 0 & 0 & 0 & 0 & C_{2323} \end{bmatrix} \begin{bmatrix} d\sigma_{11} \\ d\sigma_{22} \\ d\sigma_{33} \\ d\sigma_{12} \\ d\sigma_{13} \\ d\sigma_{23} \end{bmatrix} \quad (24)$$

where

$$C_{1111} = C_{2222} = C_{3333} = \frac{2}{\sqrt{3}} * \frac{1}{(4\sqrt{3} G_s^2 \sigma_0)^{1/3}} * \left[(1-\nu_s)^{2/3} + \frac{2-\nu_s}{(1-\nu_s)^{1/3}} \right] \quad (25)$$

$$C_{1122} = C_{1133} = C_{2233} = \frac{1}{\sqrt{3}} * \frac{1}{(4\sqrt{3} G_s^2 \sigma_0)^{1/3}} * \left[2(1-\nu_s)^{2/3} - \frac{2-\nu_s}{(1-\nu_s)^{1/3}} \right] \quad (26)$$

$$C_{1212} = C_{1313} = C_{2323} = \frac{4}{\sqrt{3}} * \frac{1}{(4\sqrt{3} G_s^2 \sigma_0)^{1/3}} * \left[(1-\nu_s)^{2/3} + \frac{1}{4} \frac{2-\nu_s}{(1-\nu_s)^{1/3}} \right] \quad (27)$$

Notice that, unlike Eq. 18 for the sc array, the compliance matrix [C] in Eq. 24 is not diagonal. However, it becomes diagonal and it corresponds to an isotropic elastic medium with $\nu = 0$, if $\nu_s = 0$, similarly to that found for the sc in Section 5.1. For an initial cross-anisotropic or biaxial loading, $\sigma_{22} = \sigma_0 + \sigma_a$ and $\sigma_{11} = \sigma_{33} = \sigma_0$, followed by arbitrary, small stress increments*, the form of [C] is still that of Eq. 24, and the compliances in Eq. 24 are:

$$C_{1111} = C_{2222} = C_{3333} = \frac{2}{3\sqrt{3}} * \frac{1}{4\sqrt{3} G_s^2 \sigma_0}^{1/3} * \left[1 + \frac{1}{3} \left(\frac{\sigma_a}{\sigma_0} \right) \right]^{-1/3} * \left[(1-\nu_s)^{2/3} + \right. \quad (28)$$

$$\left. + \frac{2-\nu_s}{(1-\nu_s)^{1/3}} \right]$$

* See footnote, Appendix A.3.

$$C_{1122} = C_{1133} = C_{2233} = \frac{-2}{\sqrt{3}} * \frac{1}{4\sqrt{3} G_s^2 \sigma_0}^{1/3} * \left[1 + \frac{1}{3} \left(\frac{\sigma_a}{\sigma_0} \right) \right]^{-1/3} * \left[(1-\nu_s)^{2/3} - \frac{2-\nu_s}{2(1-\nu_s)} \right] \quad (29)$$

$$C_{1212} = C_{1313} = C_{2323} = \frac{1}{3\sqrt{3}} * \frac{1}{4\sqrt{3} G_s^2 \sigma_0}^{1/3} * \left[1 + \frac{1}{3} \left(\frac{\sigma_a}{\sigma_0} \right) \right]^{-1/3} * (1-\nu_s)^{2/3} + \frac{2-\nu_s}{(1-\nu_s)^{1/3}} \quad (30)$$

As it can be seen in the above equations 25-30, ν_s and ν_p are again proportional to $(\sigma_0)^{1/6}$ for the body centered cubic array, since the corresponding moduli are proportional to $(\sigma_0)^{1/3}$; this is a characteristic common to all regular cubic arrays (Duffy and Mindlin, 1957, Duffy, 1959, Makhlof and Stewart, 1967). However, again it is possible to modify the exponents empirically, and $(\sigma_0)^{1/3}$ can be replaced by $(\sigma_0)^{1/2}$ when measurements and predictions are compared.

Threshold strain calculations were performed for this body-centered array in the case of triaxial loading, starting from an isotropic pressure σ_0 , for which the array yields and fails (while the array tends to lock under pure shear loading). Again, the threshold strain, γ_t , obtained for the array is a function of the confining pressure, $(\sigma_0)^{2/3}$, and for an array of quartz spheres (using the properties for quartz in Table 3), $\gamma_t = 3.44 \times 10^{-3} \sigma_0^{2/3}$, with σ_0 in psi and γ_t in inches/inch. This gives slightly lower values of γ_t than those obtained from the simple cubic array of quartz spheres in Section 5.1, $\gamma_t = 4.53 \times 10^{-3} \sigma_0^{2/3}$. The plots

for these two expressions of γ_t are compared in Fig. 27, while Fig. 31a) presents detailed axial stress-strain curves up to the threshold (failure). For the usual range of values of confining pressure for soils, both of them agree well with $\gamma_t \approx 10^{-2}\%$ experimentally observed in sands.

The body centered cubic array also has some deficiencies when compared to the behavior of actual sands. First, it remains isotropic even when loaded under anisotropic loads, as shown in Appendix A. Second, in this anisotropic loading case the wave propagation velocities are not proportional to the product of the principal stresses in the directions of propagation and polarization (as measured in sands), but rather they are proportional to the mean stress, as can be verified from Eqs. 28-30. Finally, this array locks under pure shear loading, and in fact it locks under a number of different shear loading paths depending upon their orientations and initial stress state. However, the bcc array adds to our understanding of the general problem, as it is a medium dense ($e = 0.47$) array, located within the range between the densest, face centered cubic array ($e = 0.35$) and the loosest, simple cubic array ($e = 0.91$).

5.3 Face Centered Cubic Array (fcc)

The Face Centered Cubic Array sketched in Fig. 26 is one of the two densest arrays, and it has been investigated by several researchers (Duffy and Mindlin 1957, Ko and Scott 1969, Hendron 1963). The differential stress-strain relationship for this medium was derived by Duffy and Mindlin (1957). The array has 12 contacts per sphere, and unfortunately it is statically indeterminate for most loading situations; as a consequence, closed form solutions are available only for the case of

isotropic confining pressure. In the case of biaxial loading a qualitative solution does exist, but the compliances at the contacts have not yet been evaluated. Computation of these compliances is a formidable task due to the indeterminacy of the problem and the variation of the forces from contact to contact.

The incremental constitutive law under isotropic confining pressure was used by Duffy and Mindlin to compare the theoretical and experimental rod wave velocities through a bar composed of face centered cubic arrays of spheres (Fig. 13).

For the case of isotropic loading followed by small stress increments, $d\sigma_{ii}$, $d\sigma_{ij}$, the stiffness matrix has the form shown below:

$$\begin{bmatrix} d\sigma_{11} \\ d\sigma_{22} \\ d\sigma_{33} \\ d\sigma_{12} \\ d\sigma_{13} \\ d\sigma_{23} \end{bmatrix} = \begin{bmatrix} S_{1111} & S_{1122} & S_{1133} & 0 & 0 & 0 \\ S_{2211} & S_{2222} & S_{2233} & 0 & 0 & 0 \\ S_{3311} & S_{3322} & S_{3333} & 0 & 0 & 0 \\ 0 & 0 & 0 & S_{1212} & 0 & 0 \\ 0 & 0 & 0 & 0 & S_{1313} & 0 \\ 0 & 0 & 0 & 0 & 0 & S_{2323} \end{bmatrix} \begin{bmatrix} d\epsilon_{11} \\ d\epsilon_{22} \\ d\epsilon_{33} \\ d\epsilon_{12} \\ d\epsilon_{13} \\ d\epsilon_{23} \end{bmatrix} \quad (31)$$

$$S_{1111} = S_{2222} = S_{3333} = \left[\frac{3G_s^2 \sigma_0}{2(1-\nu_s)^2} \right]^{1/3} * \frac{4-3\nu_s}{2-\nu_s} \quad (32)$$

$$S_{1122} = S_{1133} = S_{2233} = \left[\frac{3G_s^2 \sigma_0}{2(1-\nu_s)^2} \right]^{1/3} * \frac{\nu_s}{2(2-\nu_s)} \quad (33)$$

$$S_{1212} = S_{1313} = S_{2323} = \left[\frac{3G_s^2 \sigma_0}{2(1-\nu_s)^2} \right]^{1/3} * \frac{4-3\nu_s}{(2-\nu_s)} \quad (34)$$

Similar to that discussed previously for Eq. 24 and the bcc array, the stiffness matrix [S] in Eq. 31 becomes isotropic and diagonal only if $\nu_s = 0$. In that case, all diagonal terms are identical and equal to:

$$S_{ijkl} = 2 \left(\frac{3G_s^2 \sigma_0}{2} \right)^{1/3} \quad (35)$$

and the Poisson's ratio of the array is $\nu = 0$.

If the face centered cubic array is consolidated under a transversely isotropic state of stress, with $\sigma_{11} = \sigma_0 + \sigma_a$, $\sigma_{22} = \sigma_{33} = \sigma_0$, and $\sigma_{12} = \sigma_{13} = \sigma_{23} = 0$, the situation becomes more complicated, since in the case of a non isotropic loading the forces vary from contact to contact and each compliance is different. To obtain a stress-strain relation for an anisotropic loading path, the derivation must be performed anew, distinguishing between contacts with different loading histories.

The differential stress strain law for this case appears in great detail in the original paper by Duffy and Mindlin (1957); it is identical in form to Eq. (31), except that now the expressions for S_{ijkl} are not known. Thurston (1958) extended the results of Duffy and Mindlin to a set of 18 equations and 18 unknowns.

The fcc array was subjected analytically to the conditions of a triaxial test by Brauns (1968) and Brauns and Leussink (1970), who derived theoretical expressions between stress and strain at finite levels for an array of glass spheres (Fig. 31b). These expressions were

later compared to experimental data obtained in triaxial tests on regular fcc packings of glass and steel spheres (see Appendix B3).

Thurston and Deresiewicz (1959) derived expressions for the uniaxial compression of an fcc array when applied concurrently with a related isotropic pressure. Again, the theoretical results were compared with experimental results obtained through compression of bars of steel bearing spheres arranged in fcc array, with good agreement.

5.4 Cubical-Tetrahedral (ct) and Tetragonal-Sphenoidal (ts) Arrays

The elastic constants relating stress to strain increments for the Cubical Tetrahedral and Tetragonal Sphenoidal arrays that have been consolidated isotropically were derived by Makhlof and Stewart (1967). The procedure for determining those constants is the same as in the other arrays described in detail by Duffy and Mindlin (1957).

The corresponding constitutive law for the Cubical Tetrahedral array has the same form as Eq. 31, but now

$$S_{1111} = S_{2222} = \frac{3}{4k} \frac{1}{3}(1+3k) * \left[\frac{3}{2} \frac{G_s^2 \sigma_o}{(1-\nu_s^2)} \right]^{1/3} \quad (36)$$

$$S_{3333} = \left(\frac{4}{2} \right)^{1/3} * \left[\frac{3}{2} \frac{G_s^2 \sigma_o}{(1-\nu_s^2)} \right]^{1/3} \quad (37)$$

$$S_{1122} = \frac{3^{1/3} (1-k)}{4k} * \left[\frac{3}{2} \frac{G_s^2 \sigma_o}{(1-\nu_s^2)} \right]^{1/3} \quad (38)$$

$$S_{1212} = \frac{\sqrt{3} (1+k)}{5k} 3^{1/3} * \left[\frac{3}{2} \frac{G_s^2 \sigma_o}{(1-\nu_s^2)} \right]^{1/3} \quad (39)$$

$$S_{1313} = S_{2323} = \frac{2*3^{1/3}}{5k} * \left[\frac{3}{2} \frac{G_s^2 \sigma_o}{(1-\nu_s^2)} \right]^{1/3} \quad (40)$$

$$\text{where } k = \frac{2 - \nu_s}{2(1-\nu_s)} \quad (41)$$

As we can see from the above equations, the Cubical Tetrahedral array differs from the simple cubic, the body centered cubic and the face centered cubic arrays in that it does not exhibit cubic anisotropy, but rather transverse or hexagonal isotropy, as is also the case of the Hexagonal Close Packed array (Duffy, 1959) and of the Tetragonal-Sphenoidal Array.

The constitutive law for the Tetragonal-Sphenoidal array appears also in Makhoul and Stewart (1967). However, not enough detail is provided in this reference for a full understanding of the results, which are quite complex, as the representative unit prism is not symmetric. Unfortunately, the original reference (Makhoul, 1963) could not be found

by the authors*, thus preventing a better understanding of this array.

5.5 Comparison of Different Cubic Arrays

The analytical results on the three regular cubic arrays discussed in Sections 5.1-5.2-5.3: simple cubic, body centered cubic and face centered cubic, were compared as part of the current research. This was done to gain further insight into the behavior of granular media, and as a necessary intermediate step toward the investigation of more elaborated and realistic particulate models.

All these arrays generally exhibit cubic anisotropy (crystal-type behavior) under an isotropic confining pressure σ_0 . In the three arrays, it was found that the necessary and sufficient condition for the array to become isotropic under σ_0 is for the Poisson's ratio of the spheres, ν_s , to be equal to zero. If $\nu_s = 0$, the incremental stiffness (and compliance) matrix for the three arrays is diagonal. Although the Poisson's Ratio of quartz $\nu_s \approx 0.15$, (see Table 3), is certainly different from

*The differential constitutive laws for the cubical tetrahedral and the tetragonal sphenoidal arrays are either not applicable to our research or they are erroneous. As one can see from Eqs. 36-40, contrary to general belief (Duffy 1959), the cubical tetrahedral array does not become isotropic under isotropic loading. This is a serious deficiency vis-a-vis our research, as sands are uniform and more or less isotropic under isotropic load. Consequently, the cubical tetrahedral array will not be used here. As for the tetragonal sphenoidal array, the results are not complete, and since the representative volume element of this array is not symmetric, completion of the stress strain relation in Makhlof and Stewart (1967) appears to be a major task. The inexistence of the primary source for this array, Makhlof (1963), made it impossible for the authors to clarify the above aspects; therefore no results will be used here for the cubical-tetrahedral and tetragonal-sphenoidal array.

zero, it is low enough to make this " $\nu_s = 0$ assumption", needed for isotropy, a reasonable one for quartz sands, at least as a first approximation. If $\nu_s = 0$ is assumed, the Poisson's Ratio of the array is also computed to be $\nu = 0$ for the same three arrays. It must be noted that for the range $0 \leq \nu_s \leq 0.5$, values up to $\nu \approx 0.13$ are computed for the same arrays (see Fig. 32). Therefore, the fact that a value $\nu = 0$ results for the array as soon as $\nu_s = 0$ is assumed does not seem to be so far off either. It is interesting to note that measurements of V_p and V_s by Stokoe and his coworkers on an actual sand consolidated isotropically provided a similarly low value of $\nu \approx 0.10$ (Knox et al. 1982, Kopperman et al. 1982, Lee 1985). In any case, even with $\nu_s \neq 0$, the cubic anisotropy of these expressions for ν arrays is not pronounced; the error resulting from computing the moduli between the extreme values of ν_s does not exceed 3.3% (Duffy, 1959).

The above three cubic arrays, starting from an isotropic σ_0 state, were loaded statically in triaxial compression or pure shear up to failure, that is up to gross sliding, and computations were performed and are displayed here for their stress-strain curves and threshold/failure strains (Figs. 27, 28 and 31). A graph of obliquity, σ_{22}/σ_0 at failure versus the intergranular friction coefficient between spheres, f , was also computed and is plotted in Fig. 33. The curves obtained for the arrays in this figure were also compared to the obliquity obtained assuming the Mohr-Coulomb Failure law:

$$\frac{\sigma_{22}}{\sigma_0} = \frac{1+\sin\phi}{1-\sin\phi} = \tan^2\left(45 + \frac{\phi}{2}\right), \text{ with } \tan\phi = f$$

To be able to fail the simple cubic array in triaxial compression, this medium was compressed by a force parallel to one of the face diagonals of the unit volume of the array, that is along a [110] direction (Deresiewicz, 1959).

The same cubic arrays also give excellent results when predicting the influence of anisotropic consolidation on shear wave velocity; this is shown in Fig. 34 by a plot of normalized shear wave velocity vs stress ratio $K = \sigma_{22}/\sigma_0$. In this plot, $V_s(K)$ and $V_s(1)$ are the values of the shear wave velocity, V_s , computed for the anisotropic case (K) and for the isotropic loading condition ($K=1$), respectively, for directions of propagation and polarization parallel or perpendicular to σ_{22} . The same plot includes data measured by Stokoe et al. (1985) and Lee (1985) on dry sand in the large cubic testing facility at the University of Texas, with excellent agreement between analytical predictions and the experimental data.

The shear modulus at very small strains, G_{\max} , computed for these same three cubic arrays under a given isotropic stress, σ_0 , is plotted in Fig. 35 as a function of the coordination number (= number of contacts/sphere). As expected, the higher the coordination number, the stiffer the array, with essentially a linear relation between the two parameters; it is interesting that for a given σ_0 the straight lines in Fig. 35 extrapolate down to zero, suggesting that G_{\max} is essentially proportional

to the coordination number (a similar plot was obtained by Yanagisawa, 1983). Therefore, adding contacts to the spheres has the same effect on the stiffness of a regular array as increasing the number of springs in a system of equal, parallel, elastic springs. A derived plot is the graph between the shear wave velocity, $V_s = (G_{\max}/\rho)^{1/2}$ versus void ratio and isotropic pressure σ_0 (Fig. 36a) for the same three arrays. This last figure is especially interesting, as the trend observed in actual sands is very similar (compare analytical curves with measured data in sands in Fig. 36b), except that the absolute values of V_s in the real soils are much smaller, by a factor of two or three. For example, for $e = 0.47$, corresponding to the bcc array, and $\sigma_0 = 30 \text{ psi} = 4,320 \text{ psf}$, $V_s \approx 1,800 \text{ fps}$ is predicted by the analytical model in Fig. 36a), while $V_s \approx 1,100 \text{ fps}$ has been measured in rounded grained sands. Therefore, Figs. 35 and 36 strongly suggest that the dependency of G_{\max} and V_s on void ratio observed in real soils is explained mainly by the increase in the number of contacts as the void ratio decreases.

Even though the above results are encouraging, the regular arrays are still very crude analytical models of actual granular soils, and results such as shown in Fig. 36a are not easy to interpolate to intermediate void ratios. A significant improved model is discussed in the following section.

CHAPTER 6

AN ANALYTICAL MODEL OF GRANULAR SOIL OF ARBITRARY VOID RATIO UNDER ISOTROPIC PRESSURE

Smith et al. (1929) found experimentally that a random arrangement of equal spheres, after enough shaking and tapping has been applied to it, seems to be composed of regular arrays, representing dense and loose clusters distributed within the random granular medium. The measurements showed that all spheres had between 6 and 12 contacts per sphere, which corresponds exactly to the theoretical range for regular arrays.

Additional experimental work by Bernal and Mason (1960), Bernal et al. (1964), Scott (1960), Davis (1974), as well as Shahinpoor and Shahrpass (1982), and Finney (1983), Figs. 37 and 38), has confirmed that 2-D and 3-D random assemblages of equal spheres tend to crystalize. Consequently, at the present time, it is generally accepted that an assemblage of equal spheres can be modelled by a combination of regular arrays, (Finney 1983, Backman et al. 1983).

In this section, a model of granular soil is proposed which consists of clusters of the three cubic arrays discussed in Section 5.5, with the additional assumption that for the spheres $v_s = 0$. In this model, the three cubic arrays, having different void ratios and inherent stiffnesses, occur in proportions such as to give the desired macroscopic void ratio of the "soil". In Section 6.3, the relation between G_{\max} , void ratio and σ_0 applied to this soil model is calculated using the self consistent method, and the results are compared with G_{\max} measured in actual sands.

6.1 The Self Consistent Method

One of the most commonly used procedure for describing the behavior of macroscopically isotropic composite elastic media is the "Self Consistent Scheme".

This "Self Consistent Scheme" was first devised by Hershey (1954) and Kroner (1958) as a means to model the behavior of isotropic and anisotropic polycrystalline materials. Such materials are just one phase media, but because of the random or partially random orientation of the crystals, are heterogeneous, their elastic properties vary with position within the medium, and discontinuities in properties exist across some crystal interfaces.

In these original applications of the method to polycrystalline aggregates, a single anisotropic crystal was viewed as a spherical or ellipsoidal inclusion within an infinite medium; this infinite medium had the (still unknown) isotropic elastic properties of the aggregate. Then the medium, with the inclusion in it, was subjected to a uniform stress or strain field applied at large distances from the inclusion. Next, the orientation average of the stress or strain inside the inclusion was assumed to be equal to ("consistent with") the corresponding applied value of stress or strain. Thus the "self-consistent" name of the method. This formulation provided enough equations to solve for the isotropic effective properties of the medium (Christensen, 1979).

Improvement of this self consistent scheme and its extension to multiphase media are due to Hill (1965) and Budiansky (1965), who developed the method to be used here. This improved method represents an

approximate analysis for the prediction of the overall (macroscopic) elastic moduli of a multiphase medium composed of a coherent mixture of several isotropic, linearly elastic materials or phases. The medium is assumed to consist of contiguous, irregular zones containing these constituent materials, and the shapes of these zones are assumed not to deviate much from spherical. The spatial distribution of the phases is assumed to be such that the composite medium is macroscopically (i.e. at a scale much larger than the dimensions of the zones), both homogeneous and isotropic. Now, if an N -phase medium of total volume V is defined, such that the aggregate volume of all zones containing the i^{th} phase is V_i , the volume concentration is $c_i = V_i/V$, and c_i is also equal to the probability that any arbitrary point within the medium is located within a zone of the i^{th} material. It should be noted that in the limiting case of very small concentrations, c_1, c_2, \dots, c_{N-1} , the first $N-1$ phases will tend to appear as isolated inclusions in a matrix consisting of the N^{th} phase.

In order to obtain the effective overall (macroscopic) shear, G^* , and bulk, K^* , moduli of the medium, a uniform stress field is applied at its boundaries. Then, the stress and strain field, in each of the phases is evaluated as explained in the next paragraph. Once the fields are determined for all materials, the effective moduli, G^* and K^* , can be calculated by equating the strain energies of the macroscopic medium and of the phases. Again, the problem reduces to a number of coupled equations for K^* and G^* , which are in terms of the properties of the individual materials and of their volume concentrations (Budiansky, 1965). This

method has been severely criticized for taking enormous liberties with the geometrical arrangement of the phases (Christensen, 1979). To calculate the elastic field in each material, the geometry of the different zones containing the phase is successively rearranged to view the phase as a single inclusion. However, the method is relatively simple and in many instances, when used with caution, gives very good results. Furthermore, it has been proven by Hill (1965) that this "Self Consistent Method" yields results for G^* and K^* which always lie between the Voigt and Reuss bounds, that is, the spatial average of the moduli of the phases (Voigt bound, springs-in-parallel) and of the reciprocal of the moduli, or compliances of the phases (Reuss bound, springs-in-series).

The evaluation of the stress and strain fields in each of the phases is performed for the isotropic case by the solution of the problem of the elastic field inside an ellipsoidal elastic inclusion (Eshelby, 1957). It was shown by Eshelby that the elastic field inside an ellipsoidal isotropic elastic inclusion embedded in an isotropic elastic medium is uniform; this is an extremely important conclusion as it eliminates the need for averaging the fields within the inclusion phase and simplifies enormously the formulation. Later, it was shown that the stress and strain fields inside an orthotropic inclusion embedded in an orthotropic medium are also uniform, as long as the cross section of the inclusion is quadratic (Kinoshita and Mura, 1971).

The averaging of the shear moduli of all phases by a strain energy balance between the medium and the inclusions yields:

$$\frac{1}{G^*} = \frac{1}{G_N} + \sum_{i=1}^{N-1} c_i \left(1 - \frac{G_i}{G_N}\right) \left(\frac{\bar{\gamma}_i}{\tau^\circ}\right) \quad (42)$$

$$\frac{1}{K^*} = \frac{1}{K_N} + \sum_{i=1}^{N-1} c_i \left(1 - \frac{K_i}{K_N}\right) \left(\frac{\bar{\epsilon}_{v_i}}{\sigma^\circ}\right) \quad (43)$$

where G^* , K^* are the desired macroscopic moduli; K_i , G_i ($i = 1, 2, \dots, N$) are the moduli of the i^{th} phase, $c_i = V_i/V$ is the volume concentration, and $\bar{\gamma}_i$, $\bar{\epsilon}_{v_i}$ are the values of the average shear strain and volumetric strain respectively, inside the phase. The parameters τ° and σ° are the shear stress and isotropic pressure applied at the boundary of the medium.

The Eshelby (1957) solution gives

$$\bar{\gamma}_i = \frac{\tau^\circ}{G^* + \beta^*(G_i - G^*)} \quad (44)$$

$$\bar{\epsilon}_{v_i} = \frac{\sigma^\circ}{K^* + \alpha^*(K_i - K^*)} \quad (45)$$

where α^* , β^* are components of the Eshelby S-tensor; for the case of spherical inclusions they are:

$$\alpha^* = \frac{1 + \nu^*}{3(1 - \nu^*)} \quad (46)$$

$$\beta^* = \frac{2}{15} \frac{(4 - 5\nu^*)}{(1 - \nu^*)} \quad (47)$$

where ν^* is the macroscopic Poisson's ratio of the medium:

$$\nu^* = \frac{3K^* - 2G^*}{6K^* + 2G^*} \quad (48)$$

By "smearing out", that is, by replacing the matrix surrounding each inclusion (phase) by the desired resultant macroscopic medium, equations (42) and (43) reduce to:

$$\sum_{i=1}^N \frac{c_i}{1 + \beta^* \left(\frac{G_i}{G^*} - 1 \right)} = 1 \quad (49)$$

$$\sum_{i=1}^N \frac{c_i}{1 + \alpha^* \left(\frac{K_i}{K^*} - 1 \right)} = 1 \quad (50)$$

which are symmetrical for the various phases. Therefore, Budiansky (1965) has suggested to use Equations 49 and 50 for arbitrary concentrations of the constituents of the composite medium as described previously. Furthermore, Budiansky simplified equations 44 and 45 to:

$$\bar{\gamma}_1 = \frac{\tau^0}{G^*} \left[\frac{1}{1 + \beta^* \left(\frac{G_i}{G^*} - 1 \right)} \right] \quad (51)$$

$$\bar{\epsilon}_{v1} = \frac{\sigma_0^0}{K^*} \left[\frac{1}{1 + \alpha^* \left(\frac{K_i}{K^*} - 1 \right)} \right] \quad (52)$$

A comparison of Eq. 51 with results obtained through statistical finite element methods, suggests that the above equations do indeed model the continuum described previously, including the assumption that the stress and strain fields of the phases are approximately independent of

location (Fig. 39, see also Petrakis, 1983).

Finally, Equations 46-50 have to be solved simultaneously to yield the desired values of the macroscopic elastic moduli, G^* , K^* . These resultant macroscopic moduli are estimates of the overall elastic constants of the multiphase medium, and, as mentioned before, they invariably lie between the Reuss and Voigt bounds. Other solutions may provide narrower bounds for the actual solution (Hashin and Shtrikman, 1963); however, the Self Consistent solution, in certain cases, also falls between these narrower bounds, thus showing its capability for providing accurate results (Hill, 1965).

6.2 The Model

The Self Consistent Method is applied here to evaluate the elastic constants of a random assemblage of equal, rough elastic spheres that has been consolidated isotropically and has a prescribed mean void ratio \bar{e} . The spheres are assigned the elastic properties of quartz, and the assemblage is assumed to be composed of random zones, with each zone constituted by a large number of spheres arranged in either of three regular cubic arrays.

Recently, Shahinpoor (1981) modelled a random 2-D array of equal steel spheres as a combination of Voronoi cells, derived an expression for the probability density function of the void ratio, $p(e)$, and checked experimentally this analytical $p(e)$ by means of an optical scanning technique, Fig. 37 (see also Shahinpoor and Shahrpass, 1982). The expression for $p(e)$ is:

$$p(e) = \frac{\lambda \exp(-\lambda e)}{\exp(-\lambda e_{\min}) - \exp(-\lambda e_{\max})} \quad (53)$$

$$\text{where } \bar{e} = \frac{1}{\lambda} + \frac{e_{\min} \exp(-\lambda e_{\min}) - e_{\max} \exp(-\lambda e_{\max})}{\exp(-\lambda e_{\min}) - \exp(-\lambda e_{\max})} \quad (54)$$

λ is obtained from the mean void ratio, \bar{e} , of the distribution $p(e)$. As mentioned before, it is reasonable to model a uniform, rounded-grained sand as a random combination of zones corresponding to regular cubic arrays, and this was the approach taken in this work. The sand medium is assumed to be composed of regular arrays in the fashion of Figs. 37 and 38, where each randomly oriented Voronoi polyhedron is one of these zones, and contains a regular array with many spheres. A cross section of this 3-D medium could be visualized approximately by the actual photograph of the 2-D medium in Fig. 37b; in this, the black spots are spheres and the white are voids, and zones of regular packings can be clearly observed. The macroscopic moduli of the whole medium will be determined from the properties of these zones through the self consistent scheme.

As a first step, the probability density function of the void ratio, $p(e)$, Eq. 53, was transformed to the probability density function of the porosity, $p(n)$, with the basic equation (Benjamin and Cornell, 1970):

$$p(n) = \left| \frac{de}{dn} \right| p(e)$$

as the mean of the porosity distribution, \bar{n} , coincides with the macroscopic (measured) porosity of the "soil", unlike the mean void ratio \bar{e} , which is not identical to the macroscopic void ratio (Petrakis, 1983).

Then, the probability density function of the porosity, $p(n)$, was discretized into three segments of influence, corresponding respectively to the porosities of the three regular cubic arrays (see Fig. 40): sc ($n = 0.48$), bcc ($n = 0.32$) and fcc ($n = 0.26$). The values of n_{\min} and n_{\max} used for all calculations were those of the sc and fcc arrays.

For example, for a prescribed macroscopic porosity $\bar{n} = 0.35$ corresponding to a mean void ratio $\bar{e} = 0.54$, the calculation illustrated in Fig. 40 allowed determining the following three volume concentrations, c_i :

<u>Array</u>	<u>n_i</u>	<u>c_i</u>
sc	0.48	0.1934
bcc	0.32	0.5921
fcc	0.26	0.2143

The medium with these three phases was then subjected to an isotropic boundary confining pressure, σ^0 , and subsequently subjected to small boundary stress increments $d\sigma_{ij}^0$, from which the corresponding elastic, very small strain increments at the boundaries, and the mean cubic medium moduli K^* and G^* were evaluated.

If we now assume that the phases are quadratic (elliptical or circular) in cross section we can apply the Self Consistent method. The assumption that the "zones" are quadratic in cross-section is important, since if the resulting stress and strain fields are uniform (see Section 6.1) within each "zone", the "zone" can be replaced by the representative cube of each cubic array (Figs. 24-26) and the corresponding constitutive

laws are given by Eqs. 18, 24 and 31. Since in turn these relations depend upon the pressure acting on each inclusion or phase, the value of the stress field at the boundary of each of these phases and inside it can be readily obtained from Eshelby's (1957), and Budiansky's (1965) results:

$$\frac{-1}{\sigma_0} = \sigma_0^0 \frac{K_1}{K^*} \left[\frac{1}{1 + \alpha^* \left(\frac{K_1}{K^*} - 1 \right)} \right] \quad (55)$$

where the value of α^* depends upon the shape of the zone, (Eshelby, 1957), which here has been assumed to be spherical for simplicity. Note that this value of $\frac{-1}{\sigma_0}$ is independent of the location of the zone, and is thus the same for all zones containing the same regular cubic array or phase.

Equation 55 is then replaced into Eqs. 18, 24 and 31, and the problem finally reduces to the solution of the following equations for the three phases:

$$\frac{-1}{\sigma_0} = \sigma_0^0 \frac{K_i}{K^*} \left[\frac{1}{1 + \alpha^* \left(\frac{K_i}{K^*} - 1 \right)} \right] \quad ; i = 1, 2, 3 \quad (56)$$

$$\sum_{i=1}^3 \frac{C_i}{1 + \beta^* \left(\frac{G_i}{G^*} - 1 \right)} = 1.0 \quad (57)$$

$$\sum_{i=1}^3 \frac{C_i}{1 + \alpha^* \left(\frac{K_i}{K^*} - 1 \right)} = 1.0 \quad (58)$$

$$\alpha^* = \frac{1 + \nu^*}{3(1 - \nu^*)} \quad (59)$$

$$\beta^* = \frac{2}{15} \frac{(4 - 5\nu^*)}{(1 - \nu^*)} \quad (60)$$

$$\nu^* = \frac{3K^* - 2G^*}{6K^* + 2G^*} \quad (61)$$

where $K_i = K_i(\sigma_0)$, $G_i = G_i(\sigma_0)$ for the three phases are obtained with Eqs. 10, 16 and 23 for $i = 1, 2, 3$, corresponding, respectively, to the simple cubic, body centered cubic and face centered cubic regular arrays.

6.3 Application to Quartz Sand

The proposed model was evaluated using as input the elastic parameters of quartz for the individual spheres, which are $E_s = 11.0 \times 10^6$ psi and $\nu_s = 0.15$ (White, 1965, Ko & Scott, 1967, Lambe and Whitman, 1969, see Table 3), and for a wide range of isotropic confining pressures. The values of the computed shear modulus G^* are plotted on solid lines in Figs. 41, 42 and 43 versus confining pressure $\sigma_0 = \sigma_0^0$, for $e = 0.46$, $e = 0.54$, and $e = 0.58$, respectively. The values of the bulk modulus, K^* , were also computed, and Fig. 44 contains a plot of confining pressure versus volumetric strain predicted by the model for $e = 0.54$, where the volumetric strain was derived from this computed bulk modulus, $\bar{\epsilon}_v = \sigma_0^0 / K^*$.

As mentioned before in connection with Fig. 36, regular arrays are much stiffer, up to 3.5 times stiffer, than actual uniform, rounded sands, and this constitutes a serious deficiency of the model. However, Drnevich and Richart (1970) have succeeded in increasing significantly the shear stiffness of dry, rounded, uniform Ottawa quartz sand by applying millions of cycles of a shear strain slightly greater than the threshold strain in a resonant column device.

Figures 41, 42 and 43 also include as data points the resonant column experimental results obtained by Drnevich (1967), and Drnevich and Richart (1970), for the same macroscopic void ratios, $e = 0.46$, $e = 0.54$ and $e = 0.58$, used to calculate the solid lines. The lower dotted line in each figure corresponds to virgin or uncycled sand as predicted by the Hardin and Black (1966) correlation, which is essentially identical to the Hardin and Richart correlation depicted in Fig. 36(b). In Figs. 41-43, two trends may be clearly observed: a) as the number of cycles, N , increases, the test results steadily approach the model values until, at $N = 1$ to 2×10^7 cycles the agreement becomes excellent; and b) the slope of the line of shear modulus vs confining pressure decreases from about $1/2$ in the uncycled state to the theoretical $1/3$ after, approximately, 1×10^6 cycles. The reason for some of the points showing more scatter is probably because those points were cycled more than others with the same void ratio, or because their void ratios were slightly differed.

In the above tests, the sand specimens were cycled at strains which, although larger than the threshold strain, were small enough so that no significant densification occurs, and indeed the change in measured

(macroscopic) void ratios between virgin and cycled specimens was very little or negligible; thus, densification is certainly not the explanation for the observed threefold increase in the sand stiffness. Drnevich and Richart (1970) speculated in their paper that the above behavior could be due to wearing of the contacts, increase of the contact areas or formation of additional contacts. The authors think that this third reason explains the phenomenon completely, as illustrated by the comparison with the model in Figs. 41-43, and by the relation between stiffness and number of contacts in Fig. 35. It is known that in a random array of spheres there may be less contacts than in regular packings (see Smith et al., 1929) and, furthermore, it is possible to have contacts which do not transmit any load (dead contacts). By continuous cycling such as performed by Drnevich and Richart in their tests these contacts were made load-transmitting and new ones were formed until all or most possible contacts were created and the stiffness of the sand coincided with that predicted by the model. It is interesting that the creation of contacts can also be achieved by high isotropic confining pressures (Duffy and Mindlin, 1958, Deresiewicz 1958, see also Fig. 13).

The analytical model proposed herein describes exactly this: since it assumes that the sand is a random assemblage of regular arrays of spherical grains, it implies that the number of contacts is the maximum possible. Furthermore, as shown by Duffy and Mindlin (1957) and Deresiewicz (1958), and as illustrated by Fig. 13, when the number of contacts increases the pressure dependency of the moduli tends to change from $1/2$ to $1/3$. All of this is interpreted by the model, which is shown

AD-A191 927

MICROMECHANICAL MODELING OF GRANULAR SOIL AT SMALL
STRAIN BY ARRAYS OF EL. (U) RENSSELAER POLYTECHNIC INST
TROY NY DEPT OF CIVIL ENGINEERING. E PETRAKIS ET AL.

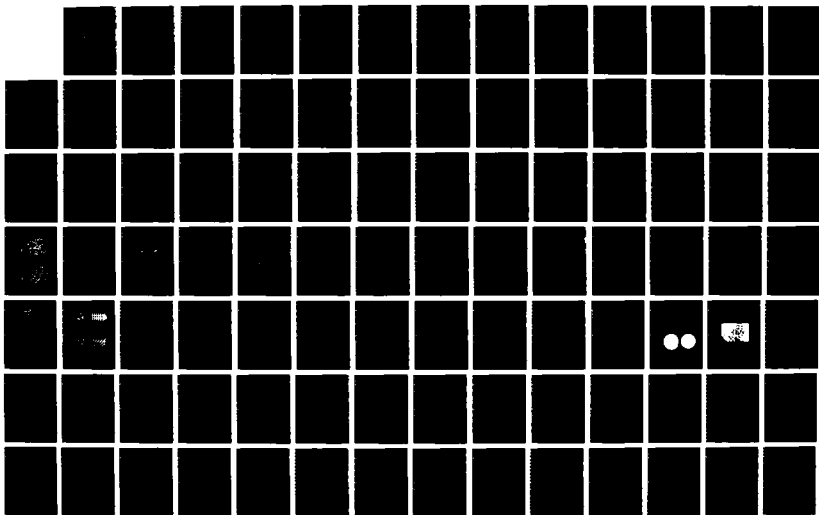
2/4

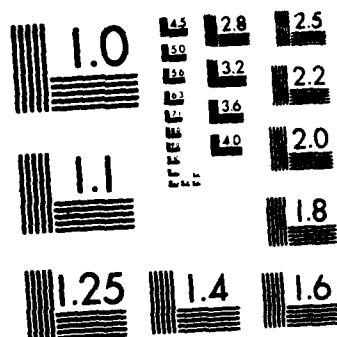
UNCLASSIFIED

28 SEP 87 RP1-CE-87-82 AFOSR-TR-88-0137

F/G 8/10

NL





MICROCOPY RESOLUTION TEST CHART
NATIONAL BUREAU OF STANDARDS 1963 A

here to represent the limiting state, in terms of number of contacts and of stiffness, that a sand can reach.

Figure 44 shows the confining pressure σ_0^0 vs. volumetric strain, $\bar{\epsilon}_v$, measured by Drnevich and Richart on the same Ottawa sand specimens discussed above, for a virgin specimen and for a specimen after 1×10^6 cycles of shear strain. Unfortunately, no data is available for sand specimens cycled with more than 1×10^6 cycles. In the figure, lines have been passed which approximately represent these experimental data. The line predicted by the model is also plotted, and again it is clear that the cycling increased the bulk modulus of the soil, thus making it approach the predicted model curve, as the number of contacts increases toward the theoretical, maximum value. It would be interesting to compare the difference between the analytical results and the experimental values for both moduli, K^* and G^* at a given cycling state. The experimental values for the case of hydrostatic compression (Fig. 44) are closer to the model predicted curve than the measurements with shear (Figs. 41-43), for a comparable number of cycles. This is explained by the fact that, once the spheres have approached each other due to the cycles of shearing, an increase in σ_0^0 can complete the formation of many contacts, thus further increasing the stiffness of the soil.

CHAPTER 7

A TWO-DIMENSIONAL NUMERICAL MICROMECHANICAL MODEL FOR THE STRESS-STRAIN BEHAVIOR OF A GRANULAR SOIL AT SMALL STRAINS

In the preceeding chapter a closed form solution was obtained for the elastic constants of a random configuration of equal, rough, elastic spheres having an arbitrary macroscopic void ratio and subjected to isotropic loading. This was done through the use of the Self-Consistent Method, using a minimum number of assumptions, and it contributed to a greatly improved understanding of the small strain behavior of sands under isotropic conditions. The fact that this analytical solution was obtained with relatively small effort should be attributed to the high level of symmetry in such a system under isotropic pressure.

Logically, the next step should have been to investigate the possibility of obtaining equivalent rigorous solutions for the case of a similar random configuration of equal, elastic, rough spheres, but now subjected to anisotropic loading. Unfortunately, this proved impossible, not only because of the lower level of symmetry in this case, which made the combination of three or more phases for the medium impossible, but also because anisotropic loading induces early yielding (sliding) between some particles in the individual phases. Therefore, an elastic solution was not possible. An elastic, perfectly-plastic rigorous solution would have been in principle feasible, but, again, the pressure dependence of the properties of the phases made the problem intractable.

As mentioned in Section 4.2, for years researchers have been modeling the elastoplastic behavior of polycrystalline aggregates using a variety of analytical, semianalytical, and numerical techniques. As discussed previously, exhibit an analogous behavior to that of the sands, Therefore, it seems logical to attempt formulating the problem of a random packing of equal spheres subjected to an arbitrary stress path, in a manner similar to that used for crystals. This can be achieved by devising an aggregate of regular arrays such as that of Chapter 6, describing the force-deformation at the intergranular contacts through the nonlinear numerical techniques described in Section 4.1 (subroutine CONTACT), and resorting to a nonlinear finite element simulation.

7.1 Aggregate Description

In order to model the behavior of granular soil at small strains, a numerical simulation was developed which calculates the response of a random aggregate of equal, elastic, rough spheres under an arbitrary boundary stress state, σ_{ij}^0 . For this, a finite element analysis was performed in which the element corresponded to a simple cubic array. Each element contains an undetermined number of spheres, assumed to be subjected to a uniform stress field, so that four spheres represent the above element (Duffy and Mindlin, 1957); the element configuration appears in Fig. 45. Several specific media were used in these simulations, each medium consisting of a number of simple cubic arrays in two dimensions (a mono-layer of equal spheres assembled in simple cubic patterns), oriented in such a way so as to resemble a statistically isotropic random aggregate.

The effect of the shape of the "grain boundaries", in this case the gap between elements which are oriented differently, and of any localized orientation concentrations on the macroscopic behavior was not studied here, since a statistically uniform medium was sought to interpret the macroscopic behavior of a granular soil. Each of the above elements is a simple cubic array, randomly oriented, and the number of elements used in each of these media varies from 16 (4X4) to 64 (8X8) as illustrated in Fig. 46 and Figs. D1 through D2 in Appendix D. Therefore, the medium has the same properties of the simple cubic array in terms of void ratio and coordination number.

The simple cubic array was selected as the basis for all simulations due to its simplicity. It is extremely difficult, for example, to implement numerically a constitutive law for the body-centered cubic array since the contact forces and displacements are coupled. For another alternative, the face-centered cubic array, the task is impossible as the array is statically indeterminate. However, it was felt that the inability of varying the void ratio or the coordination number (number of contacts per particle) did not unduly constrain the simulations, which were expected to provide useful insights into the behavior of sand at small strains.

7.2 The Element

The constitutive relation of the elements described above, is an incrementally linear law which is based on the differential stress-strain expressions for the Simple Cubic array presented in Chapter 5. These incremental relations at the particle contacts are integrated through the

nonlinear program CONTACT, previously described in some detail in Section 4.1. Thus, at every increment, the displacements in the simple cubic array are computed separately for each contact, and then the results are combined following the formulation presented in Chapter 5.

Since finite element programs are implemented through the Stiffness Method, in which the displacements are the independent variables, and thus the code first computes the displacements at the nodes from the specified boundary conditions and then calculates the stresses at the Gauss points from these nodal displacements, the constitutive relation of the incremental model CONTACT (Eqn. 12) had to be inverted in order for the displacements to become the independent variables. The inverted constitutive relation is as follows:

$$d\vec{F} = \frac{2Ga}{1-\nu_s} d\alpha \hat{k} + H_p dD_t \hat{t} + fdN \hat{n} + H(dD_N - \frac{fdN}{H_0}) \hat{n} \quad (62)$$

if $dT/dN > f$

and

$$d\vec{F} = \frac{2Ga}{1-\nu_s} d\alpha \hat{k} + H_p dD_t \hat{t} + H_0 dD_N \hat{n} \quad (63)$$

if $dT/dN < f$.

In the general case in which the simple cubic array element is compressed biaxially under σ_{11} and σ_{22} (see Fig. 45), the normal strains are uncoupled and depend only on the normal relative displacements between the centers of adjacent spheres, which in turn depend only on the normal stresses. As described in Chapter 4, this occurs because the behavior at a contact subjected to a normal force is nonlinear elastic, and because the normal compliance at the contact is only functions of the normal

force. Unfortunately, this is not true for the shear strains, which are coupled with the normal stresses. The expression for the shear strain, γ_{12} , described in Section 5.1, is $\gamma_{12} = (\delta_{12} + \delta_{21})/2R$, where δ_{12} and δ_{21} are the relative tangential displacements between the centers of adjacent spheres of radius R . Therefore, the tangential displacements, δ_{12} and δ_{21} , depend on the values of both the tangential and the normal forces at the contact.

As a first step, the macroscopic normal stresses corresponding to each contact are computed directly, since the behavior of the array under compression is nonlinear elastic. Once these normal stresses and forces are determined, the tangential forces and, consequently, the shear stresses can also be computed. The shear strain, γ_{12} , supplied by the finite element program at each Gauss point, is obtained from the summation of the two tangential displacement components at both contacts, δ_{12} and δ_{21} . Since the shear stress components on the faces of the element, σ_{12} , must be equal, the problem of finding the value of σ_{12} reduces to computing the common tangential force acting on two different contacts, subjected to two different normal forces, and with the summation of the resulting tangential displacements being known ($\delta_{12} + \delta_{21} = 2R\gamma_{12}$). For this purpose, an iterative numerical technique based on the bisection method was used, and this made possible the evaluation of the tangential force and, subsequently, of the shear stress.

The stress-strain behavior of an individual element (Fig. 45) assuming quartz spheres, is shown in Fig. 47c for a biaxial state of stress, σ_{11} and σ_{22} , followed by pure shear. Figures 47a and 47b portray

the force-deformation behavior of the "weak" and "strong" contacts for the same case, respectively, where the "weak" contact is defined as that for which the normal stress is smaller (σ_{11} in this case). The properties of quartz for the spheres utilized in this calculation ($E = 295,182 \text{ Kg*cm}^2$, $f = 0.5$ and $\nu = 0.15$, White, 1964) are consistently used throughout the remainder of this work.

It should be noted that the element can not take any tensile normal stress on the slip planes, since this would imply that a contact has ceased to exist, and thus that the particles want to rearrange themselves and form a new packing⁺. Although this rearrangement obviously happens in actual sand aggregates, its simulation was too complex to implement in the present finite element code, and the decision was made to make the contact normal forces positive-definite, that is they can be positive or zero, but never negative.

A subroutine implementing the behavior of this element was coded into the nonlinear finite element program ABAQUS (1982) as a user defined material subroutine (UMAT). The listing of the subroutine as well as a flowchart appear in Appendix C. Finally, an incrementally linear analysis was done using plane strain eight-noded elements with reduced integration.

⁺For the simple cubic array element considered herein, simple analytical considerations show that if both σ_{11} and σ_{22} are positive definite, then no tensile stress can exist in any direction if the friction coefficient f is less than 1, as is the case here.

CHAPTER 8

MONOTONIC LOADING SIMULATIONS OF THE AGGREGATE

As a first step, a number of monotonic loading cases were simulated in an attempt to define the macroscopic behavior of the aggregate. The medium was subjected to several loading paths ranging from hydrostatic compression, to hydrostatic compression followed by some combination of shear and compression.

In most of these simulations, an attempt was made to keep the mean stress constant, so as to have the simulations contained on one π -plane, and the microscopic behavior was closely monitored in order to verify that the necessary assumptions of the constitutive law were satisfied. Finally, one simulation was also made with variable mean stress in order to investigate the behavior of the aggregate under biaxial compression.

8.1 Isotropic Compression

In one of the first simulations, medium 1 with 16 elements was subjected to a monotonically increasing hydrostatic pressure, first to $\sigma_0^0 = 3 \text{ Kg}^*/\text{cm}^2$ and then up to $\sigma_0^0 = 5 \text{ Kg}^*/\text{cm}^2$, and it was observed that both the macroscopic and microscopic (element) response exhibit a locking nonlinear elastic behavior, similar to that observed in sand (Fig. 48).

8.2 Isotropic Compression Followed by Pure Shear

As a second step, the isotropy of the media used was verified by loading them isotropically up to $\sigma_0^0 = 1 \text{ Kg}^*/\text{cm}^2$, followed by pure shear applied incrementally. This was accomplished by imposing on each medium a predetermined direction of the major principal stress. The values used

for the angle, α , between the major principal stress and the vertical direction of the medium, (Fig. 49a), were 0° (compression in the vertical direction); 22.5° ; 45° (pure shear in the vertical and horizontal planes); 67.5° ; and 90° (extension in the vertical direction). The results of these simulations are shown in Fig. 50 as plots of the applied deviator stress, $\sigma_1^0 - \sigma_2^0$, versus the resultant shear strain, $\gamma = \epsilon_1 - \epsilon_2$. Fig. 50 includes results of media with 16 and 64 elements. In total, four media were used: three with 16 and one with 64 elements, including the two media in Fig. 46. Figs. 51-53 include the stress-strain behavior of two individual elements for the compression of medium 2 under constant mean stress and for $\alpha = 0^\circ$. The stress-strain behavior of all 16 elements for the same medium and same loading case appears in Appendix E.

It can be seen in Fig. 50 that the aggregate is indeed isotropic under isotropic pressure, as expected. Since Fig. 50 shows that the difference between the stress-strain behavior of the 16-element and 64-element media is not significant, it was decided that for subsequent parametric studies, as well as for monitoring the stress-strain behavior of each element, any of the less costly 16-element media could be used as representative of the aggregate.

8.3 Isotropic Compression Followed by Biaxial Compression

A 16-element medium (medium 1 of Fig. 46) was compressed with the mean stress variable, in a manner similar to that of a soil specimen in a triaxial device (see the 45° stress path in Fig. 54). That is, the medium was first compressed isotropically under $\sigma_0^0 = 1.0 \text{ Kg}^*/\text{cm}^2$, and then σ_1 was increased in a vertical direction while σ_2 remained constant,

$\sigma_2 = \sigma_0^0 = 1.0 \text{ Kg*/cm}^2$. The stress-strain curve calculated for this medium is shown in Fig. 55, and the behavior for two individual elements is presented in Figs. 56 and 57. The σ - ϵ behavior of all 16 elements for the same medium and same loading case appears in Appendix F. The nonlinearity of the medium here is even less pronounced than in the simulations with constant mean stress (Fig. 50), since in Fig. 55 there is no lateral unloading. The Poisson's ratio of the medium was also computed from this numerical simulation, and it was found to vary from 0.02 to 0.05 (Fig. 58), thus agreeing well with values measured experimentally on dry sand at the University of Texas (Lee, S., 1985). The obliquity at failure was the same as in the simulations with the constant mean stress, as illustrated in Fig. 54.

8.4 Yielding and Failure Considerations

In the numerical simulations of pure shear summarized in Fig. 50, it was observed that the yielding/failure process of the medium occurs in two successive stages. In the first stage, a growing number of "soft" elements, oriented more or less parallel to the directions of the applied shear stress, slide and this sliding accounts for the increasing nonlinearity of the curves in Fig. 50, as the shear strain, $\gamma = \epsilon_1 - \epsilon_2$, increases from 0 to values around 0.1×10^{-3} . At these larger values of shear strain, typically around 20% of the elements have already slid (failed). In the second stage, occurring at about $\gamma = \epsilon_1 - \epsilon_2 = 0.16 \times 10^{-3}$, one or several of the "stiff" elements, oriented more or less perpendicular to the direction of the shear stress, and which had not yet slid, tend to separate as the normal force at the contact becomes zero, the correspond-

ing ratio shear/normal force at the contact reaches f , and the element slides. This, of course, is related to the fact that the normal contact force is allowed to be zero but not negative. Once some of the "stiff" elements fail due to this tendency to separate, a growing number of both "soft" and "stiff" elements slide in the next increment(s) by a combination of shear stress increase and separation tendency, thus precipitating the failure of the medium, occurring at $\tau_f = 0.448 \text{ Kg*/m}^2$. This is close, but slightly less than the yield stress of the simple cubic array subjected to pure shear in the directions of the array: $\tau = (0.5)/(1) = 0.5 \text{ Kg*/cm}^2$. This value of the failure stress is much less than the value of $1.536\sigma_y$ calculated for the polycrystalline aggregates, as discussed in Section 4.2. This difference in values, between the simple cubic and the fcc polycrystalline aggregate, occurs, among other reasons, because the simple cubic element is not allowed to take any tensile stresses during the stress redistribution which takes place when an increasing number of the elements slide.

To further verify this sequence of events just described, a special 64-element medium was defined (Fig. D3 in Appendix D) and subjected to shear at constant mean stress. This new medium was constructed in such a way as to provide an insight into this complex "failure" phenomenon, by having only two extreme element orientations: the four elements at the center are oriented at $\beta = 0^\circ$, see Fig. 49b ("stiff" elements), while the other sixty, surrounding those four, are oriented at 45° ("soft" elements), that is parallel to the orientation of the maximum shear stress. Consequently, the "soft" elements are expected to slide first; and if

then the "stiff" elements were to fail by a tendency to separate, the above observations on the "failure" sequence would be confirmed. Indeed, when some of the $\beta = 45^\circ$ elements surrounding the $\beta = 0^\circ$ "stiff" elements had slid, (due to roundoff error all "soft" elements did not fail at the same time, but were sufficiently close to sliding to be considered to fail at the same time), negative (tensile) stresses developed in all "stiff" elements, which eventually slid until, finally, the global stiffness matrix became singular and the simulation was terminated. The stress-strain behavior in three representative elements is shown in Figs. 59-61; as it can be seen, the element behavior is similar to the one which appears in Figs. 51-53. Thus, the failure of the aggregate should be attributed to this "localization" phenomenon, which is similar to that observed in metals (Dieter, 1976).

This "failure" of the aggregate, defined here by the sequence of phenomena previously described which at the end results in the global stiffness matrix of the medium becoming singular, is associated with a generalized tendency of the particles to slide, separate and rearrange themselves into more stable positions. This corresponds roughly to the changes in geometry occurring in actual sands at the threshold strain, $\gamma_t = 0.1$ to 0.2×10^{-3} (Dobry et al., 1982), as verified by the fact that "failure" of the medium in Fig. 50 occurs at a shear strain, $\gamma = \epsilon_1 - \epsilon_2 = 0.16 \times 10^{-3}$.

In addition to the simulations already discussed in which the 16 and 64-element media were sheared at constant mean stress after isotropically compressing them with $\sigma_0^0 = 1 \text{ Kg}^*/\text{cm}^2$, two similar runs were done on

medium 2 (16-elements), but with $\sigma_0^0 = 0.5 \text{ Kg}^*/\text{cm}^2$ and $2 \text{ Kg}^*/\text{cm}^2$. In these two runs, the medium failed at $\tau_f = 0.224$ and $\tau_f = 0.896 \text{ Kg}^*/\text{cm}^2$, respectively. Therefore, in all pure shear simulations following σ_0^0 , $\tau_f/\sigma_0^0 = 0.448$. This defines the "failure surface" shown in Fig. 54 for the aggregate, where the corresponding three stress paths for $\sigma_0^0 =$ constant are also included. The observed, and proposed, failure surface is a cone of the Von Mises type with the slope of the directrix being 0.448, or slightly less than the coefficient of intergranular friction, $f = 0.5$ (fig. 54).

8.5 Discussion of Results

As it can be seen in the simulations discussed above, the media used represent well some aspects of the behavior of actual, uniform, rounded sand, by being isotropic under isotropic pressure, yielding in shear and locking under hydrostatic compression. Therefore, these "random" media have the desirable properties of the simple cubic array without its problematic inherent anisotropy (see Chapter 5).

Since the elements are randomly oriented, discontinuities in the strain field are expected across element boundaries. It was found that the maximum strain jump at the nodes was one to two orders of magnitude smaller than the minimum strain value in the 16-element media, and three orders of magnitude smaller in the 64-element medium. This is thought to be satisfactory in both cases and it shows that, as expected, the spatial accuracy of the solution improves as the number of elements increases.

Even though the macroscopic behavior in Fig. 50 is not far from being linear almost until "failure", the microscopic behavior is not;

this can be seen in Figs. 51-53 and Appendix E, where the individual element stress-strain curves are shown for the 16-element medium 2. The macroscopic "linearity" in Fig. 50 is thus a consequence of the interaction between all the elements.

The stress field inside each element was found to be close to uniform, thus verifying a basic assumption made at the outset of this study. The normalized element stresses $2\sigma_{11}/(\sigma_1^0 - \sigma_2^0)$, $2\sigma_{22}/(\sigma_1^0 - \sigma_2^0)$ and $2\sigma_{12}/(\sigma_1^0 - \sigma_2^0)$, are plotted against the applied shear strain $\epsilon_1 - \epsilon_2$ for all element orientations (8 orientations) in Figs. G1-G8, Appendix G. Furthermore, in the normalized element strain, $2\epsilon_{1j}/\epsilon_1 - \epsilon_2$, is plotted versus the applied difference in principal strain, $\epsilon_1 - \epsilon_2$ in Figs. G9-G16 of the same Appendix G. It can be observed that the element stress and strain fields remain almost constant during loading.

Moreover, it was observed that the stress field was more or less uniform throughout the medium in all simulations, except very close to failure, and that the element behavior was essentially independent of its locations and a function only of the orientation, β , of that element, (see Fig. 49b and Figs. E1-E17 in Appendix E). The value of the uniform stress, σ_{1j} for each element was approximately the applied macroscopic stress, σ_{ij}^0 resolved in that particular orientation, $\sigma_{1j} = \sigma_{ij}^0 n_i n_j$, where σ_{ij}^0 is the stress applied at the boundary of the medium and $n_i n_j$ are direction cosines. This was true in all runs. This is illustrated by Figs. 62-64, which show the variation of $2\sigma_{11}/(\sigma_1^0 - \sigma_2^0)$, $2\sigma_{22}/(\sigma_1^0 - \sigma_2^0)$ and $2\sigma_{12}/(\sigma_1^0 - \sigma_2^0)$, versus the element orientation, β . It must be remembered that σ_{11} , σ_{22} and σ_{12} are the element stresses oriented along the axes of

the cubic array (Fig. 45). The three plots in Figs. 62-64 include σ_{11} , σ_{22} and σ_{12} calculated for all elements, (and all stress increments (with the rectangles indicating the range of values for each increment), in three pure shear simulations ($\alpha = 0^\circ$, 45° , and 90°), and the curves correspond to the assumption of uniform stress field throughout the medium. It can be seen that the assumption of the independence of the element stresses on element location is fully verified by the plots. It should be noted that this is identical to the assumption of stress uniformity in the early work of Taylor (1938), and very similar to the results obtained by Lin (1964) and Budiansky and Wu (1962) for an assemblage of elastoplastic crystals.

CHAPTER 9

CYCLIC LOADING SIMULATIONS OF THE AGGREGATE

The 16-element media were subjected to a number of stress paths with complete stress reversal in order to study the stress-strain behavior of the aggregate under cyclic loading, and also to compute dynamic properties such as the damping ratio.

9.1 Cyclic Isotropic Compression

The (16-element) medium 1 was subjected to an isotropic stress of $\sigma_o^o = 3.0 \text{ Kg*/cm}^2$ followed by a complete isotropic cycle with amplitude of 2.0 Kg*/cm^2 , that is σ_o^o was first increased to 5 Kg*/cm^2 and then decreased to 1 Kg*/cm^2 , and then back to 5 Kg*/cm^2 . The stress-strain behavior of this medium is shown in Fig. 65, which shows a nonlinear elastic behavior similar to that of actual sand (Ko and Scott, 1967).

9.2 Isotropic Compression Followed by Cyclic Shear Loading

The same 16-element medium, consolidated isotropically to $\sigma_o^o = 1.0 \text{ Kg*/cm}^2$, was also cycled under pure shear ($\alpha = 45^\circ$) conditions, with an amplitude of shear stress, $\tau_c = 0.2, 0.3, 0.35, 0.4$ and 0.43 Kg*/cm^2 . The hysteresis loops for $\tau_c = 0.2, \tau_c = 0.35, \tau_c = 0.40$ and $\tau_c = 0.43 \text{ Kg*/cm}^2$ appear in Figures 66a, 66b, 67a and 67b respectively.

Computation of Dynamic Properties and Wave Velocities

The secant shear moduli, G , obtained from the pure shear simulations at different α 's for the constant mean stress case (Fig. 50), were normalized with respect to the shear moduli at very small strains, G_{\max} ,

obtained in the same simulation, and the corresponding values of G/G_{\max} versus shear strain are plotted in Fig. 68a, where they are compared to the bounds proposed by Seed and Idriss (1970) from actual tests on sands. The corresponding damping ratio, λ , was obtained from the loops under cyclic pure shear (Figs. 66a, 66b, 67c, 67d) with the expression:

$$\lambda = \frac{1}{2\pi} \frac{\Delta W}{\tau \gamma}$$

where ΔW is the area of the stress-strain loop, τ and γ are the maximum values of the shear stress and shear strain, respectively, during the cycle (see Fig. 69). The values of damping ratio obtained in cyclic pure shear are plotted against cyclic shear strain γ in Fig. 68b. Figure 68 corresponds to simulations done at a mean stress of $1.0 \text{ Kg}^*/\text{cm}^2$. Figure 68 also includes the corresponding curves for G/G_{\max} and damping ratio for the case of pure shear along the slip planes of a simple cubic array, computed by Dobry et al. (1982). Since the slope of the G/G_{\max} and damping ratio versus γ curves in Fig. 68 for the aggregate studied herein is flatter than that of the simple cubic array, its behavior is more realistic when compared to actual sand. This "stiffer" behavior of the aggregate, as compared to that of a single cubic array, should be attributed to the interaction between the elements of the medium.

9.3 Constrained Moduli of the Aggregate and P-Wave Velocities Under Biaxial Compression

The small strain constrained moduli, D_{ij} , were obtained from the "triaxial" simulation previously discussed (Isotropic Compression Followed by Biaxial Compression, Section 8.3). The values of D_{ij} were

computed in both principal (vertical and horizontal) directions. In order to increase the accuracy of the calculation at these small stress and strain increments, and to fully account for the stress-induced anisotropy of the aggregate, the 64-element medium (medium 4) was used. The medium was loaded to the desired biaxial stress ratio, $K = \frac{\sigma_1^0}{\sigma_2^0}$, and then very small stress increments with appropriate signs were applied, $\Delta\sigma_1^0, \Delta\sigma_2^0$, the corresponding differences in strain were computed and, finally, the small strain constrained moduli of the medium, D_{11}, D_{22} were computed in both directions. The results of this simulation are shown in Figs. 70a and 70b as plots of the normalized constrained moduli of the medium, $\frac{D_{22}^{(K)}}{D_{22}^{(1)}}$ and $\frac{D_{11}^{(K)}}{D_{11}^{(1)}}$ versus the stress ratio $K = \frac{\sigma_1^0}{\sigma_2^0}$, where $D_{11}^{(K)}$ is the constrained modulus at a given K , and $D_{11}^{(1)}$ the corresponding constrained modulus under the initial isotropic stress, σ_0^0 . The same figure also includes data points from a number of measurements on sand obtained in the large cubic facility at the University of Texas at Austin (Kopperman et al., 1982), which were performed during a test with conditions similar to those assumed in this numerical simulation. The agreement between experimental results and numerical simulations in fig. 70a and 70b is excellent. Consequently, the main conclusion obtained from the University of Texas laboratory results, that the P-wave velocity propagating along a principal stress direction is only a function of the value of that principal stress is fully predicted by the numerical experiment. Therefore, as previously hypothesized by the authors, this effect is due to the particulate nature of the soil, and its analytical modeling necessarily requires taking into account this particulate nature.

CHAPTER 10

CONCLUSION

A particulate mechanics model has been developed for describing the elastic response of an assemblage of identical, elastic, rough spheres of arbitrary macroscopic porosity, n , subjected to an isotropic pressure, σ_0 . The model is based on the Mindlin-Deresiewicz theory of bodies in contact and takes into account the spatial variation of porosity. The model assumes that the assemblage is composed of random clusters of several regular arrays of various porosities and it computes the macroscopic moduli by means of the Self Consistent Method.

The predictions of the model, specialized for the case of quartz spheres, were compared to measurements of the shear modulus, G_{\max} , on uniform quartz sands, with good qualitative agreement; however, the analytical "sands" were as much as 3.5 times stiffer than the actual soils. This is explained by the fact that sands have less effective contacts per grain than theoretically predicted for a given porosity, n . However, when the sand is prestrained by millions of shearing cycles slightly above the threshold strain, the shear modulus approaches the theoretical value without changing the macroscopic porosity, n , as the theoretical number of contacts is slowly realized. Thus, the model exhibits excellent agreement with results on heavily prestrained sand, and it also provides upper bounds for small strain shear and bulk moduli for rounded, uniform sands.

Finally, a nonlinear finite element formulation is established which interprets the behavior of granular soil at small strains. This

formulation also considers the soil as an aggregate of different packings of equal spheres, but this time, for simplicity, only the simple cubic packing is used. The inherent anisotropy of the simple cubic packing is eliminated by orienting the same packing randomly in several directions. The model incorporates the nonlinear constitutive model CONTACT for describing the force-deformation behavior at the contact, and results are obtained for several stress paths. Specifically, the recent compressional wave velocity measurements on anisotropically consolidated, dry sand are simulated. These experimental measurements have shown that the P-wave velocity depends only on the principal stress on the direction of wave propagation; this was predicted by the numerical simulation. Furthermore, the comparison of the normalized constrained moduli between the finite element model and the measurements is excellent, thus validating the micromechanics approach used to the problem.

Both phenomena described above, the increase in the stiffness of a granular soil and the dependence of the P-wave velocity only on the principal stress in the direction of wave propagation, had not previously been fully interpreted or modelled analytically. Their interpretation and modeling here was made possible only through a micromechanical approach, which takes into account the particulate nature of the granular soil responsible for the above phenomena. Therefore, the method of modeling rounded, uniform granular soil as an aggregate of regular packings of equal, elastic, rough spheres leads to simple and accurate results.

CHAPTER 11

REFERENCES

- ABAQUS (1982), Users' Manual, Version 4, Hibbit, Karlsson and Sorensen, Inc., Providence, RI.
- Backman, B.F., Brown, C.B., Jowitt, P.W. and Munro, J. (1983), "Statistical Mechanics of Granular Materials," Advances in the Mechanics and the Flow of Granular Materials, Vol. I, M. Shahinpoor, ed., Trans. Tech. Publications, Clausthal-Zellerfeld, Fed. Republic of Germany.
- Benjamin, J.R. and Cornell, C.A. (1970), Probability, Statistics and Decision for Civil Engineers, McGraw Hill.
- Bernal, J.D. and Mason, J. (1960), Co-ordination of Randomly Packed Spheres, *Nature*, Vol. 188, pp. 910-911.
- Bernal, J.D., Knight, K.R. and Cherry, I. (1964), Growth of Crystals from Random Close Packing, *Nature*, Vol. 202, pp. 852-854.
- Bishop, J.F.W. and Hill, R. (1951), "A Theory of the Plastic Distortion of a Polycrystalline Aggregate under Combined Stresses," *Phil. Mag.*, Ser. 7, Vol. 42, pp. 414-427.
- Bishop, J.F.W. and Hill, R. (1951a), "A Theoretical Derivation of the Plastic Properties of a Polycrystalline Face-Centered Metal," *Phil. Mag.*, Ser. 7, Vol. 42, pp. 1298-1307.
- Brandt (1955), "A Study of the Speed of Sound in Porous Media," *J. Appl. Mech.* 22, pp. 479-486.
- Brauns, J. (1968), *Über den Einfluss des Einzelkornbruches auf die Belastbarkeit von Haufwerken, besonders von regelmässigen Kugelpackungen, im Dreiaxialversuch*, PhD Dissertation, Univ. Karlsruhe.
- Brauns, J. and Leussink (1970), *Über mechanische Eigenschaften von Kugelpackungen, verfahrenstechnik* 4, 1, S.5-8.
- Brown, C.B. (1978), "The Use of Maximum Entropy in the Characterization of Granular Media," Proceedings US-Japan Seminar on Continuum Mechanical and Statistical Approaches in the Mechanics of Granular Materials, Cowin and Satake, editors, pp. 98-109.
- Budiansky, B., Hashin, Z. and Sanders, L. (1960), "The Stress Field of a Slipped Crystal and the Early Plastic Behavior of Polycrystalline Materials," *Plasticity, Proc. 2nd Symposium on Naval Structure Mech.*, pp. 239-258, Pergamon Press.

- Budiansky, B. and Wu, T. (1962), "Theoretical Prediction of Plastic Strains of Polycrystals," Proceedings, 4th US Nat. Congr. Appl. Mech., pp. 1175-1185.
- Budiansky, B. (1965), "On the Elastic Moduli of Some Heterogeneous Materials," Jmps 1965, Vol. 13, pp. 223-227.
- Canova, G.R., Kocks, U.F. and Jonas, J.J. (1984), "Theory of Torsion Texture Development," Acta Metall., Vol. 32, No. 2, pp. 211-226.
- Canova, G.R., Kocks, U.F., Tome, C.N. and Jonas, J.J. (1985), "The Yield Surface of Textured Polycrystals," J. Mech. Phys. Solids, Vol. 33, No. 4, pp. 371-397.
- Cattaneo, C. (1938), "Sul contatto di due corpi elastici," Atti Acad. naz. Lincei Rc., Ser. 6, 27, 342-348, 434-436, 474-478.
- Chen, W.F. (1975), Limit Analysis and Soil Plasticity, Elsevier Scientific Publishing Co., Amsterdam, The Netherlands.
- Christensen, R.M. (1979), Mechanics of Composite Materials, John Wiley & Sons, Inc. New York.
- Cowin and Satake, editors (1978), Continuum Mechanical and Statistical Approaches in the Mechanics of Granular Materials, Proceedings of US-Japan Seminar, Sendai, Japan, June 1978.
- Cundall, P.A. and Strack, P.A. (1983), "Modeling of Microscopic Mechanisms in Granular Material," in Mechanics of Granular Materials: New Models and Constitutive Relations, Jenkins and Satake, editors, pp. 137-149.
- Dantu, P. (1957), "Contribution a l'Etude Mechanique et Geometrique des Millieux Pulverulents," Proc. of the 4th Int. Conf. on Soil Mech. and Found. Eng., London.
- Davis, R.A. (1974), "A Discrete Probabilistic Model for Mechanical Response of a Granular Medium," Ph.D. Dissertation, Columbia Univ.
- Davis, R.A. and Deresiewicz, H. (1977), "A Discrete Probabilistic Model for Mechanical Response of a Granular Medium," Acta Mechanica, 27, pp. 69-89.
- Deresiewicz (1958), "Mechanics of Granular Matter," Advances in Applied Mechanics, V, pp. 233-306, Academic Press Inc, New York.
- Deresiewicz, H. (1958a), "Stress-Strain Relations for a Simple Model of a Granular Medium," J. Appl. Mech., Trans. ASME, Sept., pp. 402-406.

- Deresiewicz, H. (1973), "Bodies in Contact with Applications to Granular Media," included in R.D. Mindlin and Applied Mechanics, G. Herrmann, Editor, Pergamon Press, New York.
- Dieter, G.E. (1976), Mechanical Metallurgy, McGraw Hill, New York.
- DiMaggio, F.L. and Sandler, I.S. (1971), "Material Model for Granular Soils," Journal of the Engineering Mechanics Division, ASCE, Vol. 97, pp. 935-950.
- Dobry, R. and Athanasiou-Grivas, D. (1978), "Stress-Strain Relation for Soils Under Earthquake Loading: Technical Background," Report No. 78-2, Department of Civil Engineering, Rensselaer Polytechnic Institute, Troy, NY.
- Dobry, R., Powell, D.J., Yokel, F.Y. and Ladd, R.S. (1980), "Liquefaction Potential of Saturated Sand - The Stiffness Method," Proc. Seventh World Conference on Earthquake Engineering, Istanbul, Turkey, September, Vol. 3, pp. 25-32.
- Dobry, R., Stokoe, K.H. II, Ladd, R.S. and Youd, T.L. (1981), "Liquefaction Susceptibility from S-Wave Velocity," Proc. Session on In Situ Tests on Evaluate Liquefaction Susceptibility, ASCE National Convention, St. Louis, Missouri, October.
- Dobry, R., Yokel, F.Y. and Ladd, R.S. (1981a), "Liquefaction Potential of Overconsolidated Sands in Moderately Seismic Areas," Proc. Conf. on Earthquake and Earthquake Engineering in the Eastern U.S., Knoxville, TN, September.
- Dobry, R., Ladd, R.S., Yokel, F.Y., Chung, R.M. and Powell, D. (1982), "Prediction of Pore Water Pressure Buildup and Liquefaction of Sands During Earthquakes by the Cyclic Strain Method," Building Science Series 138, National Bureau of Standards.
- Dobry, R. and Petrakis, E. (1984), "Sand Compaction in Cyclic Shear - A Statistical-Model," Proceedings 5th ASCE-EMD Specialty Conference, Laramie, Wyoming, August.
- Drnevich, V.P. (1967), "Effects of Strain History on the Dynamic Properties of Sand," Ph.D. Dissertation, University of Michigan, Ann Arbor.
- Drnevich, V.P. and Richart, F.E., Jr. (1970), "Dynamic Prestraining of Dry Sand," Journal of the SMFD, ASCE, 96, SM2, March, pp. 453-469.
- Drucker, D.C. and Prager, W. (1952), "Soil Mechanics and Plastic Analysis or Limit Design," Quarterly of Applied Mathematics, Vol. 10, pp. 157-165.

- Duffy, J. and Mindlin, R.D. (1957), "Stress-Strain Relations and Vibrations of a Granular Medium," J. Appl. Mech., Trans. ASME, Dec., pp. 585-593.
- Duffy, J. (1959), "A Differential Stress-Strain Relation for the Hexagonal Close-Packed Array of Elastic Spheres," J. Appl. Mech., 26, pp. 88-94.
- Dyvik, R., Dobry, R., Thomas, G.E. and Pierce, W.G. (1982), "Influence of Consolidation Shear Stresses and Relative Density on Threshold Strain and Pore Pressure During Cyclic Straining of Saturated Sand," Research Report No. CE-82-11, Department of Civil Engineering, Rensselaer Polytechnic Institute, Troy, NY.
- Eshelby, J.D. (1957), "The determination of the elastic field of an ellipsoidal inclusion and related problems," Proc. R. Soc. London, vol. A241, 376.
- Field, W.G. (1963), "Towards the Statistical Definition of a Granular Mass," 4th Australia -New Zealand Conf. on Soil Mech. and Found. Eng., pp. 143-148.
- Filep, L. (1936), "Egynelo qom bokol allo halmazok, Vizugyi Kolzlemanyek, Budapest.
- Finney, J.L. (1985), "Structure and Properties of Granular Materials: Guidelines from Modelling Studies of Liquids and Amorphous Solids," Advances in the Mechanics and the Flow of Granular Materials, Vol. I, M. Shahinpoor, ed., Trans. Tech. publications, Clansthal-Zellerfeld, Fed. Republic of Germany.
- Gassmann, F. (1951), "Elastic Waves Through a Packing of Spheres," Geophysics, 16, pp. 673-685 and (1953) 18, p. 269.
- Grivas, D. and Harr, M.E. (1974), "Particle Contacts in Discrete Materials," Indiana Academy of Science, Engineering Division.
- Hara, G. (1935), "Theorie der Akustischen Schwingungsausbreitung in Gekornen Substanzen und Experimentelle Untersuchungen an Kohlepulver," Elektrische Nachrichten-Technik 12, pp. 191-200.
- Hardin, B.O. and Richart, F.E., Jr. (1963), "Elastic Wave Velocities in Granular Soils," Journal of the Soil Mechanics and Foundations Division, ASCE, Vol. 89, No. SM1, February, pp. 33-65.
- Hardin, B.O. and Black, W.L. (1966), "Sand Stiffness Under Various Triaxial Stresses," J. Soil Mechanics and Foundation Div. Proc. ASCE, Vol. 94, No. SM2, pp. 27-42.

- Hardin, B.O. and Drnevich, V.P. (1972), "Shear Modulus and Damping in Soils: Measurements and Parameter Effects," Proc. ASCE, 98, No. SM6, June, pp. 603-624. Hardin, B.O. (1978), "The Nature of Stress-Strain Behavior of Soils," Proc. ASCE Specialty Conference on Earthquake Engineering and Soil Dynamics, Pasadena, California, Vol. 1, pp. 3-90.
- Hardin, B.O. (1978), "The Nature of Stress-Strain Behavior of Soils," Proc. ASCE Specialty Conference on Earthquake Engineering and Soil Dynamics, Pasadena, California, Vol. 1, pp. 3-90.
- Hardin, B.O. (1980), "Discussion to 'Anisotropic Shear Modulus Due to Stress Anisotropy' by S.K. Roesler," Journal of the Geotechnical Engineering Division, ASCE, Vol. 106, No. GT8, August, pp. 956-958.
- Harr, M.E. (1977), Mechanics of Particulate Media - A Probabilistic Approach, McGraw Hill, N.Y.
- Hashin, Z. and Shtrikman, S. (1963), "A Variational Approach to the Theory of the Elastic Behaviour of Multiphase Materials," JMPS, Vol. 11, 127.
- Hendron (1963), "The Behavior of Sand in One-Dimensional Compression," Ph.D. Thesis, University of Illinois, Dept. of Civil Engineering.
- Hershey, A.V. (1954), "The Elasticity of an Isotropic Aggregate of Anisotropic Cubic Crystals," J. Appl. Mechanics, Vol. 21, 236.
- Hershey, A.V. (1954), "The Plasticity of an Isotropic Aggregate of Anisotropic Face-Centered Cubic Crystals," Journal of Applied Mechanics, ASME, Sept., pp. 241-249.
- Hertz, H. (1882), "Ueber die Berührungsfester Elastischer Körper," J. rene angew. Math. 92, pp. 156-171.
- Hill, R. (1950), The Mathematical Theory of Plasticity, Clarendon Press, Oxford.
- Hill, R. (1965), "A Self-Consistent Mechanics of Composite Materials," JMPS, Vol. 13, pp. 213-222.
- Hill, R. (1967), "The Essential Structure of Constitutive Laws for Metal Composites and Polycrystals," JMPS, Vol. 15, pp. 79-95.
- Horne, M.R. (1965), "The Behavior of an Assembly of Rotund, Rigid, Cohesionless Particles," Proc. Royal Society, Series A., Vol. 286.
- Ishlinsky, A. Iu. (1954), Ukr. Mat. Zhurnal, 6, 314.

- Iwan, W.D. (1967), "On a Class of Models for the Yielding Behavior of Continuous and Composite Systems," *Journal of Applied Mechanics*, Vol. 34, pp. 612-617.
- Iwasaki, T., Tatsuoka, F. and Takagi, Y. (1978), "Shear Moduli of Sands Under Cyclic Torsional Shear Loading," *Soils and Foundations*, Vol. 18, No. 1, March, pp. 39-56.
- Jenkins and Satake, editors (1983), Mechanics of Granular Materials: New Models and Constitutive Relations, Proceedings of US-Japan Seminar, Ithaca, New York, August 1982.
- Kinoshita, N. and Mura, T. (1971), Elastic Fields of Inclusions in Anisotropic Media *Physica status solidi* (a)5, 759.
- Knox, D.P., Stokoe, K.H., II and Kopperman, S.E. (1982), "Effect of State of Stress on Velocity of Low-Amplitude Shear Waves Propagating Along Principal Stress Directions in Dry Sand," *Geotechnical Engineering Report GR82-23*, Civil Engineering Department, The University of Texas at Austin.
- Ko, H.Y. and Scott, R.F. (1967), "Deformation of Sand in Hydrostatic Compression," *J. Soil Mech. Found. Div., Proc. ASCE*, 93, pp. 137-156.
- Konishi, J. (1978), "Microscopic Model Studies on the Mechanical Behavior of Granular Materials," Proceedings US-Japan Seminar on Continuum Mechanical and Statistical Approaches in the Mechanics of Granular Materials, Cowin and Satake, editors, pp. 27-46.
- Kopperman, S.E., Stokoe, K.H., II and Knox, D.P. (1982), "Effect of State of Stress on Velocity of Low-Amplitude Compression Waves Propagating Along Principal Stress Directions in Sand," *Research Report GR22-22*, Department of Civil Engineering, University of Texas at Austin.
- Kroner, E. (1958), Berechnung der Elastischen Konstanten des Vielkristalls aus den Konstanten des Einkristalls. *Zeitschrift für Physik*, Bd 151, S504-518.
- Lade, P.V. and Duncan, J.M. (1975), "Elastoplastic Stress-Strain Theory for Cohesionless Soil," *Journal of Geotechnical Engineering Division, ASCE*, Vol. 101, No. GT10, pp. 1037-1053.
- Lambe, T. and Whitman, R. (1969), Soil Mechanics, John Wiley & Sons, New York.
- Lawrence, F.V. (1965), "Ultrasonic Shear Wave Velocities in Sand and Clay," Massachusetts Institute of Technology, Department of Civil Engineering, Research Report R65-05, January.

- Lee, S.H.H. (1985), "Investigation of Low Amplitude Shear Wave Velocity in Anisotropic Material," Ph.D. Dissertation, Univ. Texas at Austin, TX.
- Lin, T.H. (1964), "Slip and Stress Fields of a Polycrystalline Aggregate at Different Stages of Loading," JMPS, Vol. 12, pp. 391-408.
- Lin, T.H. and Ito, M. (1965), "Theoretical Plastic Distortion of a Polycrystalline Aggregate under Combined and Reversed Stresses," JMPS, Vol. 13, pp. 103-115.
- Lin, T.H. and Ito, M. (1966), "Theoretical Plastic Stress-Strain Relationship of a Polycrystal and the Comparisons with the Von Mises and the Tresca Plasticity Theories," Int. J. Engng. Sci., Vol. 4, pp. 543-561.
- Love, A.E.H. (1927), A Treatise on the Mathematical Theory of Elasticity, Cambridge University Press.
- Makhlouf, H. (1963), "Stress-Strain Relation and Irrotational Wave Motion of Granular Media," Doctoral Thesis, Carnegie Institute of Technology.
- Makhlouf, H. and Stewart (1967), "Elastic Constants of Cubical-Tetrahedral and Tetragonal Sphenoidal Arrays of Uniform Spheres," Proc. Intl. Symposium on Wave Propagation and Dynamic Properties of Earth Materials, Albuquerque, NM, Aug.
- Mindlin, R.D. (1949,) "Compliance of Elastic Bodies in Contact," Journal of Applied Mechanics, Sept., pp. 259-268.
- Mindlin, R.D., Mason, W.P., Osmer, T.F. and Deresiewicz, H. (1951), "Effects of an Oscillating Tangential Force on the Contact Surfaces of Elastic Spheres," Proc. 1st U.S. National Congress of Appl. Mech., ASME, pp. 203-208.
- Mindlin, R.D. and Deresiewicz, H. (1953), "Elastic Spheres in Contact Under Varying Oblique Forces," J. Appl. Mech., Trans. ASME, Sept., pp. 327-344.
- Mogami, T. (1965), "A Statistical Theory of Mechanics of Granular Materials," J. Fac. Engng., Univ. of Tokyo (B), Vol. 28, pp. 65-79.
- Morgenstern, M. (1963), "Maximum Entropy of Granular Materials," Nature, Vol. 200, pp. 559-560.
- Mroz, Z. (1967), "On the Description of Anisotropic Workhardening," Journal of Mechanics and Physics of Solids, Vol. 15, pp. 163-175.
- Mroz, Z. (1969), Acta Mech., 7 (2-3), (199-212).

- Mroz, Z., Norris, V.A. and Zienkiewicz, O.C. (1978), "An Anisotropic Hardening Model for Soils Its Applications to Cyclic Loading," *International Journal for Numerical and Analytical Methods in Geomechanics*, Vol. 2, pp. 203-221.
- Mroz, Z., Norris, V.A. and Zienkiewicz, O.C. (1979), "Application of an Anisotropic Hardening Model in the Analysis of Elasto-Plastic Deformation of Soils," *Geotechnique*, Vol. 29, No. 1, pp. 1-34.
- Munro, J. and Jowitt, P.W. (1974), "Information Theory and Granular Materials," Civil Eng. Dept., Imperial College of Science and Techn., London.
- National Research Council (1985), Report on "Liquefaction of Soils," Washington, D.C.
- Nemat-Nasser, S. and Mehrabadi, M. (1983), "Stress and Fabric in Granular Masses," in Mechanics of Granular Materials: New Models and Constitutive Relations, Jenkins and Satake, editors, pp. 1-8.
- Oda, M. (1974), "A Mechanical and Statistical Model of Granular Material," *Soils and Found.*, Japanese Soc. of S.M. & F.E., Vol. 14, No. 1, pp. 13-27.
- Oda, M., Konishi, J. and Nemat-Nasser, S. (1983), "Experimental Micromechanical Evaluation of the Strength of Granular Materials; Effects of Particle Rolling," in Mechanics of Granular Materials: New Models and Constitutive Relations, Jenkins and Satake, editors, pp. 21-30.
- Oner, M. (1984), "Analysis of Fabric Changes During Cyclic Loading of Granular Soils," *Proc. 8th World Conf. on Earthquake Engineering*, San Francisco, July.
- Perry, D.C. and Brown, C.B. (1981), "Compliance of Assemblage of Unlike Elastic Spheres," *Journal of the Engineering Mechanics Division*, ASCE, Vol. 107, No. EMI, February, pp. 149-167.
- Petrakis, E. (1983), "A Statistical Model to Predict Compaction of Dry Sand During Cyclic Simple Shear Loading: Model and Applications," M.S. thesis, Rensselaer Polytechnic Institute, Troy, NY.
- Prager, W. (1955), *Proc. Institution of Mechanical Engineers*, Vol. 169, pp. 44-57.
- Prevost, J.H. (1977), "Mathematical Modelling of Monotonic and Cyclic Undrained Clay Behavior," *International Journal for Numerical and Analytical Methods in Geomechanics*, Vol. 1, pp. 195-216.

- Prevost, J.H. (1978), "Plasticity Theory for Soil Stress-Strain Behavior," Journal of the Engineering Mechanics Division, ASCE, Vol. 104, No. EM5, pp. 1177-1194.
- Prevost, J.H. and Hoeg, K. (1975), "Effective Stress-Strain-Strength Model for Soils," Journal of the Geotechnical Engineering Division, ASCE, Vol. 101, No. GT3, pp. 259-278.
- Pyke, R.M. (1973), "Settlement and Liquefaction of Sands under Multi-Directional Loading," Ph.D. Dissertation, University of California, Berkeley.
- Reyes, S.F. (1966), "Elastic-Plastic Analysis of Underground Openings by the Finite Element Method," Ph.D. Thesis, University of Illinois, Urbana, Ill.
- Richart, F.E., Hall, J.R. and Woods, R.D. (1970), Vibrations of Soils and Foundations, Prentice-Hall Inc., New Jersey.
- Roesler, S.K. (1979), "Anisotropic Shear Modulus Due to Stress Anisotropy," Journal of the Geotechnical Engineering Division, ASCE, Vol. 105, No. GT5, July, pp. 871-880.
- Koscoe, K.H. (1970), "The Influence of Strains in Soil Mechanics," Geotechnique, 20, 129-170.
- Rowe, P.W. (1962), "The Stress-Dilatancy Relation for Static Equilibrium of an Assembly of Particles in Contact," Proc. Roy. Soc., A269, pp. 500-527.
- Schmertmann, J.H. (1978), "Effect of Shear Stress on Dynamic Bulk Modulus of Sand," U.S. Army Engineering Waterways Experiment Station, Technical Report S-78-16, October.
- Scott, G.D. (1960), Packing of Equal Spheres, Nature, Vol. 188, pp. 908-909.
- Scott, R. and Ko, H. (1969), "Stress-Deformation and Strength Characteristics," State-of-the-Art Report, Proceedings Seventh Int. Conf. on Soil Mechanics and Foundation Engineering, Mexico City, pp. 1-47.
- Seed, H.B. and Idriss, I.M. (1970), "Soil Moduli and Damping Factors for Dynamic Response Analyses," Earthquake Engineering Research Center Report No. EERC 70-10, University of California, Berkeley.
- Seridi, A. and Dobry, R. (1984), "An Incremental Elastic-Plastic Model for the Force-Displacement Relation at the Contact Between Two Spheres," Research Report, Dept. of Civil Engineering, Rensselaer Polytechnic Institute, Troy, N.Y.

- Serrano, A.A. and Rodrigues-Ortiz, J.M. (1973), "A Contribution to the Mechanics of Heterogeneous Granular Media," Symp. on Plast. and Soil Mech., Cambridge, England.
- Shahinpoor, M. (1981), "Statistical Mechanical Considerations on Storing Bulk Solids," Bulk Solids Handling, Vol. 1, February, pp. 31-36.
- Shahinpoor, M. and Shahrpas, A. (1982), "Frequency Distribution of Voids in Monolayers of Randomly Packed Equal Spheres," Bulk Solids Handling, Vol. 2, 4, pp. 825-838.
- Silver, M.L. and Seed, H.B. (1971), "Volume Changes in Sands during Cyclic Load-ing," JSMFD, ASCE, Vol. 97, No. SM-9, pp. 1171, Sept.
- Smith, W.O., Foote, P.D. and Busang, P.F. (1929), "Packing of Homogeneous Spheres," Phys. Rev., 34, pp. 1271-1274.
- Sokolnikoff, I.S. (1956), Mathematical Theory of Elasticity, McGraw Hill, New York.
- Stokoe, K.H. II, Roesset, J.M., Knox, D.P., Kopperman, S.E. and Suddhiprakarn, C. (1980), "Development of a Large-Scale Triaxial Testing Device for Wave Propagation Studies," Geotechnical Engineering Report GR80-10, University of Texas at Austin.
- Stokoe, K.H. II, Lee, S.H.H. and Knox, D.P. (1985), "Shear Moduli Measurements under True Triaxial Stresses," Advances in the Art of Testing Soils Under Cyclic Conditions, Khoslo Vijay, ASCE, Detroit, MI.
- Takahashi, T. and Sato, Y. (1950), "On the Theory of Elastic Waves in Granular Substance," Bulletin Earthquake Research Institute Tokyo University, 28, pp. 37-43.
- Tatsuoka, F., Iwasaki, T., Fukushima, S. and Sudo, H. (1979), "Stress Conditions and Stress Histories Affecting Shear Modulus and Damping of Sand under Cyclic Loading," Soil and Foundations, Japanese Society of Soil Mechanics and Foundation Engineering, Vol. 19, No. 2, pp. 29-43.
- Taylor, G.I. (1938), "Plastic Strain in Metals," J. Inst. Metals, Vol. 62, p. 307P.
- Thurston, C.W. and Deresiewicz, H. (1959), "Analysis of a Compression Test of a Model of a Granular Medium," Journal Applied Mechanics, June, pp. 251-158.
- Thurston, C.W. (1958), "Stress Strain Relations and Vibration of a Granular Medium," Discussion, Journal of Applied Mechanics, June, pp. 310-311.

- Van Vlack (1964), Elements of Materials Science, 2nd Edition, Addison-Wesley, Reading, MA.
- Vicente, E. and Dobry, R. (1983), "Pore Water Pressure Increase in Loose Saturated Sand at Level Sites During Three Directional Earthquake Loading," Report CE-83-9-1, Dept. of Civil Engineering, Rensselaer Polytechnic Institute, Troy, NY.
- Walton, K. (1978), "The Oblique Compression of Two Elastic Spheres," J. Mech. Phys. Solids, Vol. 26, pp. 139-150.
- Walton, K. (1987), "The Effective Elastic Moduli of a Random Packing of Spheres," J. Mech. Phys. Solids, Vol. 35, pp. 213-226.
- White, J.E. and Sengbush, R.L. (1953), "Velocity Measurements in Near-Surface Formation," Geophysics, Vol. 18, pp. 54-69.
- White, J.E. (1965) Seismic Waves, McGraw-Hill, New York.
- Whitman, R.V., Miller, E.T. and Moore, P.J. (1964), "Yielding and Locking of Confined Sand," Journal of the Soil Mechanics and Foundations Division, Proceedings, ASCE, Vol. 90, No. SM4, pp. 57-84, July.
- Woods, R.D. (1978), "Measurement of Dynamic Soil Properties," Proceedings of the Earthquake Engineering and Soil Dynamics Conference, ASCE, Pasadena, CA, June 19-21, Vol. 1, pp. 91-178.
- Yanagisawa, E. (1978), "Relation Between the Dynamic Shear Modulus and Void Ratio in Granular Media," Proceedings US-Japan Seminar on Continuum Mechanical and Statistical Approaches in the Mechanics of Granular Materials, Cowin and Satake, editors, pp. 64-70.
- Yanagisawa, E. (1983), "The Influence of Void Ratio and Stress Condition on the Dynamic Shear Modulus of Granular Media," Advances in the Mechanics and the Flow of Granular Materials, Vol. II, M. Shahinpoor, ed., Trans. Tech. Publications, Clausthal-Zellerfeld, Fed. Republic of Germany.
- Youd, T.L. (1972), "Compaction of Sands by Repeated Shear Straining," Journal of the SMFD, ASCE, 98, SM7, July, pp. 709-725.
- Yu, P. and Richart, F.E., Jr. (1984), "Stress Ratio Effects on Shear Modulus of Dry Sands," Journal of Geotechnical Engineering, Vol. 110, No. 3, March, pp. 331-345.

TABLES

Type of Packing	Other Name	Symbol Used in this report	Coordination Number (Number of Contacts Per Sphere)	Spacing of Layers	Volume of Unit Prism	Density	Porosity	Void Ratio
							n	e
Simple Cubic	-----	sc	6	2R	$8R^3$	$\pi/6$	0.4764	0.9098
Body Centered Cubic	-----	bcc	8	$4R/\sqrt{3}$	$64R^3/3^{3/2}$	0.2165π	0.32	0.47
Cubical Tetrahedral	-----	ct	8	2R	$4\sqrt{3}R^3$	$\pi/3\sqrt{3}$	0.3954	0.65
Tetragonal-Sphenoidal	-----	ts	10	$R\sqrt{3}$	$6R^3$	$2\pi/9$	0.3019	0.4325
Hexagonal Closed Packed	tetrahedral	hcp	12	$R\sqrt{2}$	$4\sqrt{2}R^3$	$\pi/3\sqrt{2}$	0.2595	0.3504
Face Centered Cubic	pyramidal	fcc	12	$2R\sqrt{2}/3$	$4\sqrt{2}R^3$	$\pi/3\sqrt{2}$	0.2595	0.3504

Table 1. Properties of Regular Arrays of Equal Spheres
(Deresciewicz, 1958, Van Vlack, 1964).

Coordination Number	Symbol	Porosity	Void Ratio	Cell Number
4	[1,1,2]	0.7181	2.5673	1
	[1,0,3]	0.6599	1.9403	2
	[2,0,2]	0.6599	1.9403	3
5	[1,2,2]	0.6933	2.2605	4
	[2,1,2]	0.6298	1.7012	5
	[1,2,3]≡[1,3,1]	0.5969	1.4808	6
	[1,1,3]	0.5790	1.3753	7
	[1,0,4]	0.5382	1.2635	8
	[2,0,3]	0.5373	1.1612	9
6	[2,2,2]	0.6298	1.7012	10
	[2,2,2]	0.5578	1.2614	11
	[1,2,3]	0.5374	1.2594	12
	[1,3,2]	0.5546	1.2452	13
	[2,2,2]≡[3,0,3]≡[1,4,1]	0.4764	0.9098	14
	[2,0,4]	0.4746	0.9033	15
	[1,2,4]≡[2,2,3]	0.5132	1.0542	16
7	[2,3,2]	0.5063	1.0255	17
	[3,1,3]	0.4918	0.9677	18
	[1,4,2]≡[1,5,1]	0.4389	0.7822	19
	[2,2,4]	0.4642	0.8664	20
8	[1,5,2]	0.3985	0.6625	21
	[2,2,4]	0.3954	0.6540	22
	[3,2,3]≡[2,4,2]≡[1,6,1]	0.3954	0.6529	23
	[4,0,4]	0.3198	0.4702	24
	[1,4,4]	0.3866	0.6303	25
9	[2,5,2]≡[1,6,2]	0.3520	0.5432	26
	[2,4,4]≡[1,6,3]	0.3343	0.5022	27
	[2,5,3]	0.3127	0.4550	28
	[4,2,4]≡[2,6,2]	0.3019	0.4327	29
10	[2,6,3]	0.2813	0.3908	30
11	[3,6,3]≡[4,4,4]	0.2595	0.3504	31

Table 2. Feasible Regular Arrays or "Cells" (Shahinpoor, 1981). Coordination No. = N = No. of Contacts per Sphere. $[u,m,l]$ gives No. of Contacts of Spheres with Layer Above, Same Layer and Layer Below: $N = u + m + l$.

Young's Modulus	$E_s = 11 \times 10^6$ psi
Poisson's Ratio	$\nu_s = 0.15$
Coefficient of Intergranular Friction	$f = 0.5$

Table 3 Properties of Quartz Used in this Report

[Note that Lambe and Whitman (1969) reported a different value $\nu_s = 0.31$ for quartz, which in turn was used for the calculations in Dobry et al. (1982). The lower value $\nu_s = 0.15$ used herein is more realistic and was obtained from White (1964) and Ko and Scott (1967)]

FIGURES

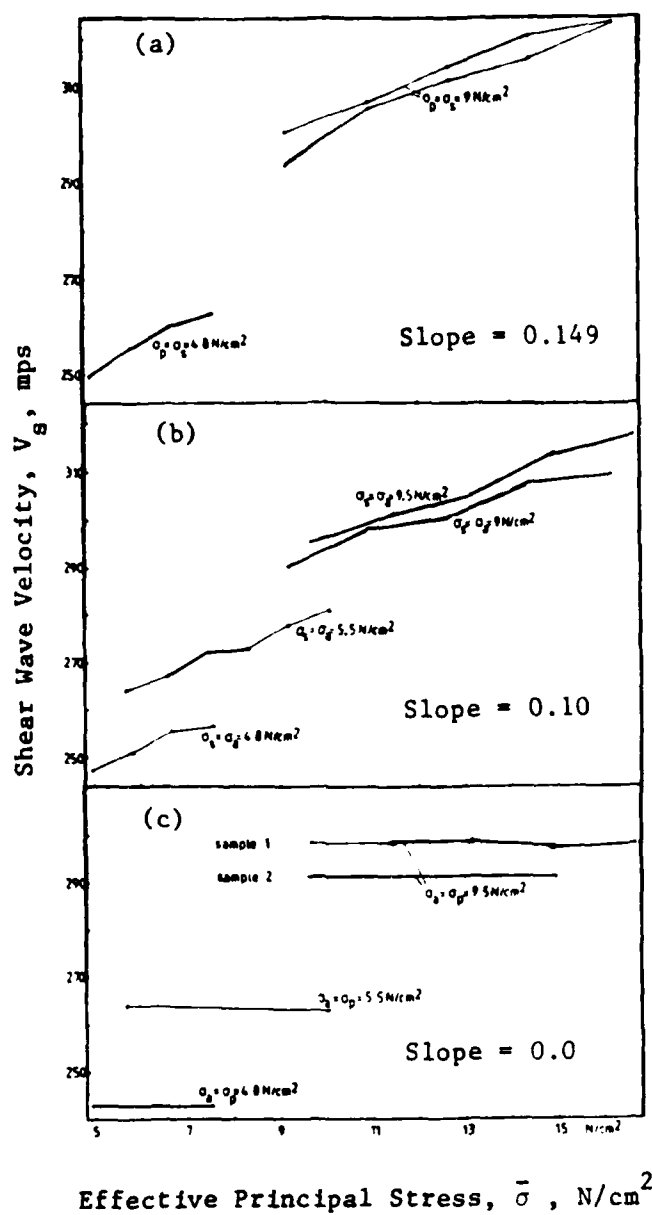
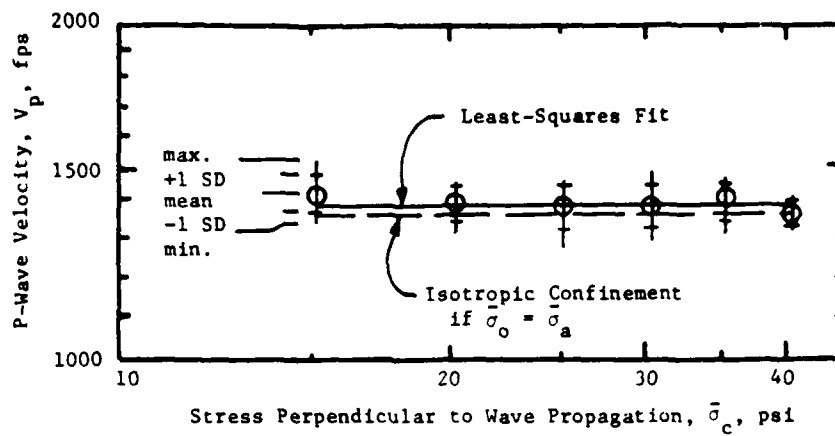
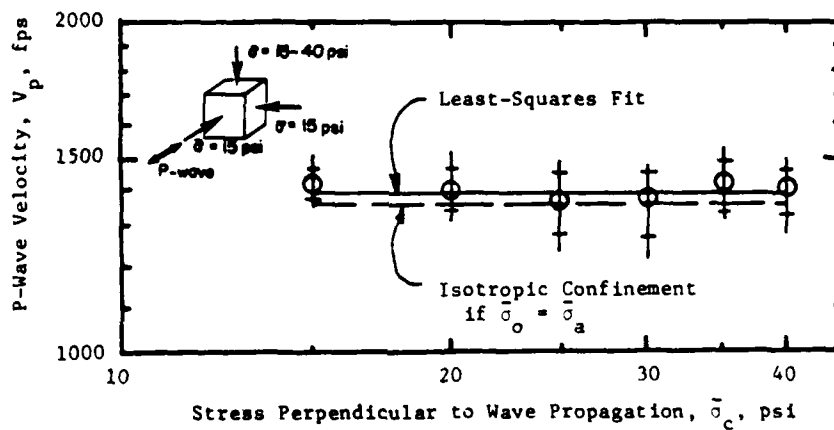


Figure 1. Variation of V_s with Principal Stress in (a) Direction of Wave Propagation, (b) Direction of Polarization (Particle Motion) and (c) Out-of-Plane Direction (Roesler, 1979)



a) Loading



b) Unloading

Figure 2. Effect on V_p of Principal Stress, σ_c , Perpendicular to Wave Propagation for Biaxial Loading Case (Kopperman et al., 1982)

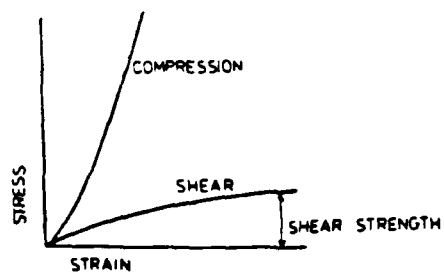


Figure 3. Stress-Strain Curves for Monotonic Loading of Dry Granular Soils.

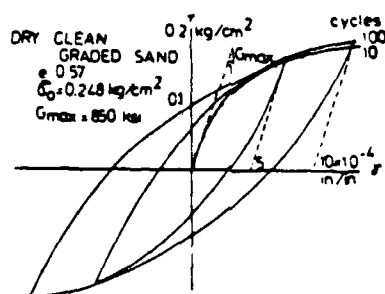


Figure 4. Stress-Strain Hysteresis Loops for Reversed Loading (Hardin and Drnevich, 1972) .

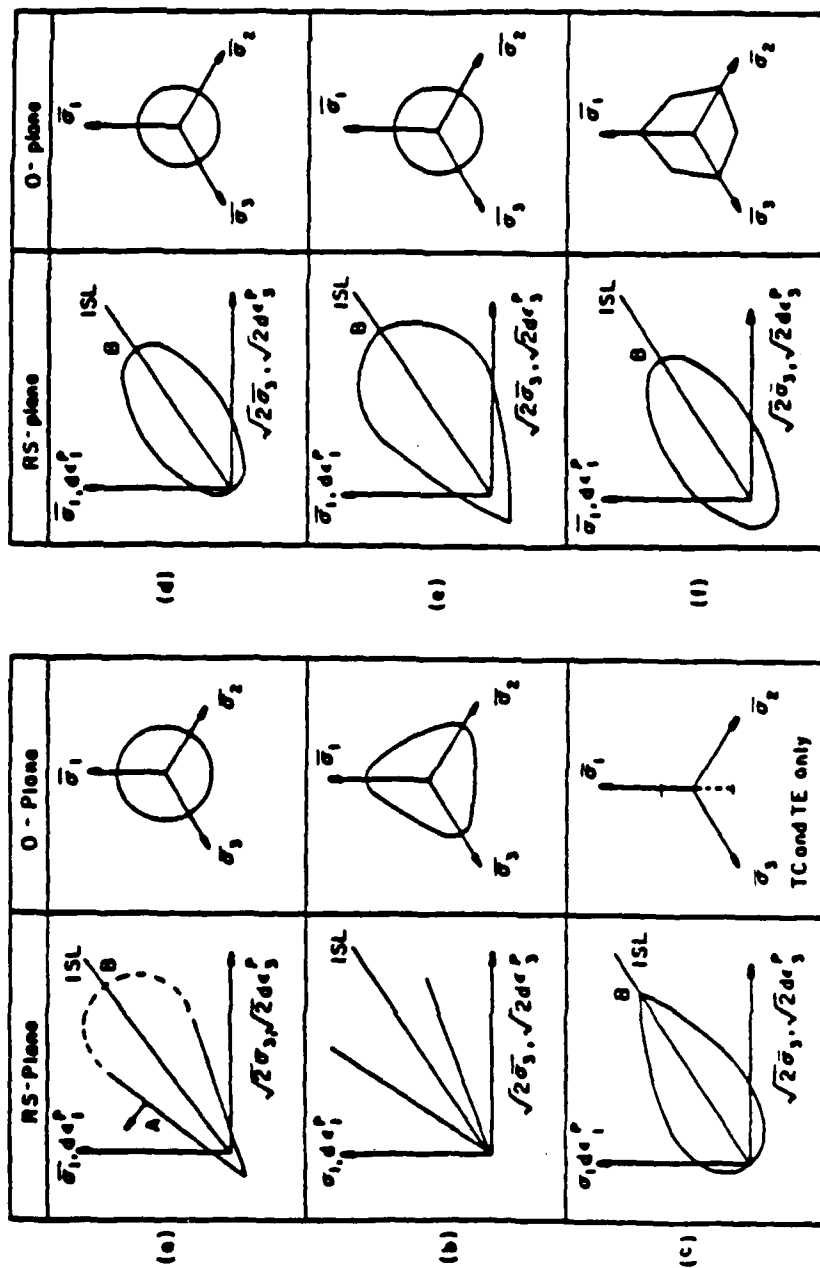


Figure 5. Plastic Potential Surfaces: (a) Drucker et al., (b) Lade and Duncan, (c) Original Cam-Clay, (d) Modified Cam-Clay, (e) DiMaggio and Sandler, (f) Zienkiewicz et al. (Hardin, 1978)

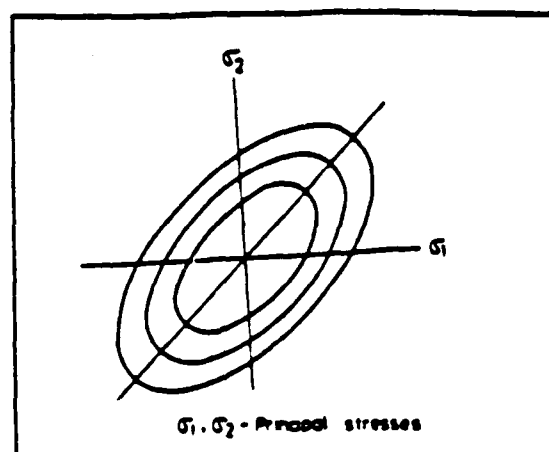


Figure 6. Isotropic Hardening Model (Chen, 1975)

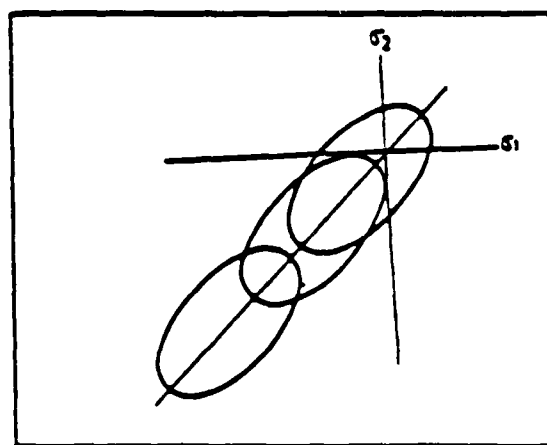


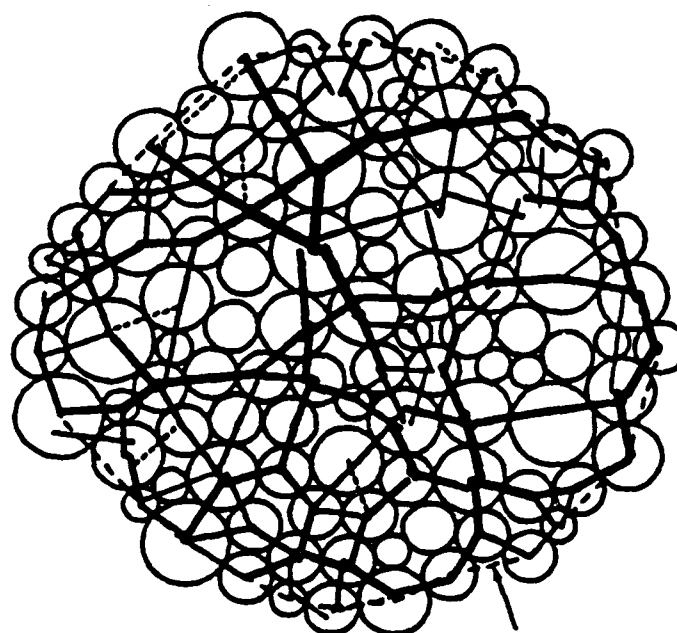
Figure 7. Kinematic Hardening Model (Chen, 1975)

Initial state of 100-disc
test: isotropic boundary
stress

Maximum force:
0.1379E+09

S. STRESS:
(1,1) -1.500E+06
(1,2) 0.000E+00
(2,1) 0.000E+00
(2,2) -1.500E+06

components of applied
stress tensor

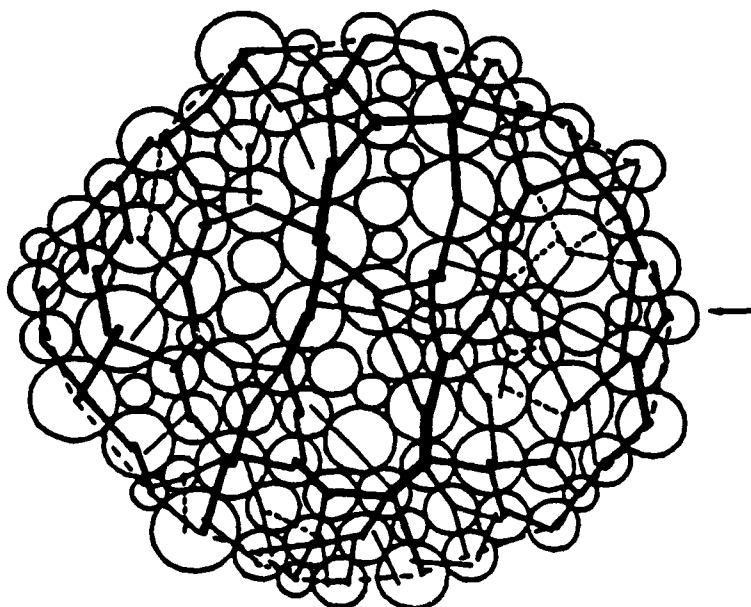


boundary particles
identified by dashed line

100-disc test: just
before failure

Maximum force:
0.1594E+09

S. STRESS:
(1,1) -1.000E+06
(1,2) 0.000E+00
(2,1) 0.000E+00
(2,2) -2.000E+06



numerically greatest
principal stress

Fig. 8 Finite Difference Simulation of a Triaxial Test on a
100-disc Model (Cundall and Strack, 1983)

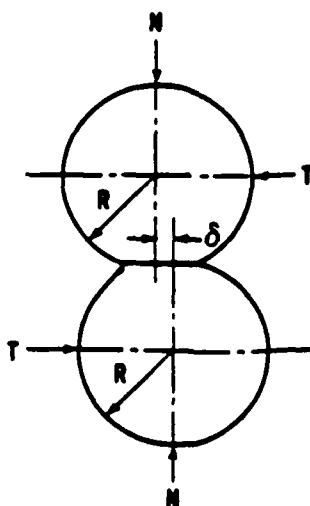


Figure 9. Elastic Spheres Under Normal and Tangential Loads

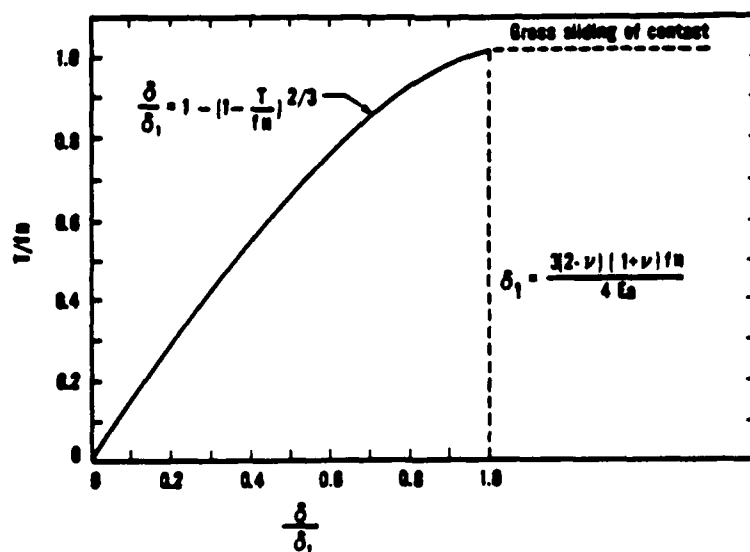


Figure 10. Tangential Force-Displacement Relation for N Constant, T Increasing (Dobry et al, 1982)

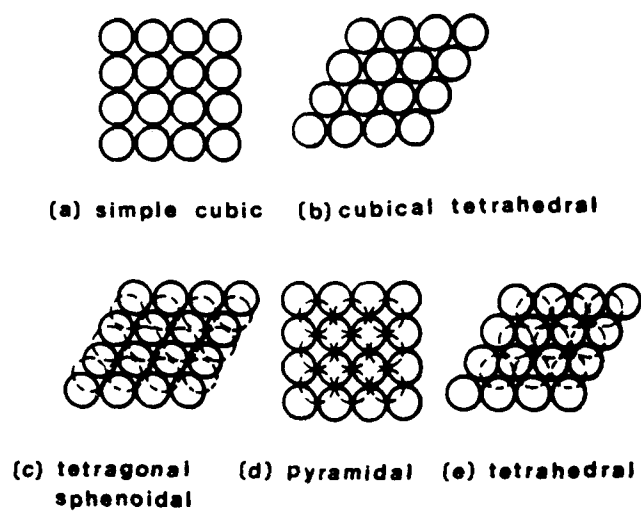


Figure 11. Regular Arrays of Equal Spheres (Deresiewicz, 1958) .

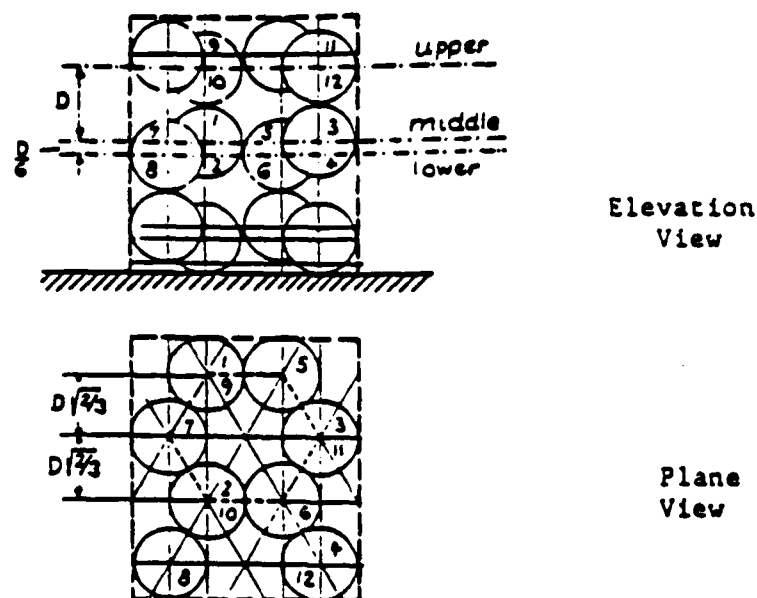


Figure 12. Regular Array No. 2 (see Table 2) (1,0,3);
 $N=4$; $n=0.6599$; $e=1.9403$

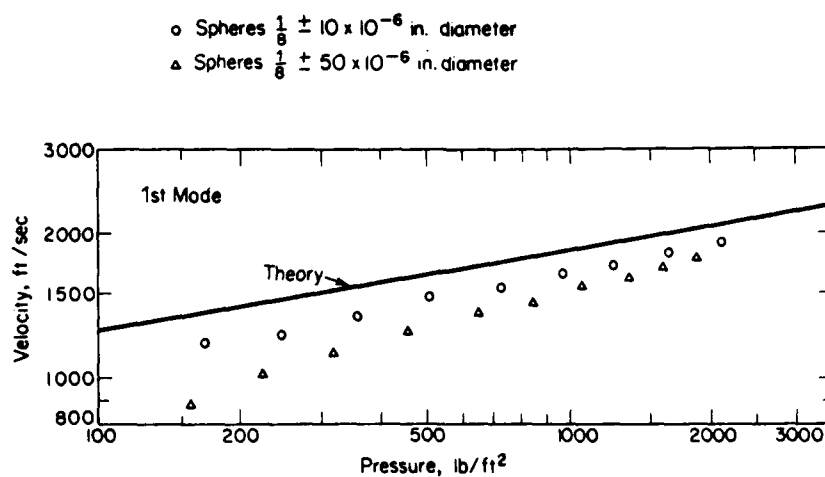


Figure 13. Rod Wave Velocity Measurements in Regular Dense Array of Steel Spheres Isotropically Loaded (Duffy and Mindlin, 1957, figure presented by Richart et al., 1970)

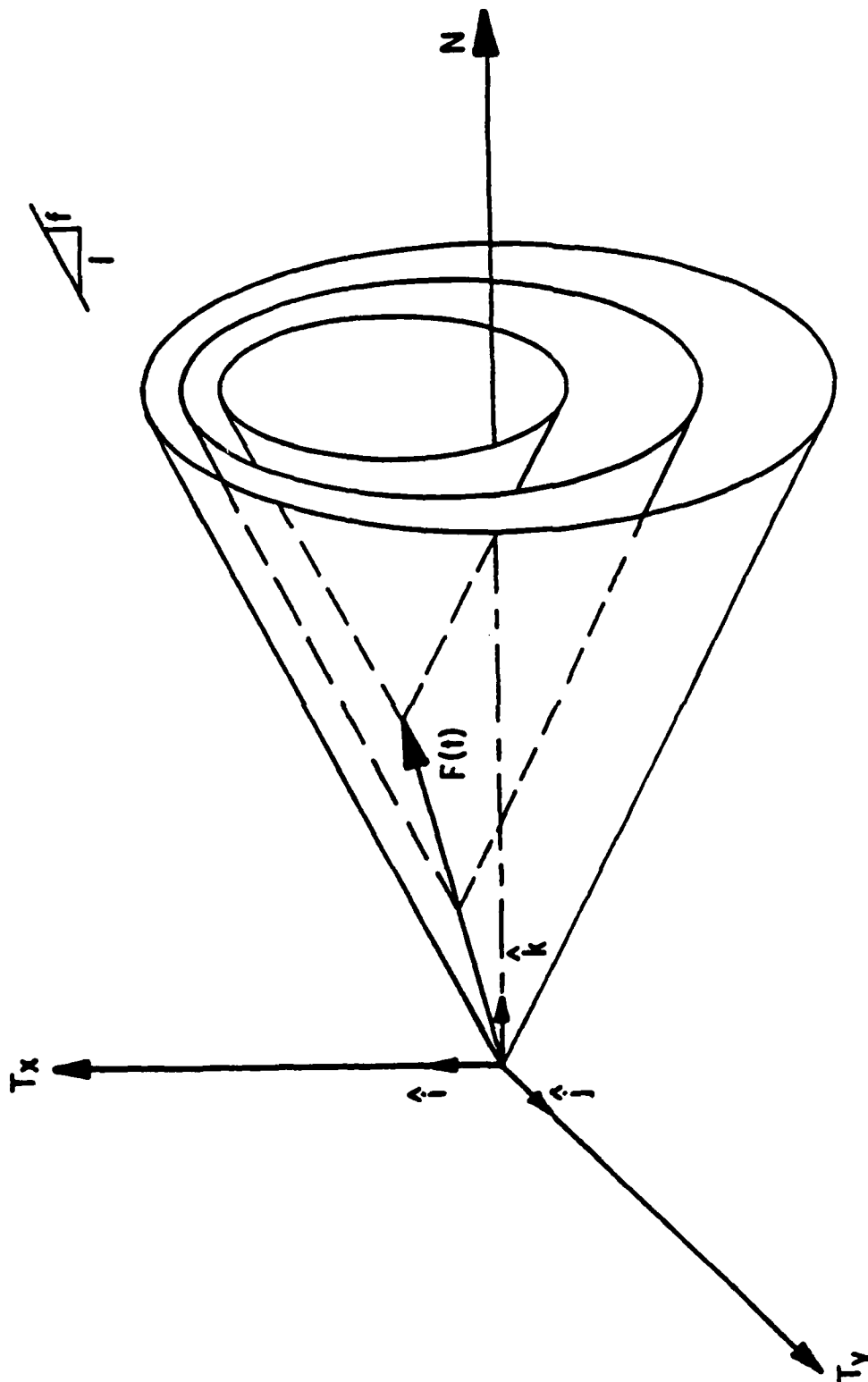


Figure 14. Contact Force Space and Conical Yield Surfaces, Elastic-Plastic Incremental Solution of Mindlin's Problem (Seridi and Dobry, 1984)

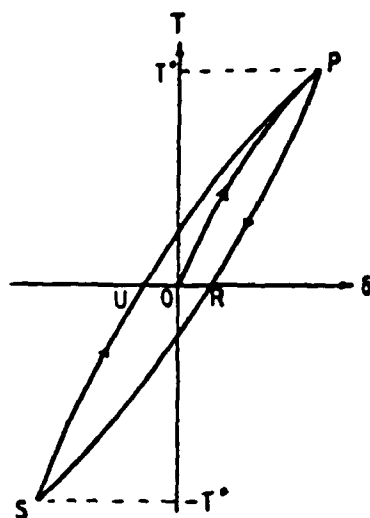


FIG. 5

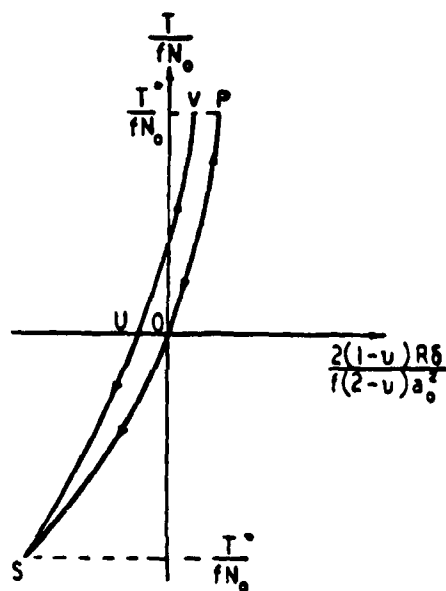


FIG. 30

Figure 15. Force-Deformation Behavior of Two Elastic Rough Spheres in Contact: Analytical Solution for Oscillating Oblique Forces (a) $dT/dN > f$ and (b) $dT/dN < f$ (after Mindlin and Deresiewicz, 1953)

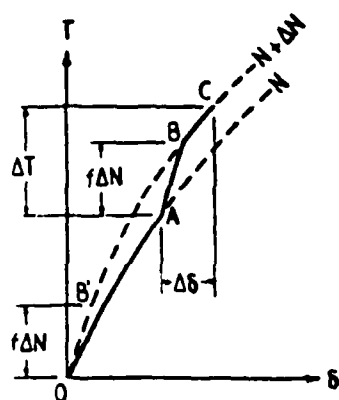


FIG. 7

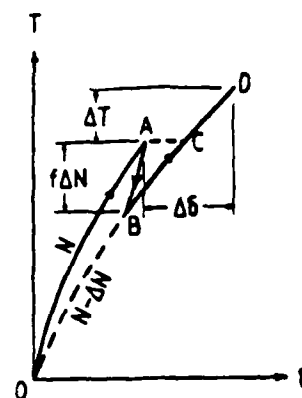


FIG. 10

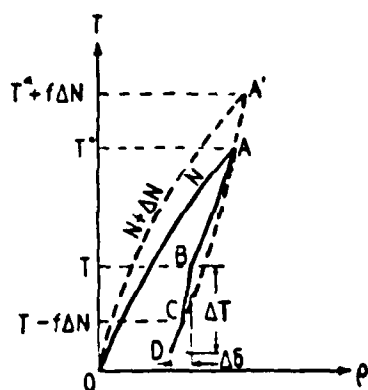


FIG. 12

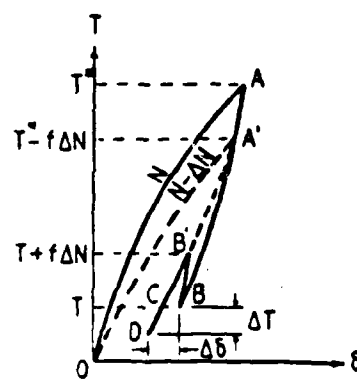


FIG. 14

Figure 16. Force-Deformation Behavior of Two Elastic Rough Spheres in Contact: Analytical Solutions for (a) Normal Force Increasing, Tangential Force Increasing; (b) Normal Force Decreasing, Tangential Force Increasing; (c) Normal Force Increasing, Tangential Force Decreasing; (d) Normal Force Decreasing, Tangential Force Decreasing (after Mindlin and Deresiewicz, 1953)

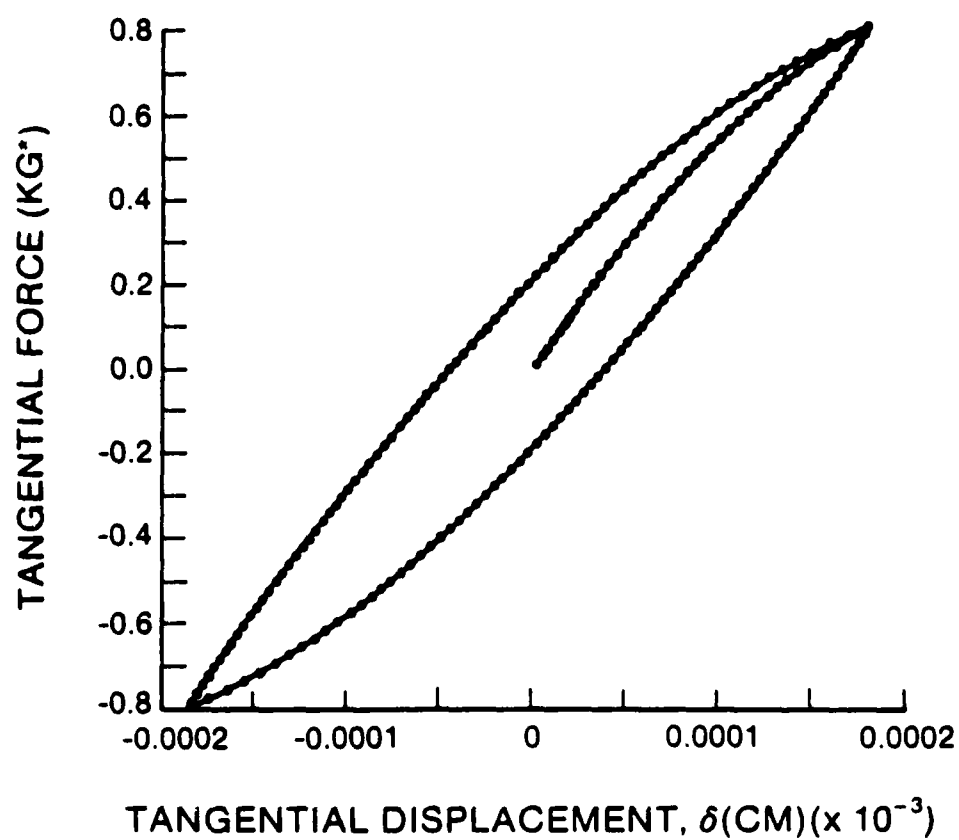


Figure 17. Numerical Simulation of the Force-Deformation Behavior for Two Equal, Elastic, Rough Spheres in Contact: Load-Displacement Relation for an Oscillating Oblique Force with $dT/dN > f$

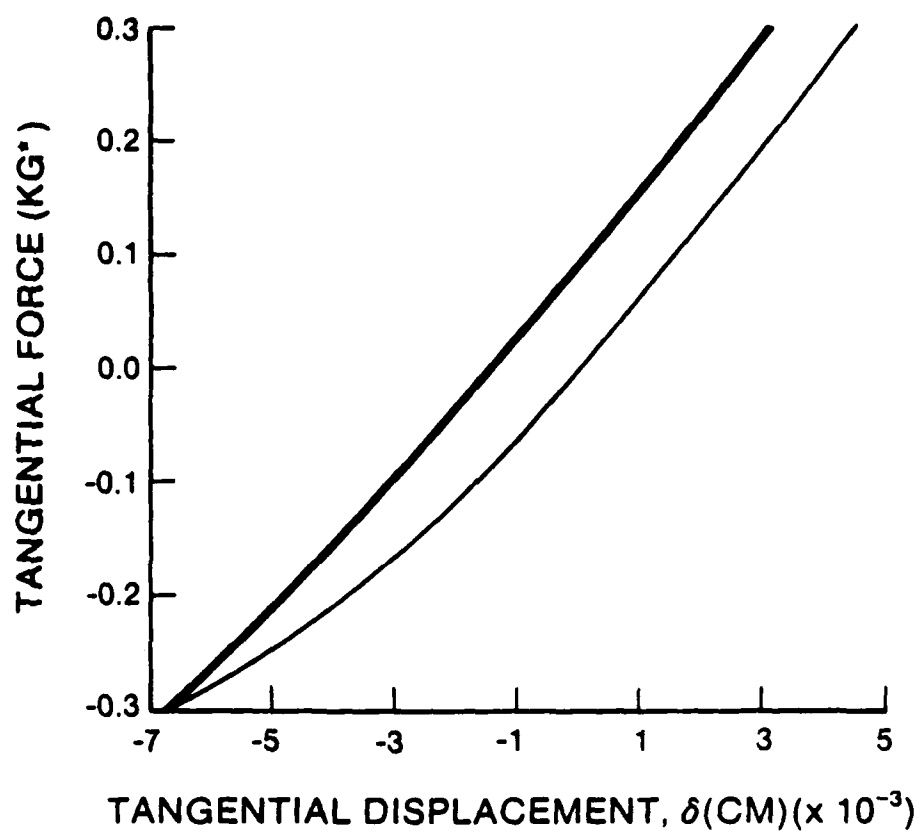


Figure 18. Numerical Simulation of the Force-Deformation Behavior for Two Equal, Elastic, Rough Spheres in Contact: Load-Displacement Relation for an Oscillating Oblique Force with $dT/dN < f$

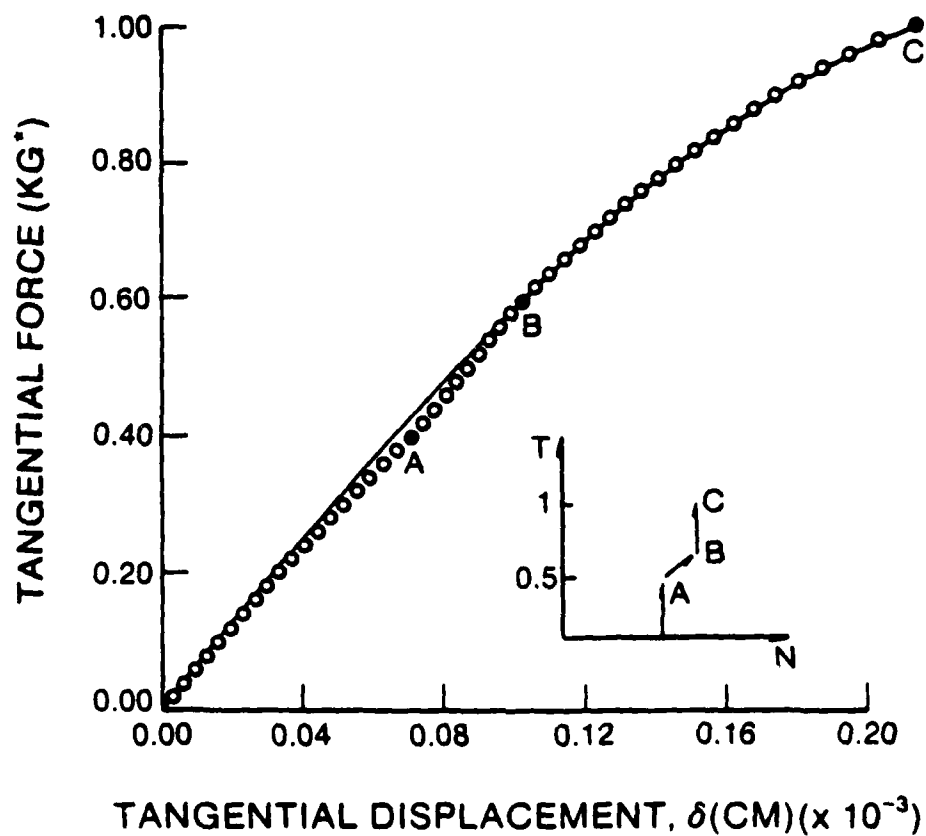


Figure 19. Numerical Simulation of the Force-Deformation Behavior for Two Equal, Elastic, Rough Spheres in Contact: Load-Displacement Relation for the Case in Which the Normal Force Increases and the Tangential Force Increases

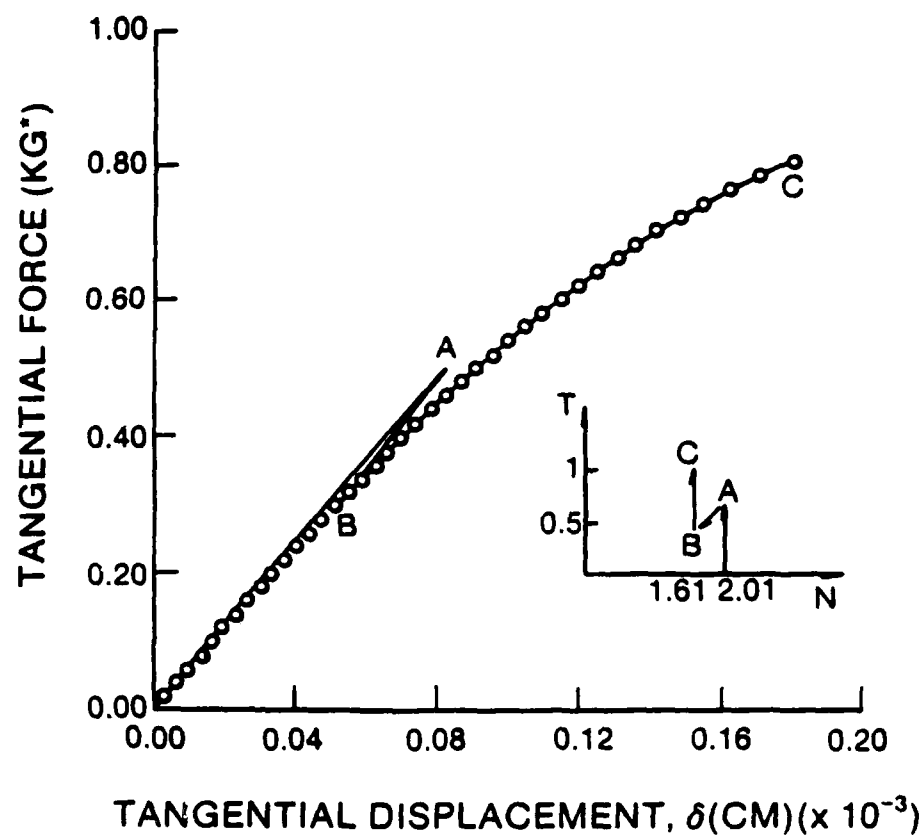


Figure 20. Numerical Simulation of the Force-Deformation Behavior for Two Equal, Elastic, Rough Spheres in Contact: Load-Displacement Relation for the Case in Which the Normal Force Decreases and the Tangential Force Increases

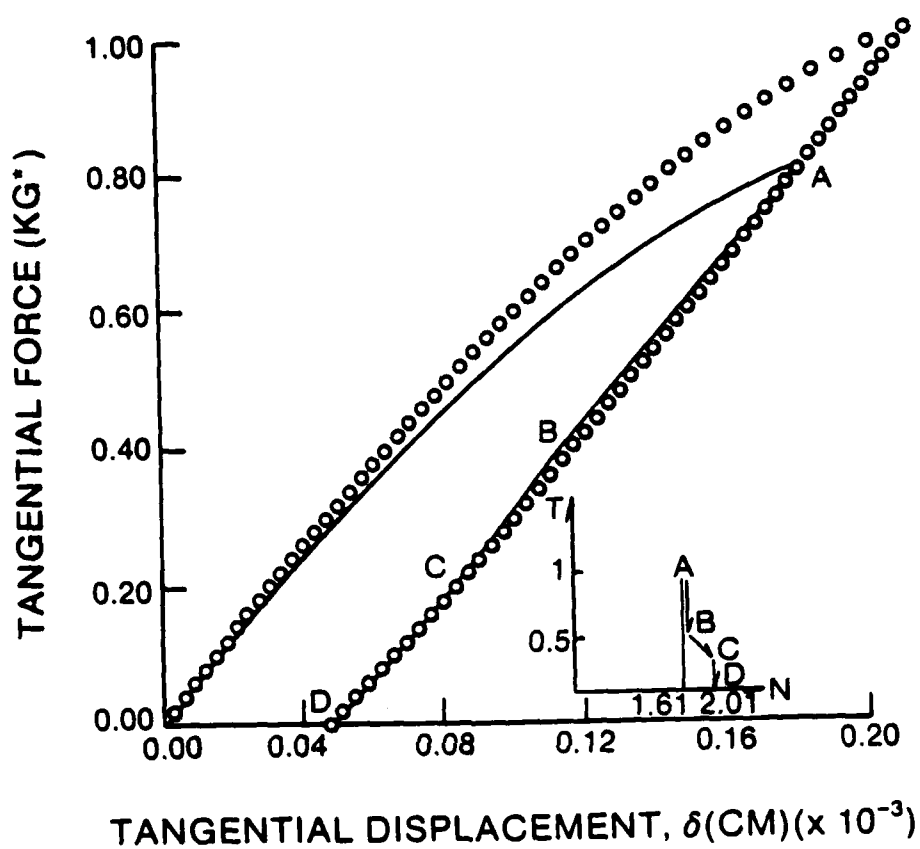


Figure 21. Numerical Simulation of the Force-Deformation Behavior for Two Equal, Elastic, Rough Spheres in Contact: Load-Displacement Relation for the Case in Which the Normal Force Increases and the Tangential Force Decreases

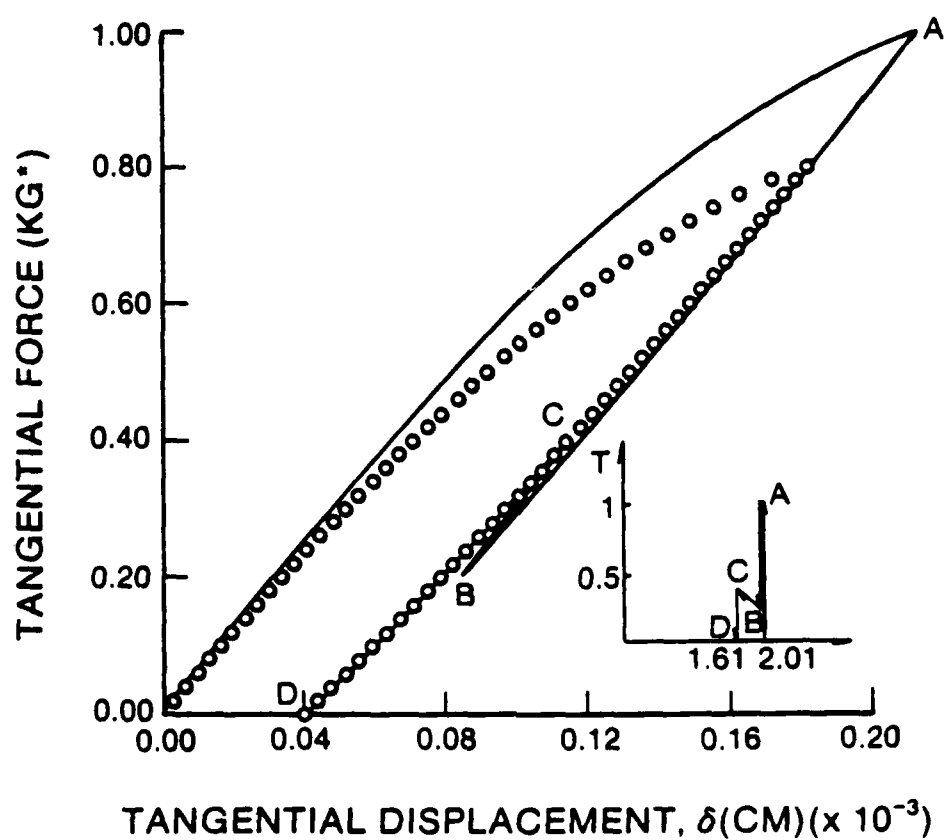


Figure 22. Numerical Simulation of the Force-Deformation Behavior for Two Equal, Elastic, Rough Spheres in Contact: Load-Displacement Relation for the Case in which the Normal Force Decreases and the Tangential Force Decreases

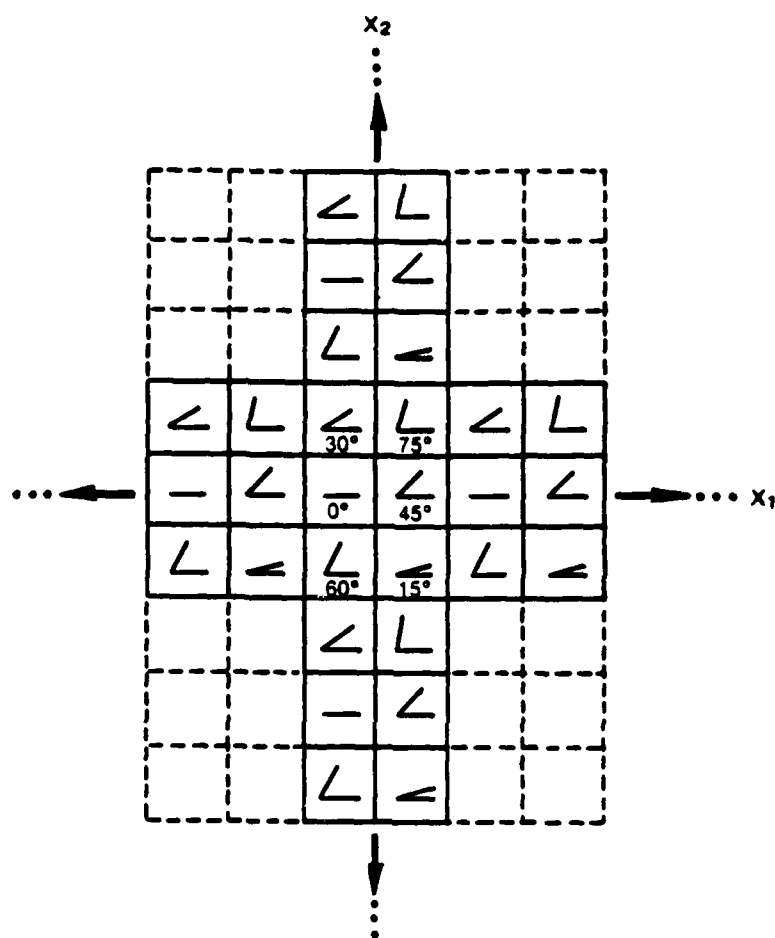
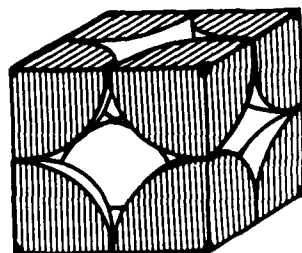


Figure 23. Repeating Six Crystal Aggregate in an Infinite Plane (Angle of Slip Shown in Each Crystal). (after Lin and Ito, 1965)



Simple Cubic Unit Cell

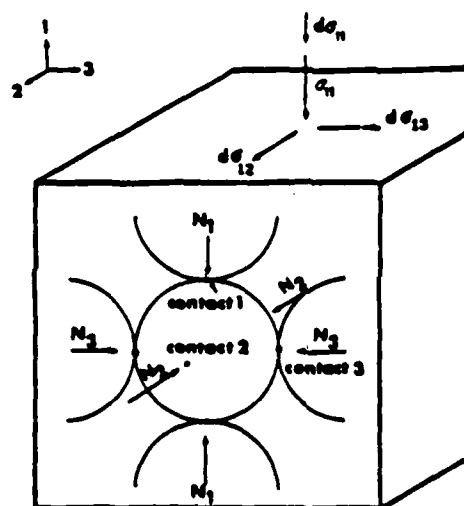
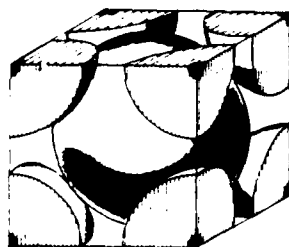
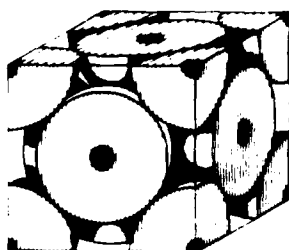


Figure 24. Regular Simple Cubic Array of Equal Spheres



a) Body-centered cubic unit cell b) Body-centered cubic structure

Figure 25. (a) Body-Centered Cubic Array of Equal Spheres;
(b) Body-Centered Cubic Array (after Van Vlack,
1964).



a) Face-centered cubic unit cell b) Face-centered cubic structure

Figure 26. (a) Face-Centered Cubic Array of Equal Spheres;
(b) Face-Centered Cubic Array (after Van Vlack,
1964).

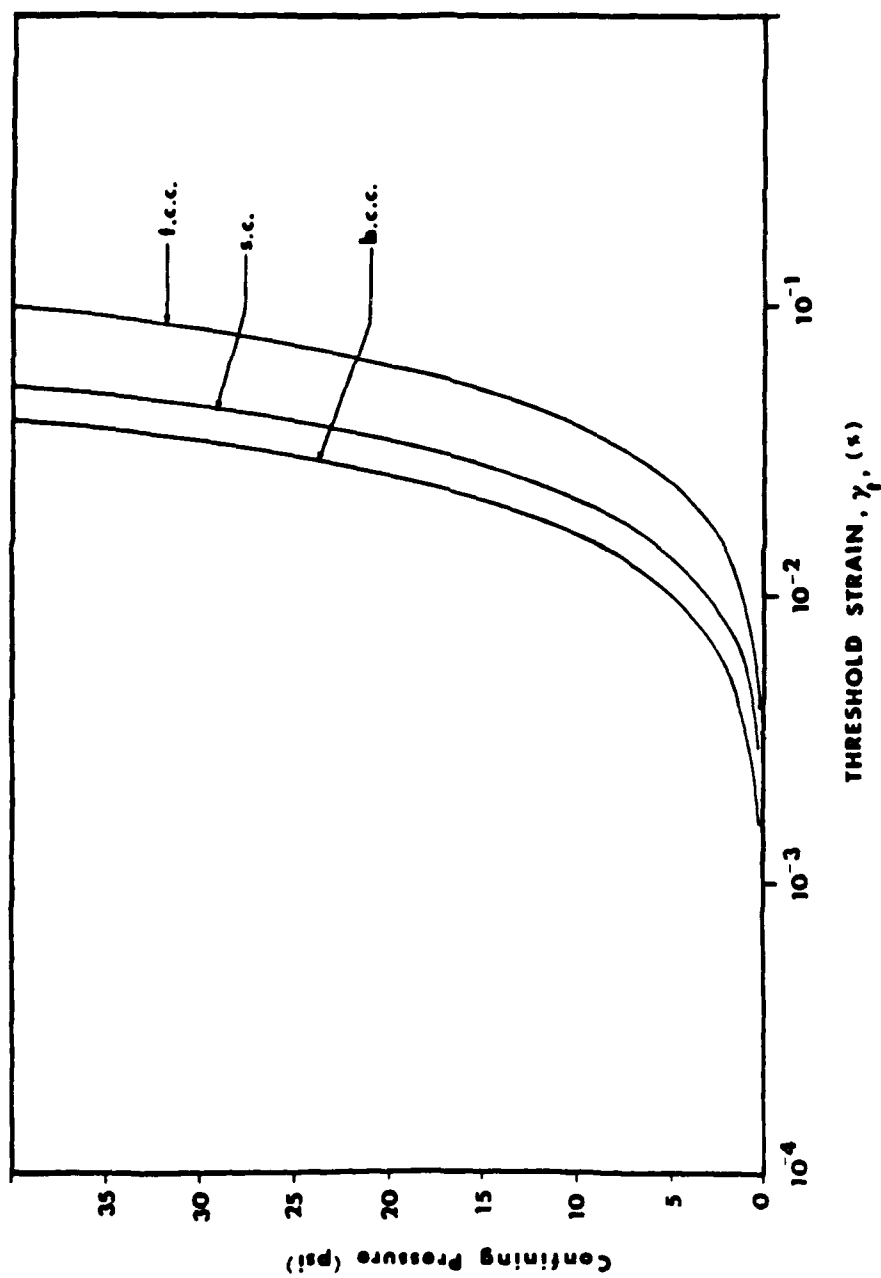


Figure 27. Threshold Strain for the Simple Cubic (sc), Body-Centered Cubic (bcc) and Face-Centered Cubic (fcc) Arrays of Quartz Spheres

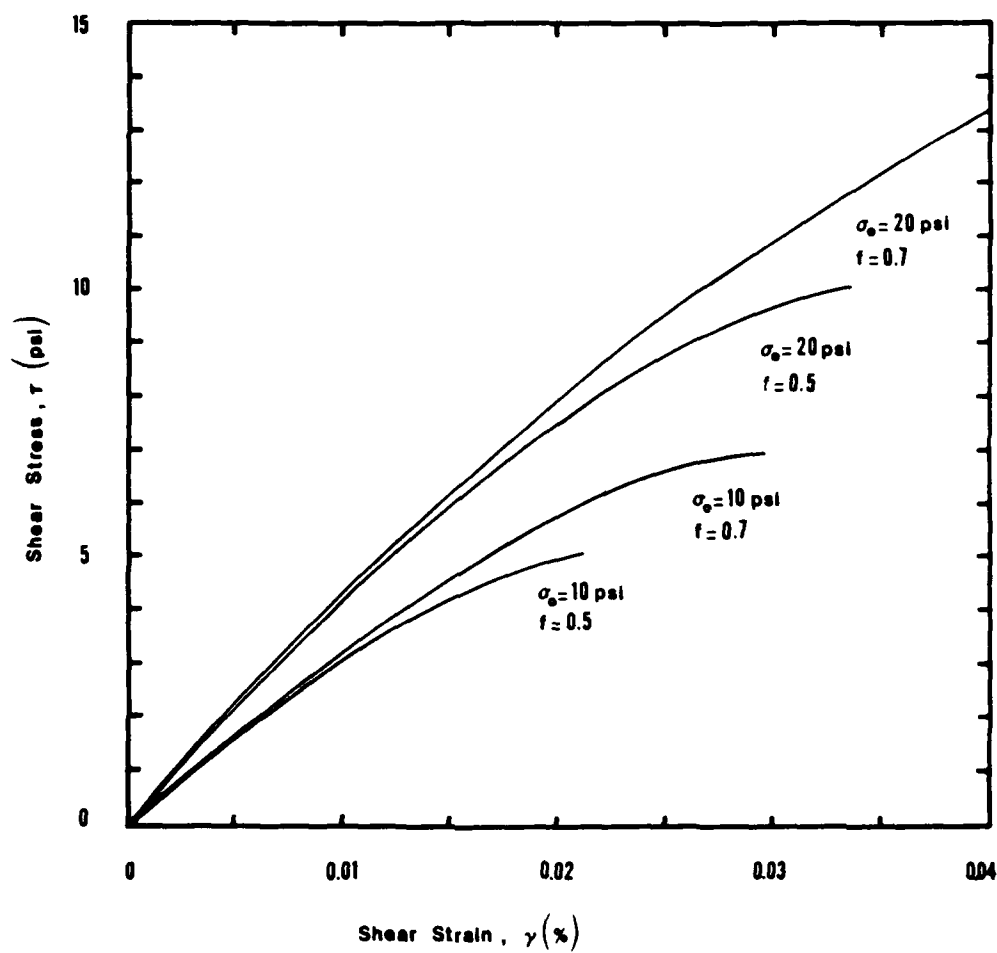


Figure 28. Shear Stress-Strain Curves for Simple Cubic Array of Quartz Spheres

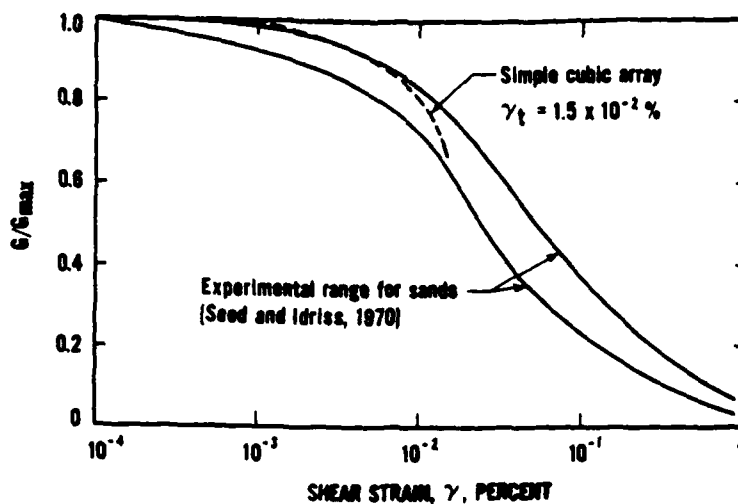


Figure 29. Secant Shear Modulus Versus Shear Strain: Comparison Between Calculated G/G_{max} for the Simple Cubic Array and Experimental Range for Sand (Dobry et al., 1982)

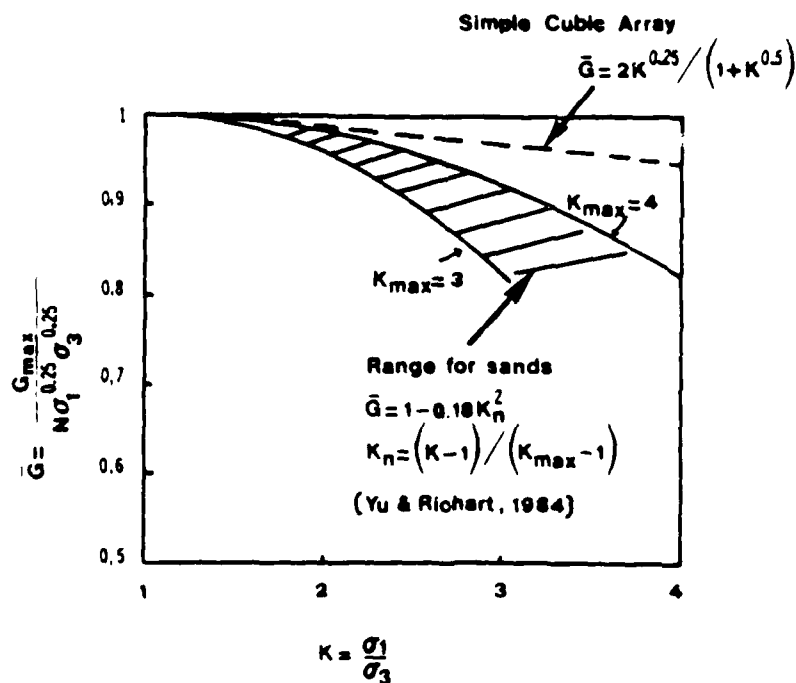


Figure 30. Influence of Stress Ratio, $K = \sigma_1/\sigma_3$ on G_{max} : Comparison Between Prediction From Simple Cubic Array and Experimental Range for Sand

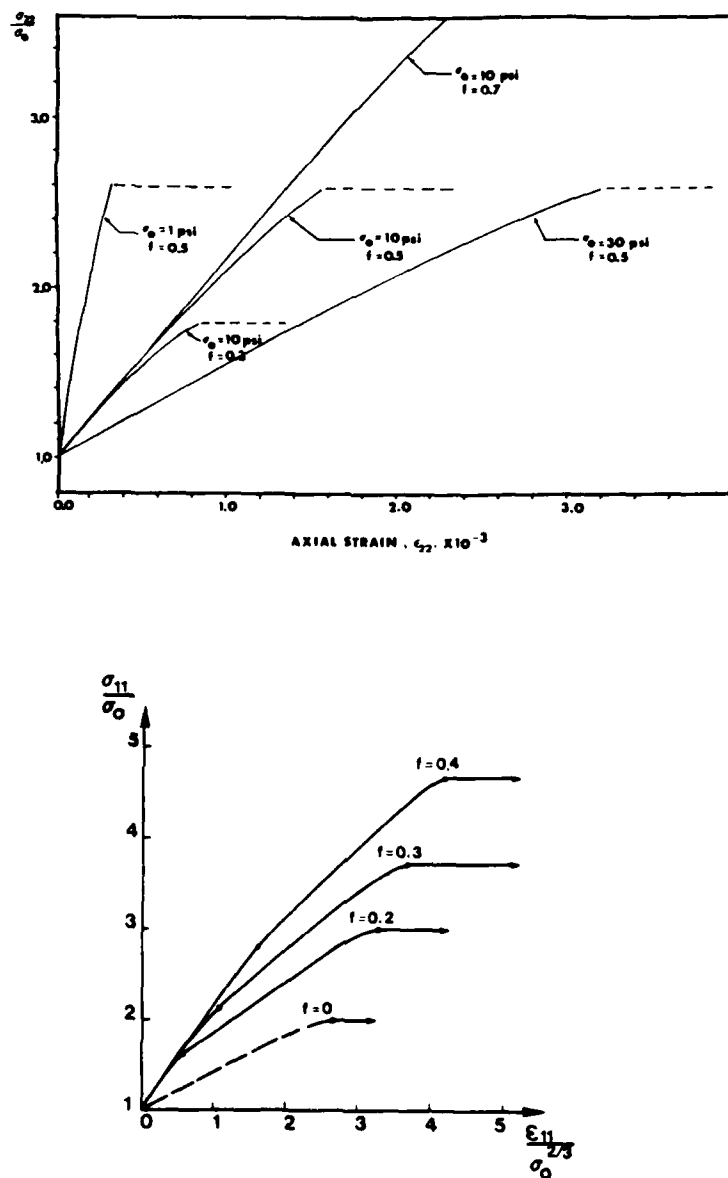


Figure 31. Triaxial Compression of Regular Arrays and Influence of the Value of Intergranular Friction, f : (a) Triaxial Compression of Body-Centered Cubic Array of Quartz Spheres and (b) Triaxial Compression of Face-Centered Cubic Array of Glass Spheres (Brauns, 1966)

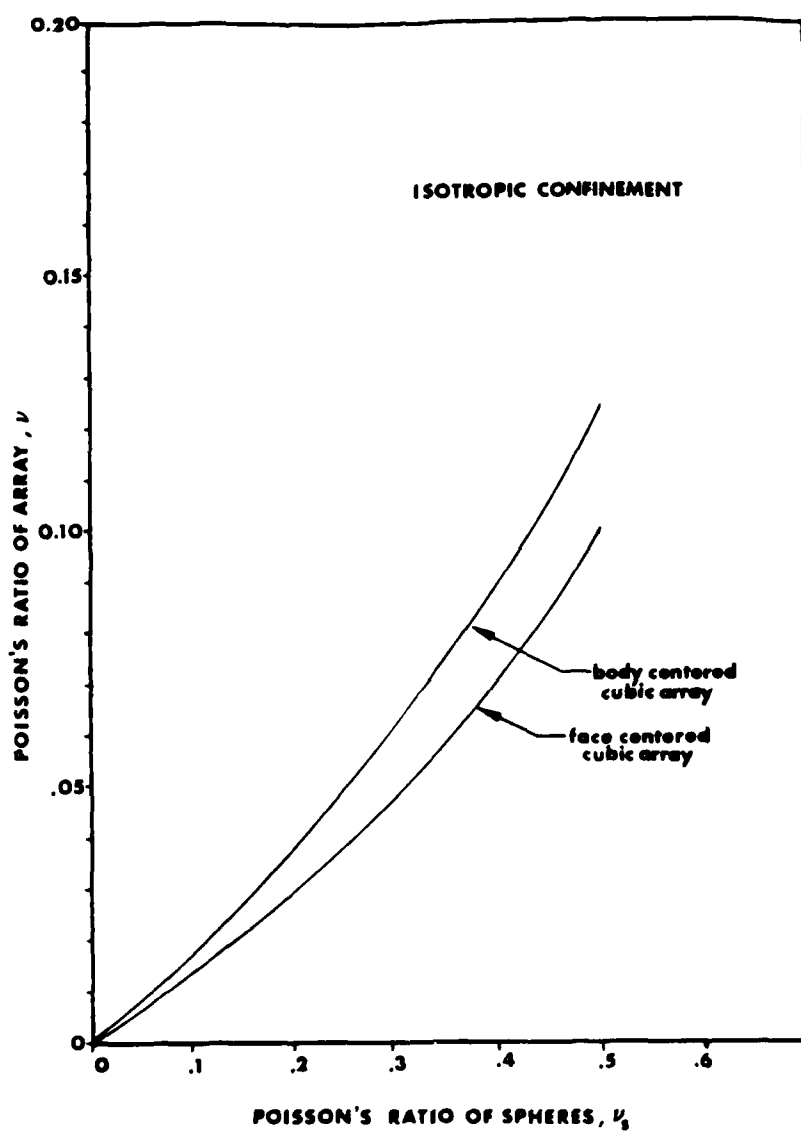


Figure 32. Poisson's Ratio of Regular Cubic Arrays, ν , as a Function of the Poisson's Ratio of the Spheres, ν_s

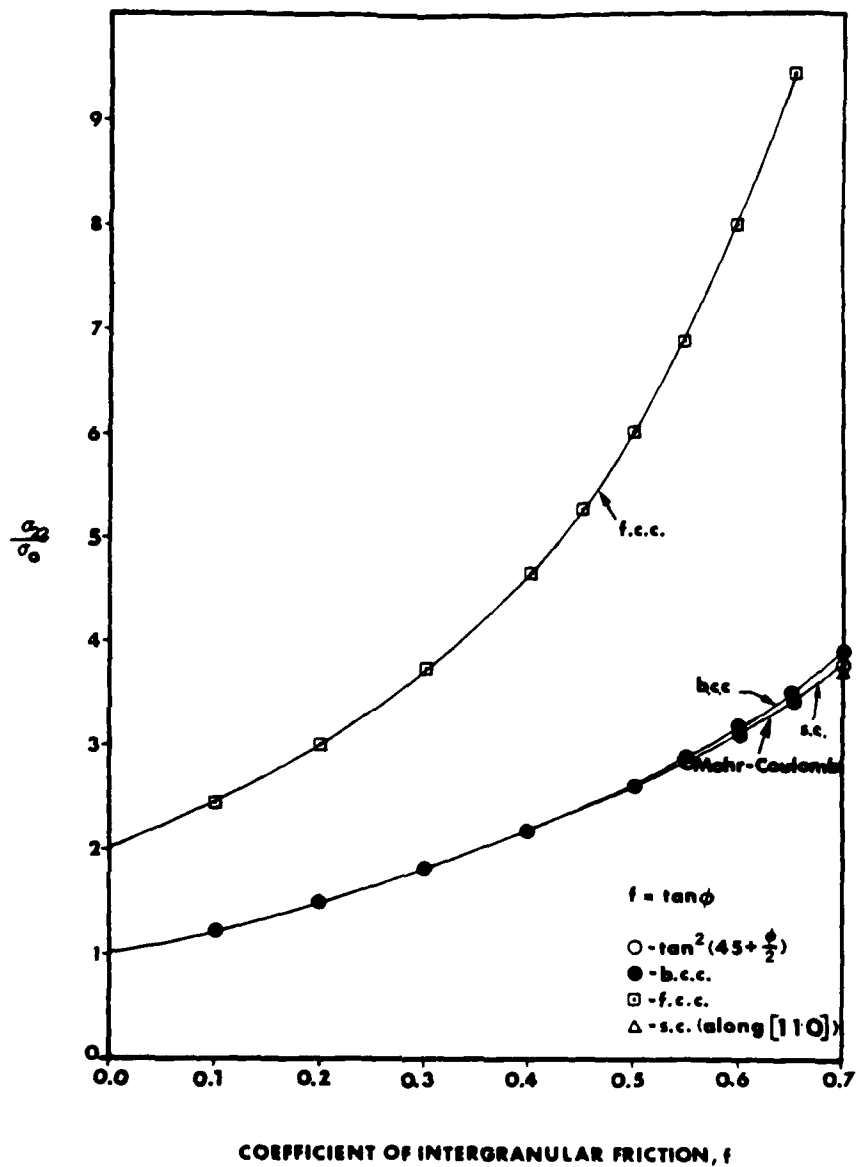


Figure 33. Triaxial Loading: Obliquity, σ_{22}/σ_0 , at Failure Versus the Coefficient of Intergranular Friction, f , for Three Regular Cubic Arrays.

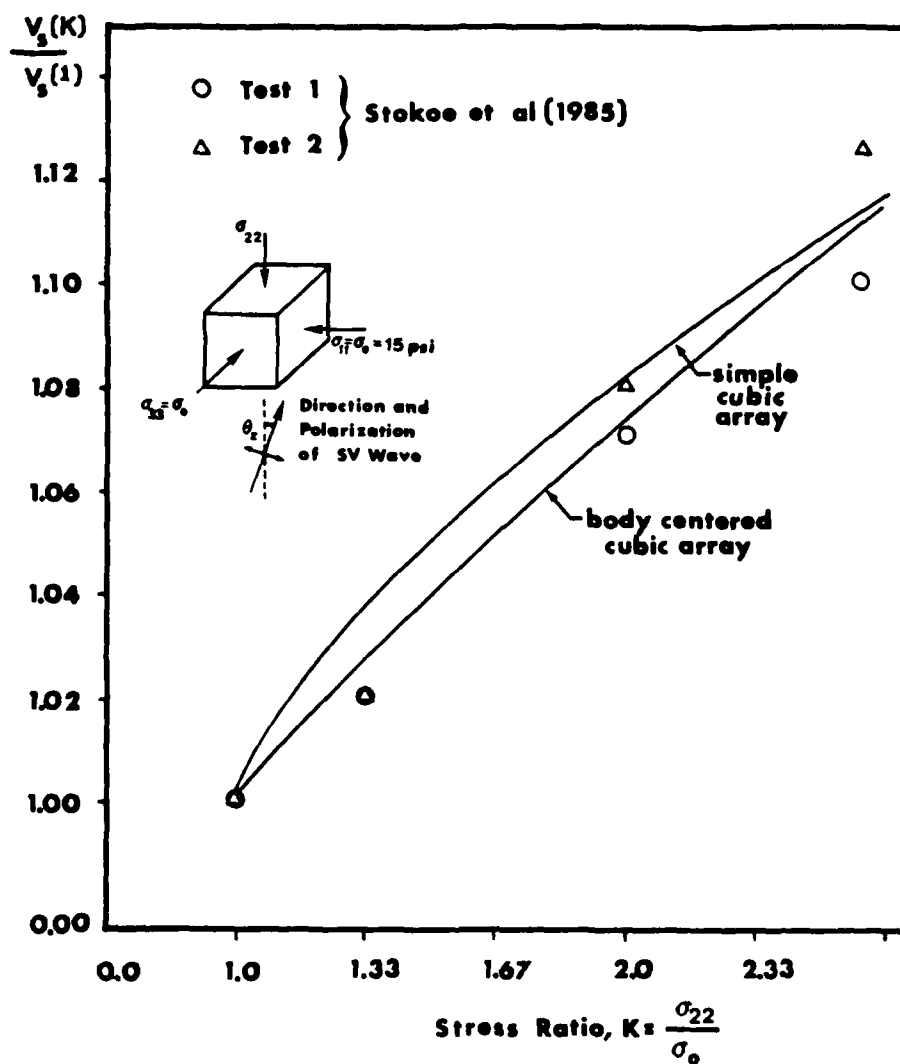


Figure 34. Shear Wave Velocity, V_s , Versus Stress Ratio, K , for Biaxial Confinement and $\theta_z = 0$: Analytical and Experimental Results.

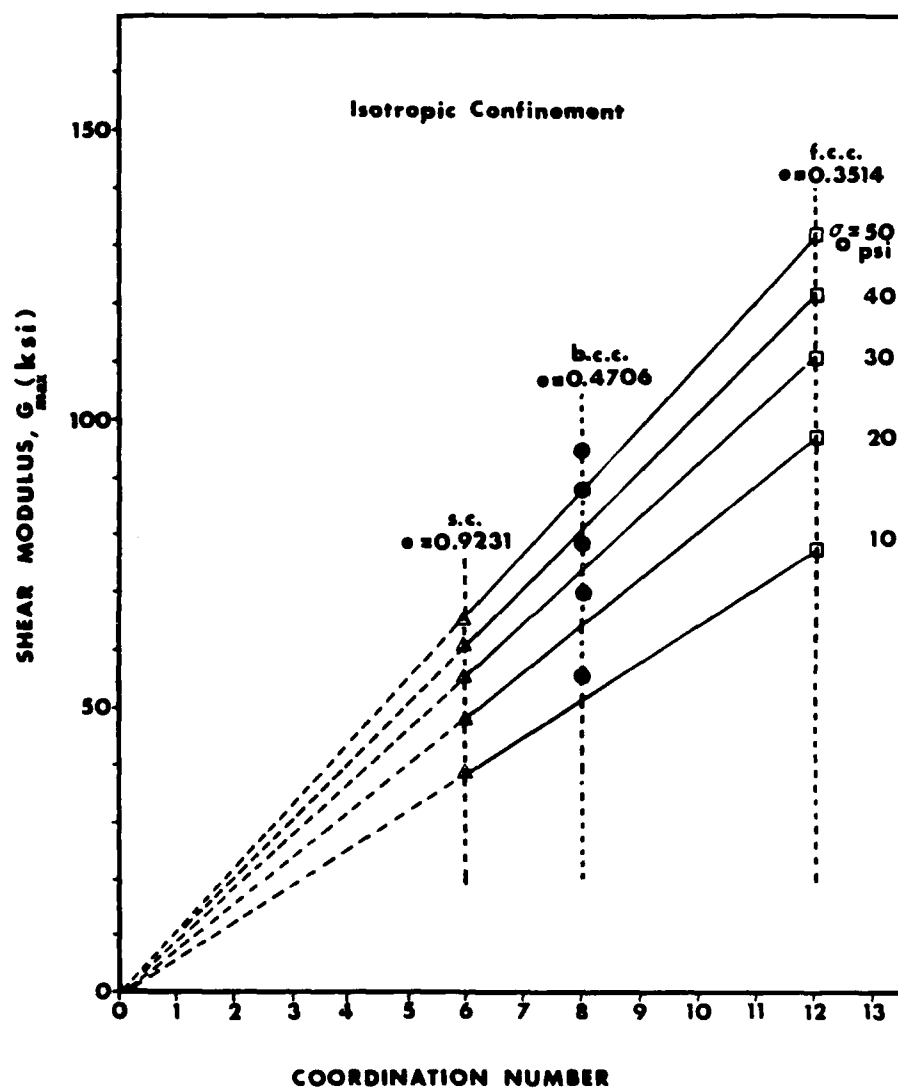


Figure 35. Shear Modulus Versus Coordination Number (= Number of Contacts per Sphere) for Regular Cubic Arrays of Quartz Spheres.

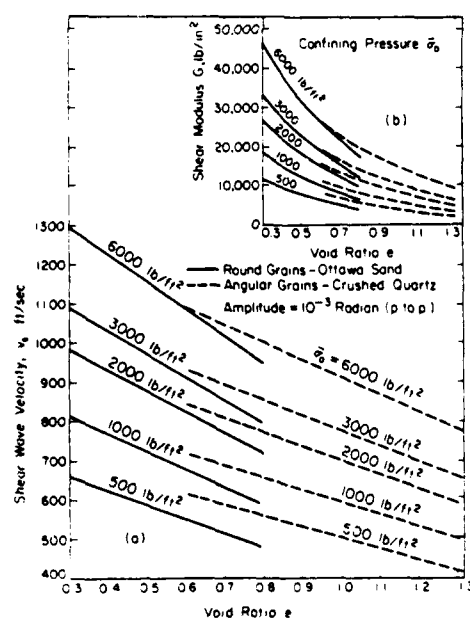
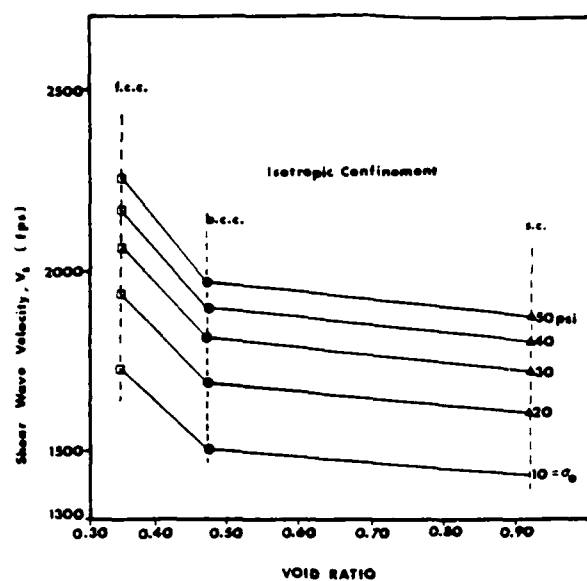


Figure 36. Shear Wave Velocity Versus Void Ratio. Comparison Between Predictions from Regular Cubic Arrays and Measurements in Quartz Sand.

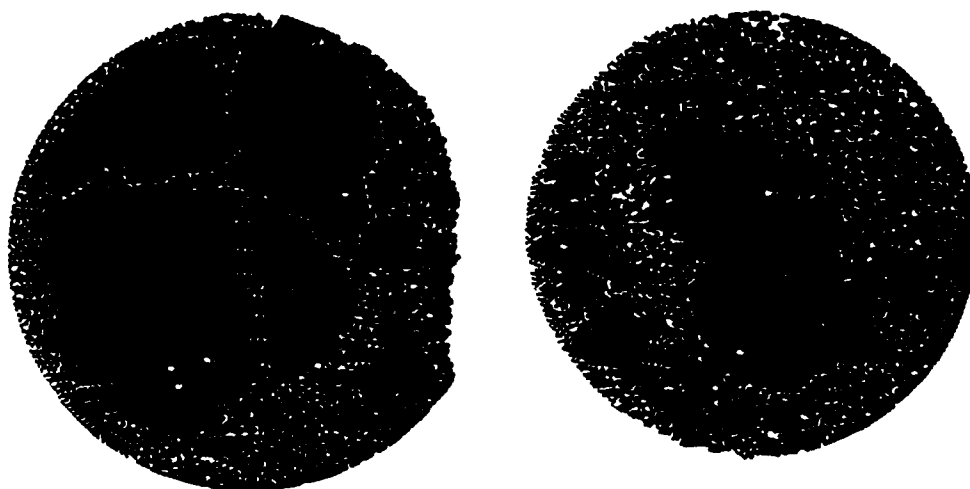
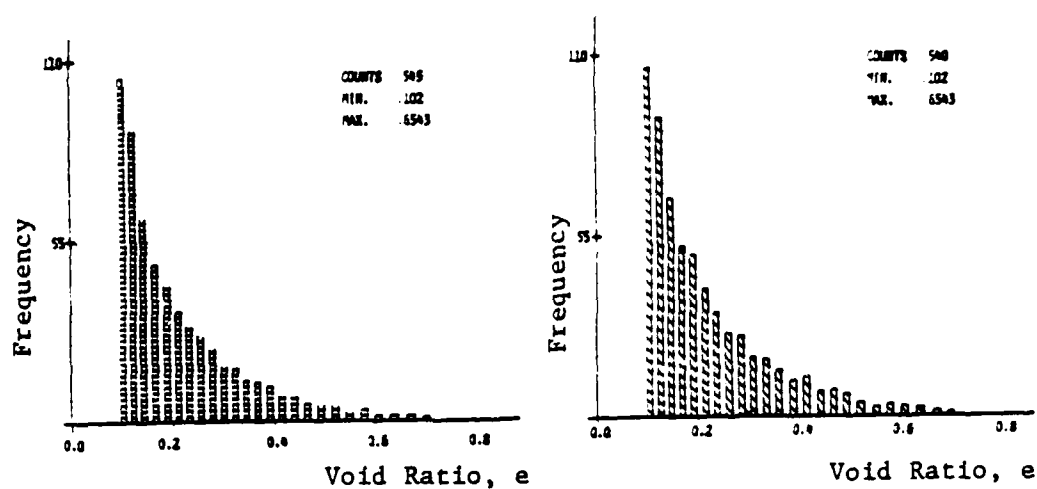


Figure 37. Histogram and Random Two-Dimensional Packing of Equal Sized Spherical Steel Balls (after Shahinpoor and Shahrpass, 1982).

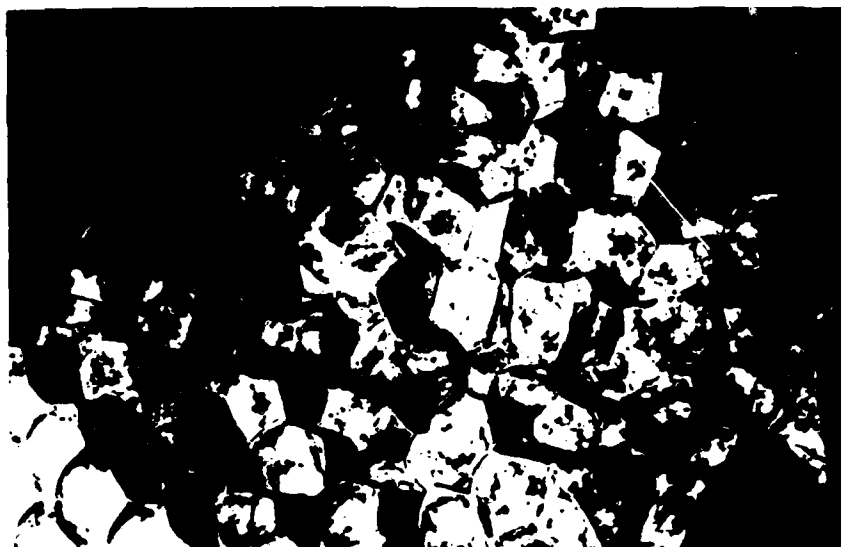


Figure 38. Cut-Away Artistic View of a Space Filling Configuration of Voronoi Polyhedra Containing Regular Arrays of Spheres (finney, 1983) .

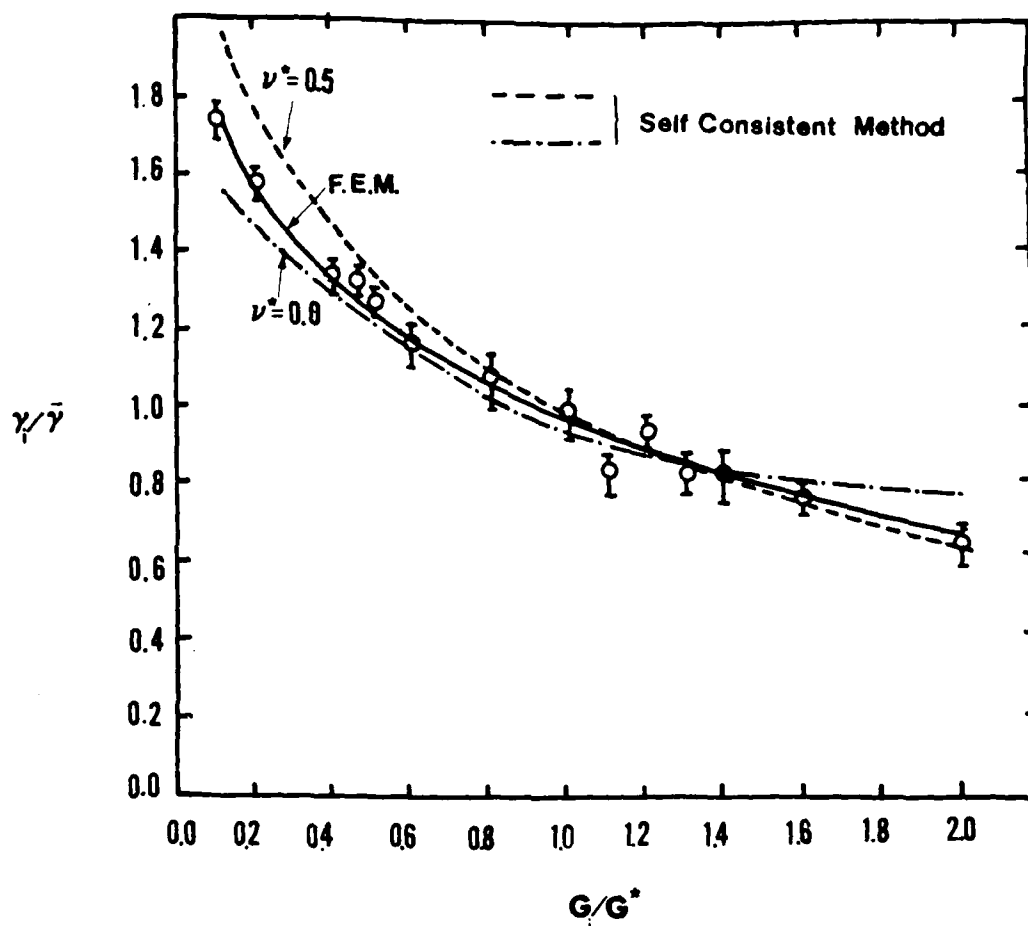


Figure 39. Shear Strain Experienced by Each Inclusion, γ_i , as a Function of its Shear Stiffness, G_i . Comparison Between Finite Element (FEM) and Self Consistent Method Results.

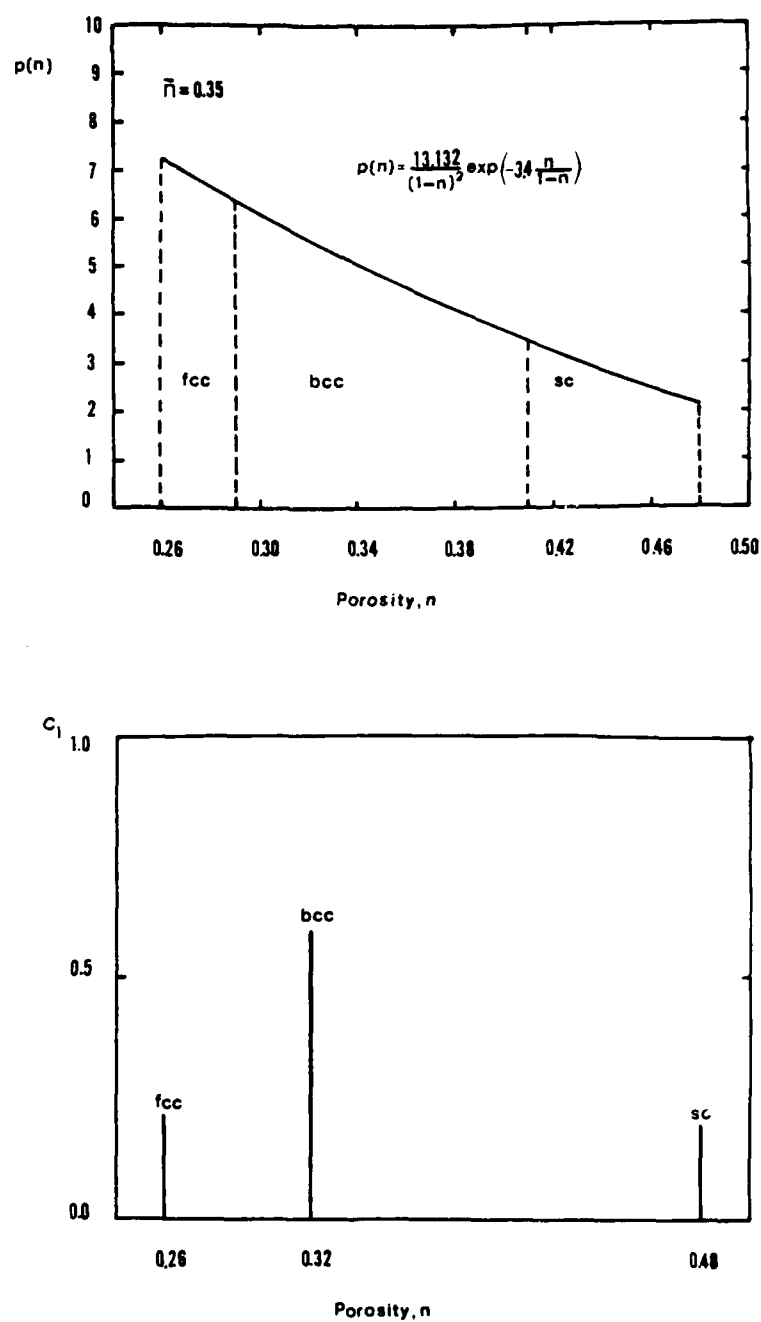


Figure 40. Discretization of Probability Density Function of Porosity, $p(n)$, to Represent a Medium of Macroscopic Porosity, $\bar{n}=0.35$, by a Combination of Three Regular Cubic Arrays.

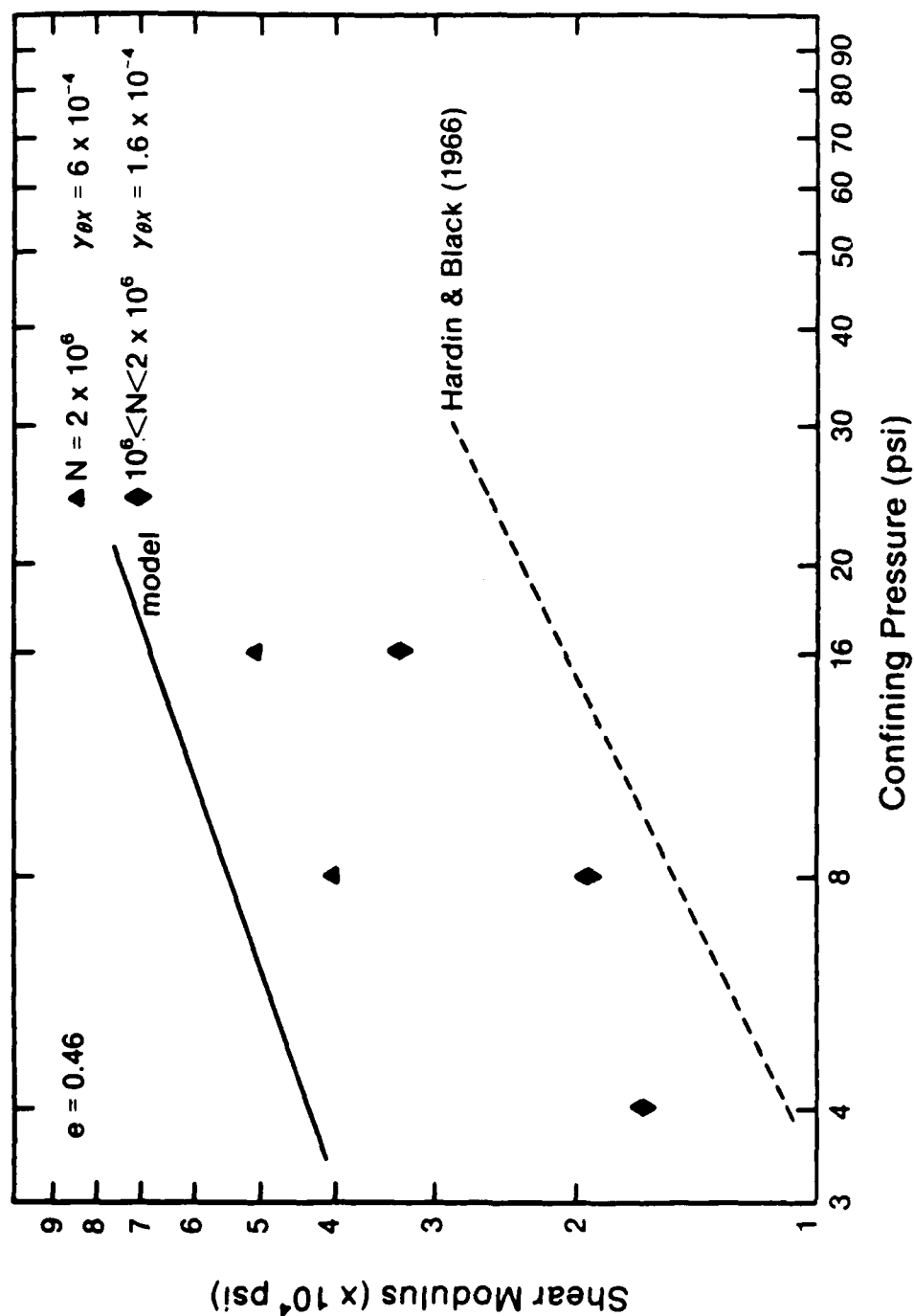


Figure 41. Shear Modulus, G_{max} , Versus Isotropic Confining Pressure Analytical and Experimental Results for $e=0.46$.

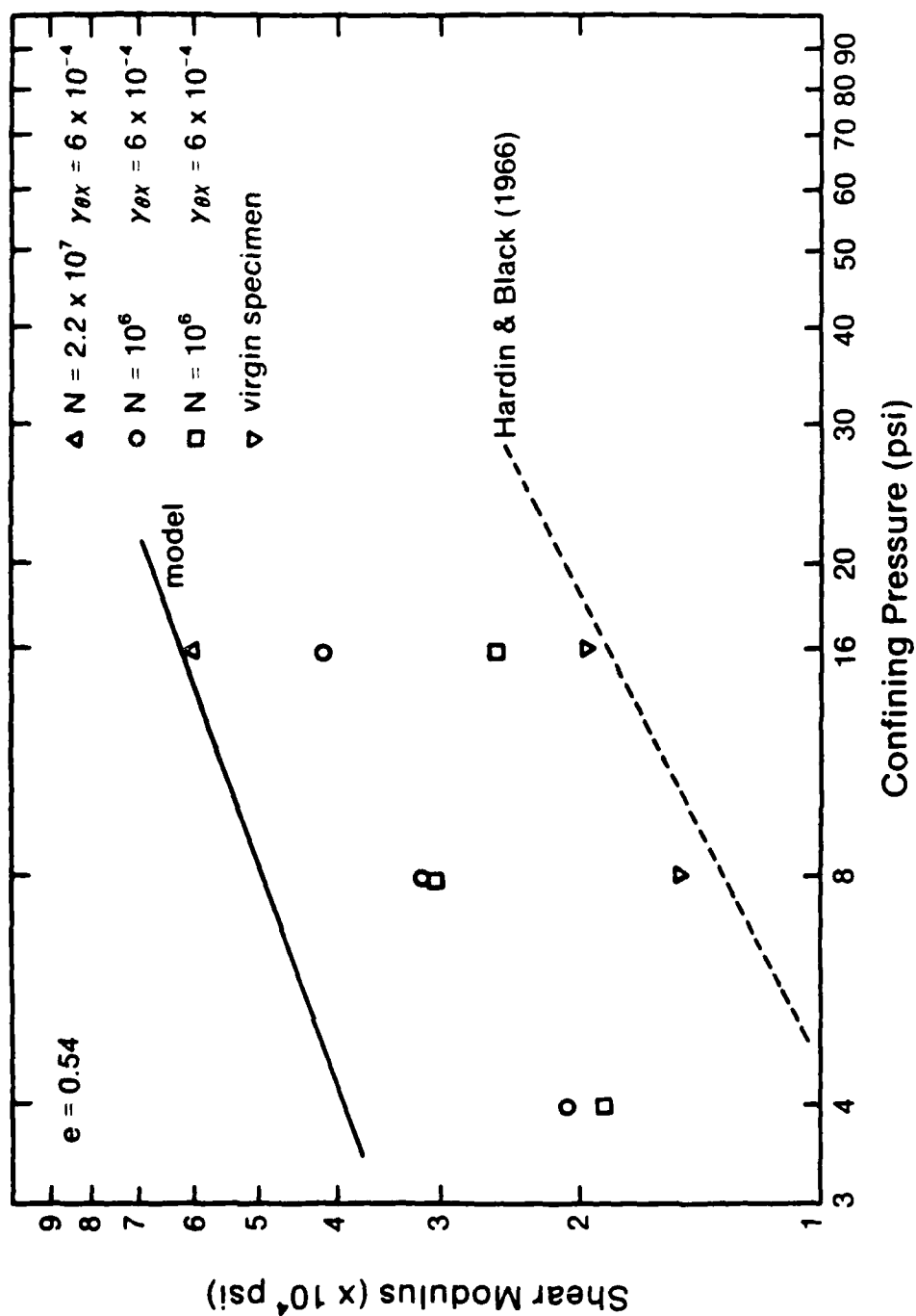


Figure 42. Shear Modulus, G_{max} , Versus Isotropic Confining Pressure Analytical and Experimental Results for $e=0.54$.

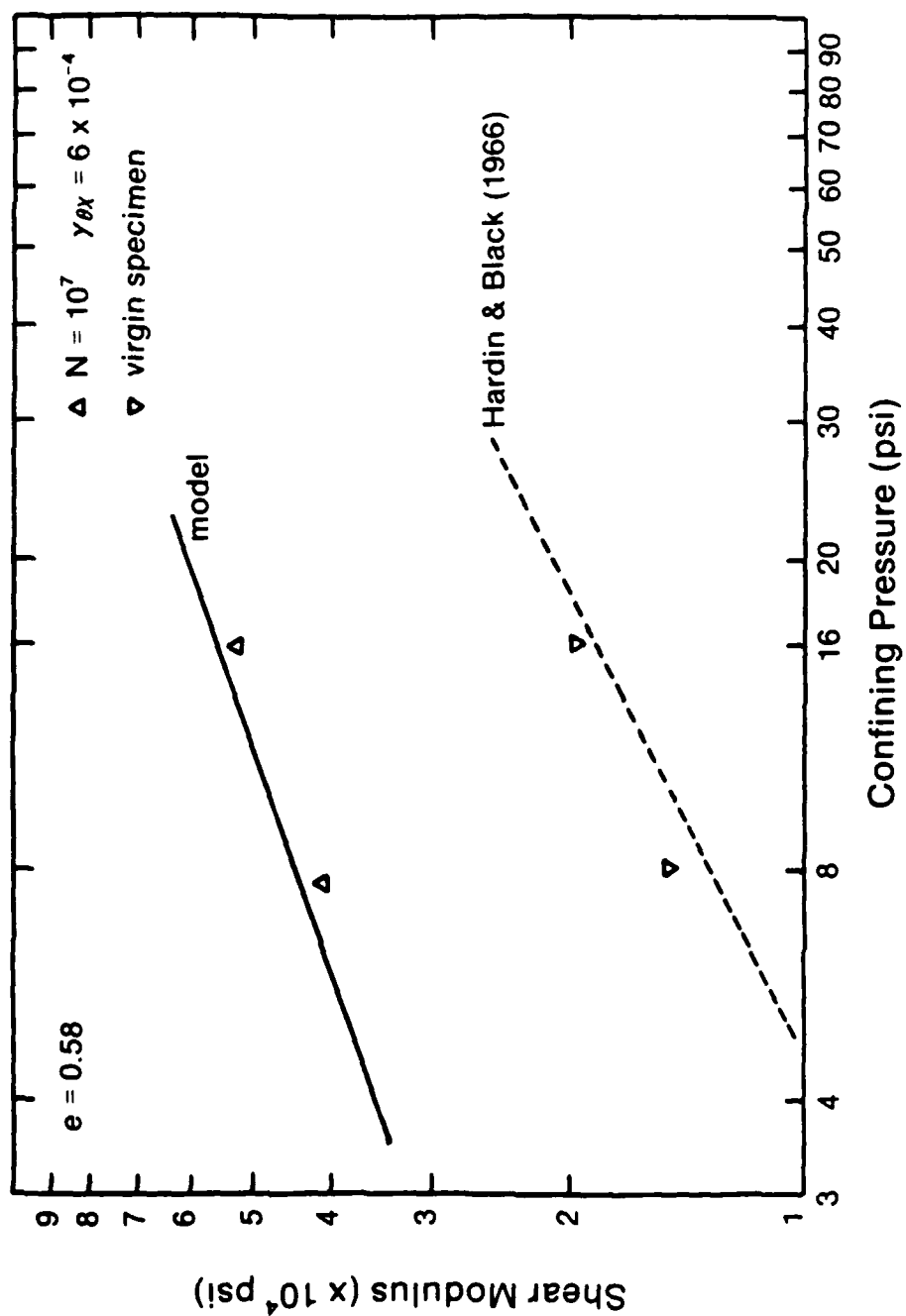


Figure 43. Shear Modulus, G_{max} , Versus Isotropic Confining Pressure Analytical and Experimental Results for $e=0.58$.

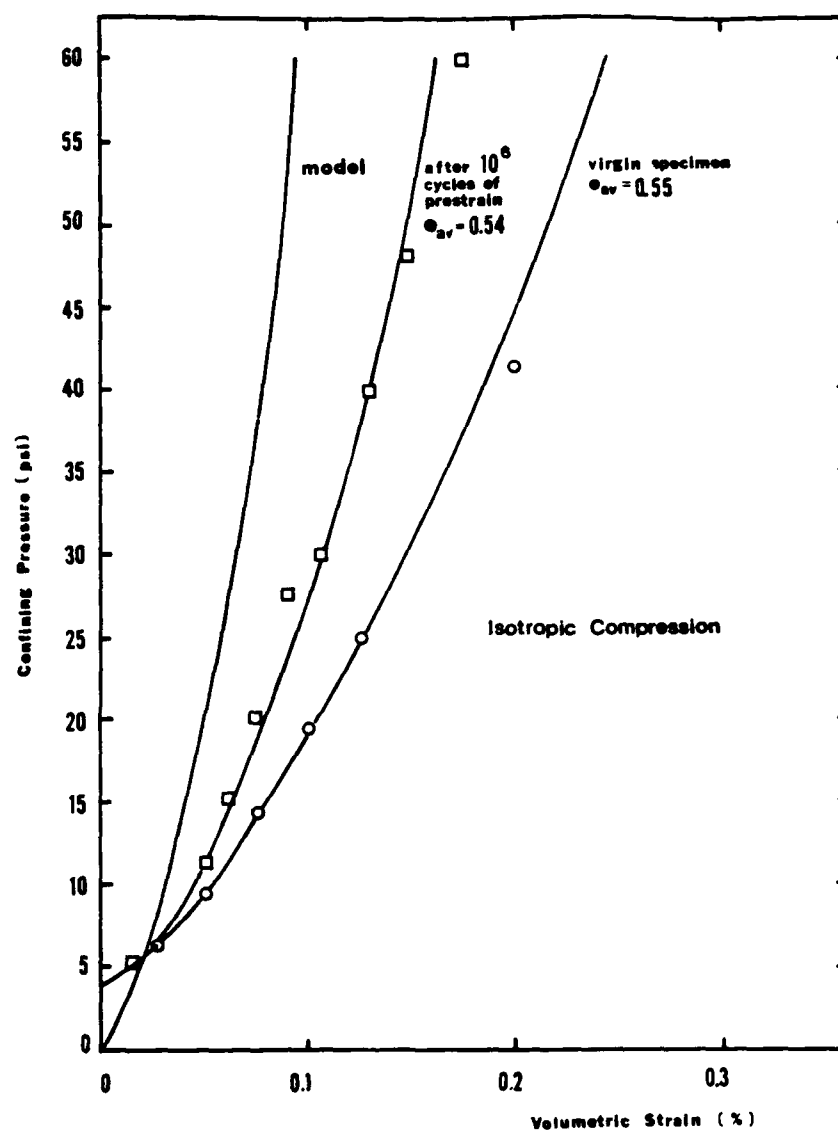


Figure 44. Confining Pressure Versus Volumetric Strain. Analytical and Experimental Results for $e=0.54$.

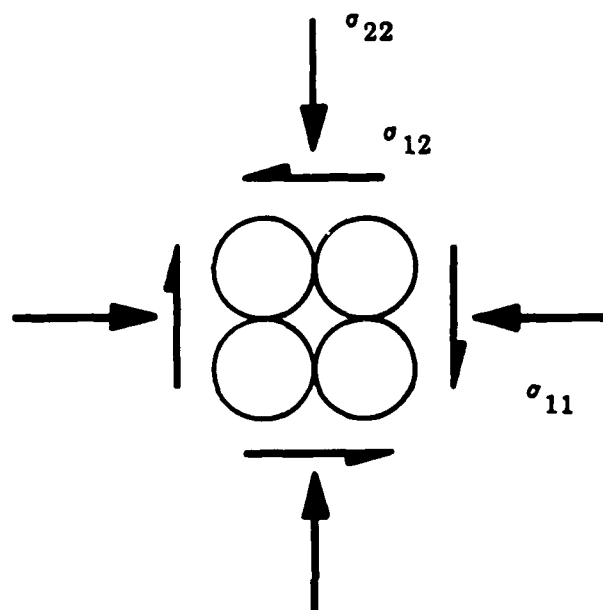
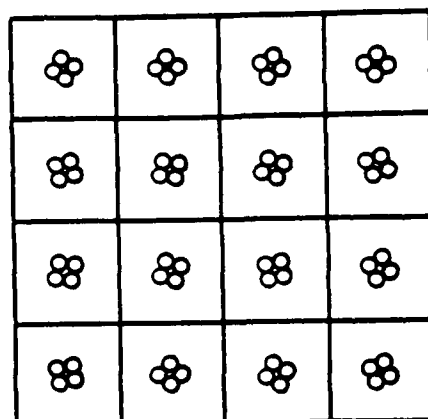
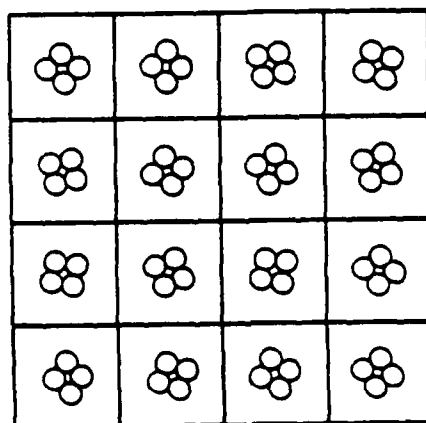


Figure 45. Stress State on a Simple Cubic Array of Identical Spheres



medium 1



medium 2

Figure 46. 16-Element Media Used in the Simulation and Angle of Orientation of Each Element.

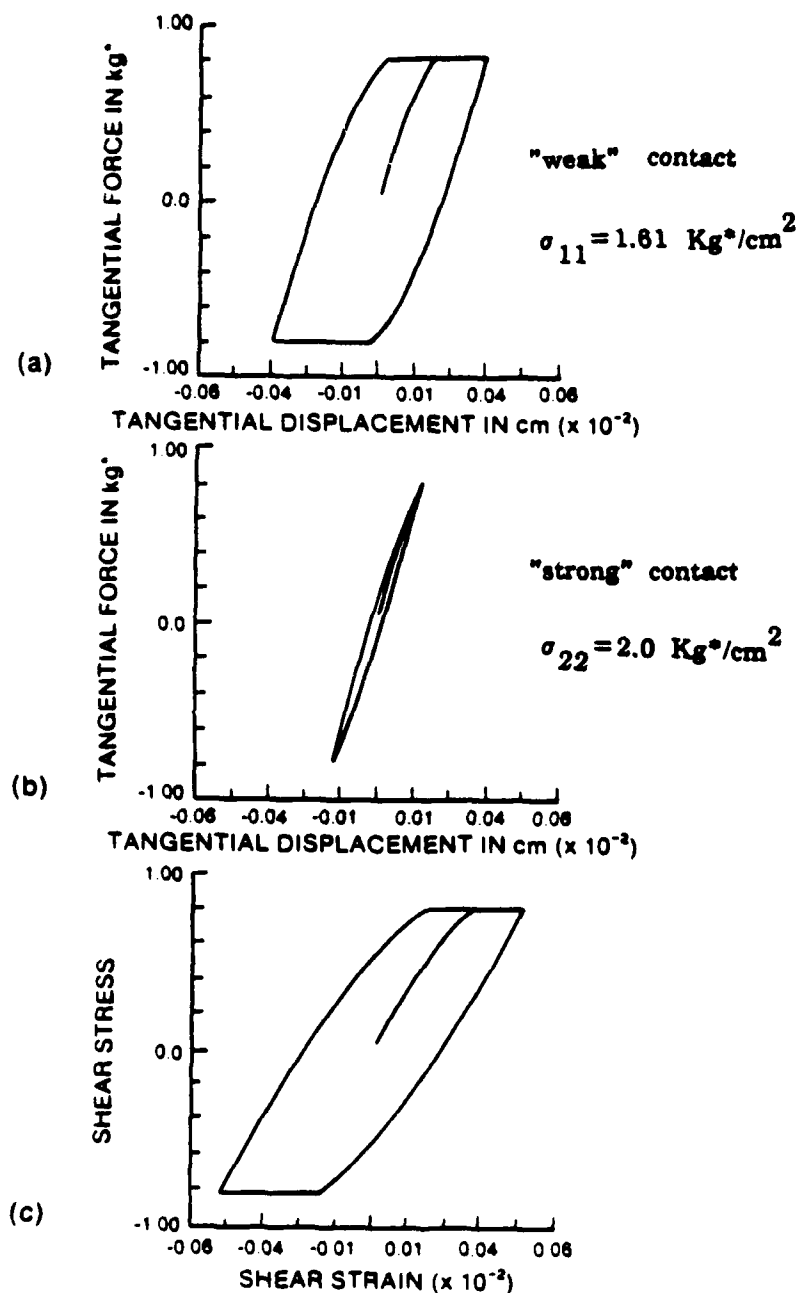


Figure 47. Stress-Strain Behavior, (c), of a Simple Cubic Array of Quartz Spheres Subjected to Biaxial Stress, $\sigma_{11}=1.61$, $\sigma_{22}=2.0 \text{ Kg}^*/\text{cm}^2$, Followed by Pure Shear, σ_{12} , to Failure. (a) and (b) Portray the Corresponding Force-Deformation Behavior of the "Weak" and "Strong" Contact, Respectively.

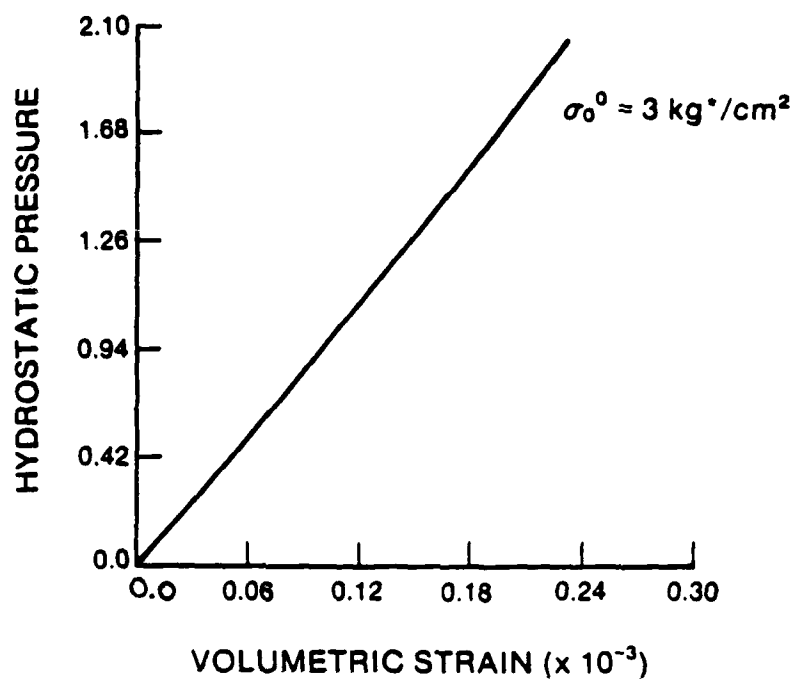


Figure 48. Medium 1: Stress-Strain Behavior for Hydrostatic Compression Loading starting from $\sigma_0^0 = 3.0 \text{ Kg}^*/\text{cm}^2$.

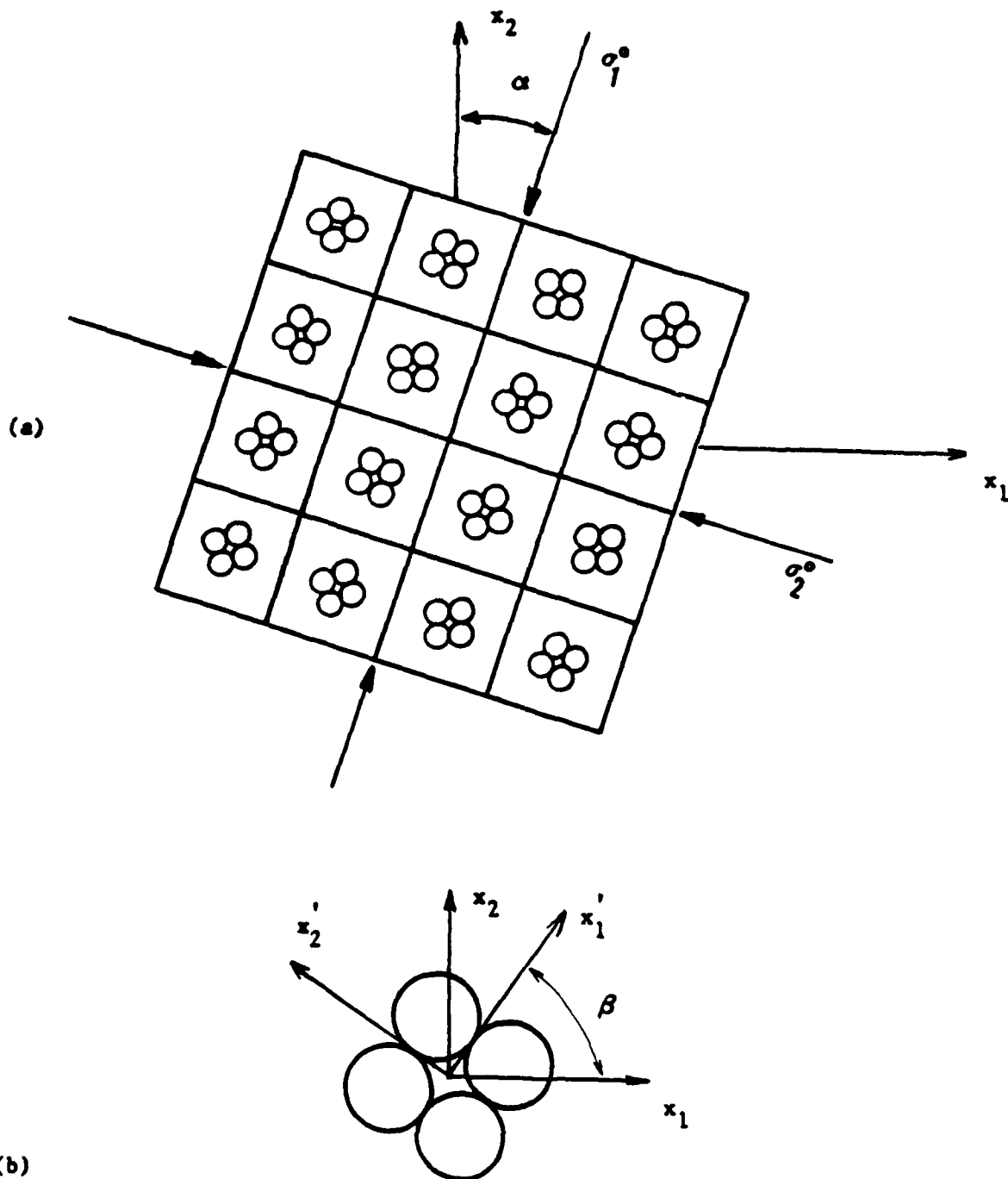


Figure 49. (a) Orientation of the Applied Principal Stresses During Pure Shear Loading with Mean Stress Constant, $\sigma_0^0 = 0.56(\sigma_1^0 + \sigma_2^0) = \text{Constant}$; (b) Orientation of an Element

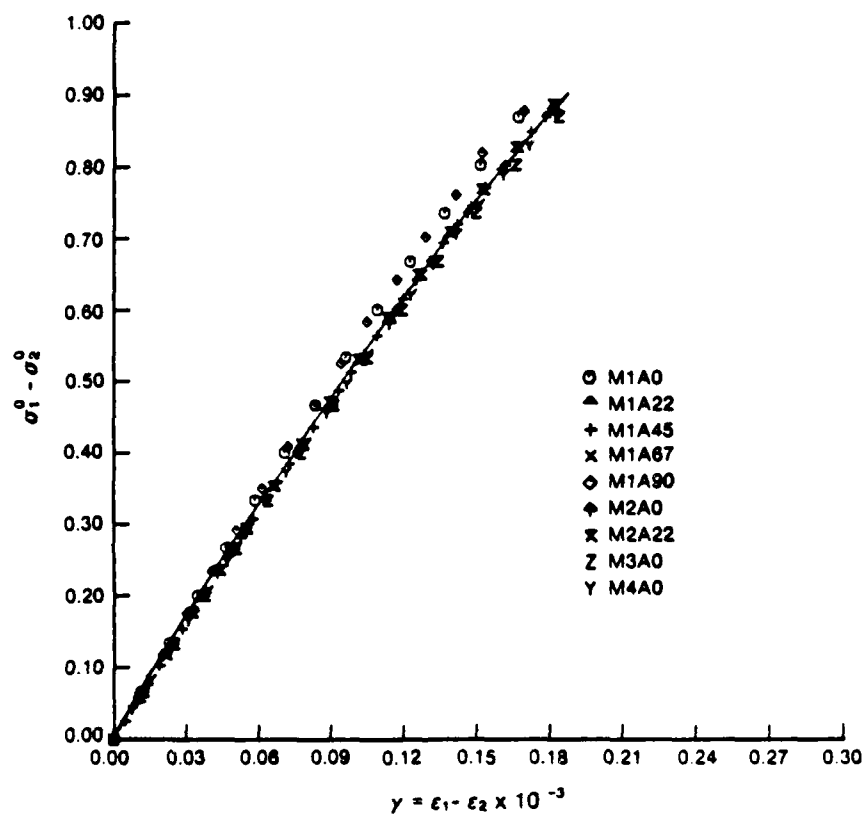


Figure 50. Difference in Applied Principal Stresses, $\sigma_1^0 - \sigma_2^0$, Versus Shear Strain, $\gamma = \epsilon_1 - \epsilon_2$, Calculated for all Media (16 nd 64 elements), and for Values of $\alpha = 0^\circ$, 22.5° , 45° , 67.5° , and 90° (MX=medium X, AYY=inclination of σ_1 is YY degrees).

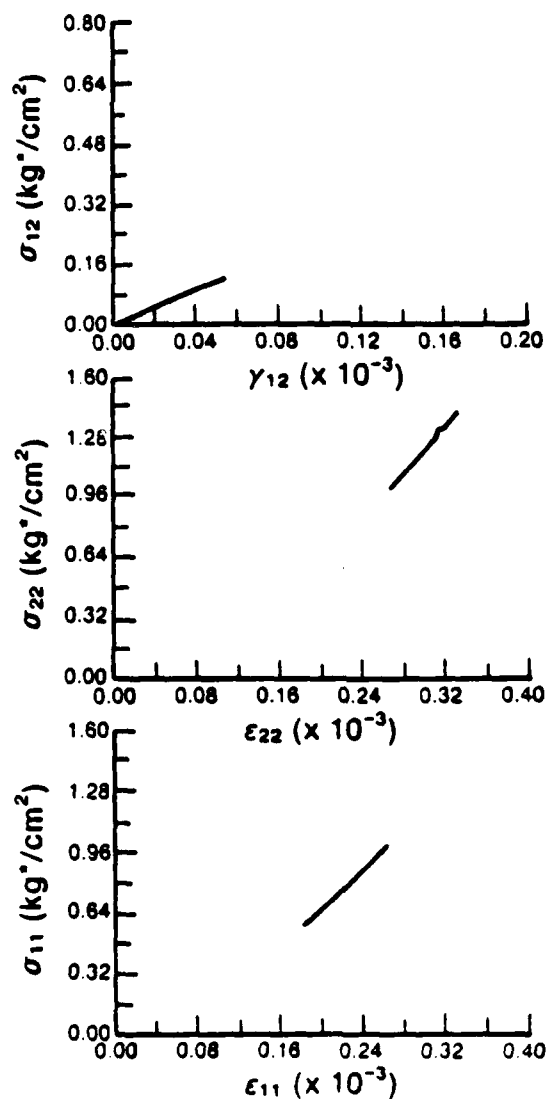


Figure 51. Medium 2: Compression with Constant Mean Stress ($\sigma_0 = 1.0 \text{ Kg}^*/\text{cm}^2$). Stress-Strain Behavior of Element E2 Oriented at $\beta = 10^\circ$.

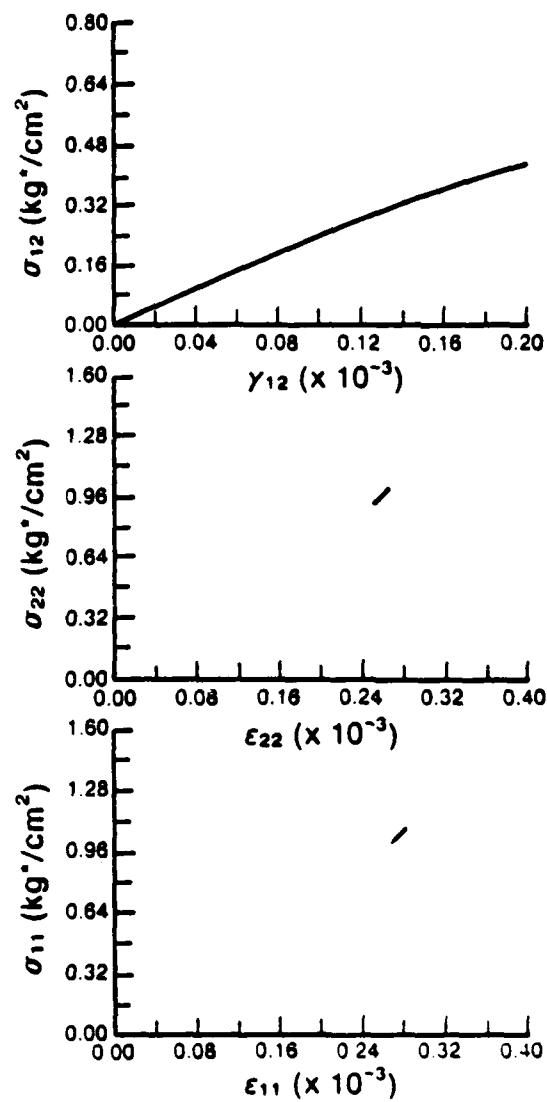


Figure 52. Medium 2: Compression with Constant Mean Stress ($\sigma_0^0 = 1.0 \text{ Kg}^*/\text{cm}^2$). Stress-Strain Behavior of Element E4 Oriented at $\beta = 50^\circ$.

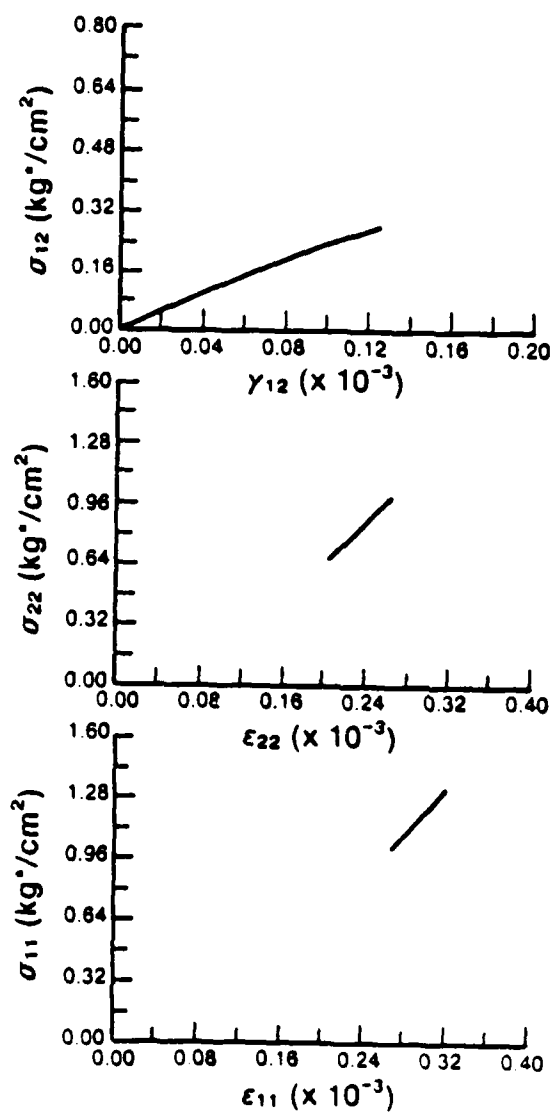


Figure 53. Medium 2: Compression with Constant Mean Stress ($\sigma_0^0 = 1.0 \text{ Kg}^*/\text{cm}^2$). Stress-Strain Behavior of Element E1 Oriented at $\beta = 70^\circ$.

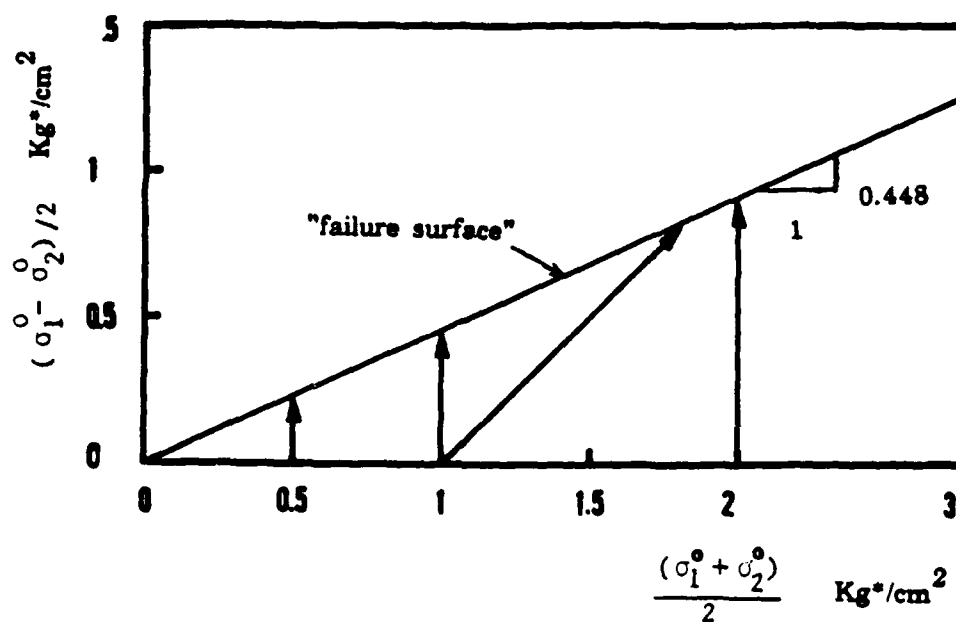


Figure 54. Failure Surface of the Aggregate, Determined From Four Stress Paths.

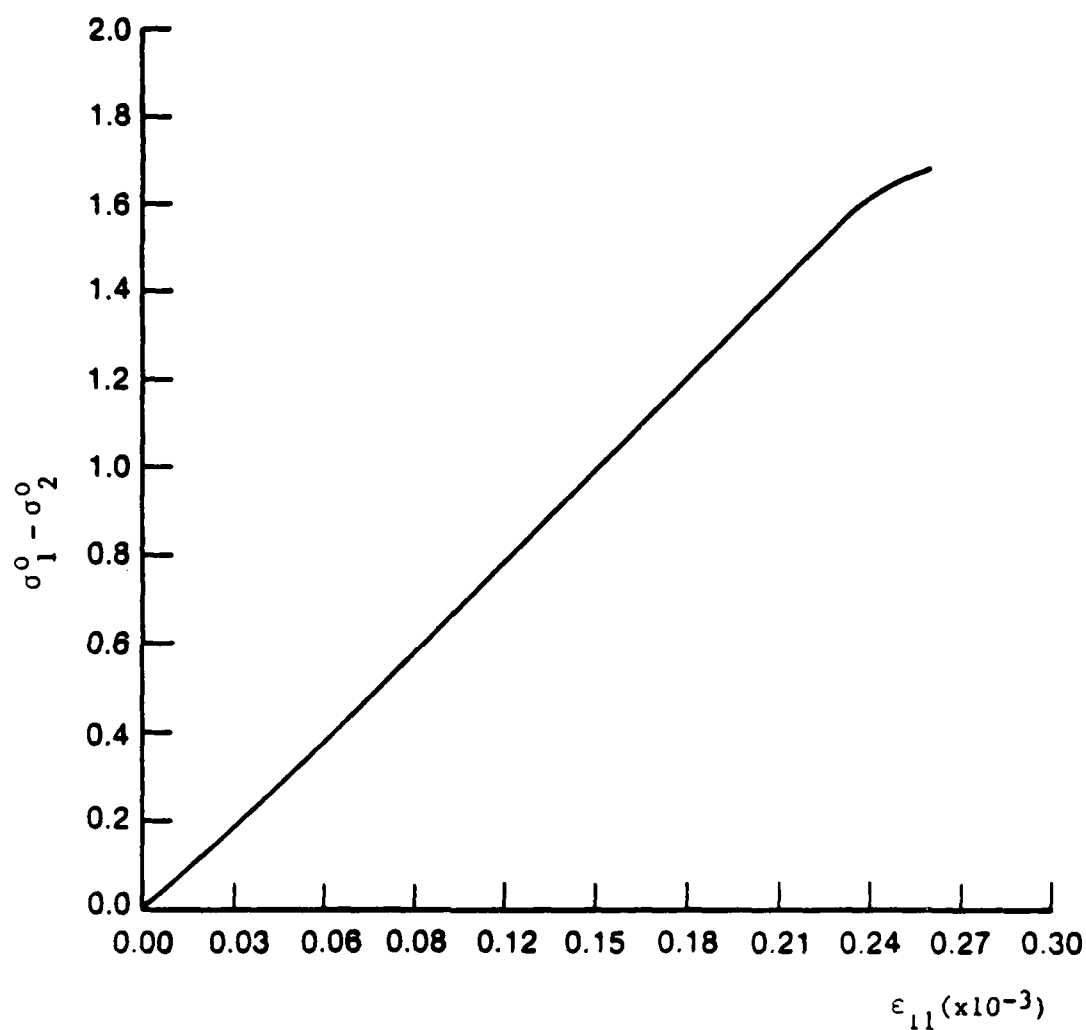


Figure 55. Medium 1: Stress-Strain Curve for the Aggregate for Compression Loading with Variable Mean Stress Following Isotropic Pressure, $\sigma_0^0 = 1 \text{ Kg } ^\star/\text{cm}^2$.

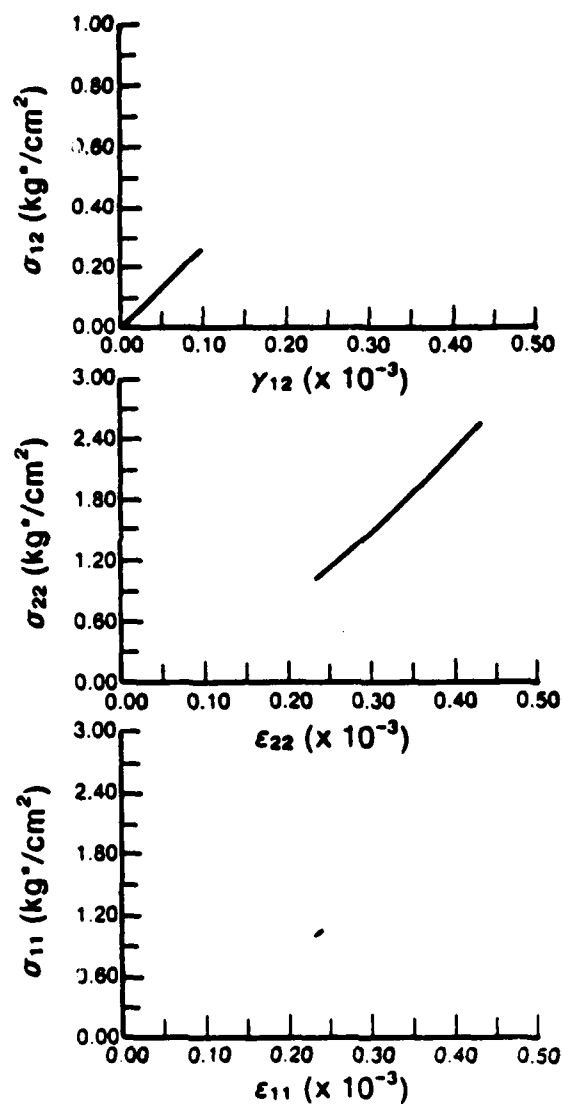


Figure 56. Medium 1: Compression with Variable Mean Stress ($\sigma_0^0 = 1.0 \text{ Kg */cm}^2$) Stress-Strain Behavior of Element E1 Oriented at $\beta = 10^\circ$.

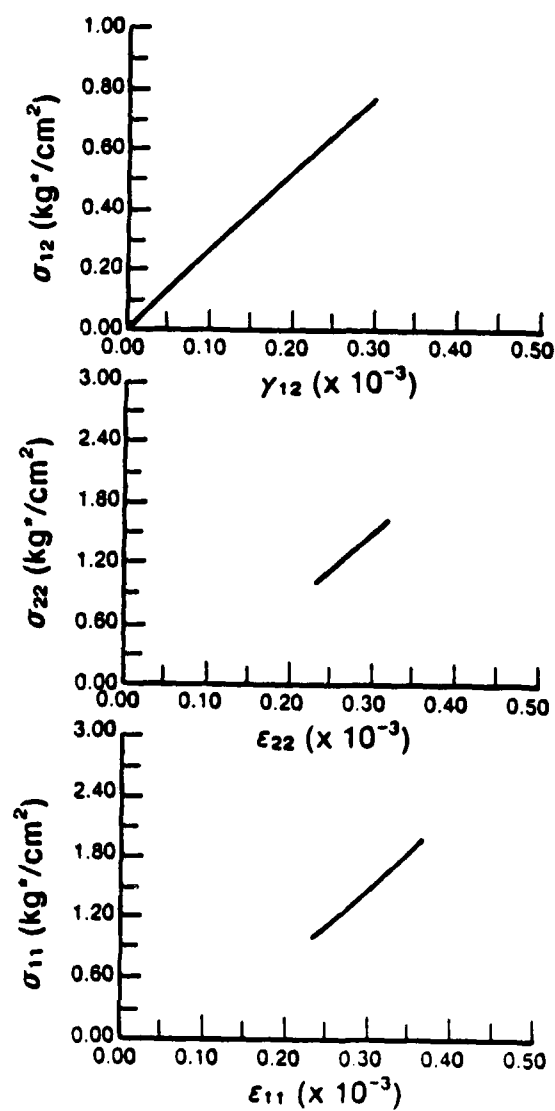


Figure 57. Medium 1: Compression with Variable Mean Stress ($\sigma_0^0 = 1.0 \text{ Kg}^*/\text{cm}^2$) Stress-Strain Behavior of Element E2 Oriented at $\beta = 50^\circ$.

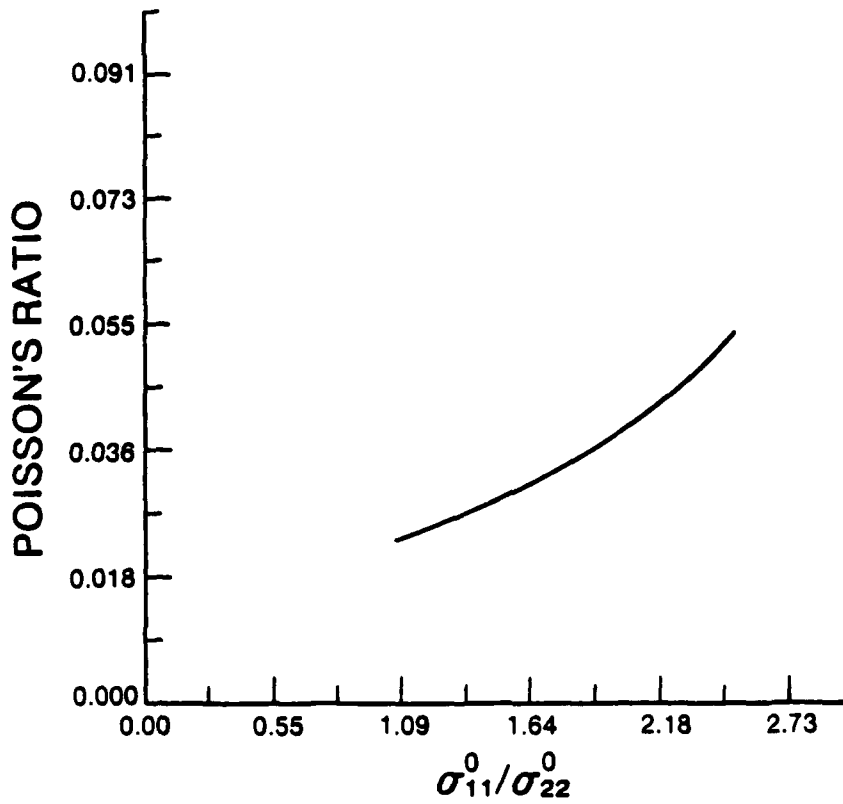


Figure 58. Poisson's Ratio for the Aggregate Calculated from the Compression with Variable Mean Stress Simulation.

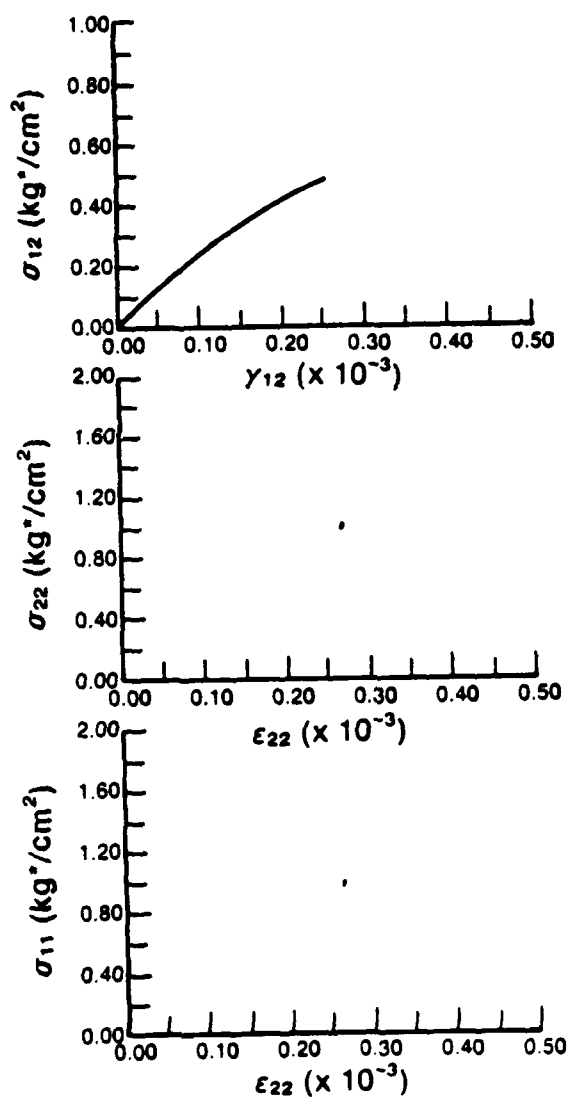


Figure 59. Medium 5: Compression with Constant Mean Stress. Stress-Strain Behavior for Element E50 oriented at $\beta=45^\circ$.

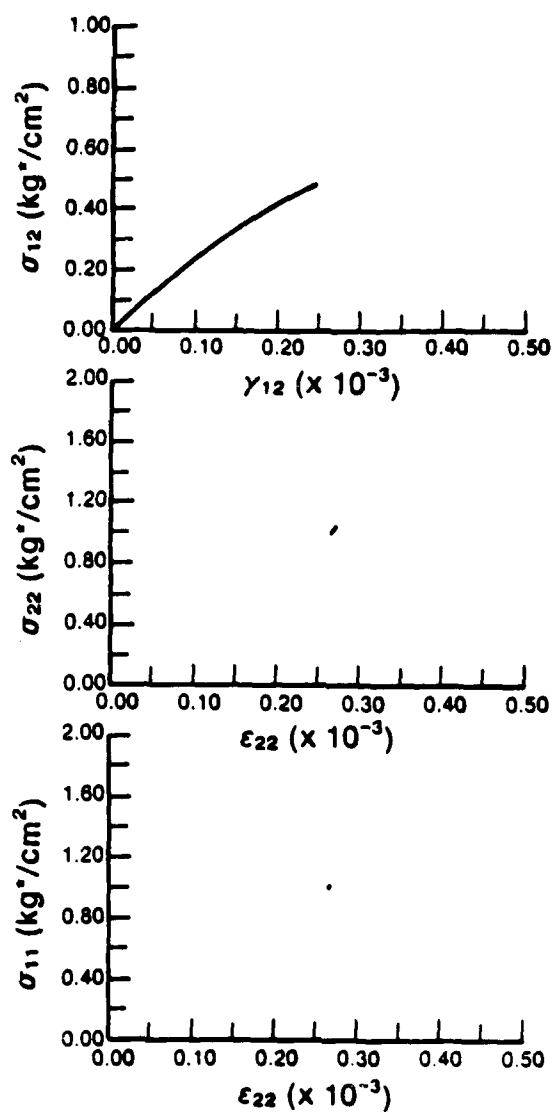


Figure 60. Medium 5: Compression with Constant Mean Stress. Stress-Strain Behavior for Element E44 oriented at $\beta=45^\circ$.

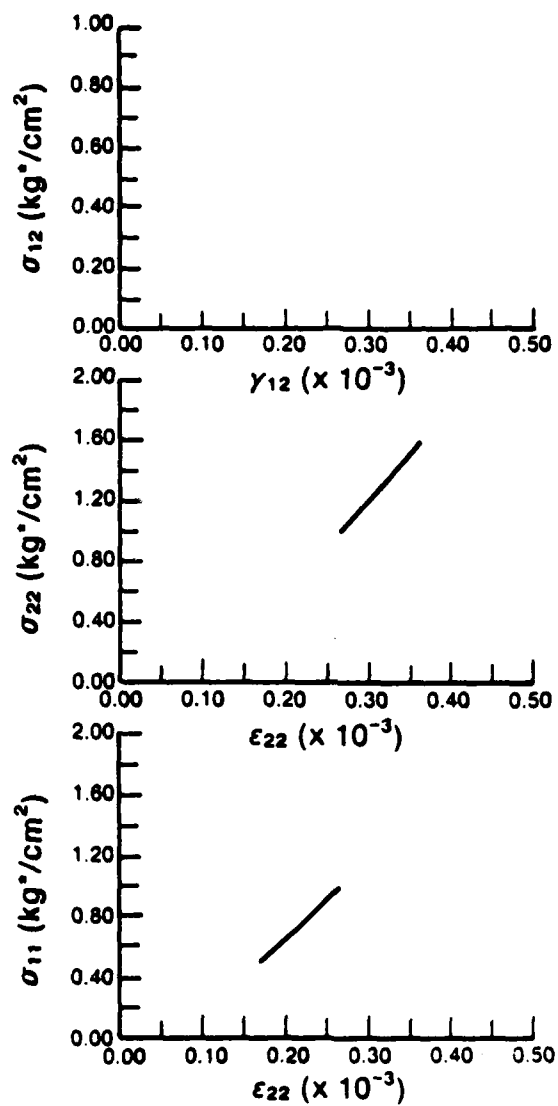


Figure 61. Medium 5: Compression with Constant Mean Stress. Stress-Strain Behavior for Element E36 oriented at $\beta=0^\circ$.

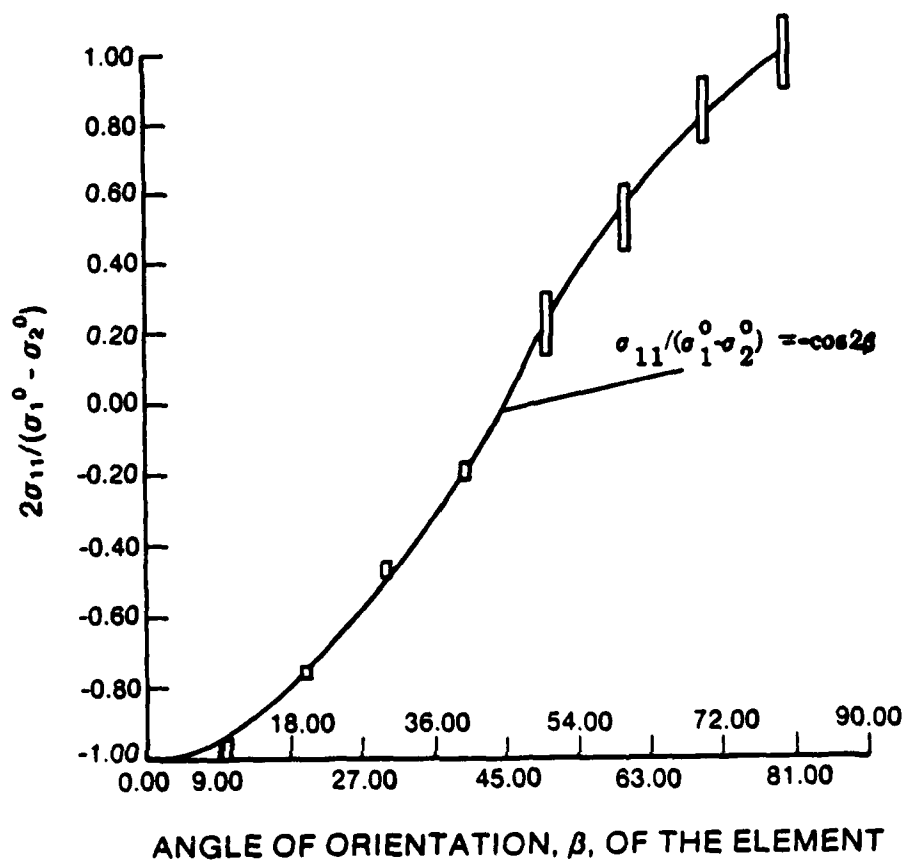


Figure 62. Medium 2: Compression with Constant Mean Stress ($\sigma_0^0 = 1.0 \text{ Kg * /cm}^2$). Normalized Element Normal Stress, $\sigma_{11}/(\sigma_1^0 - \sigma_2^0)$ Versus Angle of Orientation β , of the Element for Three Inclinations of Principal Stress, $\alpha = 0, 45$ and 90 degrees.

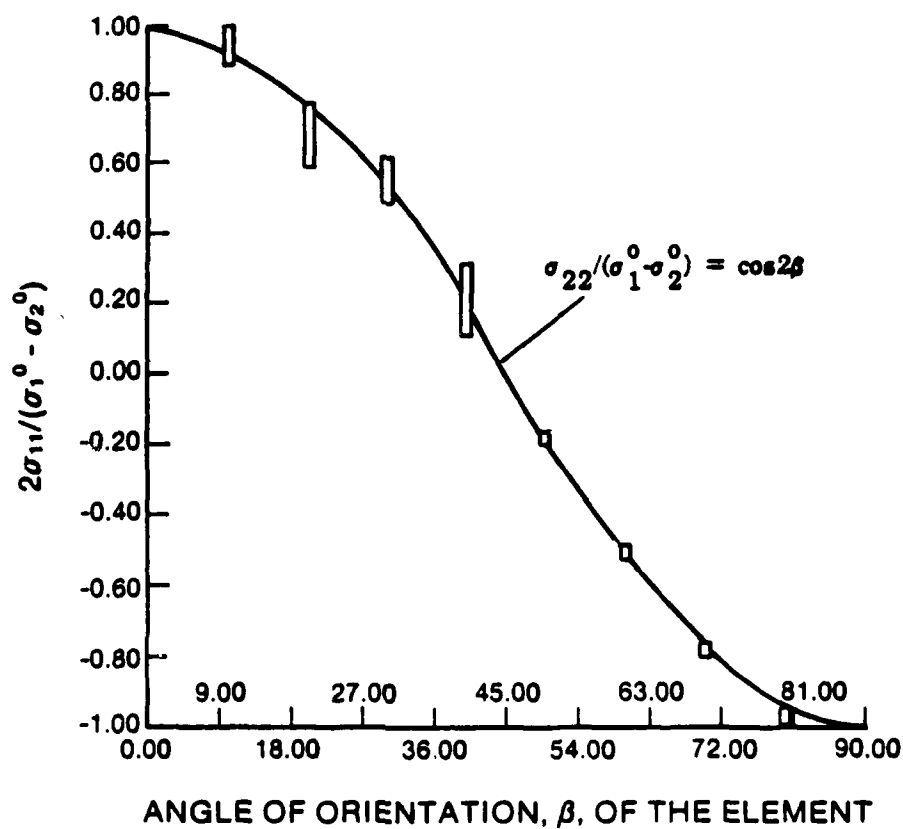


Figure 63. Medium 2: Compression with Constant Mean Stress ($\sigma_o^0 = 1.0 \text{ Kg}^*/\text{cm}^2$). Normalized Element Normal Stress, $\sigma_{22}/(\sigma_1^0 - \sigma_2^0)$ Versus Angle of Orientation β , of the Element for Three Inclinations of Principal Stress, $\alpha = 0, 45$ and 90 degrees.

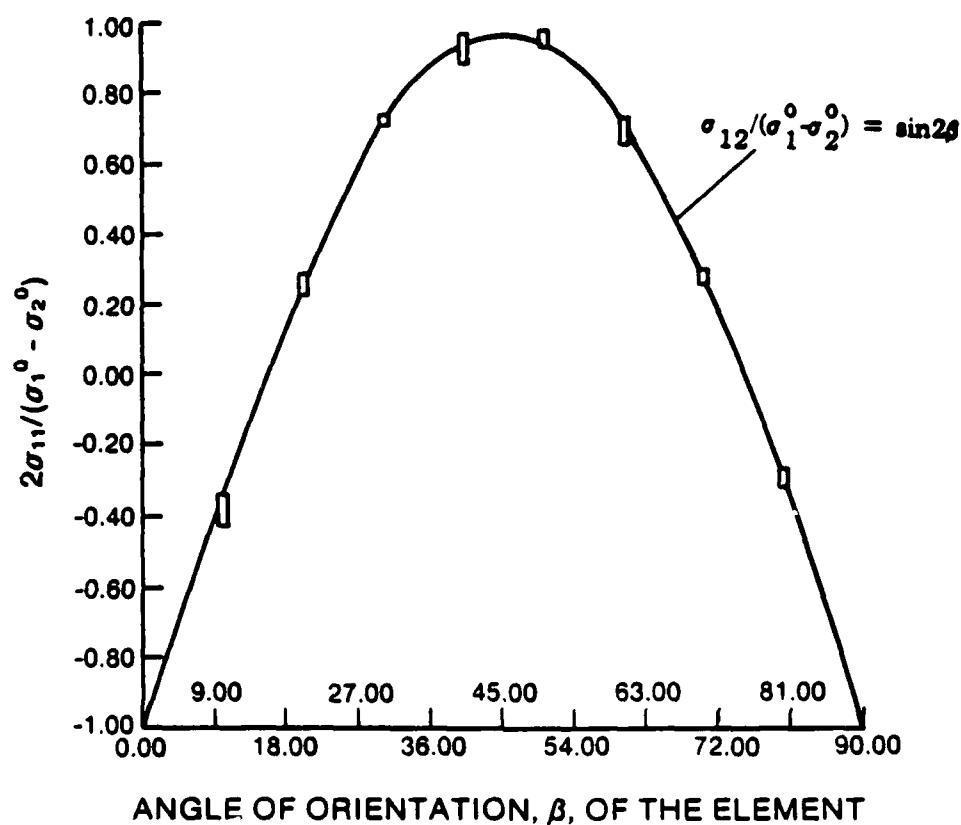


Figure 64. Medium 2: Compression with Constant Mean Stress ($\sigma_0 = 1.0 \text{ Kg */cm}^2$). Normalized Element Normal Stress, $\sigma_{12}/(\sigma_1^0 - \sigma_2^0)$ Versus Angle of Orientation β , of the Element for Three Inclinations of Principal Stress, $\alpha = 0, 45$ and 90 degrees.

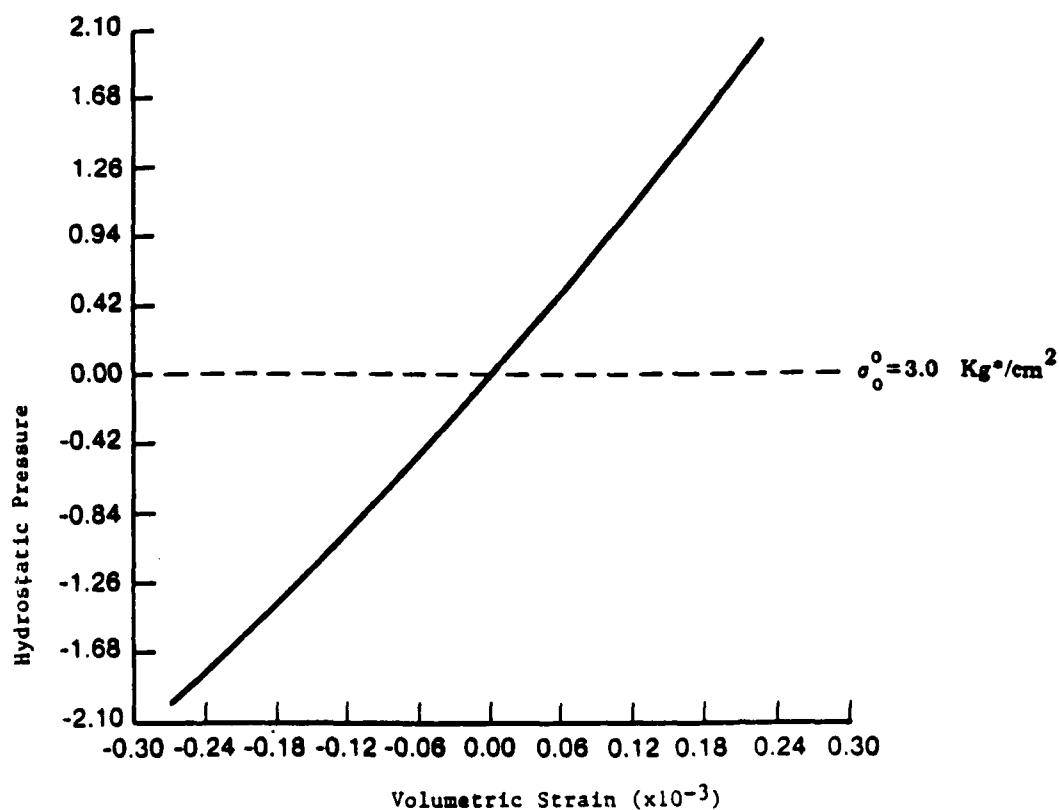
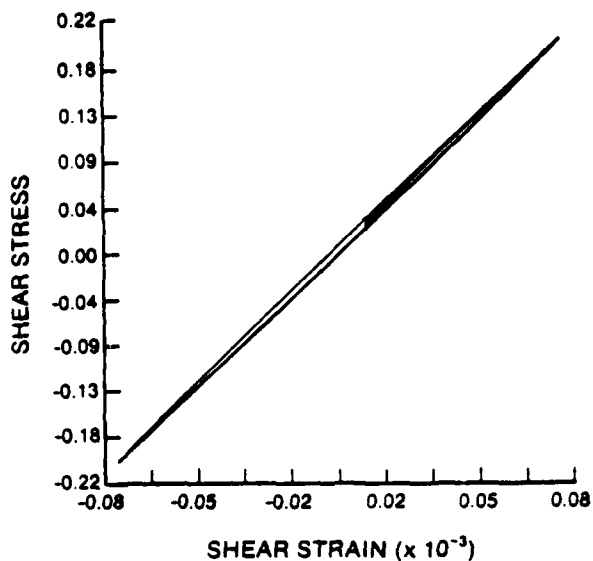
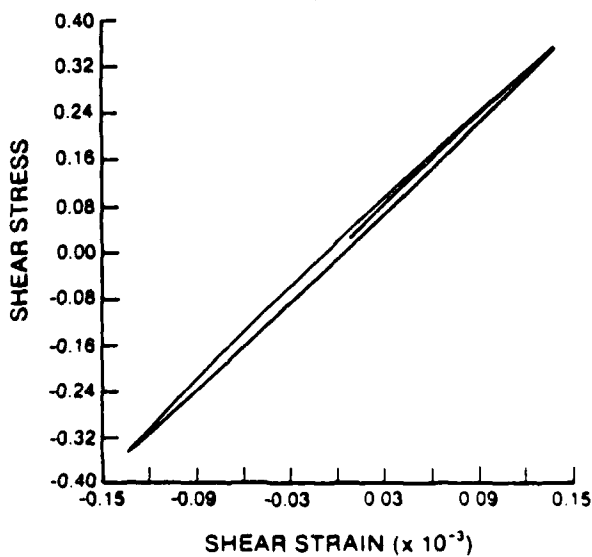


Figure 65. Medium 1: Stress-Strain Behavior for Cyclic Isotropic Loading, $\sigma_0^0 \pm \Delta\sigma_0^0$, with $\sigma_0^0 = 3 \text{ Kg}^*/\text{cm}^2$ and $\Delta\sigma_0^0 = 2 \text{ Kg}^*/\text{cm}^2$



(a)



(b)

Figure 66. Medium 1: Stress-Strain Behavior for Cyclic Pure Shear Loading Following Isotropic Compression, $\sigma_o^o = 1.0 \text{ Kg}^*/\text{cm}^2$. (a) $\tau_c = 0.20 \text{ Kg}^*/\text{cm}^2$; (b) $\tau_c = 0.35 \text{ Kg}^*/\text{cm}^2$.

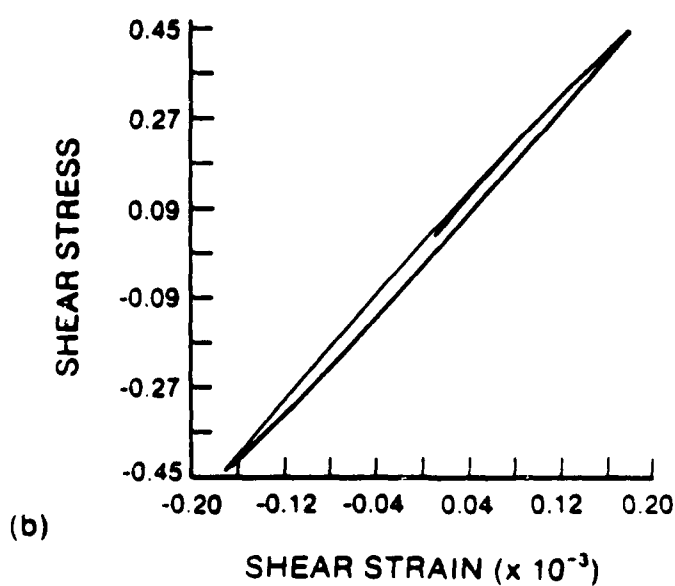
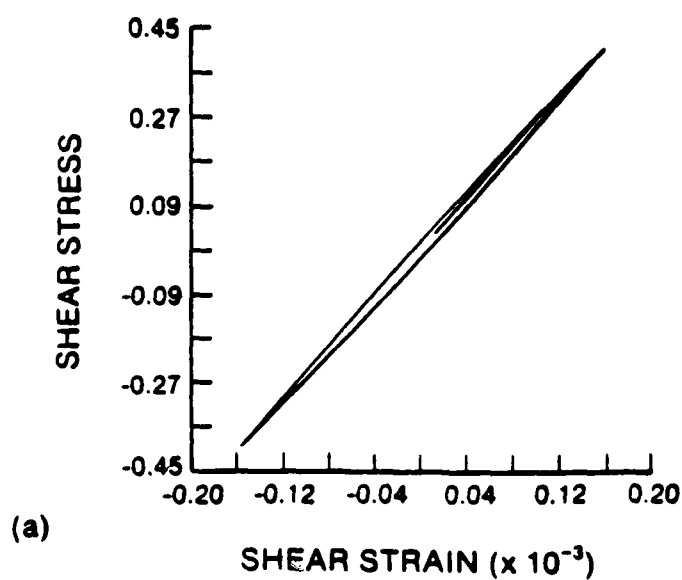


Figure 67. Medium 1: Stress-Strain Behavior for Cyclic Pure Shear Loading Following Isotropic Compression, $\sigma_o^0 = 1.0 \text{ Kg}^*/\text{cm}^2$. (a) $\tau_c = 0.420 \text{ Kg}^*/\text{cm}^2$; (b) $\tau_c = 0.43 \text{ Kg}^*/\text{cm}^2$.

AD-A191 927

MICROMECHANICAL MODELING OF GRANULAR SOIL AT SMALL
STRAIN BY ARRAYS OF EL. (U) RENSSELAER POLYTECHNIC INST
TROY NY DEPT OF CIVIL ENGINEERING. E PETAKIS ET AL.

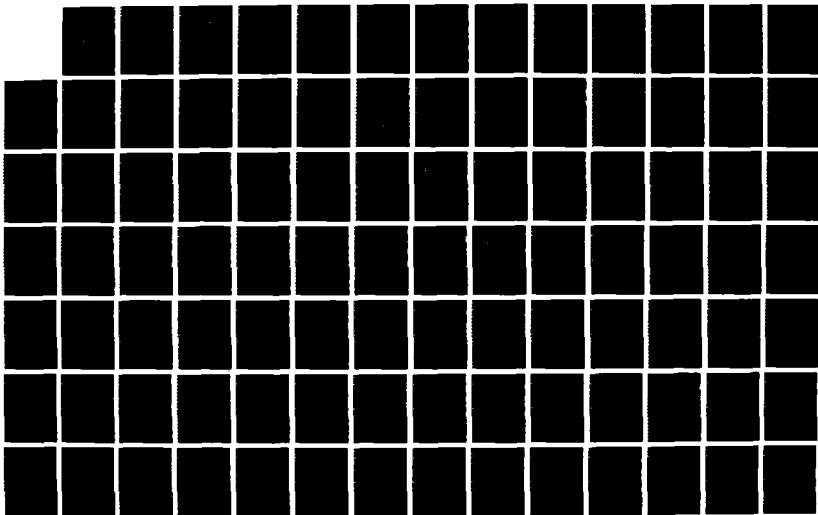
3/4

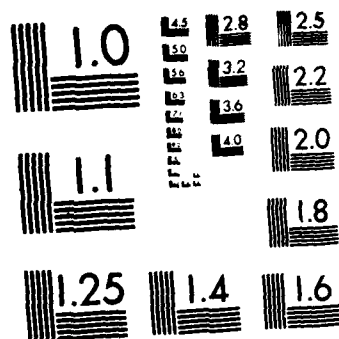
UNCLASSIFIED

28 SEP 87 RPI-CE-87-02 AFOSR-TR-88-0137

F/G 8/10

NL





MICROCOPY RESOLUTION TEST CHART
NATIONAL BUREAU OF STANDARDS 1963 A

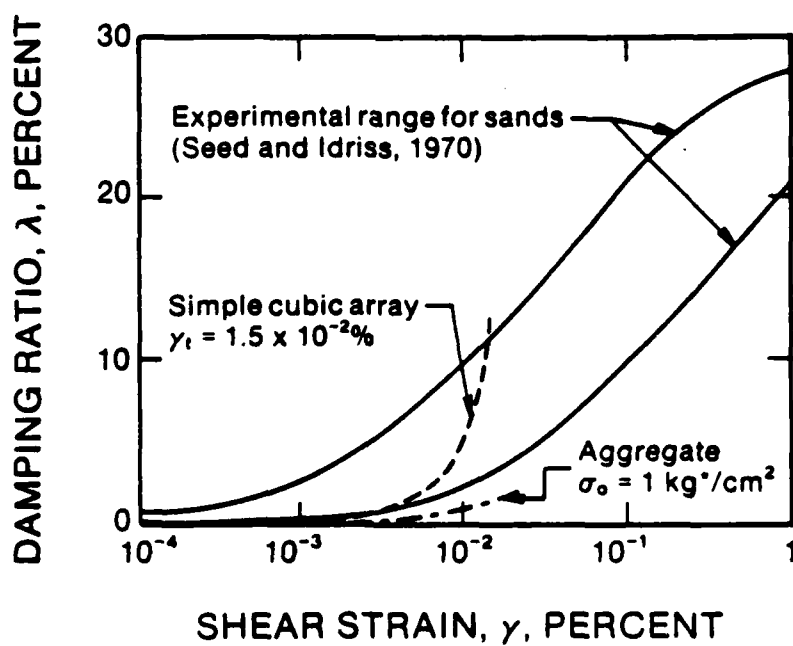
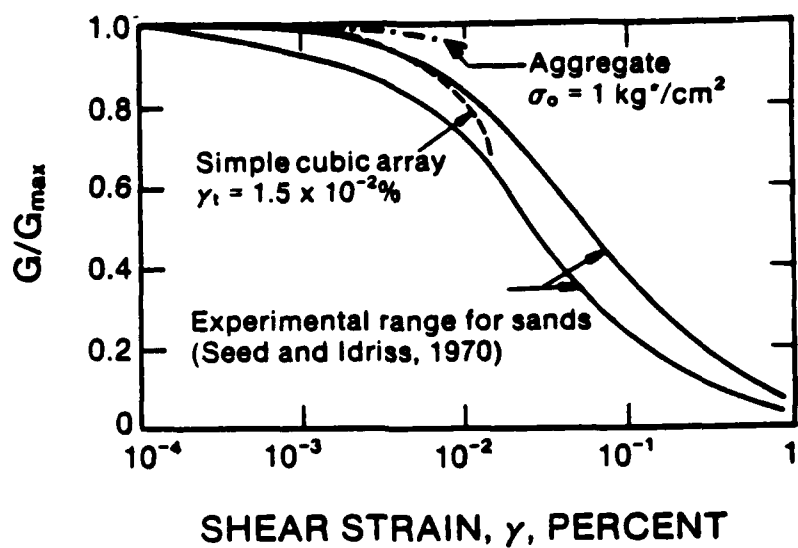


Figure 68. (a) Normalized Shear Modulus, G/G_{\max} ; (b) Damping Ratio, λ ; both Versus Shear Strain, γ . Comparison Between Values Measured in Sand, and Those Calculated with the Simulated Aggregate and the Simple Cubic Array in Pure Shear.

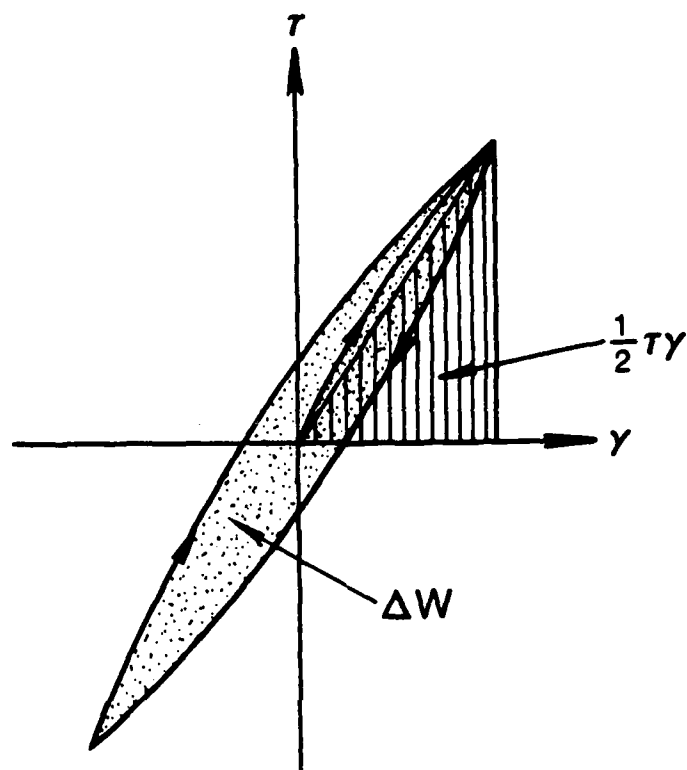


Figure 69. Computation of Damping Ratio, λ , from a Stress-Strain Loop .

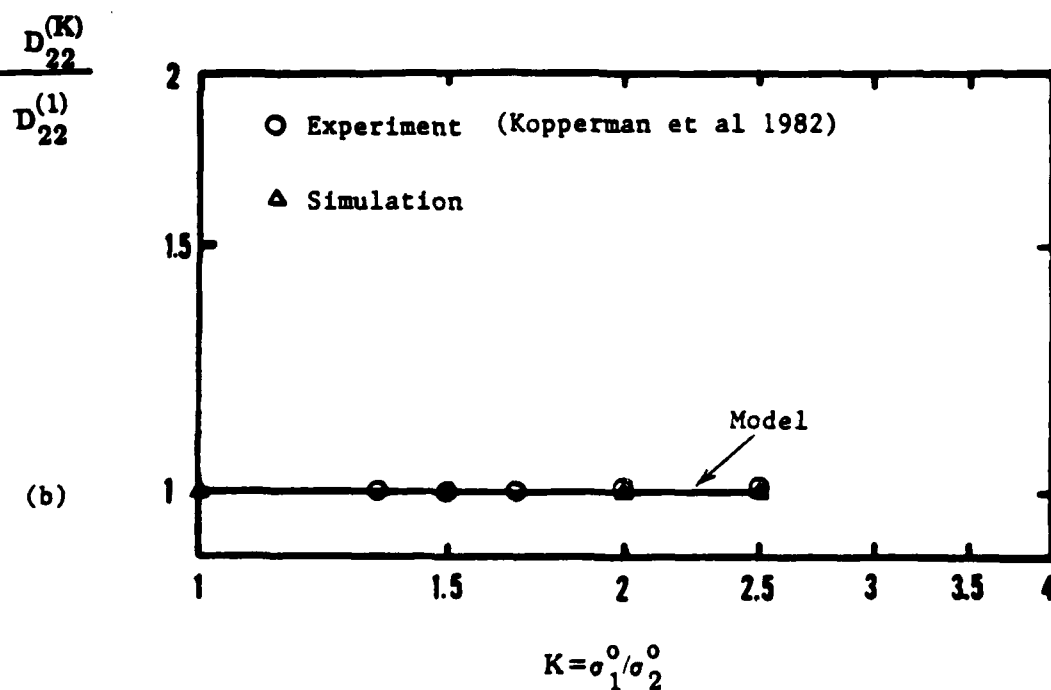
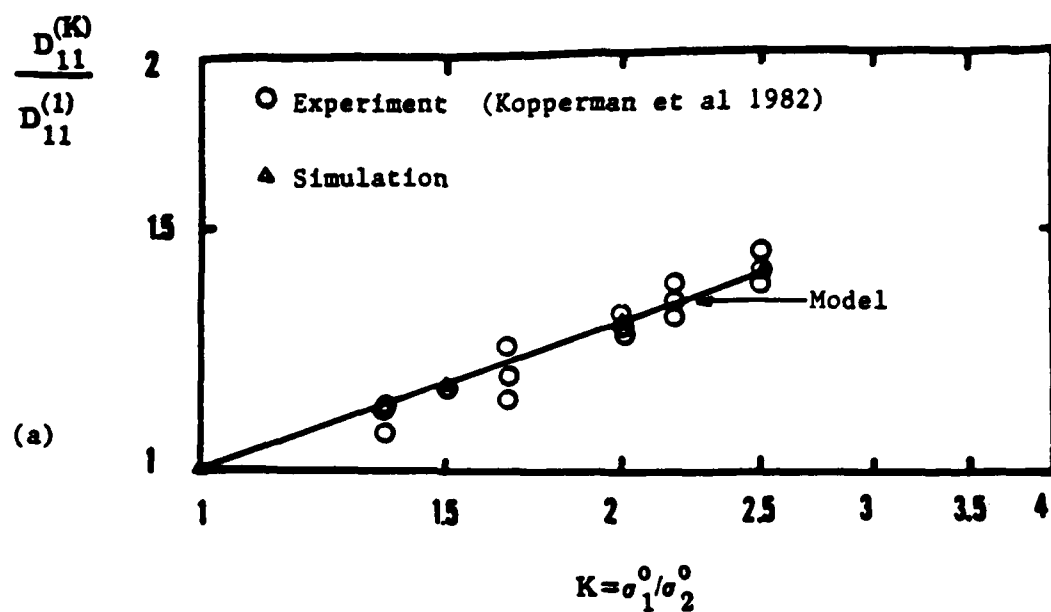


Figure 70. Normalized Constrained Moduli, D_{11}/D_{11} Versus Stress Ratio, $K = \sigma_1^0/\sigma_2^0$. Comparison Between Analytical and Experimental Results. (a) in the Direction of σ_1^0 ; and (b) in the Direction of σ_2^0 (σ_2^0 is kept constant) .

APPENDIX A

Stress-Strain Relations for a
Body Centered Cubic Array

APPENDIX A

STRESS-STRAIN RELATIONS FOR A BODY CENTERED CUBIC ARRAY

Following a procedure similar to that used for the simple cubic array by the authors and by others, incremental stress-strain relations for various states of initial stress can be obtained for the body centered cubic array.

A.1 Relation Between Stress and Contact Forces

Consider first a medium composed of identical spheres, Fig. 25b, arranged in a body centered cubic array. Take as an element of the medium the cube shown in Fig. 25c. This "elementary" cube (or representative volume), Fig. A1, is chosen to contain a sufficient portion of the medium to define the arrangement. Clearly, each sphere in the medium is in contact with 8 other spheres.

Increments of the force dP_{ij} act on the faces of the cube, Fig. A1, and they are assumed to be distributed among the spheres in proportion to their stiffness, that is to their section exposed on the faces of the cube.

The incremental stress components are defined as follows:

$$d\sigma_{ij} = \frac{1}{4} dP_{ij} / \left(\frac{16R^2}{3} \right) \quad (A1)$$

where $\frac{16R^2}{3}$ is the gross area of the face of the cube.

At each contact between spheres, the normal and tangential components of the incremental force are again designated by dN_{ij} ; with dN_{ii} being the normal component and dN_{ij} being two the tangential components.

Once more, the first step in deriving the incremental stress-strain relationships is to define the expressions for the increments in the forces at the contacts between the spheres in the cube, Fig. 25a, dN_{ij} , in terms of the increments of the applied stress $d\sigma_{ij}$. However, since this array is statically determinate for initial isotropic and transversely isotropic triaxial loading, only the equilibrium conditions are sufficient for the solution of this subproblem. However, this case is much more involved than the simple cubic array and tedious calculations have to be performed.

Fig. A2 shows one octant of a sphere at the apex H as well as the point of contact with the "central" sphere and the applied and contact forces. This octant of the sphere at H will be treated as the representative octant. Now equilibrium equations have to be written for each spherical octant at every apex and the contact forces will have to be solved for each case separately. For example for apex H, Fig. A2, the equilibrium equations are:*

$$\sum F_{x_1} = 0 \Rightarrow \frac{1}{\sqrt{3}} dN'_{33} + \frac{1}{\sqrt{2}} dN'_{31} - \frac{1}{\sqrt{6}} dN'_{32} + \frac{1}{4} dP_{11} + \frac{1}{4} dP_{13} + \frac{1}{4} dP_{12} = 0 \quad (A2)$$

$$\sum F_{x_2} = 0 \Rightarrow \frac{1}{\sqrt{3}} dN'_{33} + \frac{2}{\sqrt{6}} dN'_{32} + \frac{1}{4} dP_{22} + \frac{1}{4} dP_{12} + \frac{1}{4} dP_{32} = 0 \quad (A3)$$

* The primed symbols refer to the local coordinate system.

$$\sum F_{x_3} = 0 \Rightarrow \frac{1}{\sqrt{3}} dN'_{33} - \frac{1}{\sqrt{2}} dN'_{31} - \frac{1}{\sqrt{6}} dN'_{32} + \frac{1}{4} dP_{13} + \frac{1}{4} dP_{33} + \frac{1}{4} dP_{23} = 0 \quad (A4)$$

the solution of which is:

$$dN'_{31} = -\frac{\sqrt{2}}{8} (dP_{11} - dP_{33} + dP_{12} - dP_{23}) \quad (A5)$$

$$dN'_{32} = -\frac{\sqrt{6}}{24} (dP_{11} - 2dP_{22} + dP_{33} - dP_{12} + 2dP_{13} - dP_{23}) \quad (A6)$$

$$dN'_{33} = -\frac{\sqrt{3}}{12} (dP_{11} + dP_{22} + dP_{33} + 2dP_{12} + 2dP_{13} + 2dP_{23}) \quad (A7)$$

At this point the state of stress can be defined and the constitutive law may be determined for each case (isotropic or cross-anisotropic triaxial confinement).

A.2 Isotropic State of Stress:

Applying increments of force along the three principal directions, dP_{11} , dP_{22} , dP_{33} and one at a time, on top of the isotropic confining stress, an incremental force-deformation relationship can be developed. For example, in the case of application of dP_{11} (Fig. A1) we have:

$$d\delta_{11} = -\left(\frac{1}{6} C_n + \frac{1}{3} C_t\right) dP_{11} \quad (A8)$$

$$d\delta_{22} = +\frac{1}{6} (C_n - C_t) dP_{11} \quad (A9)$$

$$d\delta_{33} = \frac{1}{6} (C_n - C_t) dP_{11} \quad (A10)$$

where C_n , C_t are the normal and tangential Compliances at the contact.

Similarly applying dP_{22} :

$$d\delta_{11} = \left(\frac{1}{6} C_n - \frac{1}{6} C_t\right) dP_{22} \quad (A11)$$

$$d\delta_{22} = -\left(\frac{1}{6} C_n + \frac{1}{3} C_t\right) dP_{22} \quad (A12)$$

$$d\delta_{33} = \left(\frac{1}{6} C_n - \frac{1}{6} C_t\right) dP_{22} \quad (A13)$$

To determine now the relation between changes in angle and forces we have to look at the difference between displacements (Fig. A1). For example, dP_{12} being applied, we have:

$$d\gamma_{23} = \frac{\delta_{33}|_A - \delta_{33}|_E}{a_{bcc}} + \frac{\delta_{22}|_A - \delta_{22}|_D}{a_{bcc}} \quad \text{etc.} \quad (A14)$$

where a_{bcc} is the length of edge of the cube. Now:

$$\delta_{33}|_A - \delta_{33}|_E = 2\left(-\frac{1}{\sqrt{3}} \delta_{33} + \frac{1}{\sqrt{2}} \delta_{13} + \frac{1}{\sqrt{6}} \delta_{23}\right) \quad (A15)$$

$$\delta_{22}|_A - \delta_{22}|_D = 0 \quad \text{etc.} \quad (A16)$$

Consequently:

$$d\gamma_{12} = \left(\frac{2}{3} C_n + \frac{1}{3} C_t\right) dP_{12} \quad (A17)$$

Evaluating the compliances

$$C_n = \frac{1-\nu_s}{2G_s a_0} \quad \text{which yields}$$

$$C_n = \frac{(1-v_s)^{2/3}}{(4\sqrt{3}G_s^2\sigma_0)^{1/3}} * \frac{1}{R} \quad (A18)$$

Similarly

$$C_t = \frac{2-v_s}{2(1-v_s)^{1/3}} * \frac{1}{(4\sqrt{3}G_s^2\sigma_0)^{1/3}} * \frac{1}{R} \quad (A19)$$

in the case that $v_s \neq 0$

$$d\delta_{11} = \left(\frac{1}{6} C_n + \frac{1}{3} C_t\right) dP_{11}$$

Substituting for C_n , C_t eqns. (A18, A19) we obtain:

$$d\delta_{11} = \frac{1}{6} \frac{(1-v_s)^{2/3}}{(4\sqrt{3}G_s^2\sigma_0)^{1/3}} \frac{1}{R} dP_{11} + \frac{1}{6} \frac{2-v_s}{(1-v_s)^{1/3}} \frac{1}{(4\sqrt{3}G_s^2\sigma_0)^{1/3}} \frac{1}{R} dP_{11} \quad (A20)$$

then:

$$d\epsilon_{11} = \frac{2}{3\sqrt{3}} \frac{1}{(4\sqrt{3}G_s^2\sigma_0)^{1/3}} \left[(1-v_s)^{2/3} + \frac{2-v_s}{(1-v_s)^{1/3}} \right] d\sigma_{11} \quad (A21)$$

$$d\sigma_{11} = \frac{3\sqrt{3} (4\sqrt{3}G_s^2\sigma_0)^{1/3}}{2 \left[(1-v_s)^{2/3} + \frac{2-v_s}{(1-v_s)^{1/3}} \right]} d\epsilon_{11} \quad (A22)$$

Similarly

$$d\epsilon_{22} = \frac{1}{3\sqrt{3}} \frac{1}{(4\sqrt{3}G_s^2\sigma_0)^{1/3}} \left[2(1-v_s)^{2/3} - \frac{2-v_s}{(1-v_s)^{1/3}} \right] d\sigma_{11} \quad (A23)$$

$$d\epsilon_{33} = d\epsilon_{22} \quad (A24)$$

Also from eqns. (A17, A18) and (A19) we have that

$$d\epsilon_{12} = \frac{4}{3\sqrt{3}} \frac{1}{(4\sqrt{3}G_s^2\sigma_0)^{1/3}} \left[(1-\nu_s)^{2/3} + \frac{1}{4} \frac{2-\nu_s}{(1-\nu_s)^{1/3}} \right] d\sigma_{12} \quad (A25)$$

Finally, the incremental stress-strain law for the isotropic case may be written as follows

$$\begin{aligned} d\epsilon_{11} &= C_{1111} d\sigma_{11} + C_{1122} d\sigma_{22} + C_{1133} d\sigma_{33} \\ d\epsilon_{22} &= C_{1122} d\sigma_{11} + C_{2222} d\sigma_{22} + C_{2233} d\sigma_{33} \\ d\epsilon_{33} &= C_{1133} d\sigma_{11} + C_{3322} d\sigma_{22} + C_{3333} d\sigma_{33} \quad \text{etc.} \end{aligned} \quad (A26)$$

where C_{ijkl} are the expressions (compliances) in the stress-strain relations, as for example, in eqn. (A21), (A22). In matrix form

$$\begin{bmatrix} d\epsilon_{11} \\ d\epsilon_{22} \\ d\epsilon_{33} \\ d\epsilon_{12} \\ d\epsilon_{13} \\ d\epsilon_{23} \end{bmatrix} = \begin{bmatrix} C_{1111} & C_{1122} & C_{1133} & 0 & 0 & 0 \\ C_{2211} & C_{2222} & C_{2233} & 0 & 0 & 0 \\ C_{3311} & C_{3322} & C_{3333} & 0 & 0 & 0 \\ 0 & 0 & 0 & C_{1212} & 0 & 0 \\ 0 & 0 & 0 & 0 & C_{1313} & 0 \\ 0 & 0 & 0 & 0 & 0 & C_{2323} \end{bmatrix} \begin{bmatrix} d\sigma_{11} \\ d\sigma_{22} \\ d\sigma_{33} \\ d\sigma_{12} \\ d\sigma_{13} \\ d\sigma_{23} \end{bmatrix} \quad (A27)$$

In order for the bcc array to be isotropic under isotropic loading the following condition must be satisfied:

$$C_{1212} = C_{1313} = C_{2323} = C_{1111} - C_{1122} \quad (A28)$$

$$C_{2211} = C_{1122} = C_{1133} = C_{2233} = C_{3311} = C_{3322} = C_{1122} \quad (A29)$$

The above conditions are satisfied only when $\nu_s = 0$; furthermore, in this case of the bcc array, as in the sc array, $C_{1122} = 0$ and the compliance matrix is diagonal.

In this case:

$$C_{1111} = C_{2222} = C_{3333} = \frac{2}{\sqrt{3}} \left(\frac{1}{4\sqrt{3} G_s^2 \sigma_0} \right)^{1/3} \quad (A30)$$

Since the compliance matrix is diagonal, its inverse, the stiffness matrix is easily computed by inverting each term: i.e.

$$\begin{bmatrix} d\sigma_{11} \\ d\sigma_{22} \\ d\sigma_{33} \\ d\sigma_{12} \\ d\sigma_{13} \\ d\sigma_{23} \end{bmatrix} = \frac{\sqrt{3}}{2} (4\sqrt{3} G_s^2 \sigma_0)^{1/3} \begin{bmatrix} 1 & & & & & \\ & 1 & & & & \\ & & 1 & & & \\ & & & 1 & & \\ & & & & 1 & \\ & & & & & 1 \end{bmatrix} \begin{bmatrix} d\epsilon_{11} \\ d\epsilon_{22} \\ d\epsilon_{33} \\ d\epsilon_{12} \\ d\epsilon_{13} \\ d\epsilon_{23} \end{bmatrix} \quad (A31)$$

and clearly the shear modulus of the array, G , is $G = \frac{\sqrt{3}}{4} (4\sqrt{3} G_s^2 \sigma_0)^{1/3}$ (A32)

At this point the Poisson's Ratio of the bcc array may be computed as follows:

$$\nu_{bcc} = \frac{|\epsilon_{33}|}{|\epsilon_{11}|} = \frac{|\epsilon_{22}|}{|\epsilon_{11}|} \quad (A33)$$

$$\nu_{bcc} = \left| \frac{(1-\nu_s)^{2/3} - \frac{2-\nu_s}{2(1-\nu_s)} \frac{1}{3}}{(1-\nu_s)^{2/3} + \frac{2-\nu_s}{(1-\nu_s)} \frac{1}{3}} \right| \quad (A34)$$

For different values of ν_s , the Poisson's Ratio of the bcc array, ν_{bcc} , may be computed; a plot of ν_{bcc} versus the Poisson's ratio of the spheres, ν_s , appears in Fig. (32) together with the variation of ν_{sc} and ν_{fcc} with ν_s for easy comparison.

A.3 Transversely Isotropic State of Stress (Triaxial Loading)

As in the case of the simple Cubic Array, the application of an anisotropic stress increment will result in a variation of the contact forces and, consequently, of the corresponding contact stiffnesses. Therefore, in order to obtain the stress strain relationships, the derivation must be performed once more distinguishing between compliances at contacts with different loading histories.*

*The computation of the compliances for the case of anisotropic loading for both the sc and the bcc arrays has been done in order for the results to be used only for the special case of wave propagation. This way, the load was assumed to reverse direction, and for this the elastic tangential compliances were used. In the general case, the load could either increase or decrease monotonically and different compliances in each case would apply.

Consider now the case of cross-anisotropic stress ("triaxial test") imposed after the array has been subjected to an initial hydrostatic stress. That is (Fig. A3):

$$\text{at } t = t_0: \sigma_{11} = \sigma_{22} = \sigma_{33} = \sigma_0 \quad (\text{A35})$$

$$t = t_1: \sigma_{11} = \sigma_{33} = \sigma_0 \quad (\text{A36})$$

$$\sigma_{22} = \sigma_0 + \sigma_a \quad (\text{A37})$$

The contact forces during this Anisotropic Loading are:

$$dN'_{31} = \pm \frac{\sqrt{2}}{8} [dP_{11} - dP_{33}] \quad (\text{A38})$$

$$dN'_{32} = \pm \frac{\sqrt{6}}{24} [dP_{11} - 2dP_{22} + dP_{33}] \quad (\text{A39})$$

$$dN'_{33} = \pm \frac{\sqrt{3}}{12} [dP_{11} - dP_{22} + dP_{33}] \quad (\text{A40})$$

in the case of transversely isotropic loading the above equations simplify to

$$dN'_{31} = 0 \quad (\text{A41})$$

$$dN'_{32} = \pm \frac{\sqrt{6}}{12} dP_a \quad (\text{A42})$$

$$dN'_{33} = \pm \frac{\sqrt{3}}{12} dP_a \quad (\text{A43})$$

This is the case of the two spheres in contact where the normal force is increasing from N_0 to $N_0 + N^*$ and the tangential force from 0 to T^* , with

$$\beta = \frac{dT}{dN} > f \text{ (Mindlin and Deresiewicz, 1953)}$$

$$\beta = \frac{dT}{dN} = \frac{dN_{32}}{dN_{33}} = 2 > f \quad (A44)$$

(usually $0.5 \leq f \leq 0.8$ for sands)

in this case the Normal Compliance, C_n , is:

$$C_n = \frac{1-\nu_s}{2G_s a}$$

$$\text{where } a^3 = \frac{3(1-\nu_s)}{8G_s} R(N_o + N) \quad (A45)$$

and finally

$$a^3 = \frac{3(1-\nu_s)}{2G_s} R^3 \sigma_o \left[1 + \frac{1}{3} \left(\frac{\sigma_a}{\sigma_o} \right) \right] \quad (A46)$$

then

$$C_n = \left[\frac{(1-\nu_s)^2}{4\sqrt{3} G 2\sigma_o} \right]^{1/3} \left[1 + \frac{1}{3} \left(\frac{\sigma_a}{\sigma_o} \right) \right]^{-1/3} \frac{1}{R} \quad (A47)$$

The Tangential Compliance, C_t , is:

$$C_t = \frac{2-\nu_s}{4G_s a} \left\{ -\theta + (1+\theta) \left[1 - (1-\theta) \frac{L^* - L}{2(1+\theta L)} \right]^{1/3} \right\} \quad (A48)$$

$$\text{where } \theta = \frac{f}{\beta}, \quad L = \frac{T}{f N_o} \quad \text{and} \quad L^* = \frac{T^*}{f N_o}$$

However, in this case, since the load decrement is small, then $L^* - L \rightarrow 0$,
therefore

$$C_t + \frac{2-\nu_s}{4G_s a} \quad (A49)$$

in this case

$$C_t = \frac{2-\nu_s}{2(1-\nu_s)^{1/3}} \left[\frac{1}{4\sqrt{3} G_s^2 \sigma_0} \right]^{1/3} \left[1 + \frac{1}{3} \left(\frac{\sigma_a}{\sigma_0} \right) \right]^{-1/3} \frac{1}{R} \quad (A50)$$

The constitutive law for this particular loading may be developed in the same manner as in the case of the isotropic loading, i.e.

$$d\delta_{22} = \left[\frac{1}{6} C_n + \frac{1}{3} C_t \right] dP_{22} \quad (A51)$$

finally

$$d\epsilon_{22} = \frac{2}{3\sqrt{3}} \left(\frac{1}{4\sqrt{3} G_s^2 \sigma_0} \right)^{1/3} \left[1 + \frac{1}{3} \left(\frac{\sigma_a}{\sigma_0} \right) \right]^{-1/3} \left[(1-\nu_s)^{2/3} + \frac{2-\nu_s}{(1-\nu_s)^{1/3}} \right] d\sigma_{22} \quad (A52)$$

for $\nu_s = 0$.

$$d\epsilon_{22} = \frac{2}{\sqrt{3}} \left(\frac{1}{4\sqrt{3} G_s^2 \sigma_0} \right)^{1/3} \left[1 + \frac{1}{3} \left(\frac{\sigma_a}{\sigma_0} \right) \right]^{-1/3} d\sigma_{22} \quad (A53)$$

in the case of isotropic loading and $\nu_s = 0$, the above reduces to

$$d\epsilon_{22} = \frac{2}{\sqrt{3}} \left(\frac{1}{4\sqrt{3} G_s^2 \sigma_0} \right)^{1/3} d\sigma_{22} \quad (A54)$$

which is the same obtained before, eqn. (A30). Analogously

$$d\epsilon_{11} = \frac{-2}{\sqrt{3}} \left(\frac{1}{4\sqrt{3} G_s^2 \sigma_0} \right)^{1/3} \left[1 + \frac{1}{3} \left(\frac{\sigma_a}{\sigma_0} \right) \right]^{-1/3} \left[(1-\nu_s)^{2/3} - \frac{2-\nu_s}{2(1-\nu_s)^{1/3}} \right] d\sigma_{22} \quad (A55)$$

For $\nu_s = 0$ this reduces to zero.

The Shear Compliance is computed as follows:

$$d\delta_{ij} = \left[\frac{2}{3} C_n + \frac{1}{3} C_t \right] dP_{ij} \quad (A56)$$

$$d\epsilon_{ij} = \frac{2}{3\sqrt{3}} \left(\frac{1}{4\sqrt{3} G_s^2 \sigma_0} \right)^{1/3} \left[1 + \frac{1}{3} \left(\frac{\sigma_a}{\sigma_0} \right) \right]^{-1/3} \left[4(1-\nu_s)^{2/3} + \frac{2-\nu_s}{2(1-\nu_s)^{1/3}} \right] d\sigma_{ij} \quad (A57)$$

For $\nu_s = 0$ this reduces to

$$d\epsilon_{ij} = \frac{2}{3\sqrt{3}} \left(\frac{1}{4\sqrt{3} G_s^2 \sigma_0} \right)^{1/3} \left[1 + \frac{1}{3} \left(\frac{\sigma_a}{\sigma_0} \right) \right]^{-1/3} d\sigma_{ij} \quad (A58)$$

For $\sigma_a = 0$ this reduces to eqn. (A31). Therefore, for the case of $\nu_s \neq 0$

$$C_{1111} = C_{2222} = C_{3333} = \frac{2}{3\sqrt{3}} \left(\frac{1}{4\sqrt{3} G_s^2 \sigma_0} \right)^{1/3} \left[1 + \frac{1}{3} \left(\frac{\sigma_a}{\sigma_0} \right) \right]^{-1/3} * \quad (A59)$$

$$* \left[(1-\nu_s)^{2/3} + \frac{2-\nu_s}{(1-\nu_s)^{1/3}} \right]$$

$$C_{1122} = C_{2233} = C_{3311} = \frac{-2}{\sqrt{3}} \left(\frac{1}{4\sqrt{3} G_s^2 \sigma_0} \right)^{1/3} \left[1 + \frac{1}{3} \left(\frac{\sigma_a}{\sigma_0} \right) \right]^{-1/3} * \\ * \left[(1-\nu_s)^{2/3} - \frac{2-\nu_s}{2(1-\nu_s)^{1/3}} \right] \quad (A60)$$

$$C_{1212} = C_{1313} = C_{2323} = \frac{1}{3\sqrt{3}} \left(\frac{1}{4\sqrt{3} G_s^2 \sigma_0} \right)^{1/3} \left[1 + \frac{1}{3} \left(\frac{\sigma_a}{\sigma_0} \right) \right]^{-1/3} * \\ * \left[4(1-\nu_s)^{2/3} + \frac{2-\nu_s}{(1-\nu_s)^{1/3}} \right] \quad (A61)$$

In this case the material will be isotropic under cross anisotropic loading only if in the compliance matrix

$$C_{1111} - C_{1122} = C_{1212}$$

Performing the calculations we see that indeed,

$$C_{1111} - C_{1122} = \frac{1}{3\sqrt{3}} \left(\frac{1}{4\sqrt{3} G_s^2 \sigma_0} \right)^{1/3} \left[1 + \frac{1}{3} \left(\frac{\sigma_a}{\sigma_0} \right) \right]^{-1/3} \left[4(1-\nu_s)^{2/3} + \frac{2-\nu_s}{(1-\nu_s)^{1/3}} \right] = C_{1212}$$

Therefore, the bcc array is isotropic under cross anisotropic loading*; this is a serious deficiency of the model and should be attributed to the symmetry of the array.

In the case that $\nu_s = 0$, the array is still isotropic but this time the compliance matrix is again diagonal:

*for the conditions specified previously.

$$\begin{bmatrix} d\epsilon_{11} \\ d\epsilon_{22} \\ d\epsilon_{33} \\ d\epsilon_{12} \\ d\epsilon_{13} \\ d\epsilon_{23} \end{bmatrix} = \frac{2}{\sqrt{3}} \left(\frac{1}{(4\sqrt{3} G^2 \sigma_0)} \right)^{1/3} \left[1 + \frac{1}{3} \left(\frac{\sigma_a}{\sigma_0} \right) \right]^{-1/3} \begin{bmatrix} 1 & 0 & 0 & 0 & 0 & 0 \\ & 1 & 0 & 0 & 0 & 0 \\ & & 1 & 0 & 0 & 0 \\ & & & 1 & 0 & 0 \\ & & & & 1 & 0 \\ & & & & & 1 \end{bmatrix} \begin{bmatrix} d\sigma_{11} \\ d\sigma_{22} \\ d\sigma_{33} \\ d\sigma_{12} \\ d\sigma_{13} \\ d\sigma_{23} \end{bmatrix}$$

(A62)

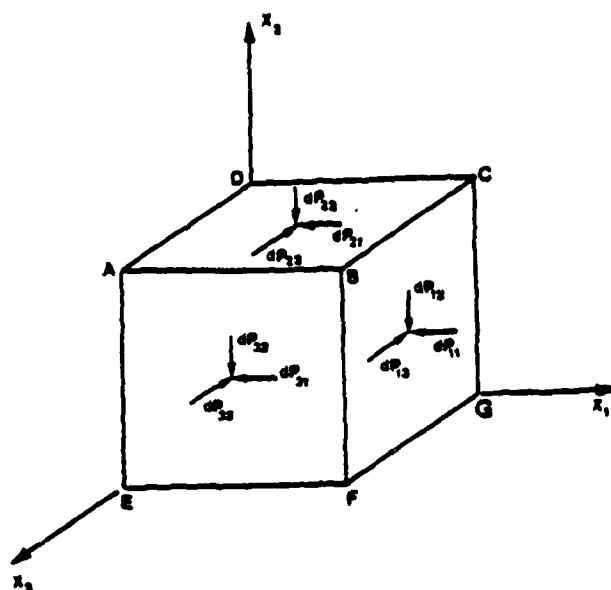


Figure A1. Representative Unit Volume and Applied Incremental Forces.

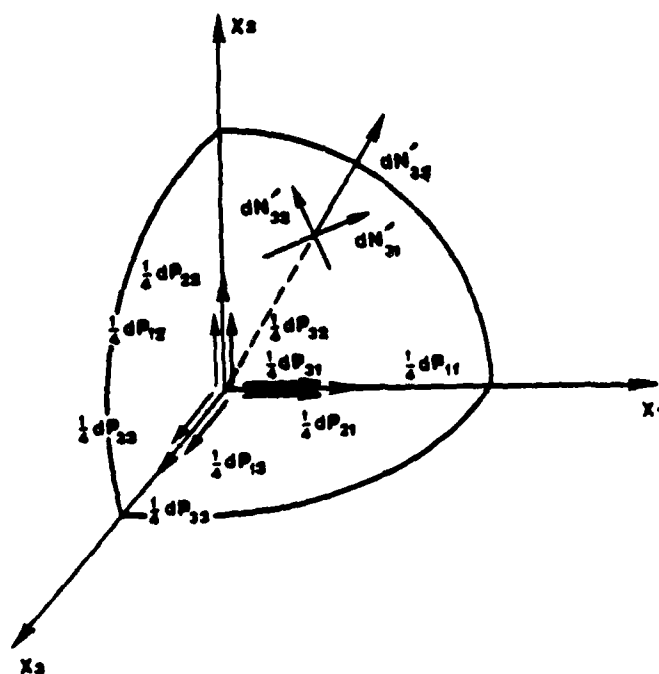


Figure A2. Octant of Sphere with Center at Apex H of the Representative Unit Volume of a bcc Array, with Applied and Contact Forces Shown.

APPENDIX B

Simulation of Triaxial and Pure Shear Loading
in Cubic Arrays

APPENDIX B

SIMULATION OF TRIAXIAL AND PURE SHEAR LOADING IN CUBIC ARRAYS

The three regular cubic arrays will be subjected to a finite loading in such a way so as to cause failure when applied along a principal direction. In the case of the simple cubic array, this corresponds to a pure shear loading, since for a triaxial loading the array locks. Conversely, the body centered cubic and the face centered cubic array will be subjected only to a triaxial loading, since for a pure shear loading the array also lock.

In order to obtain a finite stress strain relation in every case, the compliances need to be integrated along the loading path. Once this is done, finite displacements are computed and then the strains are obtained in the same manner as in the infinitesimal constitutive laws.

Finally, the load is increased until failure (gross sliding) occurs in the array; in the statically determinate arrays gross sliding at a contact translates into failure of the cubic array. In the statically indeterminate face centered cubic (fcc) array, the medium does not fail immediately, but first the number of contacts reduces from 12 to 8 when the fcc array becomes statically determinate, and then sliding at one contact becomes failure.

B.1 The Simple Cubic Array Subjected to Pure Shear Loading

Consider the Simple Cubic Array shown in Fig. 17 and consider a force T acting in the x_1 direction (Fig. A1). The s.c. array is subjected to an initial isotropic force N_0 and the value of T increases monotonically

from zero to T^* , where T^* is the value of T that causes failure in the array, while N_0 remains constant. In this case the tangential displacement is given by Mindlin (1949):

$$\delta = \frac{3(2-\nu_s)}{8G_s a} f N_0 \left[1 - \left(1 - \frac{T}{f N_0} \right)^{2/3} \right] \quad (B1)$$

$$\text{where } a^3 = \frac{3(1-\nu_s)N_0 R}{8G_s}$$

is the radius of contact.

Now $\gamma = \delta/R$; substituting the expression for a^3 into eqn. (B1) and after transforming the forces into stresses we obtain:

$$\gamma = \frac{3(2-\nu_s)}{(1-\nu_s)^{1/3}} * f \left[\frac{\sigma_0^2}{12G_s^2} \right]^{1/3} * \left[1 - \left(1 - \frac{\tau}{f \sigma_0} \right)^{2/3} \right] \quad (B2)$$

The above equation has been plotted in Fig. 28 for different values of σ_0 and f ; obviously failure occurs when

$$\tau^* = f \sigma_0 \quad (B3)$$

and at this point the value of the strain is*

$$\gamma_f = \gamma_t = \frac{3(2-\nu_s)}{(1-\nu_s)^{1/3}} * f \left(\frac{\sigma_0^2}{12G_s^2} \right)^{1/3} \quad (B4)$$

Substituting the properties of quartz (Table 3) in eqn. (B4) we obtain

$$\gamma_t = 4.5 \times 10^{-3} (\sigma_0)^{2/3} \quad (B5)$$

with σ_0 in psi.

* The value of $\nu_s = 0.15$ used here was obtained from White (1964) and other sources, and is different from $\nu_s = 0.31$ used in a previous report (Dobry et al., 1982). The value $\nu_s = 0.15$ is more representative of quartz; as a result, the values of the threshold strain γ_f computed using Eq. A66 and $\nu_s = 0.15$ are slightly different from those originally obtained by Dobry et al. (1982).

B.2 The Body Centered Cubic Array Subjected to Triaxial Loading

Consider the bcc array shown in Fig. 25, initially subjected to an isotropic stress σ_0 and consider an additional force P_a acting in the x_2 direction, Fig. A1). The bcc array is subjected to an initial isotropic stress σ_0 and the stress σ_{22} is increased monotonically from σ_0 to a value $\sigma_0 + \sigma_a$, at which sliding occurs in the array. In this case, the loading path is as follows

$$\text{at } t = t_0 \quad P_{11} = P_{22} = P_{33} = P_0 \quad (\text{B6})$$

$$\text{at } t = t_1 \quad P_{11} = P_{33} = P_0 \quad (\text{B7})$$

$$P_{22} = P_0 + P_a \quad (\text{B8})$$

The contact forces are (eqns, A5, A6, A7)

$$dN'_{31} = \pm \frac{\sqrt{2}}{8} [dP_{11} - dP_{33}] = 0 \quad (\text{B9})$$

$$dN'_{32} = \pm \frac{\sqrt{6}}{24} [dP_{11} - 2dP_{22} + dP_{33}] = \frac{\sqrt{6}}{12} dP_a \quad (\text{B10})$$

$$dN'_{33} = \pm \frac{\sqrt{3}}{12} [dP_{11} + dP_{22} + dP_{33}] = \frac{\sqrt{3}}{12} dP_a \quad (\text{B11})$$

and the ratio between the increment of the tangential force and the increment of the normal force, β , is

$$\beta = \frac{dT}{dN} = \frac{dN'_{32}}{dN'_{33}} = \sqrt{2} \quad (\text{B12})$$

In this case $\beta > f$, the coefficient of interparticle friction, therefore the values of the compliances are: (Mindlin and Deresiewicz, 1953)

a) Normal Compliance, C_n

$$C_n = \frac{1-\nu_s}{2G_{sa}} \quad (\text{B13})$$

this expression for C_n being valid no matter what the loading history of the spheres is. Now

$$a = a_0 (1 + \theta L)^{1/3} \quad (B14)$$

where

$$a_0 = \frac{3(1-\nu_s)}{8G_s} N_0 R = \frac{3(1-\nu_s)}{8G_s} \frac{3}{4} P_0 * R \quad (B15)$$

Also $\theta = \frac{f}{\beta}$

$$L = \frac{T}{fN_0}$$

The vertical displacement, δ_{22} , has two components; a δ'_{33} and a δ'_{23} component:

$$\delta_{22} = \frac{2}{3} \delta'_{33} + \frac{2}{6} \delta'_{23} \quad (B16)$$

the δ'_{33} component is computed as follows:

$$C_n = \frac{d\delta'_{33}}{dN} = \frac{1-\nu_s}{2G_s a_0} (1 + \theta L)^{-1/3} \quad (B17)$$

$$\frac{d\delta'_{33}}{dN} = \frac{1-\nu_s}{2G_s a_0} \left(1 + \frac{f}{\beta} \frac{\beta N}{fN_0}\right)^{-1/3} \quad (B18)$$

$$\delta'_{33} = \int_0^N \frac{1-\nu_s}{2G_s a_0} \left[1 + \frac{N}{N_0}\right]^{-1/3} dN \quad (B19)$$

finally

$$\delta'_{33} = 2\sqrt{3} R(1-\nu_s)^{2/3} \left(\frac{\sigma_o^2}{4\sqrt{3}G_s^2} \right)^{1/3} \left[\left(1 + \frac{1}{3} \frac{\sigma_a}{\sigma_o} \right)^{2/3} - 1 \right] \quad (B20)$$

The δ'_{23} component will be computed from the tangential compliance since it is a tangential displacement; the tangential compliance is (Mindlin and Deresiewicz, 1953):

$$C_t = \frac{2-\nu_s}{4G_s a} \left[\theta + (1-\theta) \left(1 - \frac{L}{1+\theta L} \right)^{-1/3} \right] \quad (B21)$$

Simplifying:

$$C_t = \frac{2-\nu_s}{4G_s a} \frac{1}{(1+\theta L)^{1/3}} \left[\theta + (1-\theta) \left(1 - \frac{L}{1+\theta L} \right)^{-1/3} \right] \quad (B22)$$

and finally

$$C_t = \frac{2-\nu_s}{4G_s a} * \frac{\theta}{\left(1 + \theta \frac{T}{T_o} \right)^{1/3}} + \frac{2-\nu_s}{4G_s a} (1-\theta) \left(1 + \frac{T}{T_o} (\theta-1) \right)^{-1/3} \quad (B23)$$

now

$$\frac{d\delta'_{23}}{dT} = C_{t_o} \theta \left(1 + \theta \frac{T}{T_o} \right)^{-1/3} + C_{t_o} (1-\theta) \left(1 + \frac{T}{T_o} (\theta-1) \right)^{-1/3} \quad (B24)$$

where

$$C_{t_o} = \frac{2-\nu_s}{4G_s a_o}$$

Now

$$\delta'_{23} = \int_0^T T_0 C_{t_0} \theta \left(1 + \theta \frac{T}{T_0}\right)^{-1/3} dT + C_{t_0} T_0 (1 - \theta) \left[1 + (\theta - 1) \frac{T}{T_0}\right]^{-1/3} \frac{dT}{T_0} \quad (B25)$$

finally

$$\delta'_{23} = \frac{3}{2} \left(\frac{2 - \nu_s}{4 G_s a_0}\right) f N_0 \left\{ \left[\left(1 + \frac{T}{8 N_0}\right)^{2/3} - 1 \right] - \left[\left(1 + \left(\frac{f}{8} - 1\right) \frac{T}{f N_0}\right)^{2/3} - 1 \right] \right\} \quad (B26)$$

Simplifying further and expressing the displacement in terms of stresses we obtain:

$$\delta'_{23} = \sqrt{3} f R \frac{2 - \nu_s}{(1 - \nu_s)^{1/3}} \left[\frac{\sigma_o^2}{4 \sqrt{3} G_s^2} \right]^{1/3} \left\{ \left[\left(1 + \frac{\sqrt{2} \sigma_a}{3 \sigma_o}\right)^{2/3} - 1 \right] - \left[\left(1 + \left(\frac{f}{8} - 1\right) \frac{\sqrt{2} \sigma_a}{3 f \sigma_o}\right)^{2/3} - 1 \right] \right\} \quad (B27)$$

In order to compute the vertical displacement of the array, δ_{22} , we have to substitute equations (B20) and (B27) into eqn. (B16):

$$\begin{aligned} \delta_{22} &= \frac{2}{\sqrt{3}} \delta'_{33} + \frac{2}{\sqrt{6}} \delta'_{23} \quad (B28) \\ \delta_{22} &= 4R(1 - \nu_s)^{2/3} \left(\frac{\sigma_o^2}{4 \sqrt{3} G_s^2} \right)^{1/3} \left[\left(1 + \frac{1}{3} \frac{\sigma_a}{\sigma_o}\right)^{2/3} - 1 \right] + \\ &+ \sqrt{6} f R \frac{2 - \nu_s}{(1 - \nu_s)^{1/3}} \left(\frac{\sigma_o^2}{4 \sqrt{3} G_s^2} \right)^{1/3} \left\{ \left[\left(1 + \frac{\sqrt{2} \sigma_a}{3 \sigma_o}\right)^{2/3} - 1 \right] - \left[\left(1 + \left(\frac{f}{8} - 1\right) \frac{\sqrt{2} \sigma_a}{3 f \sigma_o}\right)^{2/3} - 1 \right] \right\} \quad (B29) \end{aligned}$$

From the above equation, (B29), the stress-strain relation may be computed for the bcc array under isotropic loading, and it is:

$$\epsilon_{22} = \left(\frac{\sigma_0^2}{4\sqrt{3} G_s^2} \right)^{1/3} \{ \sqrt{3}(1-\nu_s)^{2/3} \left[\left(1 + \frac{1}{3} \frac{\sigma_a}{\sigma_0} \right)^{2/3} - 1 \right] + \frac{3\sqrt{2}}{4} f \frac{2-\nu_s}{(1-\nu_s)^{1/3}} * \right.$$

$$* \left. \left[\left(1 + \frac{\sqrt{2}\sigma_a}{3\beta\sigma_0} \right)^{2/3} - 1 \right] \left[\left(1 + \left(\frac{f}{\beta} - 1 \right) \frac{\sqrt{2}\sigma_a}{3f\sigma_0} \right)^{2/3} - 1 \right] \right\} \quad (B30)$$

The above equation is plotted in Fig. 3/a for various values of σ_0 and f . At this point, the value of σ_a/σ_0 which causes failure in the array must be determined. Failure is defined as sliding at the contacts; this time, since the bcc array is statically determinate, failure in one contact implies failure of the array. Furthermore, because of the symmetry of the array, failure will occur simultaneously at all contacts. Sliding will occur when

$$\frac{T}{N_0 + N} = f \quad (B31)$$

We know that

$$T = \frac{\sqrt{6}}{12} A \sigma_a \quad (B32)$$

$$N = \frac{\sqrt{3}}{12} A \sigma_a \quad (B33)$$

$$N_0 = \frac{\sqrt{3}}{4} A \sigma_0 \quad (B34)$$

where A is the area of the face of the bcc array. Then:

$$T = f(N_0 + N) \quad (B35)$$

$$\frac{\sqrt{6}}{12} A \sigma_{22} = f \left(\frac{\sqrt{3}}{12} A \sigma_a + \frac{\sqrt{3}}{4} A \sigma_o \right) \quad (B36)$$

$$\frac{\sqrt{2}}{3} \sigma_{22} = f \left(\frac{1}{3} \sigma_a + \sigma_o \right) \quad (B37)$$

$$\frac{\sigma_{22}}{\sigma_o} \left[\frac{\sqrt{2}}{3} - \frac{f}{3} \right] = f \quad (B38)$$

and finally, σ_a/σ_o at failure, $(\sigma_a/\sigma_o)_t$ is

$$\left(\frac{\sigma_a}{\sigma_o} \right)_f = \frac{3f}{2-f} \quad (B39)$$

If $\sigma_{22} = \sigma_o + \sigma_a$ (total stress), then

$$\left(\frac{\sigma_{22}}{\sigma_o} \right)_f = \frac{f}{\frac{\sqrt{2}}{3} - \frac{f}{3}} + 1 \quad (B40)$$

in terms of total stress (Fig. 24)

In order to compute the strain at failure, ϵ_{22f} , we must substitute the equation for $(\sigma_{22}/\sigma_o)_f$, eqn. (B39) into the stress-strain relation, eqn. (B30). Doing this we obtain

$$\epsilon_{22f} = \left(\frac{\sigma_o^2}{4\sqrt{3} G_s^2} \right)^{1/3} \{ 3(1-\nu_s)^{2/3} \left[\left(1 + \frac{f}{\sqrt{2}-f} \right)^{2/3} - 1 \right] + \frac{3\sqrt{2}}{4} f \frac{2-\nu_s}{(1-\nu_s)^{1/3}} \}^* \quad (B41)$$

$$* \left[\left[\left(1 + \frac{f}{\sqrt{2}-f} \right)^{2/3} - 1 \right] - \left[1 + \left(\frac{f}{3} - 1 \right) \frac{\sqrt{2}}{\sqrt{2}-f} \right]^{2/3} - 1 \right]$$

for the properties of quartz (Lambe and Whitman, 1964, Ko and Scott, 1967, White, 1964)

$$G_s = 4.783 \times 10^6 \text{ psi}$$

$$\nu_s = 0.15$$

$$f = 0.5$$

the strain at failure is

$$\epsilon_{22_f} = 3.438 \times 10^{-3} \sigma_o^{2/3} \text{ (in percent)} \quad (\text{B42})$$

with ϵ_{22_f} in percent and σ_o in psi,

$$\text{and } \gamma_t = \epsilon_{22_f} \text{ for } \nu_s = 0,$$

which is the threshold strain γ_t for the array. This equation is plotted in Fig. 27 together with the other expressions for γ_t for the other arrays for easy comparison.

B.3 The Face Centered Cubic Array Subjected to Triaxial Loading

The triaxial loading of a Face Centered Cubic Array was solved by Brauns and Leussink (1970). In this work, the stress-strain relationship is not obtained for the whole range of values of σ_{22}/σ_o but only for those which make the array statically determinate. It is extremely hard to determine the values of compliances for cross anisotropic loading (Duffy and Mindlin, 1957); therefore once sliding occurs and the number of contacts decreases from 12 to 8, the array becomes statically determinate and it is possible to compute a stress-strain relation up to the point which the array fails (range b -Fig. B2). Once the array has failed, simple geometric considerations make the computation over the

strain range c possible (Fig. B2).

Consider the fcc array in Fig. Bla and the cross anisotropic loading as shown. The free body diagram of the octant of sphere A is shown in Fig. Blb. The equilibrium conditions yield

$$N + T = \sqrt{2} R^2 \sigma_1 \quad (B43)$$

$$N - T + N_1 = 2\sqrt{2} R^2 \sigma_3 \quad (B44)$$

Also, the sum of the displacements around a closed path must vanish (Duffy and Mindlin, 1957), which yields

$$a_1 - a + \delta = 0 \quad (B45)$$

The normal compliance is found to be

$$C_n = \frac{da}{dN} = \frac{1-v_s}{[3(1-v_s)G_s^2 R N]^1/3} \quad (B46)$$

and the Tangential Compliance

$$C_t = \frac{d\delta}{dT} = \frac{2-v_s}{2[3(1-v_s)G_s^2 R N]^1/3} * \left[f \frac{dN}{dT} - \frac{1 - f \frac{dN}{dT}}{[1 - \frac{T}{fN}]^1/3} \right] \quad (B47)$$

The strain is

$$\epsilon_{11} = \frac{1}{2R} (a + \delta) \quad (B48)$$

Integrating the compliances and substituting the results into eqn. (B48), we find after transforming the forces into stresses that the strain, ϵ_{11} , is given by

$$\epsilon_{11} = \left[\frac{3\sqrt{2}(1-\nu_s)}{8G_s} \right]^{2/3} * \left\{ 2 \left[\frac{1}{1+f} \left(\frac{\sigma_{11}}{\sigma_{33}} \right) \right]^{2/3} - \left[2 - \frac{1-f}{1+f} \left(\frac{\sigma_{11}}{\sigma_{33}} \right) \right]^{2/3} - 1 \right\} \sigma_{33}^{2/3} \quad (\text{B49})$$

this expression being valid only for the range of $(\sigma_{11}/\sigma_{33})$ in which the array is statically determinate, that is 8 contacts per sphere (range b in Fig. B1).

Failure is defined again as sliding, but this time when the whole array fails, that is when the number of contacts from 8 reduces to none.

Using the same criteria as in the other arrays, the critical stress ratio at which the array fails is

$$\left(\frac{\sigma_{11}}{\sigma_{33}} \right)_f = 2 \frac{1+f}{1-f} \quad (\text{B50})$$

The above equation is plotted in Fig. 3lb.

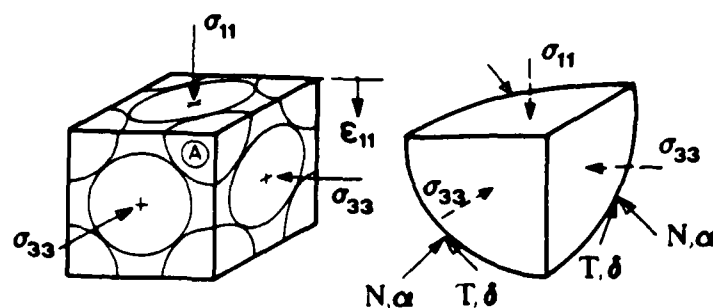


Figure B1. (a) Representative Unit Volume of an fcc Array with State of Stress (b) Sphere Centered at Apex A with Applied Stresses, Contact Forces and Displacements (Brauns and Leussink, 1970) .

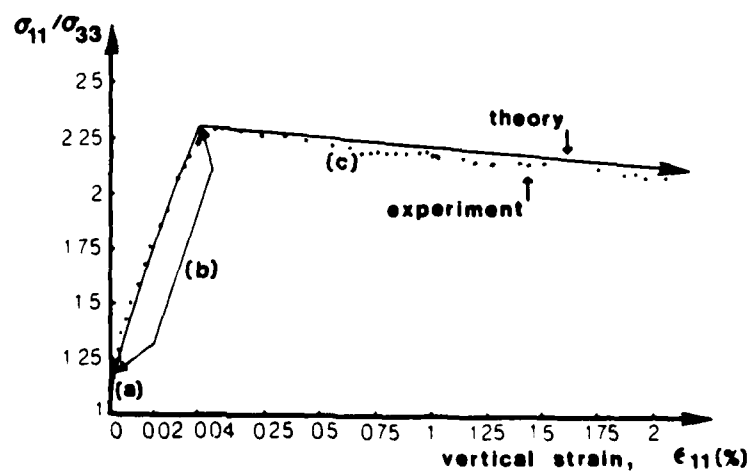


Figure B2. Triaxial Compression of an fcc Array of Glass Spheres: Analytical and Experimental Results (Brauns and Leussink, 1970) .

APPENDIX C

Program Listing of the Constitutive Law
for the Simple Cubic Array

```

C
C SUBROUTINE UMAT TO BE USED WITH THE FINITE ELEMENT PROGRAM
C ABAQUS
C *****
C
C SUBROUTINE UMAT(I,STRESS,DDSDDE,STRAN,DSTRAN,NDI,NSHR,NTENS,M)
C   IMPLICIT REAL*8(A-H,O-Z)
C   COMMON/BMATRL/GI,Z,UN,SR,DEBUG
C   COMMON/BHIST/AHIST(1,3004)
C   LOGICAL FLAG1,FLAG2,DEBUG
C   DIMENSION STRESS(NTENS),DDSDDE(NTENS,NTENS),STRAN(NTENS)
C   DIMENSION DSTRAN(NTENS),DSIGMA(4)
C   AREA=4.*SR*SR
C   DO 141 J1=1,4
C     DO 142 J2=1,4
C       DDSDDE(J1,J2)=0.D0
142 CONTINUE
141 CONTINUE
C
C CHANGE COMPRESSION INTO POSITIVE
C
C   DO 143 J3=1,3
C     STRESS(J3)=-STRESS(J3)
C     STRAN(J3)=-STRAN(J3)
C     DSTRAN(J3)=-DSTRAN(J3)
143 CONTINUE
C
C TRANSFORM STRESSES TO FORCES
C
C   TN11=STRESS(1)*AREA
C   TN22=STRESS(2)*AREA
C   TN33=STRESS(3)*AREA
C   T12=STRESS(4)*AREA
C
C COMPUTE CURRENT TOTAL NORMAL DISPLACEMENTS FROM STRAINS
C
C   DEL11=(STRAN(1)+DSTRAN(1))*2.*SR
C   DEL22=(STRAN(2)+DSTRAN(2))*2.*SR
C
C COMPUTE THE INCREMENTAL SHEAR DISPLACEMENT FROM STRAINS
C
C   DDEL12=2.*DSTRAN(4)*SR
C
C COMPUTE NORMAL FORCES AND INCREMENTS
C
C   CALL NORMAD(DEL11,TN11,TNNA,DTNA)
C   CALL NORMAD(DEL22,TN22,TNNB,DTNB)
C
C TRANSFORM FORCES TO STRESSES
C
C   DSIGMA(1)=DTNA/AREA
C   DSIGMA(2)=DTNB/AREA
C   DSIGMA(3)=0.
C
C   TOL=1.E-16
C   EPSL=1.E-16
C   ITMAX=500
C   DEYA=0.D0

```

```

DEYB=0.D0
DTYA=0.D0
ID1=1
ID2=1503
C
C
C   COMPUTE SEED FOR THE ITERATION,
C
C   IF (DSTRAN(4) .EQ. 0.) THEN
C     DEXA=0.
C     DEXB=0.
C     ITER=0
C     DTXA=0.
C     DTXB=0.
C     GO TO 1167
C   ENDIF
C
C   IF((TNNA-TNNB) .EQ. 0.) THEN
C     WRITE(3,1375)TNNA,TNNB
1375  FORMAT('TNNA-TNNB',1X,F10.6,2X,F10.6)
C     DEXA=DDEL12/2.D0
C     DEXB=DDEL12/2.D0
C     GO TO 1169
C   ELSE
C     DEXA=DDEL12/2.D0
C     DEXB=DDEL12/2.D0
C   ENDIF
C   IF((TNNA-TNNB) .GT. 0.) GO TO 1311
C
C
C   BEGIN ITERATION B
C
C     CALL CONPLD(M,ID2,TNNB,DTNB,DEXTB,DEYB,DTXB,DTYT,IDEXB)
C
C   GIVEN THE SHEAR STRAIN ITERATE TO FIND THE COMMON SHEAR FORCE
C
C   DO 1166 ITER=1,ITMAX
C     DTYB=0.D0
C     CALL CONPLF(M,ID2,TNNB,DTNB,DTXB,DTYB,DEXB,DEYB,INDEXB)
C     DEXA=DDEL12-DEXB
C     CALL CONPLD(M,ID1,TNNA,DTNA,DEXA,DEYA,DTXA,DTYA,IDEXA)
C     IF(DABS(DTXA-DTXB) .LT. TOL) GO TO 1167
C     DTXB=(DTXA+DTXB)/2.D0
1166  CONTINUE
C
C   IF( ITER .GE. ITMAX .AND. IDEXA .EQ. 1) THEN
C     DTXB=0.0
C     DTXA=0.0
C     DEXB=0.0
C     DEXA=DDEL12
C     ITER=ITMAX
C     GO TO 1167
C   ENDIF
C
C   IF( ITER .GE. ITMAX .AND. INDEXB .EQ. 1) THEN
C     DTXB=0.0
C     DTXA=0.0
C     DEXB=DDEL12
C     DEXA=0.0
C     ITER=ITMAX
C     GO TO 1167
C   ENDIF

```

```

      WRITE(3,1954)I
1954 FORMAT('WELL ITER WAS ITMAX BUT IDEX WAS NOT',IX,I5)
C
1311 CONTINUE
C
C      BEGIN ITERATION A
C
      CALL CONPLD(M, ID1, TNNA, DTNA, DEXA, DEYA, DTXA, DTT, IDET)
C
C      GIVEN THE SHEAR STRAIN ITERATE TO FIND THE COMMON SHEAR FORCE
C
      DO 1168 ITER=1, ITMAX
      DTYA=0.D0
      CALL CONPLF(M, ID1, TNNA, DTNA, DTXA, DTYA, DEXA, DEYA, IDEXA)
      DEXB=DDEL12-DEXA
      CALL CONPLD(M, ID2, TNNB, DTNB, DEXB, DEYB, DTXB, DTYB, IDEXB)
      IF(DABS(DTXA-DTXB) .LT. TOL) GO TO 1167
      DTXA=(DTXA+DTXB)/2.D0
1168 CONTINUE
C
      IF( ITER .GE. ITMAX .AND. IDEXA .EQ. 1) THEN
      DTXB=0.0
      DTXA=0.0
      DEXB=0.0
      DEXA=DDEL12
      ITER=ITMAX
      GO TO 1167
      ENDIF
C
      IF( ITER .GE. ITMAX .AND. IDEXB .EQ. 1) THEN
      DTXB=0.0
      DTXA=0.0
      DEXB=DDEL12
      DEXA=0.0
      ITER=ITMAX
      GO TO 1167
      ENDIF
C
1167 CONTINUE
      WRITE(1,1111)I, ITER, DEXA, DEXB, DTXA, DTXB
1111 FORMAT(2I5, 1X, F10.8, 1X, F10.8, 1X, F10.8, 1X, F10.8)
C
C      UPDATE CONTACT HISTORY AND STORE INTO AHIST
C
1169 CONTINUE
      CALL CONPD(M, ID1, TNNA, DTNA, DEXA, DEYA, DTXA, DTYA, IDEX1)
      CALL CONPD(M, ID2, TNNB, DTNB, DEXB, DEYB, DTXB, DTYB, IDEX2)
C
      DTXM=(DTXA+DTXB)/2.D0
      DSIGMA(4)=DTXM/AREA
      WRITE(6,1863)DSIGMA(4)
1863 FORMAT(F20.10)
C
C      COMPUTATION OF THE INCREMENTAL STIFFNESS MATRIX, STIFF
C
      AB=3.D0*(1.D0-UN)/(8.D0*GI)
      ABA=(AB*TNNA*SR)**(1./3.)
      ABB=(AB*TNNB*SR)**(1./3.)
      DDSDE(1,1)=2.D0*GI*(AB*TNNA*SR)**(1./3.)/(1.D0-UN)
      DDSDE(2,2)=2.D0*GI*(AB*TNNB*SR)**(1./3.)/(1.D0-UN)

```

```

      DDSDD(3,3)=1.D0
      IF (DSTRAN(4) .EQ. 0.) THEN
        DDSDD(4,4)=1.D0
      ELSE
        DDSDD(4,4)=DSIGMA(4)/DSTRAN(4)
      ENDIF
      IF (DDSDD(4,4) .LE. EPSL) DDSDD(4,4)=EPSL
C
C   UPDATE STRESS VECTOR
C
      STRESS(1)=STRESS(1)+DSIGMA(1)
      STRESS(2)=STRESS(2)+DSIGMA(2)
      STRESS(3)=0.D0
      STRESS(4)=STRESS(4)+DSIGMA(4)
C
C   CHANGE COMPRESSION INTO NEGATIVE
C
      STRESS(1)=-STRESS(1)
      STRESS(2)=-STRESS(2)
C
      RETURN
      END
C
C   SUBROUTINE CONPD(M,IAD1,TNN,DTN,DEX,DEY,DTX,DTY,IDEX)
      IMPLICIT REAL*8(A-H,O-Z)
      COMMON/BMATRL/GI,2,UN,SR,DEBUG
      COMMON/BHIST/AHIST(1,3004)
      DIMENSION KK1(100),KK2(100),HH1(100),HHS(100),VVX(100),
        $VVY(100),TTXS(100),TTYS(100),TTXI(100),TTYI(100),AAXS(100),
        $AAYS(100),AAXI(100),AAYI(100),IC(100)
      LOGICAL FLAG1,FLAG2,DEBUG
C*****
C  -----INITIALIZATION-----
C*****
      IDEX=0
      IN=IAD1
      DEBUG=.FALSE.
      NG=IDINT(AHIST(M,IAD1))
      DTX=0.
      DTY=0.
      NGROUP=100
C
C   PREVIOUS NORMAL FORCE, TN1
C
      TN1=TNN-DTN
C
C   MAKE SURE THERE IS A CONTACT; FOR THIS, THE NORMAL FORCE HAS TO
C   BE POSITIVE--IDEX=2 MEANS THAT THERE IS NO CONTACT
C
      IF (TNN.GT.0) GO TO 9827
      IDEX=2
      RETURN
9827 IF (NG.NE.0) GOTO 9820
C
C   CALL THE ELASTIC MODULUS OF THE CURRENT NORMAL FORCE
C
      CALL EMOD(TNN,H0)
      TX=H0*DEX
      TY=H0*DEY

```

```

      TM=DSQRT(TX*TX+TY*TY)
      DTM=TM
      IF(DTM.EQ.0.) GOTO 9840
      IF (TM .GE. Z*TNN) THEN
        INDEX=1
        TX=TX*Z*TNN/TM
        TY=TY*Z*TNN/TM
        TM=Z*TNN
      ENDIF
      DTX=TX
      DTY=TY

C----- INITIALIZE THE NEW CONTACT HISTORY -----
C
9840 NG=1
C
C      INITIAL GROUP CHARACTERISTICS
C-----MODULI AND SIZES-----
C
      HHS(1)=H0
      HHI(1)=0.
      XKKS(1)=Z*TNN
      XKKI(1)=0.

C----- INITIAL SURFACE POSITIONS -----
C      COORDINATES OF CENTRES OF MAX BOUNDARY YIELD CIRCLE
C
      AAXS(1)=0.
      AAYS(1)=0.

C      COORDIANATES OF CENTRES OF MIN BOUNDARY YIELD CIRCLE
C
      AAXI(1)=TX
      AAYI(1)=TY

C-----INITIALE REFERENCE POINTS-----
C
      TTXS(1)=0.
      TTYS(1)=0.
      TTXI(1)=TX
      TTYI(1)=TY

C-----KIND OF INITIAL GROUP-----
C
      IF(INDEX .EQ. 0) THEN
C----- NO SLIDE -----
C
        IC(1)=0
        VVX(1)=1.
        VVY(1)=1.
        VX=1.
        VY=1.
        GO TO 9910
      ELSE
C----- SLIDE OCCURS -----
C
        IC(1)=1
        VVX(1)=TX/TM

```



```

VVI(1)=TY/TM
TTXS(1)=TX
TTYS(1)=TY
IDEX=1
GO TO 9910
ENDIF

C
C--- BEGIN CALCULATION WITH THE OLD CONTACT
C
9820 DEM=DSQRT(DEX*DEX+DEY*DEY)
C
C-- CHECK IF THE MEMORY IS ENOUGH
C
    IF(NG.LT.NGROUP) GO TO 9790
    IDEX=4
    RETURN

C
C - GET THE HISTORY OF THE CONTACT FROM THE MEMORY
C
9790 CONTINUE
    DDTN=AHIST(M,IAD1+1)
    DO 9810 I=1,NG
        IAD2=IAD1+I+1
        XKKI(I)=AHIST(M,IAD2)
        XKKS(I)=AHIST(M,IAD2+NGROUP)
        HHI(I)=AHIST(M,IAD2+2*NGROUP)
        HHS(I)=AHIST(M,IAD2+3*NGROUP)
        VVI(I)=AHIST(M,IAD2+4*NGROUP)
        VVY(I)=AHIST(M,IAD2+5*NGROUP)
        TTXS(I)=AHIST(M,IAD2+6*NGROUP)
        TTYS(I)=AHIST(M,IAD2+7*NGROUP)
        TTXI(I)=AHIST(M,IAD2+8*NGROUP)
        TTYI(I)=AHIST(M,IAD2+9*NGROUP)
        AAXS(I)=AHIST(M,IAD2+10*NGROUP)
        AAYS(I)=AHIST(M,IAD2+11*NGROUP)
        AAXI(I)=AHIST(M,IAD2+12*NGROUP)
        AAYI(I)=AHIST(M,IAD2+13*NGROUP)
9810 IC(I)=IDINT(AHIST(M,IAD2+14*NGROUP))
        TX=TTXI(NG)
        TY=TTYI(NG)

C
C -----END OF INITIAL REFERENCE POINTS-----
C
    IF(DEM.EQ.0.) GOTO 9900

C
C-----UPDATING PARAMETER BEFORE INCREMENT-----
C
    HSL=HHS(NG)
    HIL=HHI(NG)
    IF(HIL.LE.0.) HIL=HSL
    XKL=XKKS(NG)
    IF(TN1.GT.0.) CALL ELAD(XKL,TN1,EML)
    HML=0.D0
    IF(EML.NE.0.) HML=XKL/EML
    NGL=NG

C
C----- CALCULATE THE CORRECT FORCE INCREMENT -----
C
    DTX=HSL*DEX
    DTY=HSL*DEY

```

```

DTM=HSL*DEM
C
C*****
C-----UNIT NORMAL VECTOR-----
C*****
C
  IF(IC(NGL).EQ.0 .OR. DTM .GT. 0.) THEN
    VX=DEX/DEM
    VY=DEY/DEM
    ELSE
    VX=VVX(NGL)
    VY=VVY(NGL)
    VKL=VK
    VKL=VK
    ENDIF
    DBN=DTX*VX+DTY*VY
    DBT=DABS(DTX*VY-DTY*VX)
C
C  FIND THE CORRESPONDING FORCE
C
  IF(DBN.LE.Z*DTN) GOTO 9900
  IF(IC(NGL).EQ.0) THEN
    DTM=(DEM+Z*DTN*(1./HIL-1./HSL))*HIL
    ELSE IF(HML.EQ.0.) THEN
    DTM=DEM*(DEM+Z*DTN*(1./HIL-1./HSL))*HIL/(DEX*VX+DEY*VY)
    ELSE
    DTM=DEM*(DEM+Z*DTN*(1./HIL-1./HSL))/((DEX*VX+DEY*VY)/HIL
    $      +DABS(DEX*VY-DEY*VX)/HML)
    ENDIF
    DTX=DEX*DABS(DTM)/DEM
    DTY=DEY*DABS(DTM)/DEM
    DBN=DTX*VX+DTY*VY
    DBT=DABS(DTX*VY-DTY*VX)
9900 TN=TNN
    TX=TX+DTX
    TY=TY+DTY
    TM=DSQRT(TX*TX+TY*TY)
C
C-----UPDATING FORCE INCREMENT-----
C
    TNL=TN
    TXL=TX
    TYL=TY
C
C-----CURRENT ELASTIC MODULUS-----
C
    CALL EMOD(TN,H0)
C
C-----CHECK IF THERE IS FAILURE-----
C
    IF(TM.LT.Z*TN) GO TO 800
    IDEX=1
    TX=TX*Z*TN/TM
    TY=TY*Z*TN/TM
    TM=Z*TN
    DTX=TX-TTXI(NG)
    DTY=TY-TTYI(NG)
    GOTO 9840
C
C-----UPDATE THE SIZES-----

```

```

C
800 DO 211 IG=1,NG
C
C----- RADIUS OF YIELD CIRCLES OF GROUP (IG) -----
C
      XKRI(IG)=XKRI(IG)+Z*DTN
      XKRS(IG)=XKRS(IG)+Z*DTN
C
C--- THIS IS TO MAKE SURE THAT NO MODULUS IS LARGER THAN H0 --
C
      IF(XKRS(IG).LT.0.) XKRS(IG)=0.
211  IF(XKRI(IG).LT.0.) XKRI(IG)=0.
C
C-----FIX THE SIZE (RADIUS) OF THE FAILURE SURFACE-----
C
      XKRS(1)=Z*TN
C
C-----UPDATING THE MODULI-----
C
      DO 215 IG=1,NG
      HHI(IG)=((1.-(XKRS(IG))/(Z*TN))**(1./3.))*H0
      HHS(IG)=((1.-(XKRI(IG))/(Z*TN))**(1./3.))*H0
215  CONTINUE
C
      G=-(TTYI(NGL)-TTYS(NGL))*DTX+(TTXI(NGL)-TTXS(NGL))*DTY
      G=-DDTN*DTX+(TTXI(NGL)-TTXS(NGL))*DTN
C
C-----UPDATE REFERENCE POINT WHEN IC=1-----
C
      DO 213 IG=1,NG
      IF(IC(IG).EQ.0) GO TO 213
      TTXS(IG)=TTXS(IG)+Z*DTN*VVX(IG)
      TTYS(IG)=TTYS(IG)+Z*DTN*VVY(IG)
      TTXI(IG)=TTXI(IG)+Z*DTN*VVX(IG)
      TTYI(IG)=TTYI(IG)+Z*DTN*VVY(IG)
213  CONTINUE
      IF (DTN) 849, 850, 851
849  IF (TX.EQ.0..AND. TY.EQ.0..AND. DTM.EQ.0.
$.AND. IC(NG).EQ.0..AND. XKRS(NG).GT.0.) THEN
      XK=XKRS(NG)
      H=H0*(1.-XK/(Z*TN))**(1./3.)
      AX=AAXS(NG)
      AY=AAYS(NG)
      ICI=0
      GOTO 60
      ENDIF
      GO TO 272
850  IF (DEM.EQ.0.)RETURN
      GO TO 272
851  IF (ABS(DBN).LT. Z*DTN) THEN
      IF (IC(NG).EQ.0..AND. G.EQ.0.) THEN
      XK=XKRS(NG)
      H=H0*(1.-XK/(Z*TN))**(1./3.)
      AX=AAXS(NG)
      AY=AAYS(NG)
      ICI=0
      GO TO 60
      ENDIF
      GO TO 273
      ENDIF
      IF (IC(NG).EQ.1..AND. DBN.EQ. Z*DTN) THEN
      XK=XKRS(NG)

```

```

H=H0*(1.-XK/(Z*TN))**(1./3.)
AX=AAXS(NG)
AY=AAYS(NG)
ICI=1
GO TO 60
ENDIF
GO TO 272
C-----A NEW ELASTIC GROUP IS CREATED-----
C-----"NG"IS INCREASED TO "NG+1"-----
C
273 CONTINUE
NG=NG+1
XK=Z*DTN
H=((1.-DTN/TN))**(1./3.))*H0
AX=AAXI(NG-1)
AY=AAZI(NG-1)
ICI=0
GO TO 60
C
C-----TO WHICH REFERENCE GROUP DOES THE FORCE POINT BELONG-----
C----- THIS IS THE SUBROUTINE SEARCH OF THE ORIGINAL PROGRAM -----
C
272 IG=0
NG=NGL
276 IG=IG+1
IF(IG.GT.NG)GOTO 273
TAXS=TX-AAXS(IG)
TAYS=TY-AAYS(IG)
RS=DSQRT(TAXS*TAXS+TAYS*TAYS)
IF(RS.GT.XKKS(IG)) GO TO 99
TAXI=TX-AAZI(IG)
TAYI=TY-AAZI(IG)
RI=DSQRT(TAXI*TAXI+TAYI*TAYI)
IF(DEBUG) WRITE(11,1234) IG,TX,TY,RS,XKKS(IG),RI,XKKI(IG)
1234 FORMAT(2X,'IG',5X,'TX',10X,'TY',10X,'RS',9X,'XKKS',9X,
. 'RI',5X,'XKKI',/15,6E12.4)
IF(XKKI(IG).GT.RI) GO TO 276
C
C-----APPROXIMATE LOADING MODULUS AND NUMBER OF-----
C-----YIELD SURFACES AFTER A LOAD INCREMENT-----
C
99 CONTINUE
NG=IG
IF(DTN.LT.0.AND.NG.NE.1.AND.IC(NGL).EQ.0.AND.G.EQ.0.)GOTO 9910
IF(IC(NG).EQ.1) THEN
C
C----- THE FORCE POINT FALLS INSIDE A GROUP OF THE SECOND KIND
C
XK=0.
TEMP11=-2.*((TX-TTXS(NG))*VVX(NG)+(TY-TTYS(NG))*VVY(NG))
IF(TEMP11.NE.0.) XK=((TX-TTXS(NG))*(TX-TTXS(NG))
$ +(TY-TTYS(NG))*(TY-TTYS(NG)))/TEMP11
ELSE
C
C----- THE FORCE POINT FALLS INSIDE A GROUP OF THE FIRST KIND
C
AA1=(TX-TTXS(NG))*(TX-TTXS(NG))+(TY-TTYS(NG))*(TY-TTYS(NG))
AA2=(TTXS(NG)-TTXI(NG))*(TTXS(NG)-TTXI(NG))
$ +(TTYS(NG)-TTYI(NG))*(TTYS(NG)-TTYI(NG))
AA3=(TTXS(NG)-TTXI(NG))*(TTXS(NG)-TTXI(NG))

```

```

$   +(TTYS(NG)-TTYI(NG))*(TTYS(NG)-TTYI(NG))
ALPH=AA3/(XKKS(NG)*XKKS(NG))-1.
BETA=(AA3+AA2)/XKKS(NG)
GAMA=AA1+AA2+AA2+AA3
IF(ALPH.NE.0.) GOTO 900
XK=0.
IF(BETA.NE.0.) XK=GAMA/(2.*BETA)
GOTO 901
900 XK=(BETA-DSQRT(BETA*BETA-ALPH*GAMA))/ALPH
ENDIF
901 IF(.NOT.DEBUG) GOTO 902
WRITE(11,134) XK,TTXS(NG),TTYS(NG),TTXI(NG),TTYI(NG),
$      VVX(NG),VVY(NG)
134 FORMAT(5X,'XK',9X,'TTXS',8X,'TTYS',8X,'TTXI',8X,'TTYI',
$      8X,'VVX',8X,'VVY',/7E12.5)
$   IF(IC(NG).EQ.0.) WRITE(11,135) AA1,AA2,AA3,ALPH,BETA,GAMA
135 FORMAT(5X,'AA1',9X,'AA2',9X,'AA3',8X,'ALPH',8X,'BETA',8X,'GAMA',
$      /6E12.5)
902 IF(XK.GE.0.AND.XK.LE.2*TN) GOTO 119
WRITE(11,134) XK,TTXS(NG),TTYS(NG),TTXI(NG),TTYI(NG),
$      VVX(NG),VVY(NG)
$   IF(IC(NG).EQ.0.) WRITE(11,135) AA1,AA2,AA3,ALPH,BETA,GAMA
INDEX=3
RETURN

C
C-----FINAL PARAMETERS-----
C
119 ICI=1
H=H0*(1-XK/(2*TN))**(1./3.)
IF(IC(NG).EQ.1) THEN
AX=TTXS(NG)-XK*VVX(NG)
AY=TTYS(NG)-XK*VVY(NG)
ELSE
AA4=(H*H*H-HHI(NG)*HHI(NG)*HHI(NG))
$   /(H0*H0*H0-HHI(NG)*HHI(NG)*HHI(NG))
AX=TTXS(NG)+(TTXI(NG)-TTXS(NG))*AA4
AY=TTYS(NG)+(TTYI(NG)-TTYS(NG))*AA4
ENDIF

C
C   FINAL PARAMETERS
C

C
C-----OUTWARD NORMAL UNIT VECTOR WHEN XK=0.-----
C
IF(XK.EQ.0.) THEN
VX=VVX(NG)
VY=VVY(NG)
DTM=DSQRT(DTX*DTX+DTY*DTY)
IF (TTXI(NG) .EQ. TX .AND. TTYI(NG) .EQ. TY .OR. DTM .EQ. 0)
$ GOTO 555
VX=DTX/DTM
VY=DTY/DTM

C
C WHEN THE LOADING IS ALONG THE CONE AND NORMAL FORCE DECREASE
C
ELSE

C
C-----OUTWARD NORMAL UNIT VECTOR WHEN R(=XK) IS DIF FROM 0.
C

```

```

VX=(TX-AX)/XK
VY=(TY-AY)/YK
ENDIF
555 IF(DEBUG)WRITE(11,197)IN,VX,VY,XK,H
197 FORMAT(3X,'IN',6X,'VX',10X,'VY',10X,'XK',8X,'H',/15,4E12.4)
C
C-----GROUP NUMBER OF THE CURRENTLY ACTIVATED -----
C-----YIELD SURFACE IS "NG+1"-----
C
NG=NG+1
C
C-----CONTINUITY OF SIZE-----
C
XKXI(NG-1)=XK
HHS(NG-1)=H
C
C COORDINATES OF CENTER OF YIELD CIRCLE OF MIN RADIUS(INFERIOR)
C
AAXI(NG-1)=AX
AAZI(NG-1)=AZ
C
C-----UPDATE FOR THE REFERENCE POINT-----
C
IF(IC(NG-1).EQ.1) GO TO 60
TTXI(NG-1)=AX
TTYI(NG-1)=AZ
AAZI(NG-1)=AZ
AAZI(NG-1)=AZ
C
C-----UPDATING THE CONFIGURATION OF THE -----
C-----YIELD SURFACES-----
C
60 CONTINUE
XKKS(NG)=XK
XKXI(NG)=0.
HHS(NG)=H0
HHI(NG)=H
AAKS(NG)=AX
AAZI(NG)=AZ
AAZI(NG)=TX
AAZI(NG)=TY
TTXS(NG)=TX
TTYS(NG)=TY
TTXI(NG)=TX
TTYI(NG)=TY
VVX(NG)=VX
VVY(NG)=VY
IC(NG)=ICI
IF(ICI.EQ.0) TTXS(NG)=AX
IF(ICI.EQ.0) TTYS(NG)=A
9910 DO 109 IG=1,NG
IF(DEBUG)WRITE(13,124)IN,IG,HHS(IG),HHI(IG),XKKS(IG),
1XKXI(IG),IC(IG)
109 IF(DEBUG)WRITE(15,124)IN,IG,AAKS(IG),AAZI(IG),AAZI(IG),
1AAZI(IG),IC(IG)
IF(DEBUG)WRITE(13,7)
IF(DEBUG)WRITE(15,7)
124 FORMAT(1X,2I5,4E12.4,15)
115 FORMAT(1X,2I5,2F12.4,15)

```

```

7  FORMAT(1X,'-----',
1,'-----')

```

```

C
C----- UPDATE THE HISTORY BEFORE LEAVING THE SUBROUTINE -----
C

```

```

      AHIST(M,IAD1)=DFLOAT(NG)
      AHIST(M,IAD1+1)=DTN
      DO 9960 I=1,NG
      IAD2=IAD1+I+1
      AHIST(M,IAD2)=XKKI(I)
      AHIST(M,IAD2+NGROUP)=XKKS(I)
      AHIST(M,IAD2+2*NGROUP)=HHI(I)
      AHIST(M,IAD2+3*NGROUP)=HHS(I)
      AHIST(M,IAD2+4*NGROUP)=VVX(I)
      AHIST(M,IAD2+5*NGROUP)=VVY(I)
      AHIST(M,IAD2+6*NGROUP)=TTXS(I)
      AHIST(M,IAD2+7*NGROUP)=TTYS(I)
      AHIST(M,IAD2+8*NGROUP)=TTXI(I)
      AHIST(M,IAD2+9*NGROUP)=TTYI(I)
      AHIST(M,IAD2+10*NGROUP)=AAKS(I)
      AHIST(M,IAD2+11*NGROUP)=AAYS(I)
      AHIST(M,IAD2+12*NGROUP)=AAXI(I)
      AHIST(M,IAD2+13*NGROUP)=AAYI(I)
9960 AHIST(M,IAD2+14*NGROUP)=DFLOAT(IC(I))
      RETURN

```

```

C-----OTHER FORMATS-----
333  FORMAT(15,7E12.4)
      END

```

```

C
C
C

```

```

      SUBROUTINE EMOD(TNP,H0)

```

```

C
C MATERIAL DEPENDENT SUBROUTINE COMPUTES THE ELASTIC
C MODULUS CORRESPONDING TO A GIVEN TN
C

```

```

      IMPLICIT REAL*8(A-H,O-Z)
      COMMON/BMATRL/GI,Z,UN,SR,DEBUG
      LOGICAL FLAG1,FLAG2,DEBUG
      AS=((3.*(1.-UN)*TNP*SR)/(8.*GI))*(.1./3.)
      H0=(4.*GI*AS)/(2.-UN)
      RETURN
      END

```

```

      SUBROUTINE ELAD(X,P,DI)

```

```

C
C MATERIAL DEPENDENT SUBROUTINE COMPUTES THE ELASTIC
C MODULUS CORRESPONDING TO A GIVEN TN
C

```

```

      IMPLICIT REAL*8(A-H,O-Z)
      COMMON/BMATRL/GI,Z,UN,SR,DEBUG
      LOGICAL FLAG1,FLAG2,DEBUG
      AS=((3.*(1.-UN)*P*SR)/(8.*GI))*(.1./3.)
      DI=((3.*Z*P*(2.-UN)*((1.-((1.-X/(Z*P))*(1.-X/(Z*P))))*(.1./3.)))/(8.*GI*AS)
      RETURN
      END

```

```

C
C

```

```

      SUBROUTINE NORMAD(EN,TN1,TNN,DTN)

```

```
9827 IF(NG,NE,0) GOTO 9820
```

```

C CALL THE ELASTIC MODULUS OF THE CURRENT NORMAL FORCE
C CALL EMOD(TNN,H0)

```



```

TX=H0*DEX
TY=H0*DEY
TM=DSQRT(TX*TX+TY*TY)
DTM=TM
IF(DTM.EQ.0.) GOTO 9840
IF(TM.GE.Z*TNN) THEN
  IDEX=1
  TX=TX*Z*TNN/TM
  TY=TY*Z*TNN/TM
  TM=Z*TNN
ENDIF
DTE=TX
DTY=TY
C
C----- INITIALIZE THE NEW CONTACT HISTORY -----
C
9840 NG=1
C
C      INITIAL GROUP CHARACTERISTICS
C-----MODULI AND SIZES-----
C
  HHS(1)=H0
  HHI(1)=0.
  XKKS(1)=Z*TNN
  XKKI(1)=0.
C
C----- INITIAL SURFACE POSITIONS -----
C
  COORDINATES OF CENTRES OF MAX BOUNDARY YIELD CIRCLE
C
  AAXS(1)=0.
  AAYS(1)=0.
C
  COORDIANATES OF CENTRES OF MIN BOUNDARY YIELD CIRCLE
C
  AAXI(1)=TX
  AAYI(1)=TY
C
C-----INITIALE REFERENCE POINTS-----
C
  TTXS(1)=0.
  TTYS(1)=0.
  TTXI(1)=TX
  TTYI(1)=TY
C
C-----KIND OF INITIAL GROUP-----
C
  IF(IDEX .EQ. 0) THEN
C----- NO SLIDE -----
C
    IC(1)=0
    VVX(1)=1.
    VVY(1)=1.
    VX=1.
    VY=1.
    GO TO 9910
  ELSE
C
C----- SLIDE OCCURS -----
C

```

```

      IC(1)=1
      VVX(1)=TX/TM
      VVY(1)=TY/TM
      TTXS(1)=TX
      TTYS(1)=TY
      IDEX=1
      GO TO 9910
      ENDIF
C
C--- BEGIN CALCULATION WITH THE OLD CONTACT
C
9820 DEM=DSQRT(DEX*DEX+DEY*DEY)
C
C-- CHECK IF THE MEMORY IS ENOUGH-----
C
      IF(NG.LT.NGROUP) GO TO 9790
      IDEX=4
      RETURN
C
C - GET THE HISTORY OF THE CONTACT FROM THE MEMORY
C
9790 CONTINUE
      DDTN=AHIST(M,IAD1+1)
      DO 9810 I=1,NG
      IAD2=IAD1+I+1
      XKKI(I)=AHIST(M,IAD2)
      XKKS(I)=AHIST(M,IAD2+NGROUP)
      HHI(I)=AHIST(M,IAD2+2*NGROUP)
      HHS(I)=AHIST(M,IAD2+3*NGROUP)
      VVX(I)=AHIST(M,IAD2+4*NGROUP)
      VVY(I)=AHIST(M,IAD2+5*NGROUP)
      TTXS(I)=AHIST(M,IAD2+6*NGROUP)
      TTYS(I)=AHIST(M,IAD2+7*NGROUP)
      TTXI(I)=AHIST(M,IAD2+8*NGROUP)
      TTYI(I)=AHIST(M,IAD2+9*NGROUP)
      AAXS(I)=AHIST(M,IAD2+10*NGROUP)
      AAYS(I)=AHIST(M,IAD2+11*NGROUP)
      AAXI(I)=AHIST(M,IAD2+12*NGROUP)
      AAYI(I)=AHIST(M,IAD2+13*NGROUP)
9810 IC(I)=IDINT(AHIST(M,IAD2+14*NGROUP))
      TX=TTXI(NG)
      TY=TTYI(NG)
C
C -----END OF INITIAL REFERENCE POINTS-----
C
      IF(DEM.EQ.0.) GOTO 9900
C
C-----UPDATING PARAMETER BEFORE INCREMENT-----
C
      HSL=HHS(NG)
      HIL=HHI(NG)
      IF(HIL.LE.0.) HIL=HSL
      XKL=XKKS(NG)
      IF(TN1.GT.0.) CALL ELAD(XKL,TN1,EML)
      HML=0.D0
      IF(EML.NE.0.) HML=XKL/EML
      NGL=NG
C
C----- CALCULATE THE CORRECT FORCE INCREMENT -----
C

```

```

DTX=HSL*DEX
DTY=HSL*DEY
DTM=HSL*DEM
C
C*****
C-----UNIT NORMAL VECTOR-----
C*****
C
  IF(IC(NGL).EQ.0) THEN
    VX=DEX/DEM
    VY=DEY/DEM
  ELSE
    VX=VVX(NGL)
    VY=VVY(NGL)
    VKL=VX
    VKL=VY
  ENDIF
  DBN=DTX*VX+DTY*VY
  DBT=DABS(DTX*VY-DTY*VX)
C
C  FIND THE CORRESPONDING FORCE
C
  IF(DBN.LE.2*DTN) GOTO 9900
  IF(IC(NGL).EQ.0) THEN
    DTM=(DEM+2*DTN*(1./HIL-1./HSL))*HIL
  ELSE IF(HML.EQ.0.) THEN
    DTM=DEM*(DEM+2*DTN*(1./HIL-1./HSL))*HIL/(DEX*VX+DEY*VY)
  ELSE
    DTM=DEM*(DEM+2*DTN*(1./HIL-1./HSL))/((DEX*VX+DEY*VY)/HIL
    $      +DABS(DEX*VY-DEY*VX)/HML)
  ENDIF
  DTX=DEX*DABS(DTM)/DEM
  DTY=DEY*DABS(DTM)/DEM
  DBN=DTX*VX+DTY*VY
  DBT=DABS(DTX*VY-DTY*VX)
9900  TN=TN
      TX=TX+DTX
      TY=TY+DTY
      TM=DSQRT(TX*TX+TY*TY)
C
C-----UPDATING FORCE INCREMENT-----
C
  TNL=TN
  TXL=TX
  TYL=TY
C
C-----CHECK IF THERE IS FAILURE-----
C
  IF(TM.LT.2*TN) GO TO 9910
  IDEX=1
  TX=TX*2*TN/TM
  TY=TY*2*TN/TM
  TM=2*TN
  DTX=TX-TTXI(NG)
  DTY=TY-TTYI(NG)
  GOTO 9840
C
9910  CONTINUE
      RETURN
      END

```



```

      HHS(1)=H0
      HHI(1)=0.
      XKKS(1)=2*TNM
      XKKI(1)=0.
C ----- INITIAL YIELD SURFACE CENTERS -----
C      COORDINATES OF CENTRES OF MAX BOUNDARY YIELD CIRCLE
      AAKS(1)=0.
      AAYS(1)=0.
C      COORDIANATES OF CENTRES OF MIN BOUNDARY YIELD CIRCLE
      AAXI(1)=TX
      AAYI(1)=TY
C-----INITIAL REFERENCE POINTS -----
      TTXS(1)=0.
      TTYS(1)=0.
      TTXI(1)=TX
      TTYI(1)=TY
C-----KIND OF INITIAL GROUP -----
      IF(INDEX.EQ. 0) THEN
C----- NO SLIDE -----
      IC(1)=0
      VVX(1)=1.
      VVY(1)=1.
      VX=1.
      VY=1.
      GO TO 9910
      ELSE
C----- SLIDE OCCURS -----
      IC(1)=1
      VVX(1)=TX/TM
      VVY(1)=TY/TM
      TTXS(1)=TX
      TTYS(1)=TY
      INDEX=1
      GO TO 9910
      ENDIF
C----- CALCULATION BEGIN WITH OLD CONTACT -----
C9820 DEM=DSQRT(DEX*DEX+DEY*DEY)
9820 CONTINUE
C
C----- STOP WHEN THE MEMORY IS NOT ENOUGH -----
C
      IF(NG.LT.NGROUP) GO TO 9789
      WRITE(3,8101) NG
8101 FORMAT('THE MEMORY OF THE YIELD SURFACE IS NOT ENOUGH',I4)
      STOP
C
C      GET THE CONTACT HISTORY FROM MEMORY
C
9789 CONTINUE
      DDTN=AHIST(M,IAD1+1)
      DO 9810 I=1,NG
      IAD2=IAD1+I+1
      XKKI(I)=AHIST(M,IAD2)
      XKKS(I)=AHIST(M,IAD2+NGROUP)
      HHI(I)=AHIST(M,IAD2+2*NGROUP)
      HHS(I)=AHIST(M,IAD2+3*NGROUP)
      VVX(I)=AHIST(M,IAD2+4*NGROUP)
      VVY(I)=AHIST(M,IAD2+5*NGROUP)
      TTXS(I)=AHIST(M,IAD2+6*NGROUP)
      TTYS(I)=AHIST(M,IAD2+7*NGROUP)

```

```

      TTZI(I)=AHIST(M,IAD2+8*NGROUP)
      TTYI(I)=AHIST(M,IAD2+9*NGROUP)
      AAIS(I)=AHIST(M,IAD2+10*NGROUP)
      AAYS(I)=AHIST(M,IAD2+11*NGROUP)
      AAXI(I)=AHIST(M,IAD2+12*NGROUP)
      AAYI(I)=AHIST(M,IAD2+13*NGROUP)
      IC(I)=IDINT(AHIST(M,IAD2+14*NGROUP))
9810  CONTINUE
      TX=TTZI(NG)
      TY=TTYI(NG)

C
C-----UPDATING PARAMETER BEFORE INCREMENT-----
C
      HSL=HHS(NG)
      HIL=HHI(NG)
      IF(HIL.LE.0.) HIL=HSL
      XKL=XKRS(NG)
      IF(TN1.GT.0.) CALL ELAD(XKL,TN1,EML)
      HML=0.D0
      IF(EML.NE.0.) HML=XKL/EML
      NGL=NG

C----- CALCULATE THE CORRECT FORCE INCREMENT -----
      DTM=DSQRT(DTX*DTX+DTY*DTY)
      IF(DTM.EQ.0.) GOTO 9900
C*****
C-----UNIT NORMAL VECTOR-----
C*****
      IF(IC(NGL).EQ.0) THEN
        VX=DTX/DTM
        VY=DTY/DTM
      ELSE
        VX=VVS(NGL)
        VY=VVS(NGL)
        VXL=VX
        VYL=VY
      ENDIF
      DBN=DTX*VX+DTY*VY
      DBT=DABS(DTX*VY-DTY*VX)

C----- TO FIND THE CORRESPONDING DISPLACEMENT -----
      IF(DBN.LE.2*DTN) THEN
        DEX=DTX/HSL
        DEY=DTY/HSL
      ELSE IF(IC(NGL).EQ.0.OR.HML.EQ.0.) THEN
        DEX=2*DTN*VX/HSL+(DBN-2*DTN)*VX/HIL
        DEY=2*DTN*VY/HSL+(DBN-2*DTN)*VY/HIL
      ELSE
        DEX=2*DTN*VX/HSL+(DBN-2*DTN)*VX/HIL+DBT*VX/HML
C      DEX=2*DTN*VX/HSL+(DBN-2*DTN)*VX/HIL+(DTX-DBN*VX)/HML
        DEY=2*DTN*VY/HSL+(DBN-2*DTN)*VY/HIL+(DTY-DBN*VY)/HML
      ENDIF
      DEM=DSQRT(DEX*DEX+DEY*DEY)
      GOTO 9900

C----- CALCULATION OF THE CURRENT YIELDING SURFACE BEGIN ---
9900  TN=TN1+DTN
      TX=TX+DTX
      TY=TY+DTY
      TM=DSQRT(TX*TX+TY*TY)
C-----UPDATING FORCE INCREMENT-----
      TNL=TN
      TXL=TX

```

```

      TYL=TY
C*****
C-----CHECK IF THERE IS FAILURE-----
C*****
C
      IF(TM.LT.Z*TN) GO TO 9910
      IDEX=1
      TX=TX+Z*TN/TM
      TY=TY+Z*TN/TM
      TM=Z*TN
      DTX=TX-TTXI(NG)
      DTY=TY-TTYI(NG)
      DBN=DTX*VX+DTY*VY
      DEK=Z*DTN*VX/HSL+(DBN-Z*DTN)*VX/HSL
      DEY=Z*DTN*VY/HSL+(DBN-Z*DTN)*VY/HSL
      IF(IC(NGL) .EQ. 0 .OR. HML .EQ. 0.) THEN
      GO TO 9840
      ELSE
      DEK=DEK+(DTX-DBN*VX)/HML
      DEY=DEY+(DTY-DBN*VY)/HML
      ENDIF
      GO TO 9840
9910 CONTINUE
      RETURN
      END

```

APPENDIX D

Media Configurations Used to Simulate
the Aggregate

E13 60°	E14 50°	E15 30°	E16 40°
E9 20°	E10 80°	E11 70°	E12 20°
E5 80°	E6 70°	E7 10°	E8 30°
E1 10°	E2 50°	E3 60°	E4 20°

medium 1

E13 30°	E14 60°	E15 70°	E16 50°
E9 40°	E10 80°	E11 20°	E12 80°
E5 20°	E6 30°	E7 60°	E8 10°
E1 70°	E2 10°	E3 40°	E4 50°

medium 2

Figure D1. Configuration of the Media Used in the Simulations and Orientation of Each Element .

E13	E14	E15	E16
20°	80°	30°	10°
E9	E10	E11	E12
40°	50°	60°	40°
E5	E6	E7	E8
60°	10°	20°	70°
E1	E2	E3	E4
70°	30°	80°	50°

medium 3

10°	50°	30°	40°	70°	80°	60°	20°
20°	70°	50°	10°	30°	50°	70°	60°
30°	40°	60°	70°	10°	60°	50°	30°
10°	20°	80°	50°	40°	30°	40°	80°
80°	30°	40°	70°	80°	70°	60°	50°
60°	10°	20°	60°	40°	50°	10°	40°
20°	40°	30°	80°	50°	20°	80°	70°
30°	60°	20°	10°	70°	10°	20°	80°

medium 4

Figure D2. Configuration of the Media Used in the Simulations and Orientation of Each Element .

45°	45°	45°	45°	45°	45°	45°	45°
45°	45°	45°	45°	45°	45°	45°	45°
45°	45°	45°	45°	45°	45°	45°	45°
45°	45°	45°	0°	0°	45°	45°	45°
45°	45°	45°	0°	0°	45°	45°	45°
45°	45°	45°	45°	45°	45°	45°	45°
45°	45°	45°	45°	45°	45°	45°	45°
45°	45°	45°	45°	45°	45°	45°	45°

medium 5

Figure D3. Configuration of Medium 5 Used in the Simulations and Orientation of Each Element .

APPENDIX E

Medium 2: Compression with Constant Mean Stress.
Element Stress-Strain Behavior

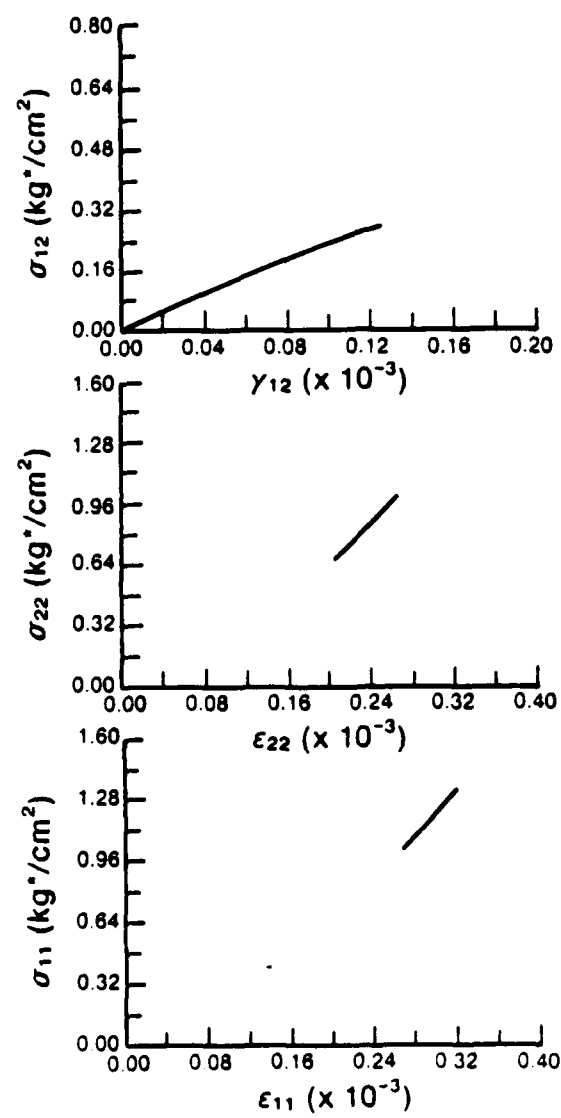


Figure E1. Medium 2: Compression with Constant Mean Stress ($\sigma_0 = 1.0 \text{ Kg}^*/\text{cm}^2$). Stress-Strain Behavior of Element E1 Oriented at $\beta = 70^\circ$.

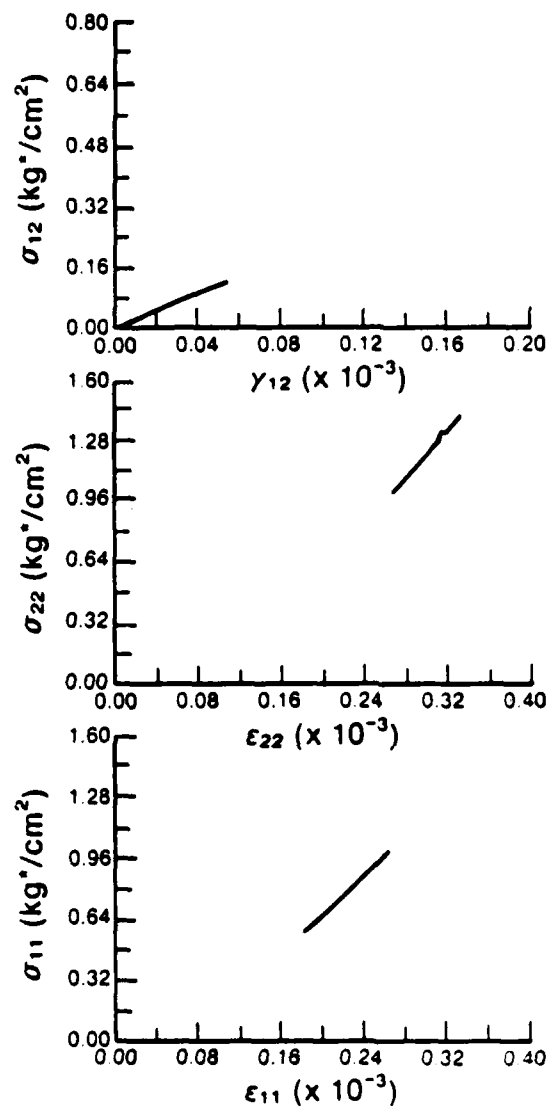


Figure E2. Medium 2: Compression with Constant Mean Stress ($\sigma_0 = 1.0 \text{ Kg}^*/\text{cm}^2$). Stress-Strain Behavior of Element E2 Oriented at $\beta = 10^\circ$.

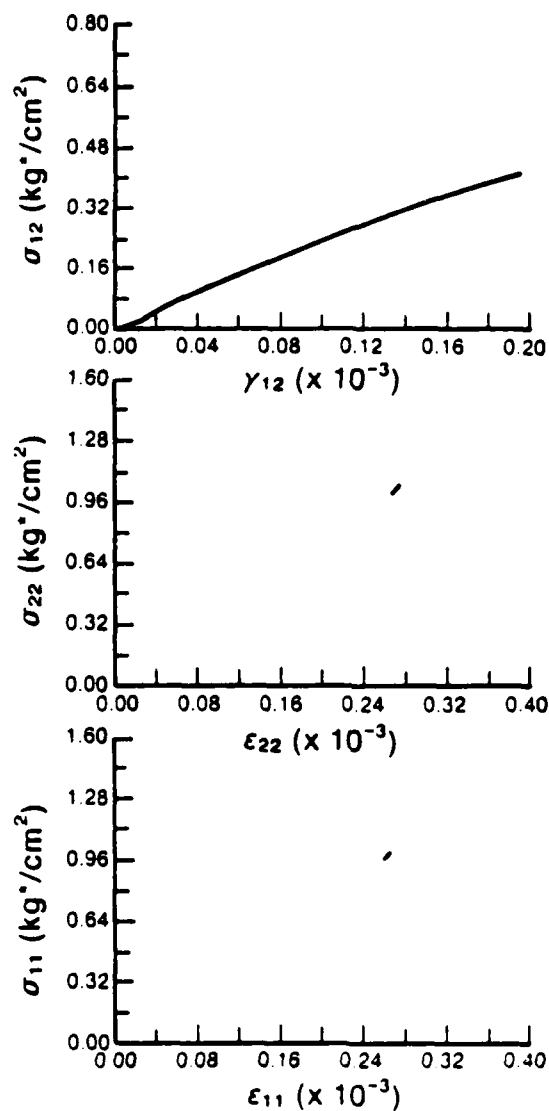


Figure E3. Medium 2: Compression with Constant Mean Stress ($\sigma_0^0 = 1.0 \text{ Kg}^*/\text{cm}^2$). Stress-Strain Behavior of Element E3 Oriented at $\beta = 40^\circ$.

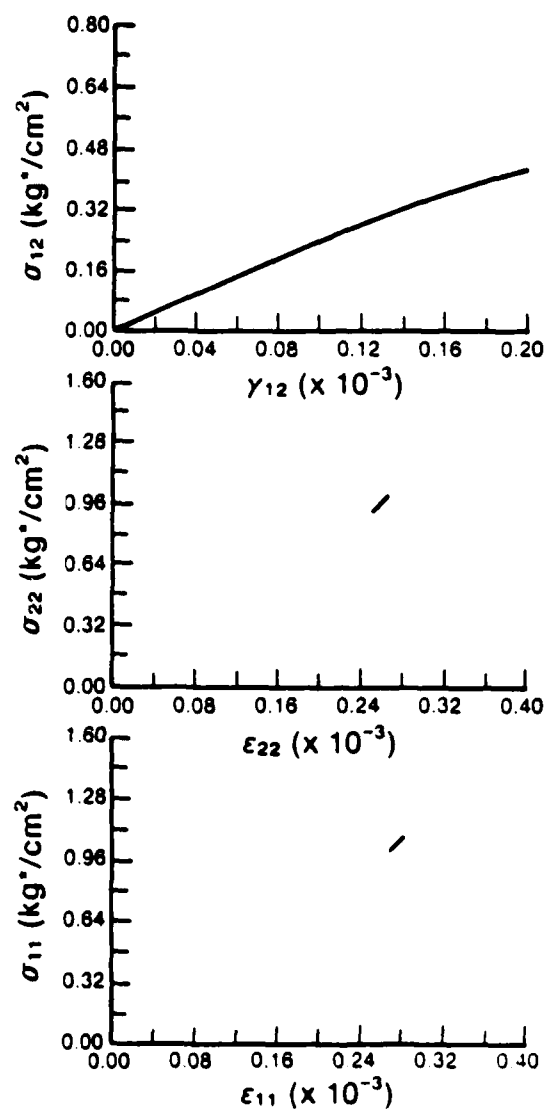


Figure E4. Medium 2: Compression with Constant Mean Stress ($\sigma_0^0 = 1.0 \text{ Kg}^*/\text{cm}^2$). Stress-Strain Behavior of Element E4 Oriented at $\beta = 50^\circ$.

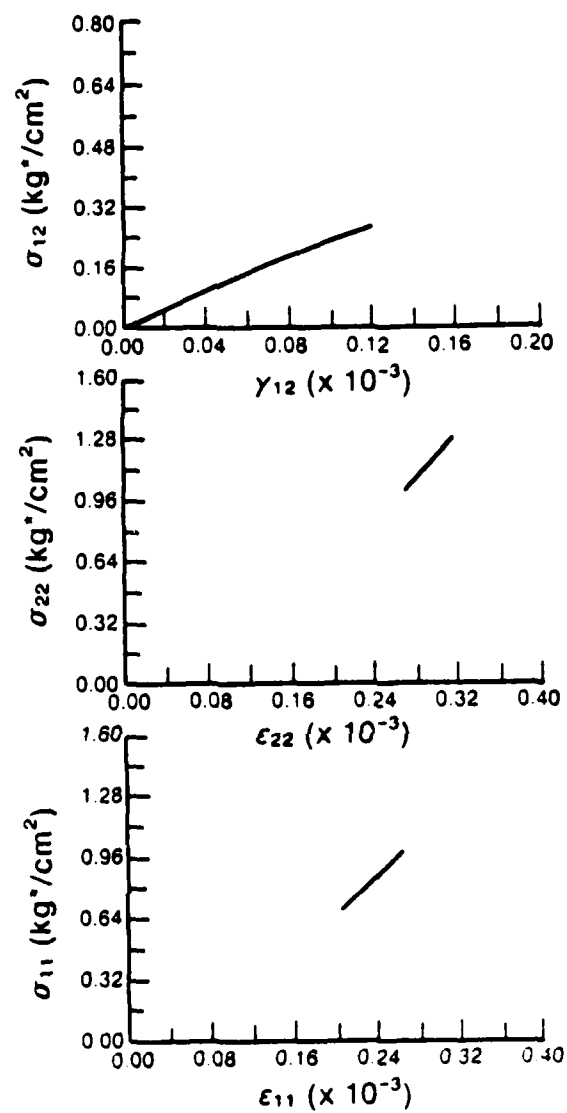


Figure E5. Medium 2: Compression with Constant Mean Stress ($\sigma_0^0 = 1.0 \text{ Kg */cm}^2$). Stress-Strain Behavior of Element E5 Oriented at $\theta = 20^\circ$.

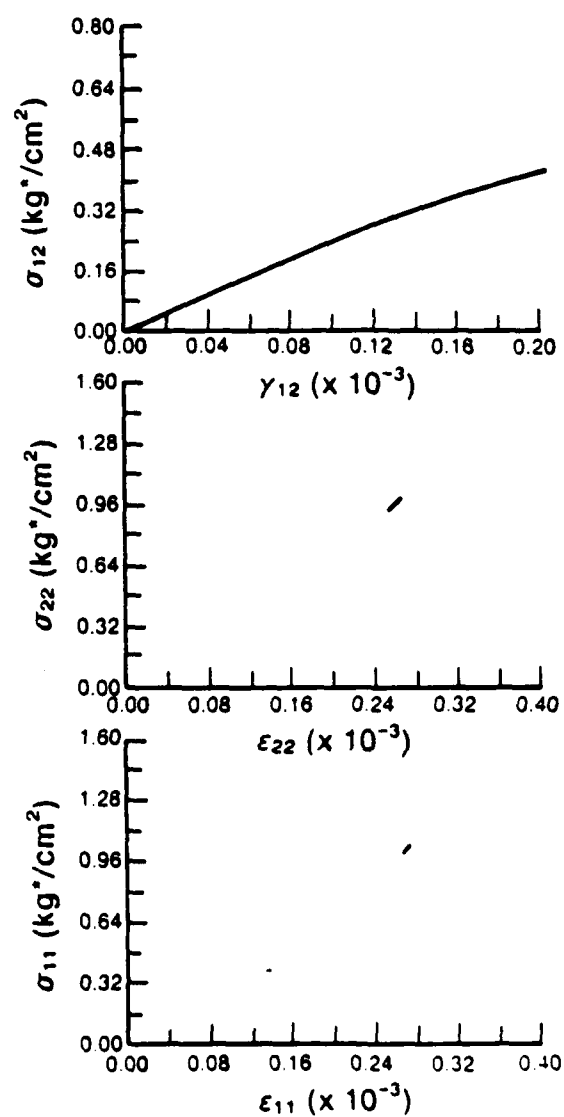


Figure E6. Medium 2: Compression with Constant Mean Stress ($\sigma_0^0 = 1.0 \text{ Kg */cm}^2$). Stress-Strain Behavior of Element E6 Oriented at $\beta = 30^\circ$.

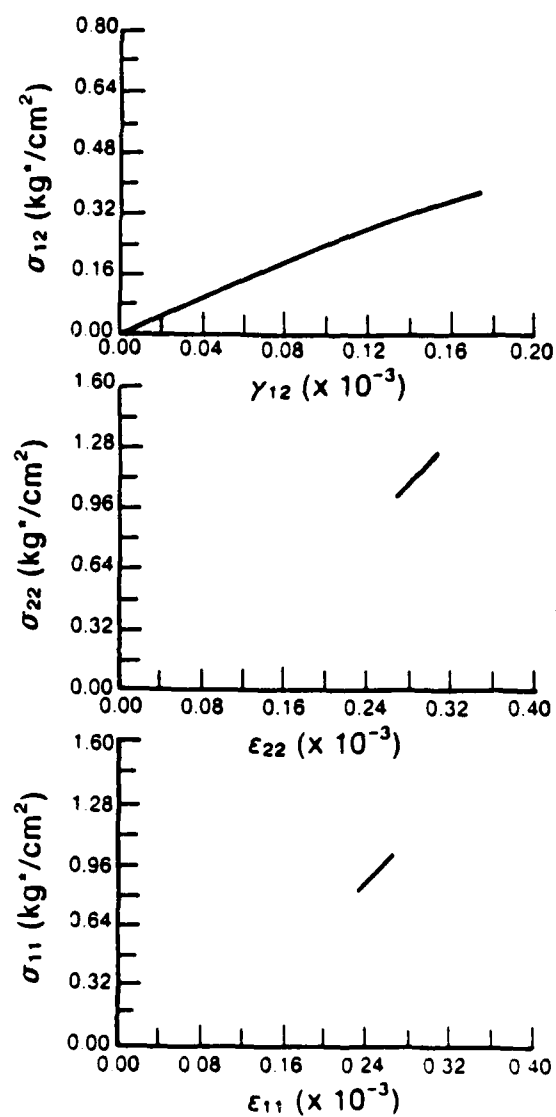


Figure E7. Medium 2: Compression with Constant Mean Stress ($\sigma_0^0 = 1.0 \text{ Kg}^*/\text{cm}^2$). Stress-Strain Behavior of Element E7 Oriented at $\beta = 60^\circ$.

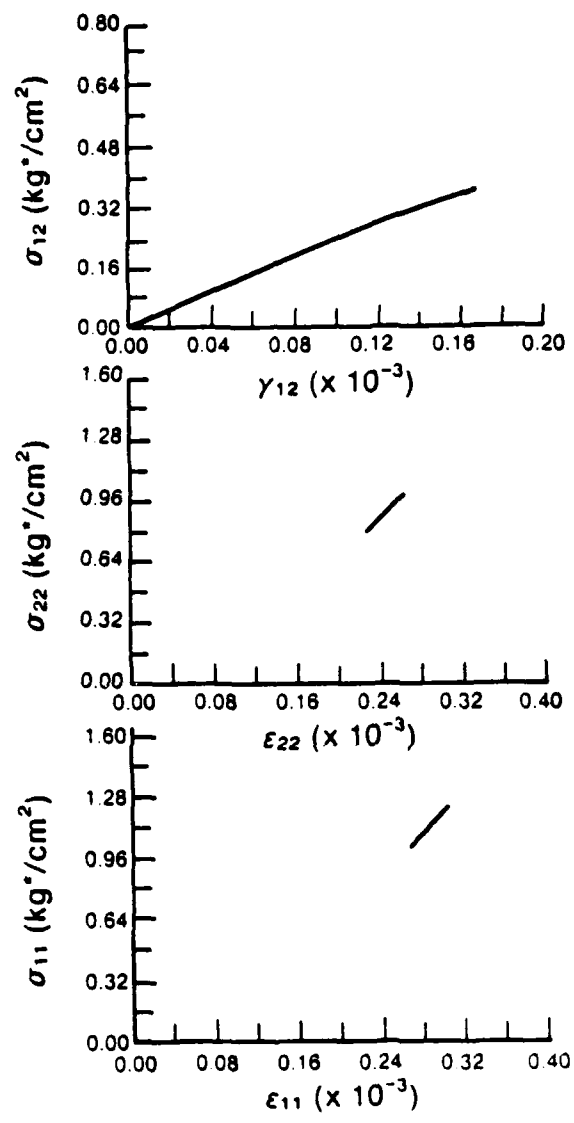


Figure E8. Medium 2: Compression with Constant Mean Stress ($\sigma_0^0 = 1.0 \text{ Kg}^*/\text{cm}^2$). Stress-Strain Behavior of Element E8 Oriented at $\beta = 10^\circ$.

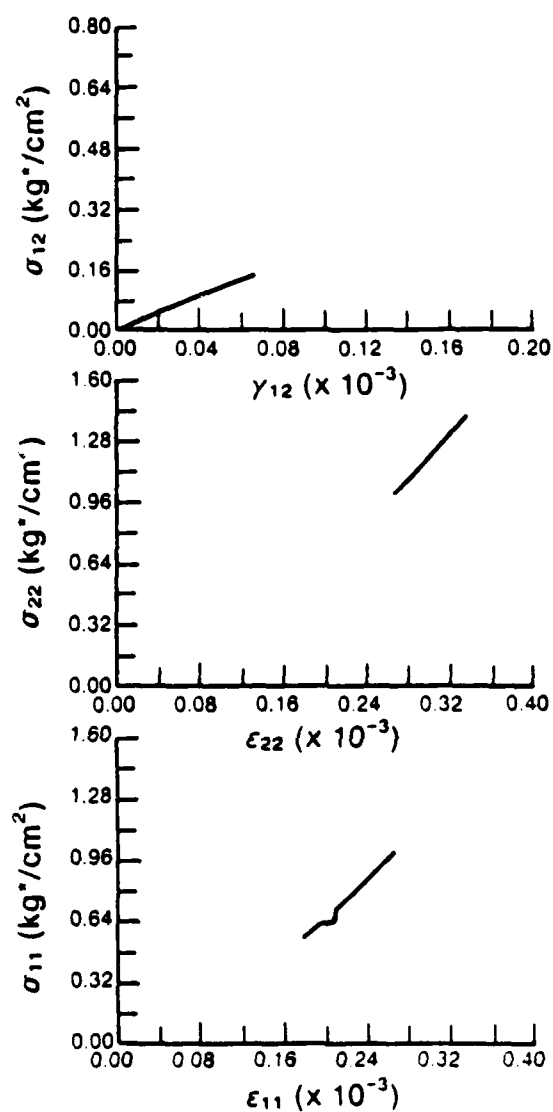


Figure E9. Medium 2: Compression with Constant Mean Stress ($\sigma_0^0 = 1.0 \text{ Kg */cm}^2$). Stress-Strain Behavior of Element E9 Oriented at $\beta = 40^\circ$.

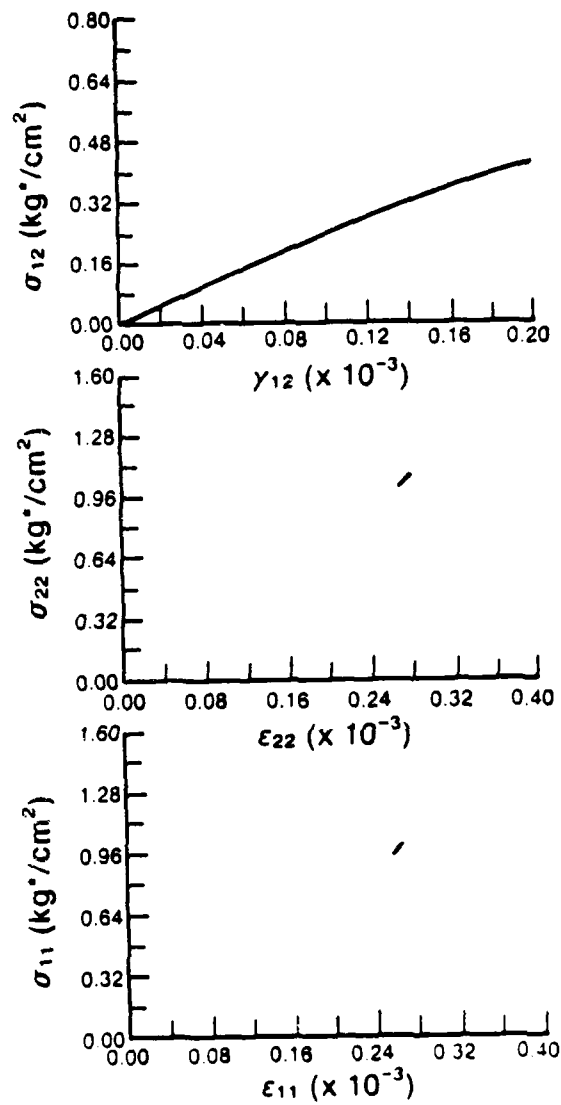


Figure E10. Medium 2: Compression with Constant Mean Stress ($\sigma_0^0 = 1.0 \text{ Kg}^*/\text{cm}^2$). Stress-Strain Behavior of Element E10 Oriented at $\beta = 80^\circ$.

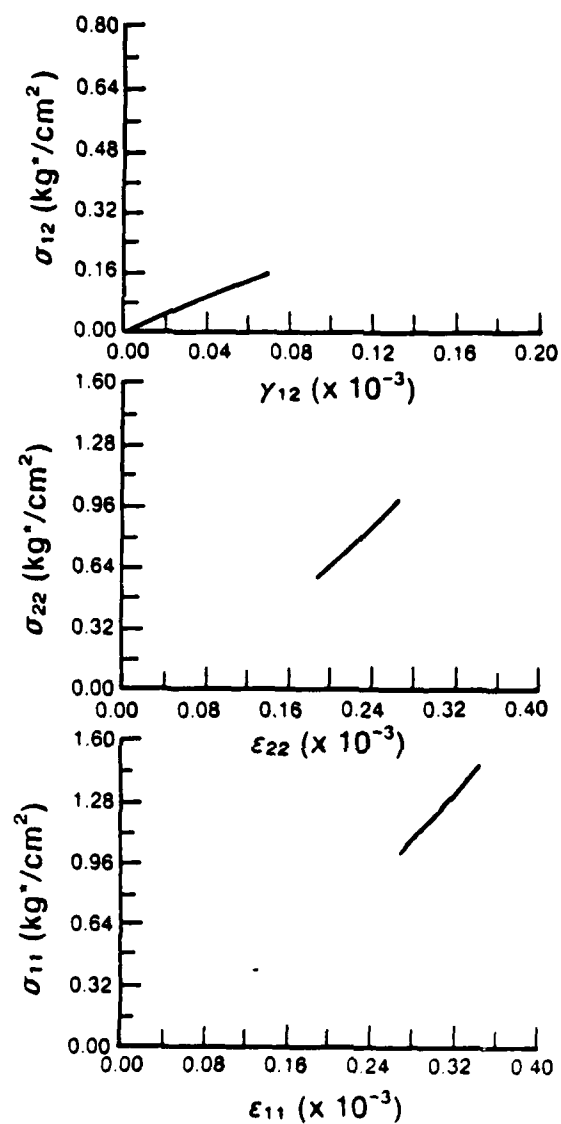


Figure Ell. Medium 2: Compression with Constant Mean Stress ($\sigma_0 = 1.0 \text{ Kg */cm}^2$). Stress-Strain Behavior of Element Ell Oriented at $\beta = 20^\circ$.

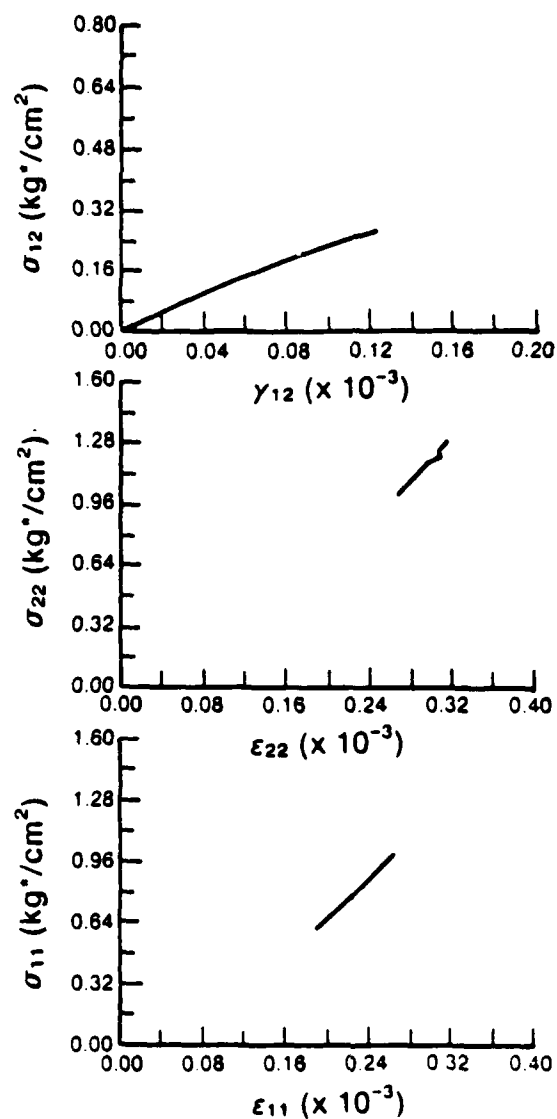


Figure E12. Medium 2: Compression with Constant Mean Stress ($\sigma_o^0 = 1.0 \text{ Kg */cm}^2$). Stress-Strain Behavior of Element E12 Oriented at $\beta = 80^\circ$.

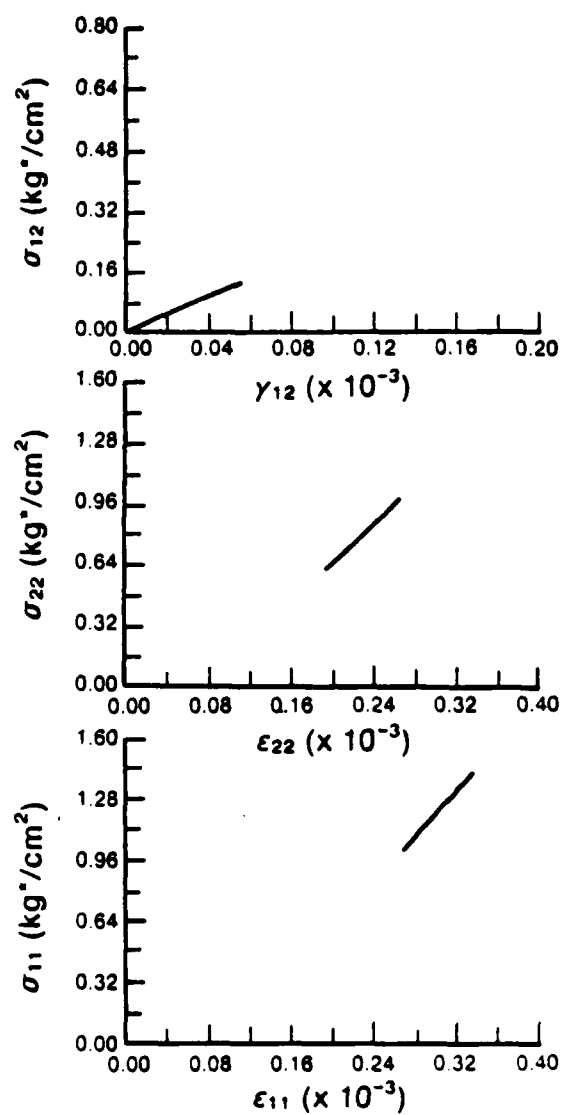


Figure E13. Medium 2: Compression with Constant Mean Stress ($\sigma_0 = 1.0 \text{ Kg}^*/\text{cm}^2$). Stress-Strain Behavior of Element E13 Oriented at $\beta = 30^\circ$.

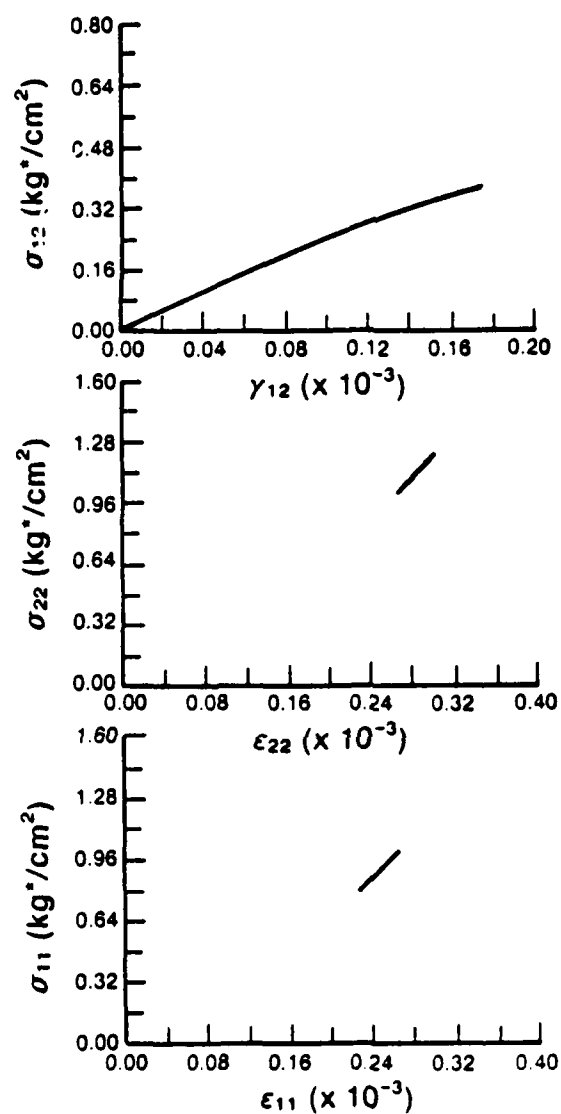


Figure E14. Medium 2: Compression with Constant Mean Stress ($\sigma_0 = 1.0 \text{ kg */cm}^2$). Stress-Strain Behavior of Element E14 Oriented at $\beta = 60^\circ$.

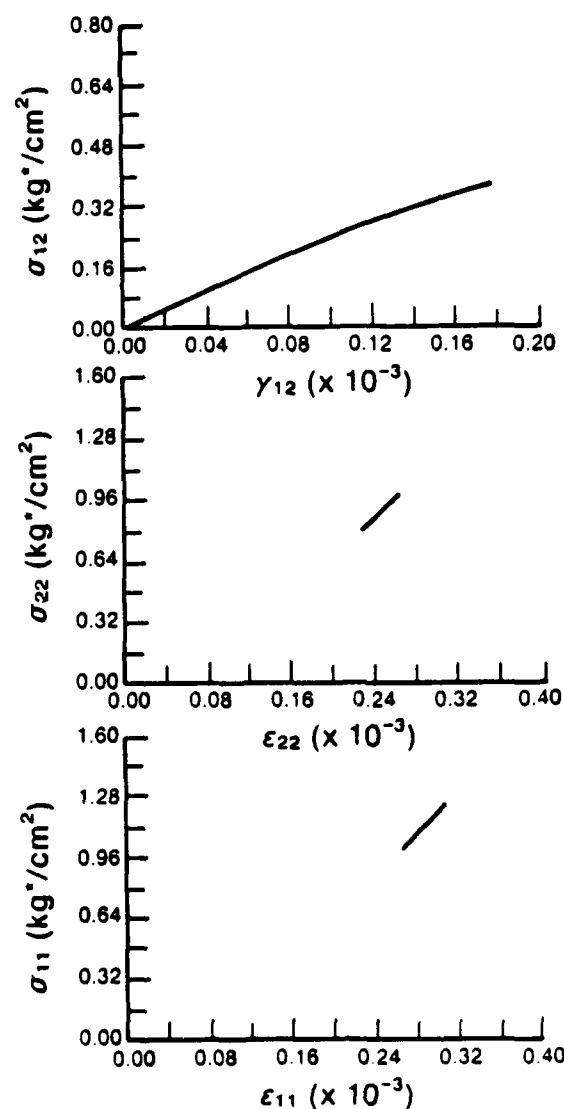


Figure E15. Medium 2: Compression with Constant Mean Stress ($\sigma_0 = 1.0 \text{ Kg}^*/\text{cm}^2$). Stress-Strain Behavior of Element E15 Oriented at $\beta = 70^\circ$.

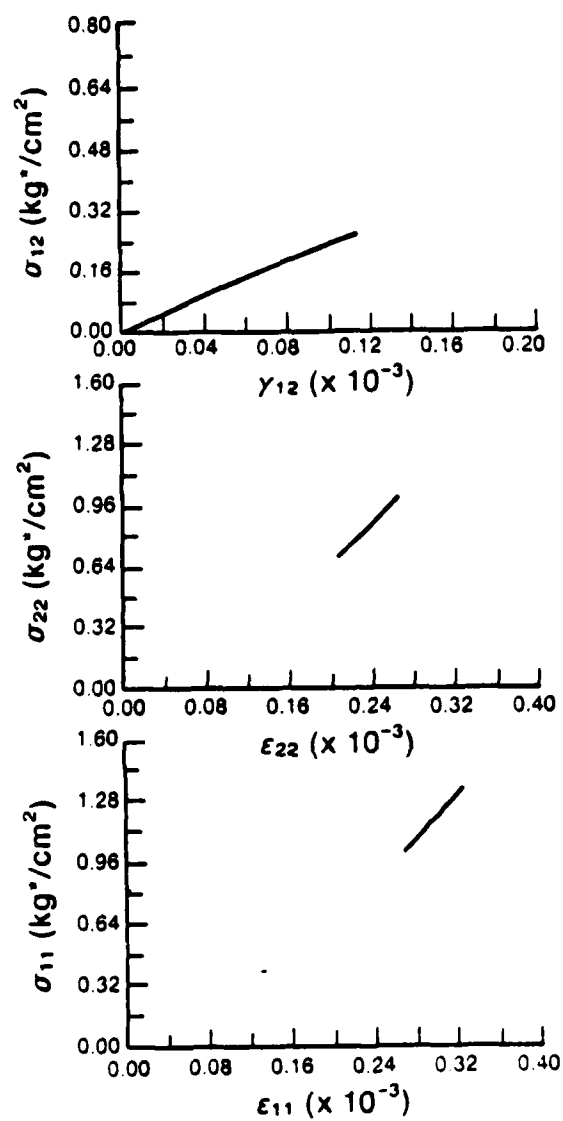


Figure E16. Medium 2: Compression with Constant Mean Stress ($\sigma_0 = 1.0 \text{ Kg}^*/\text{cm}^2$). Stress-Strain Behavior of Element E16 Oriented at $\beta=50^\circ$.

APPENDIX F

Medium 1: Biaxial Compression with Variable Mean Stress
Element Stress-Strain Behavior

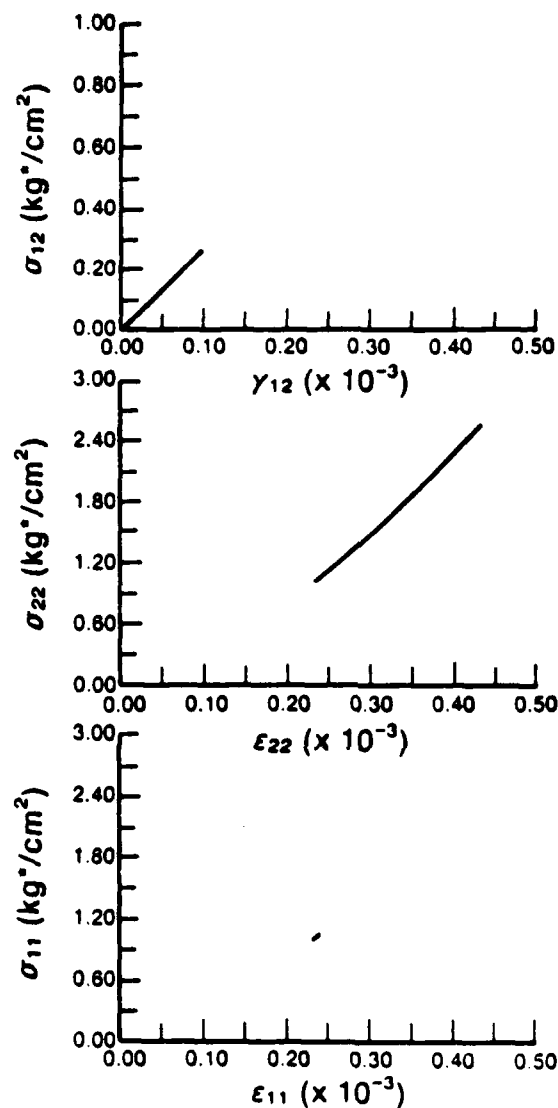


Figure F1. Medium 1: Compression with Variable Mean Stress ($\sigma_0 = 1.0 \text{ Kg */cm}^2$). Stress-Strain Behavior of Element 1 Oriented at $\beta = 10^\circ$.

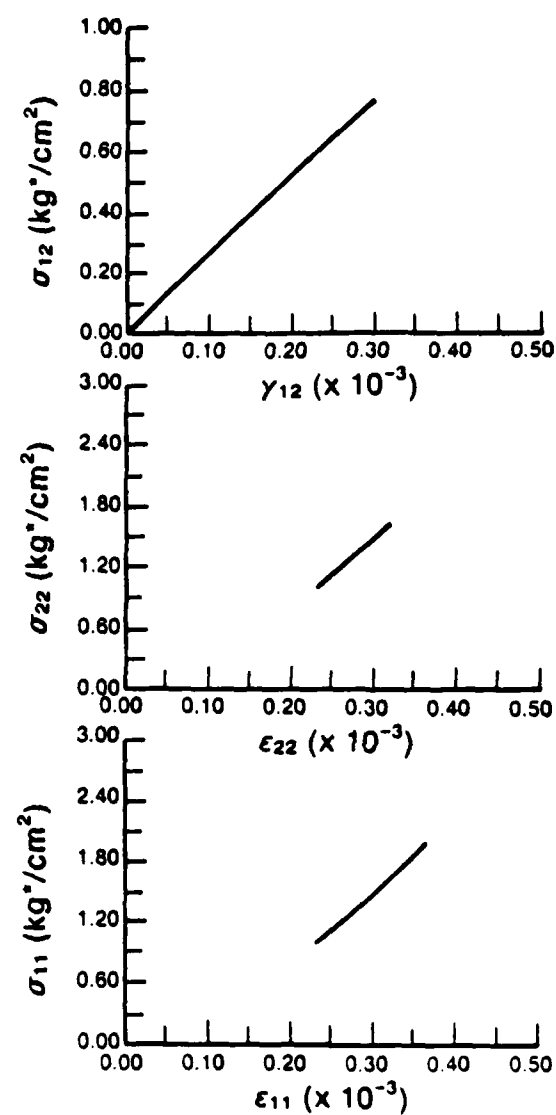


Figure F2. Medium 1: Compression with Variable Mean Stress ($\sigma_0 = 1.0 \text{ Kg*/cm}^2$). Stress-Strain Behavior of Element 2 Oriented at $\beta = 50^\circ$.

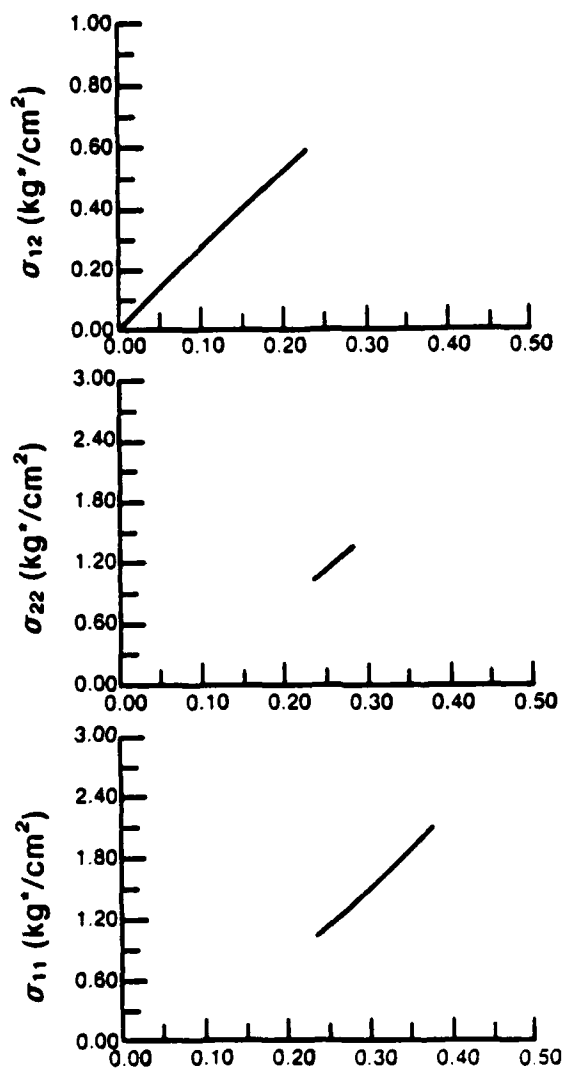


Figure F3. Medium 1: Compression with Variable Mean Stress ($\sigma_0^0 = 1.0 \text{ Kg */cm}^2$). Stress-Strain Behavior of Element 3 Oriented at $\beta = 60^\circ$.

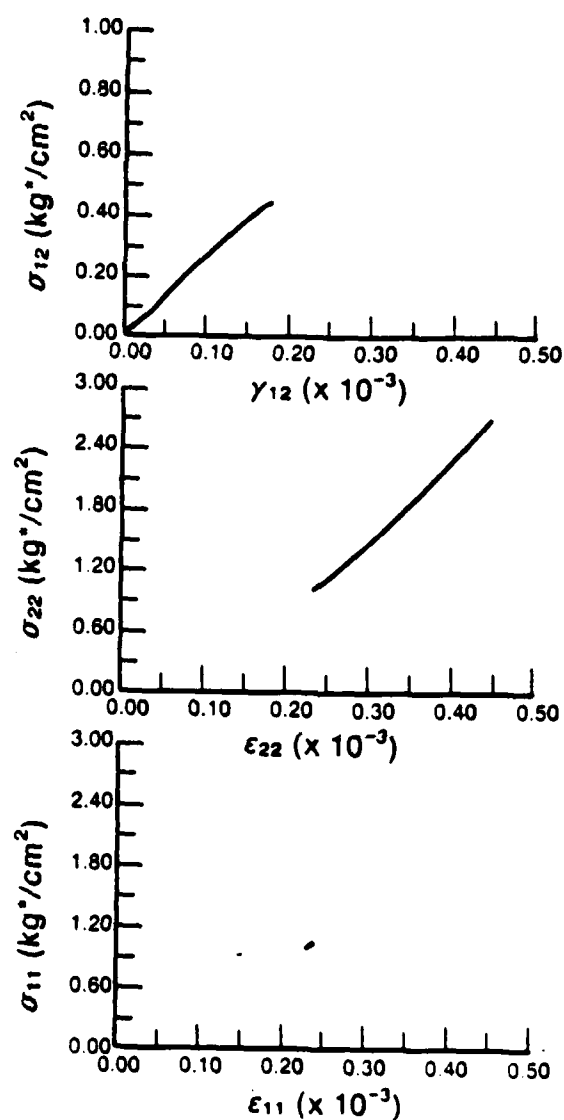


Figure F4. Medium 1: Compression with Variable Mean Stress ($\sigma_o^0 = 1.0 \text{ Kg */cm}^2$). Stress-Strain Behavior of Element 4 Oriented at $\beta = 20^\circ$.

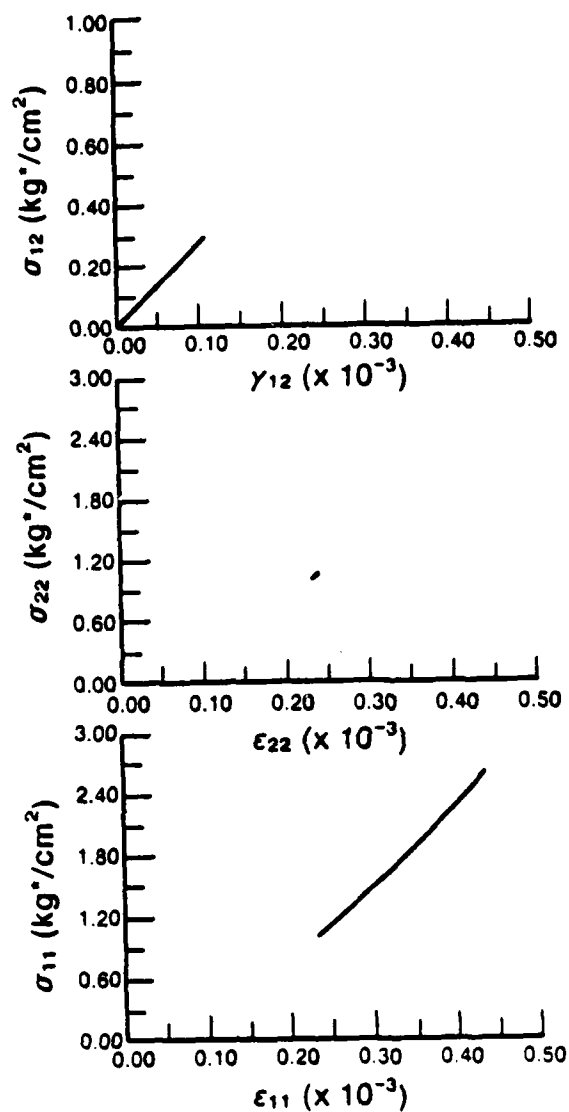


Figure F5. Medium 1: Compression with Variable Mean Stress ($\sigma_0^0 = 1.0 \text{ Kg */cm}^2$). Stress-Strain Behavior of Element 5 Oriented at $\beta=80^\circ$.

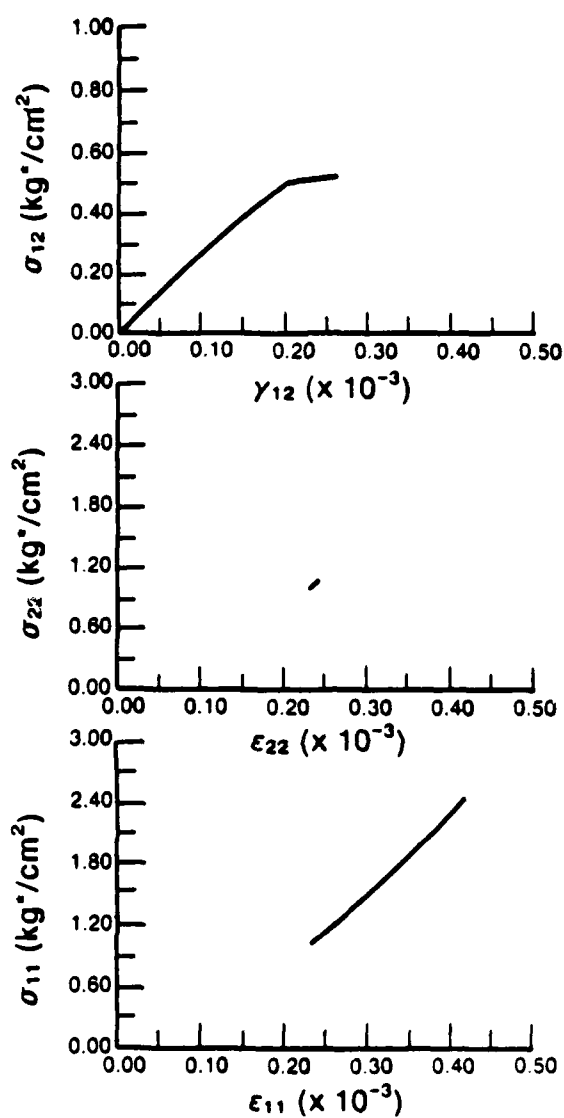


Figure F6. Medium 1: Compression with Variable Mean Stress ($\sigma_0^0 = 1.0$ Kg */cm²). Stress-Strain Behavior of Element 6 Oriented at $\beta = 70^\circ$.

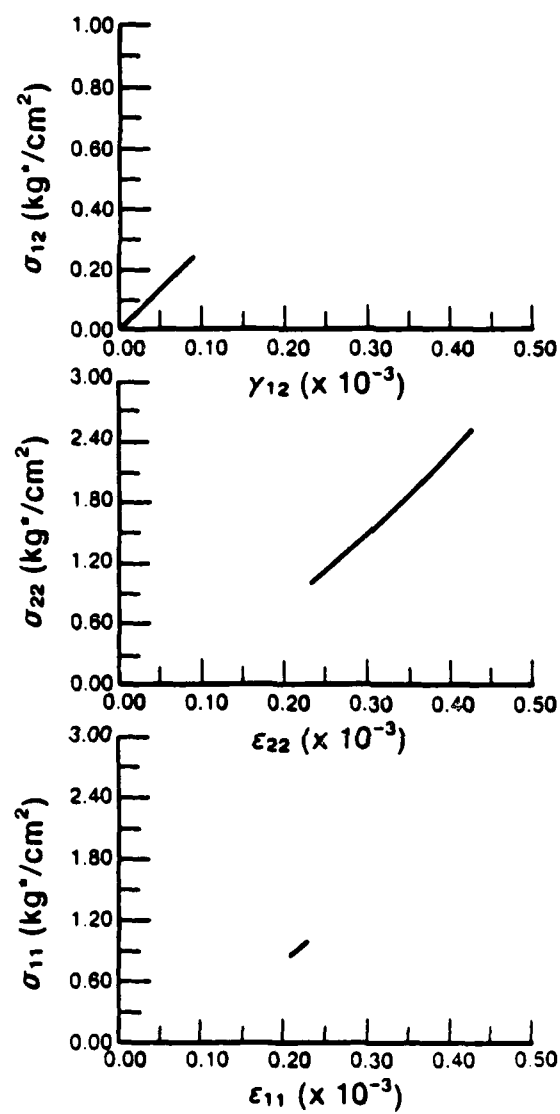


Figure F7. Medium 1: Compression with Variable Mean Stress ($\sigma_0^0 = 1.0 \text{ Kg */cm}^2$). Stress-Strain Behavior of Element 7 Oriented at $\theta = 10^\circ$.

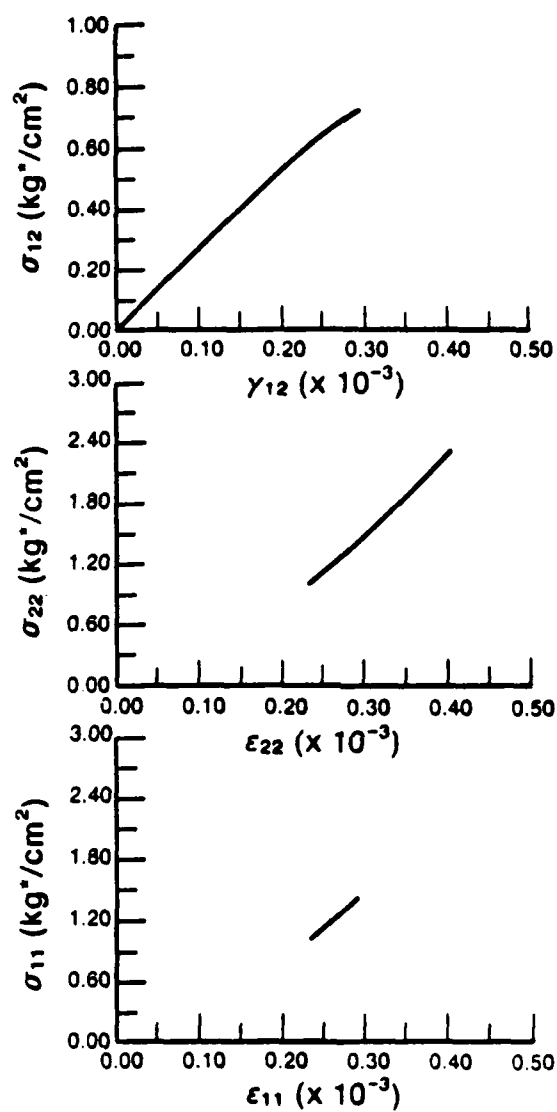


Figure F8. Medium 1: Compression with Variable Mean Stress ($\sigma_0^0 = 1.0 \text{ Kg */cm}^2$). Stress-Strain Behavior of Element 8 Oriented at $\beta = 30^\circ$.

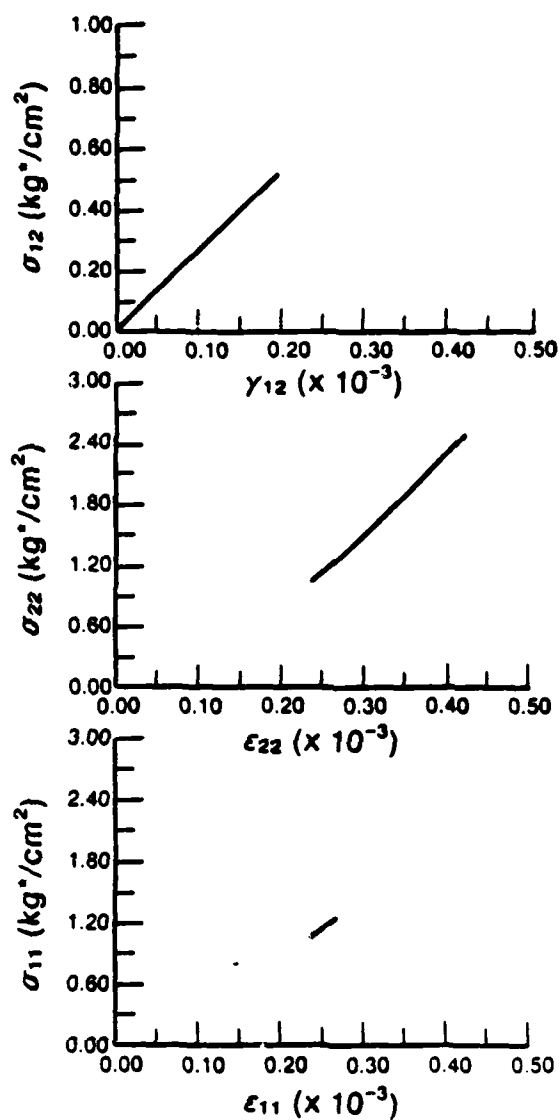


Figure F9. Medium 1: Compression with Variable Mean Stress ($\sigma_0^0 = 1.0 \text{ Kg */cm}^2$). Stress-Strain Behavior of Element 9 Oriented at $\beta = 20^\circ$.

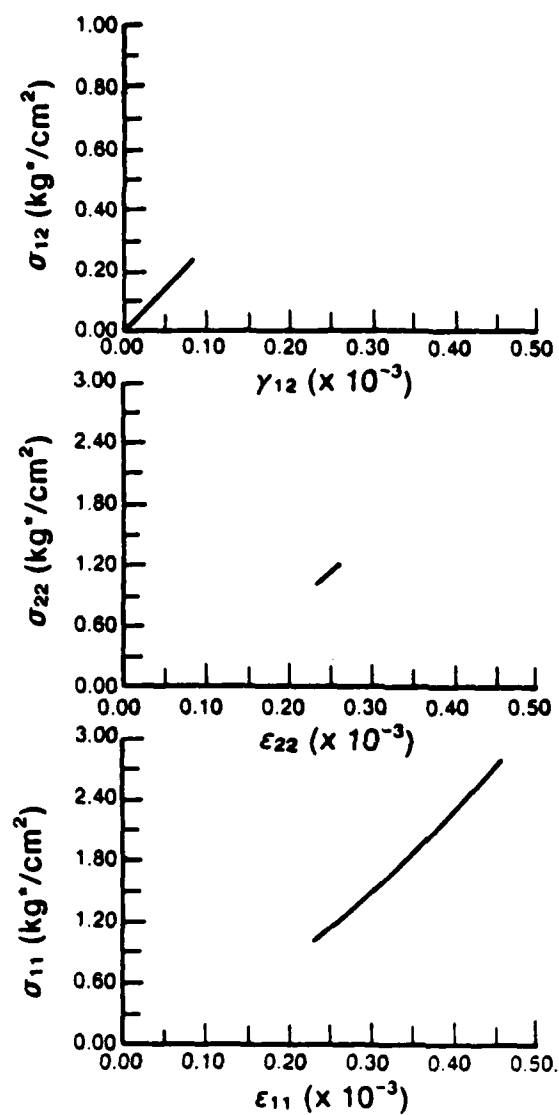


Figure F10. Medium 1: Compression with Variable Mean Stress ($\sigma_0^0 = 1.0 \text{ Kg */cm}^2$). Stress-Strain Behavior of Element 10 Oriented at $\beta = 80^\circ$.

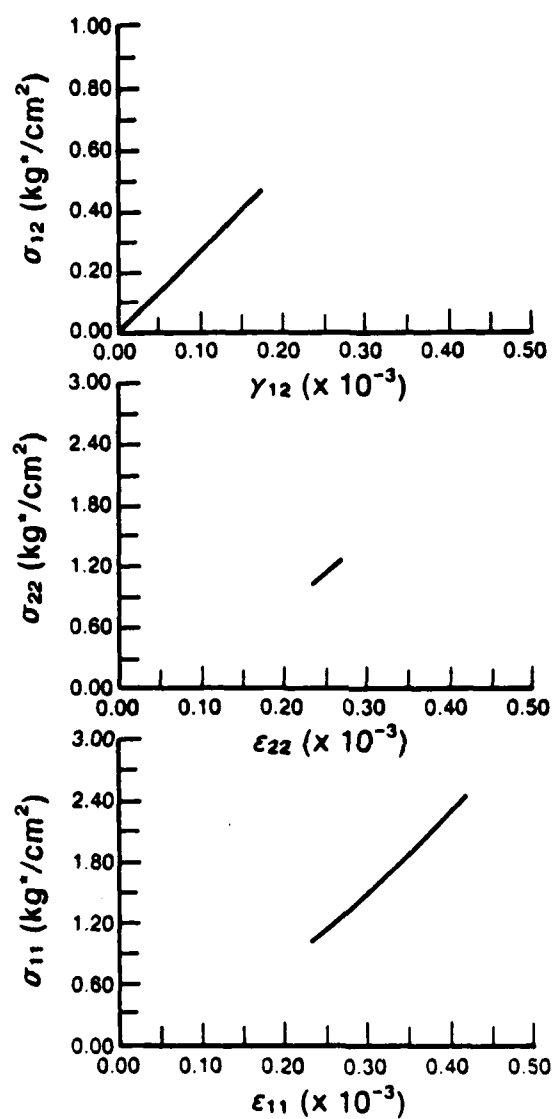


Figure F11. Medium 1: Compression with Variable Mean Stress ($\sigma_o^o=1.0$ Kg */cm²). Stress-Strain Behavior of Element 11 Oriented at $\beta=70^\circ$.

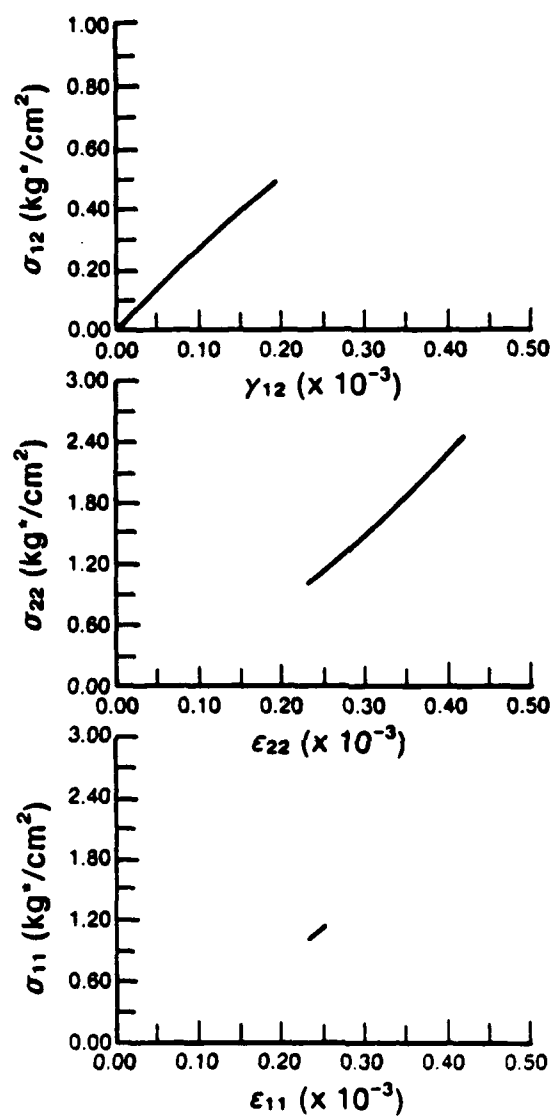


Figure F12. Medium 1: Compression with Variable Mean Stress ($\sigma_0 = 1.0 \text{ Kg */cm}^2$). Stress-Strain Behavior of Element 12 Oriented at $\beta = 20^\circ$.

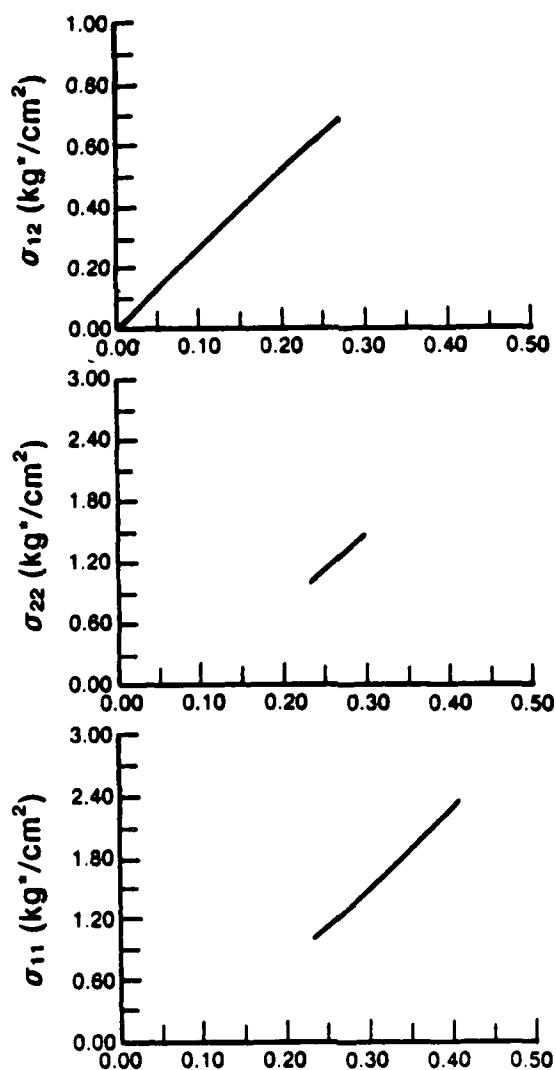


Figure F13. Medium 1: Compression with Variable Mean Stress ($\sigma_0^0=1.0$ Kg */cm²). Stress-Strain Behavior of Element 13 Oriented at $\beta=60^\circ$.

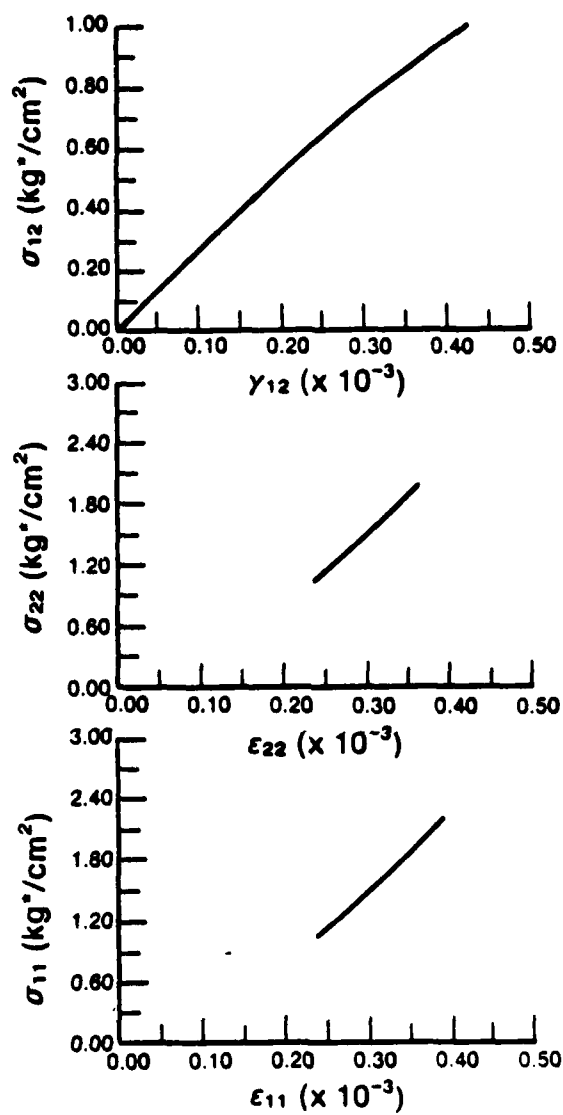


Figure F14. Medium 1: Compression with Variable Mean Stress ($\sigma_0 = 1.0 \text{ Kg}^*/\text{cm}^2$). Stress-Strain Behavior of Element 14 Oriented at $\beta = 50^\circ$.

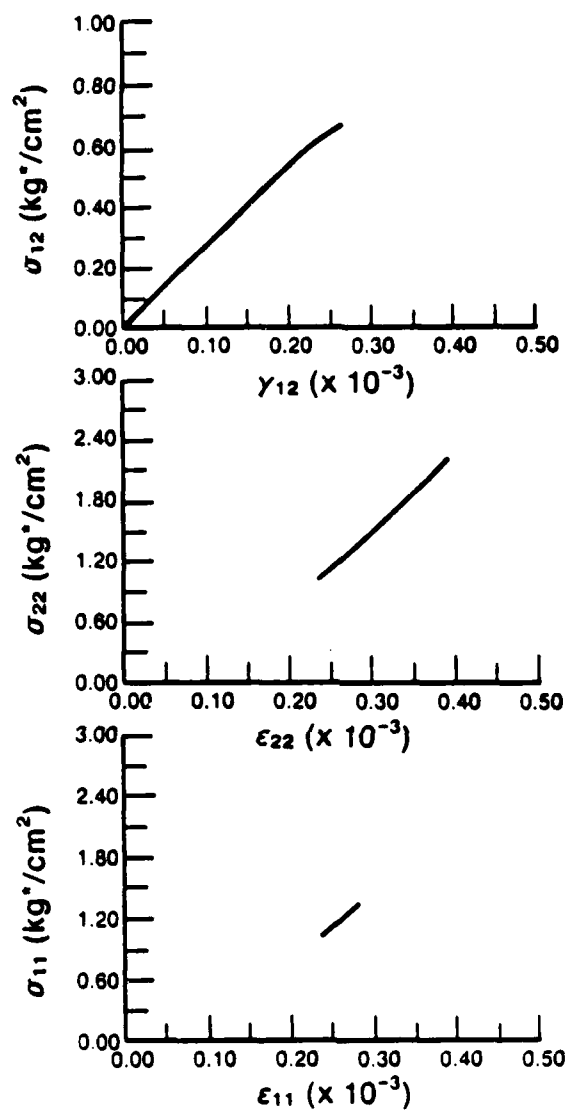


Figure F15. Medium 1: Compression with Variable Mean Stress ($\sigma_0 = 1.0 \text{ Kg */cm}^2$). Stress-Strain Behavior of Element 15 Oriented at $\beta = 30^\circ$.

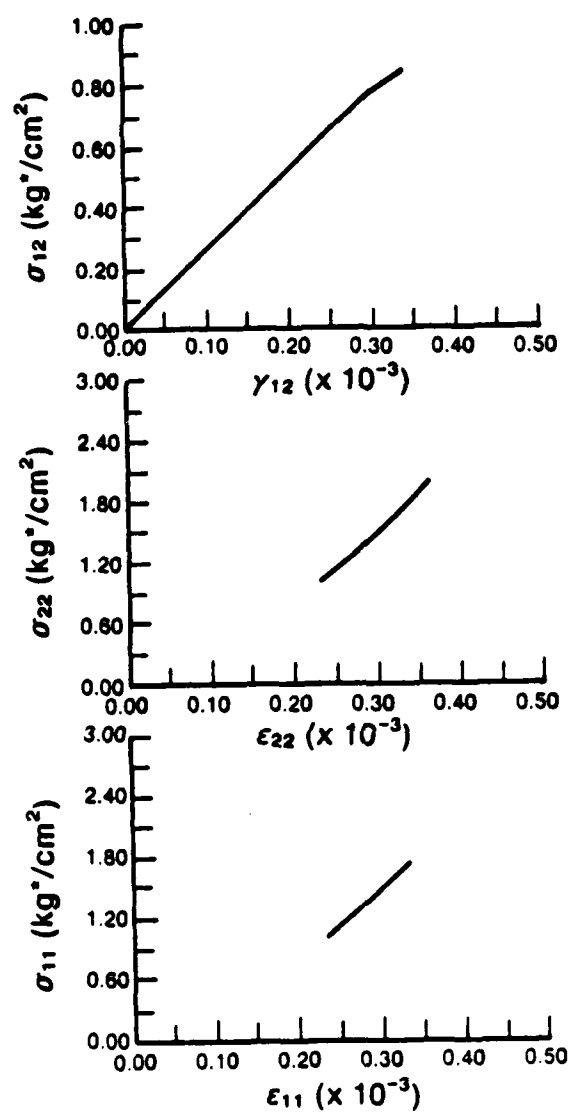


Figure F16. Medium 1: Compression with Variable Mean Stress ($\sigma_0 = 1.0 \text{ Kg}^*/\text{cm}^2$). Stress-Strain Behavior of Element 16 Oriented at $\beta = 40^\circ$.

APPENDIX G

Medium 2: Compression with Mean Stress Constant
Variation of Normalized Stress and
Strain During Loading

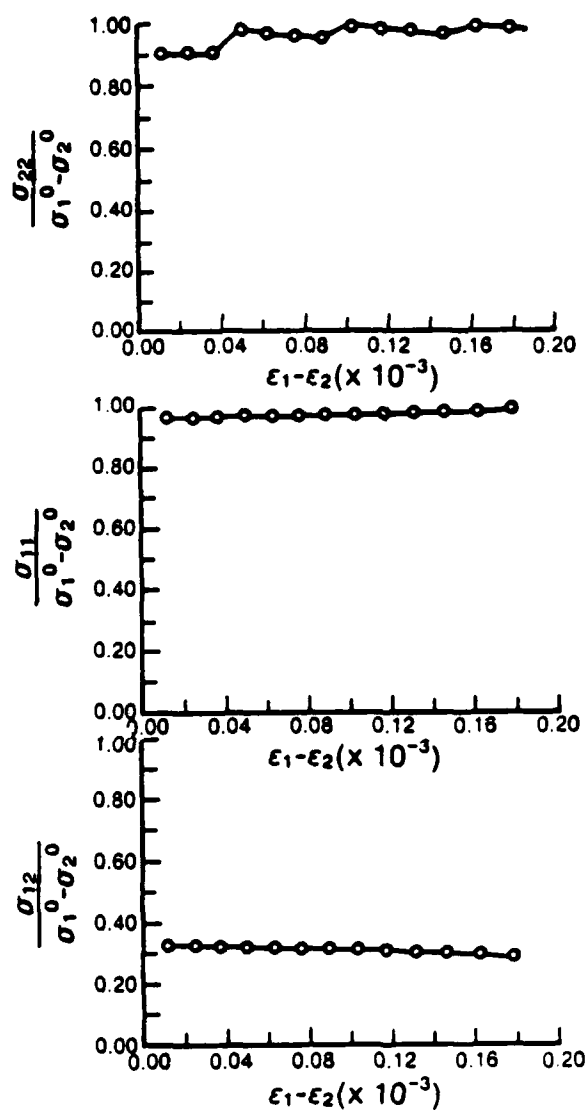


Figure G1. Medium 2: Compression with Constant Mean Stress $\sigma_0^0 = 1.0 \text{ Kg}^*/\text{cm}^2$. Normalized Element Stress Versus Applied Principal Strain Difference for All Elements Oriented 10° .

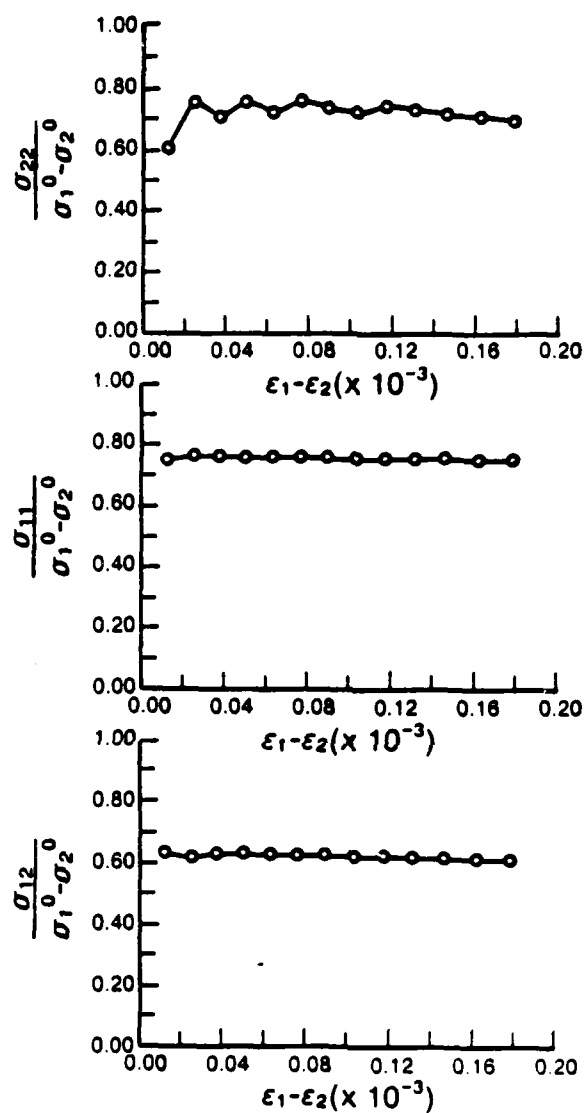


Figure G2. Medium 2: Compression with Constant Mean Stress $\sigma_0^0 = 1.0 \text{ Kg } ^\circ/\text{cm}^2$. Normalized Element Stress Versus Applied Principal Strain Difference for All Elements Oriented 20° .

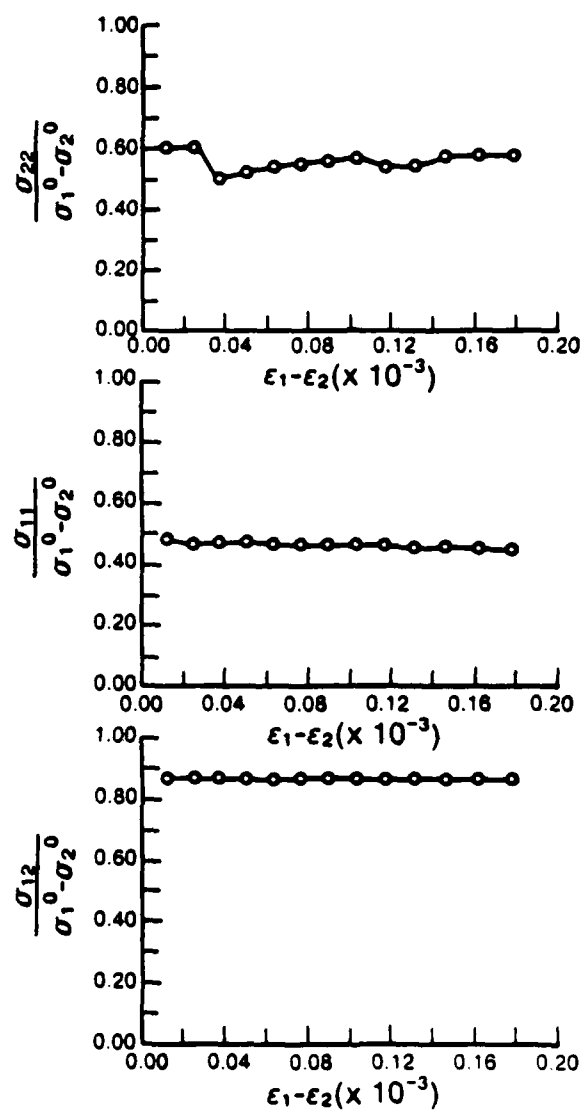


Figure G3. Medium 2: Compression with Constant Mean Stress $\sigma_o^0 = 1.0 \text{ Kg */cm}^2$. Normalized Element Stress Versus Applied Principal Strain Difference for All Elements Oriented 30° .

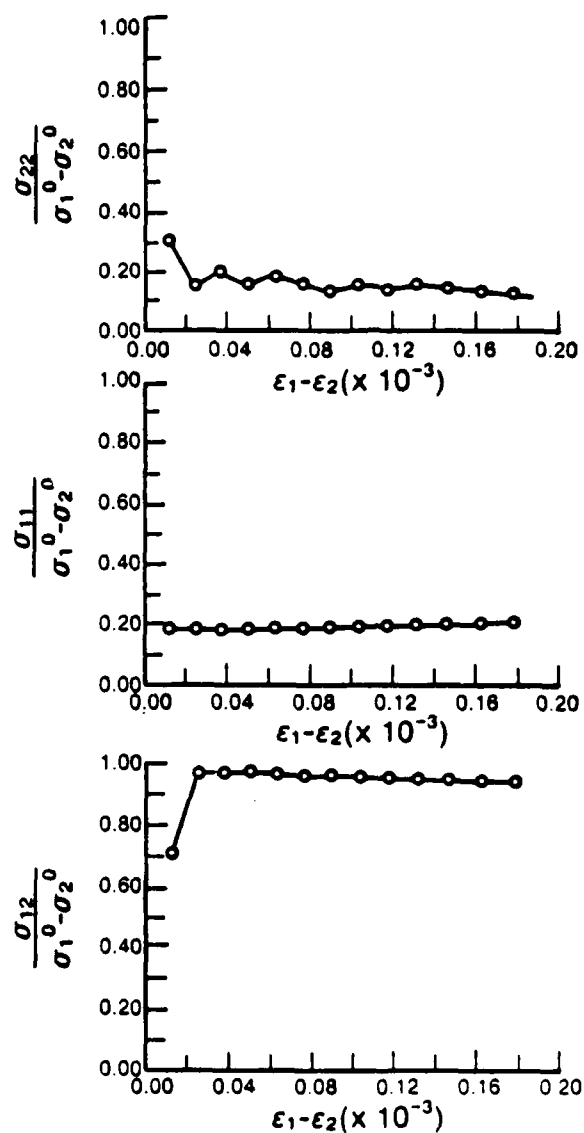


Figure G4. Medium 2: Compression with Constant Mean Stress $\sigma_0^0 = 1.0 \text{ Kg}^*/\text{cm}^2$. Normalized Element Stress Versus Applied Principal Strain Difference for All Elements Oriented 40° .

NO-A191 927

MICROMECHANICAL MODELING OF GRANULAR SOIL AT SMALL
STRAIN BY ARRAYS OF EL. (U) RENSSELAER POLYTECHNIC INST
TROY NY DEPT OF CIVIL ENGINEERING. E PETAKIS ET AL.

4/4

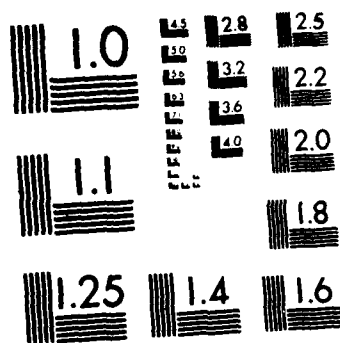
UNCLASSIFIED

28 SEP 87 RPI-CE-87-02 AFOSR-TR-88-0137

F/G 8/10

NL





MICROCOPY RESOLUTION TEST CHART
NATIONAL BUREAU OF STANDARDS 1963-A

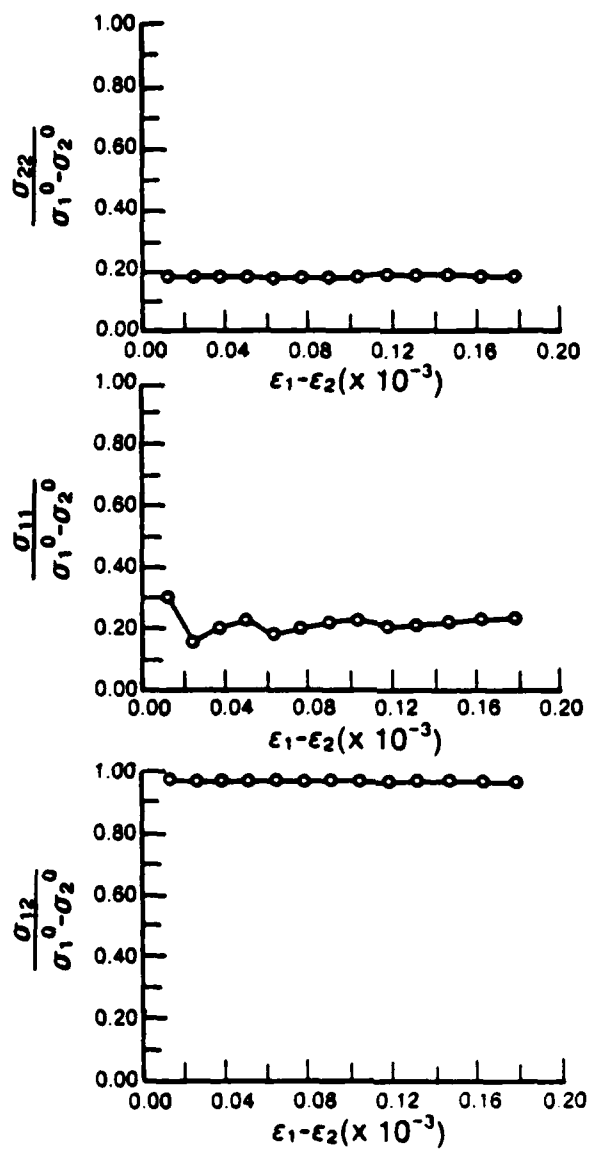


Figure G5. Medium 2: Compression with Constant Mean Stress $\sigma_0^0 = 1.0 \text{ Kg */cm}^2$. Normalized Element Stress Versus Applied Principal Strain Difference for All Elements Oriented 50° .

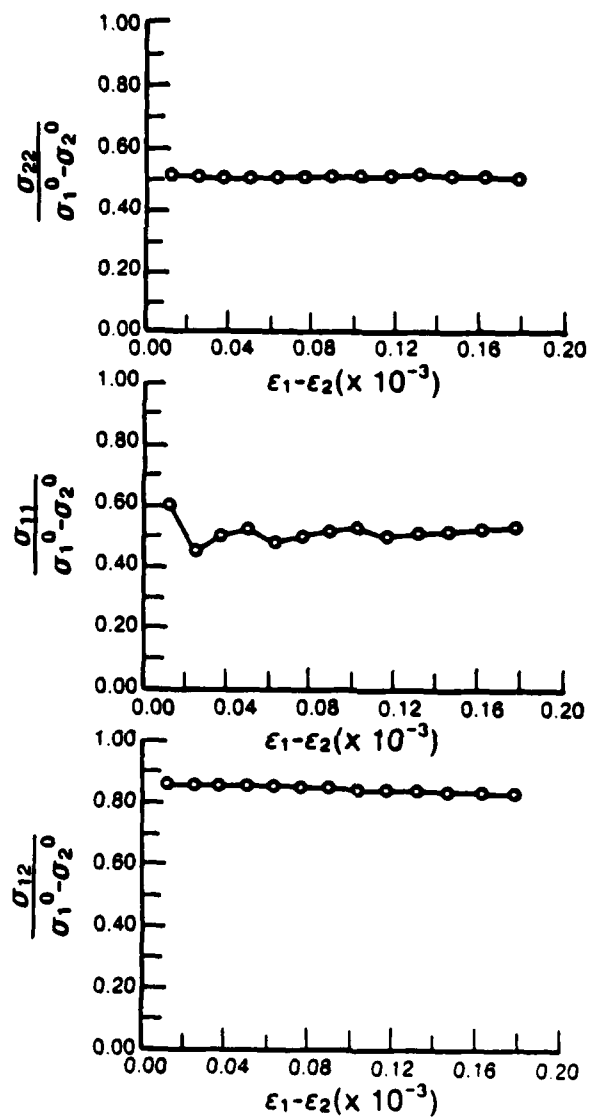


Figure G6. Medium 2: Compression with Constant Mean Stress $\sigma_0^0 = 1.0 \text{ Kg * / cm}^2$. Normalized Element Stress Versus Applied Principal Strain Difference for All Elements Oriented 60° .

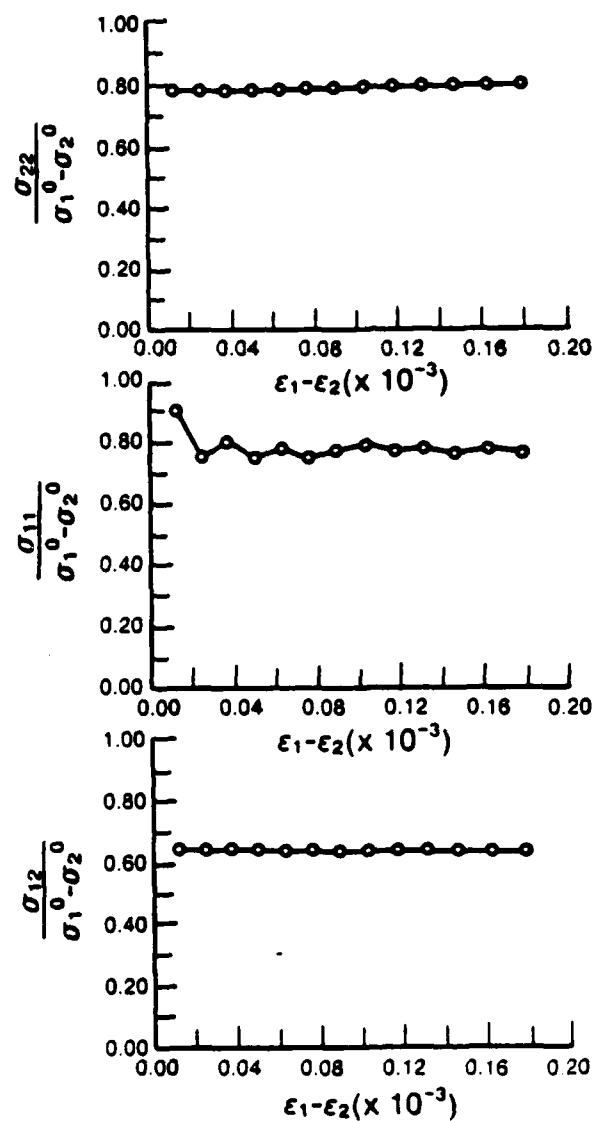


Figure G7. Medium 2: Compression with Constant Mean Stress $\sigma_o^0 = 1.0 \text{ Kg}^*/\text{cm}^2$. Normalized Element Stress Versus Applied Principal Strain Difference for All Elements Oriented 70° .

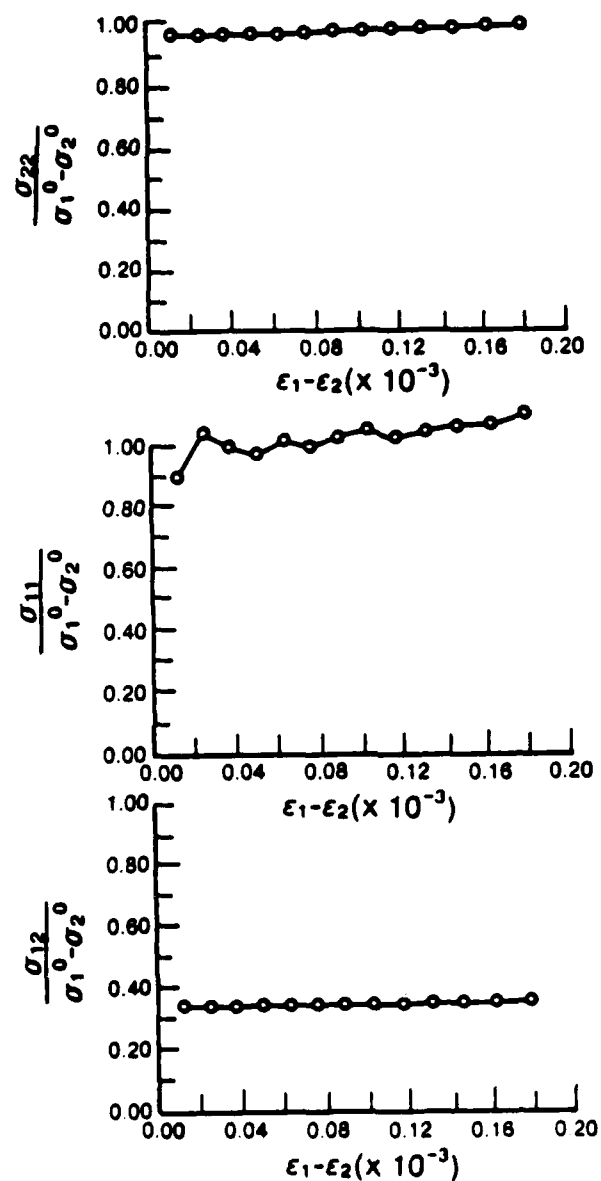


Figure G8. Medium 2: Compression with Constant Mean Stress $\sigma_0^0 = 1.0 \text{ Kg}^*/\text{cm}^2$. Normalized Element Stress Versus Applied Principal Strain Difference for All Elements Oriented 80° .

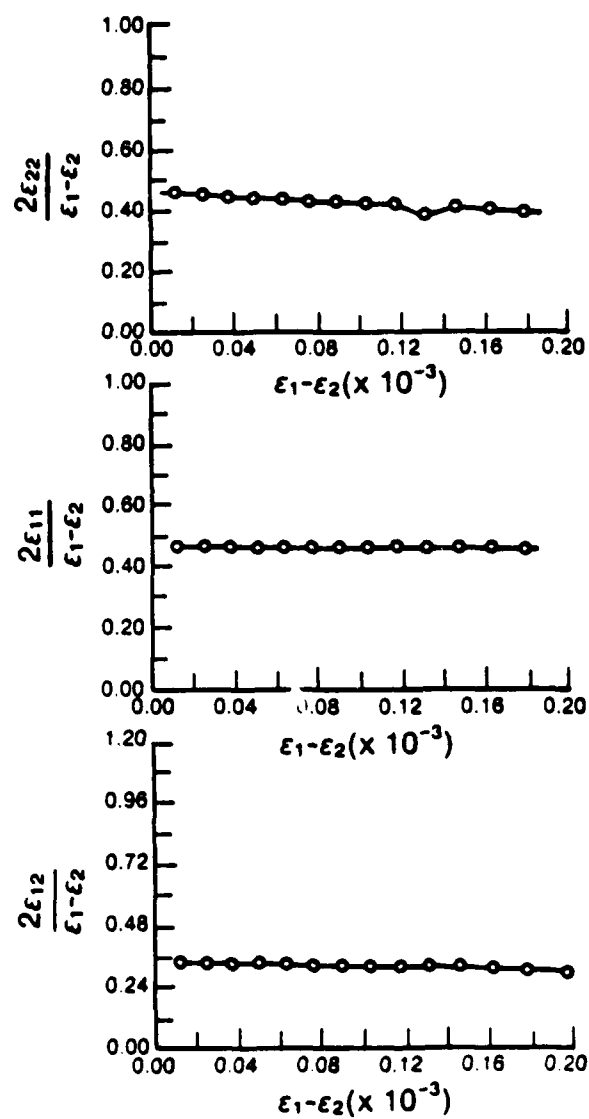


Figure G9. Medium 2: Compression with Constant Mean Stress $\sigma_0^0 = 1.0 \text{ Kg}^*/\text{cm}^2$. Normalized Element Stress Versus Applied Principal Strain Difference for All Elements Oriented 10° .

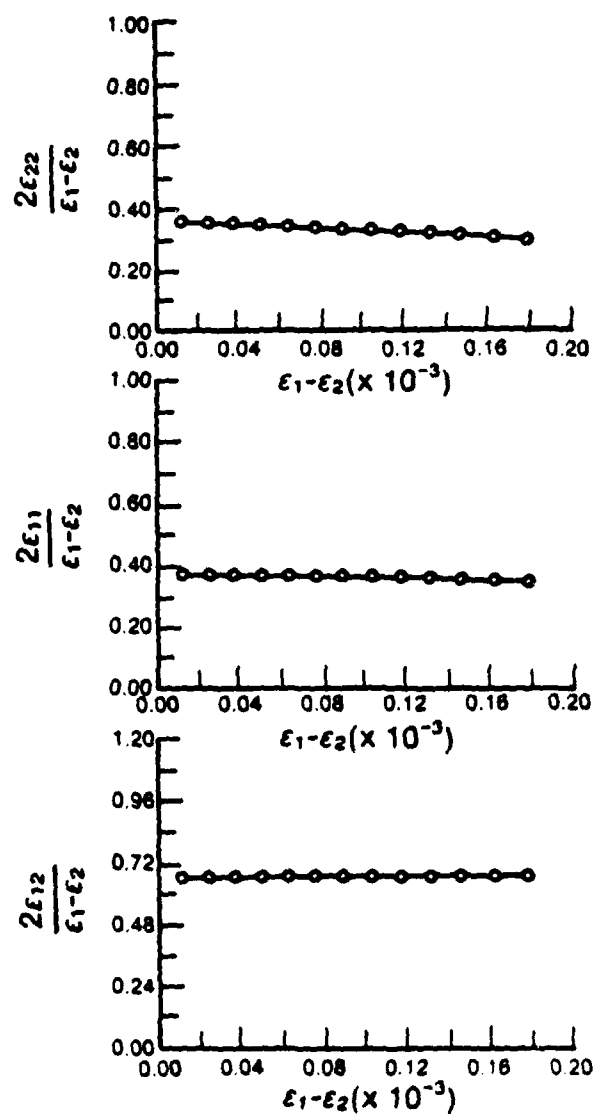


Figure G10. Medium 2: Compression with Constant Mean Stress $\sigma_0^0 = 1.0 \text{ Kg}^*/\text{cm}^2$. Normalized Element Stress Versus Applied Principal Strain Difference for All Elements Oriented 20° .

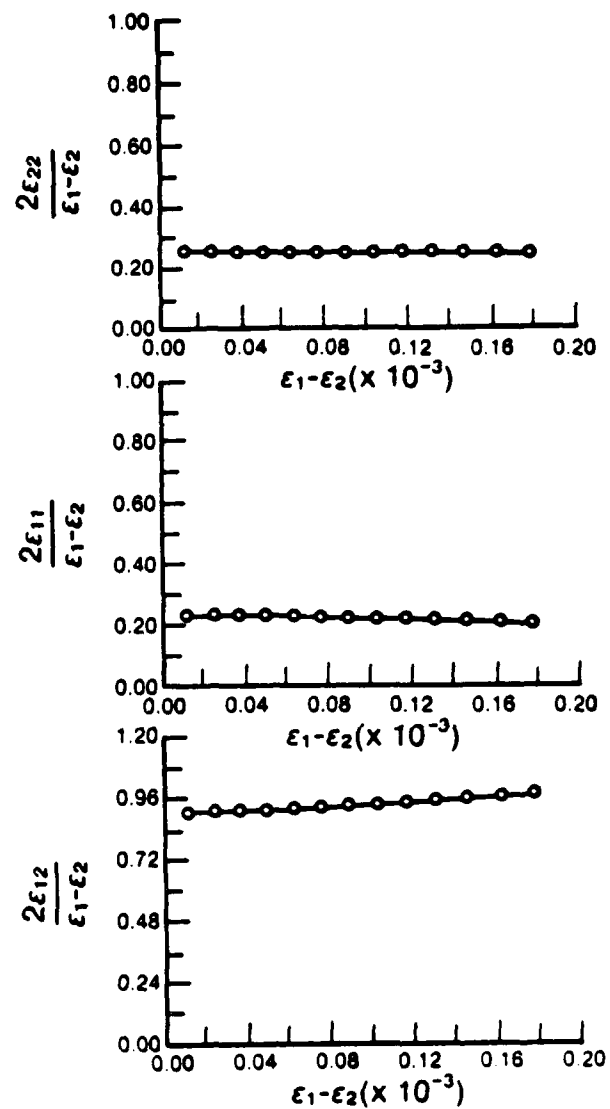


Figure G11. Medium 2: Compression with Constant Mean Stress $\sigma_0^0 = 1.0 \text{ Kg */cm}^2$. Normalized Element Stress Versus Applied Principal Strain Difference for All Elements Oriented 30° .

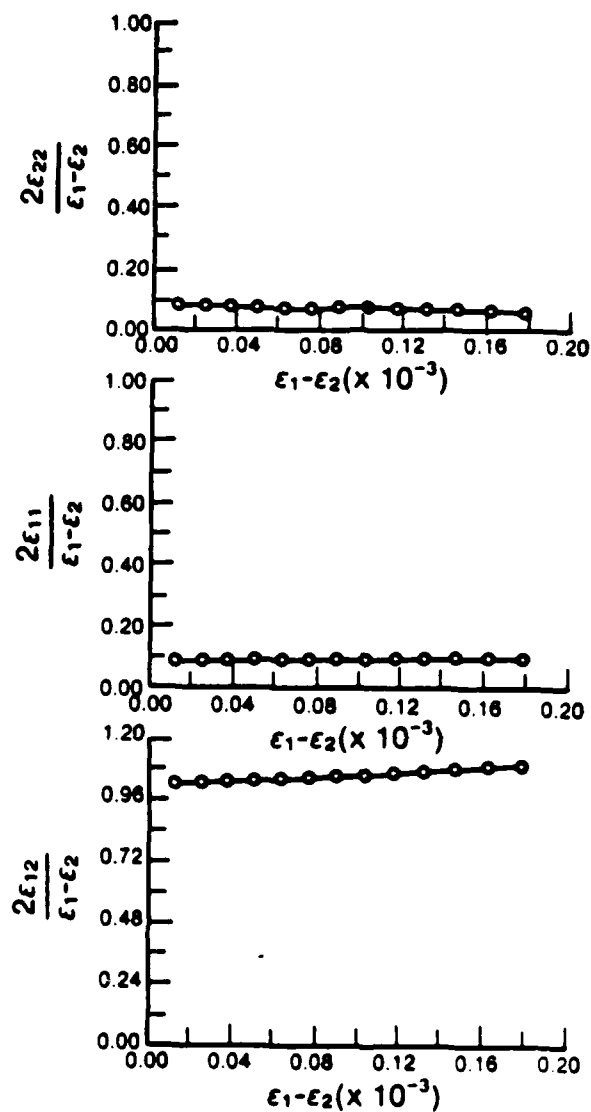


Figure G12. Medium 2: Compression with Constant Mean Stress $\sigma_0 = 1.0 \text{ Kg}^*/\text{cm}^2$. Normalized Element Stress Versus Applied Principal Strain Difference for All Elements Oriented 40° .

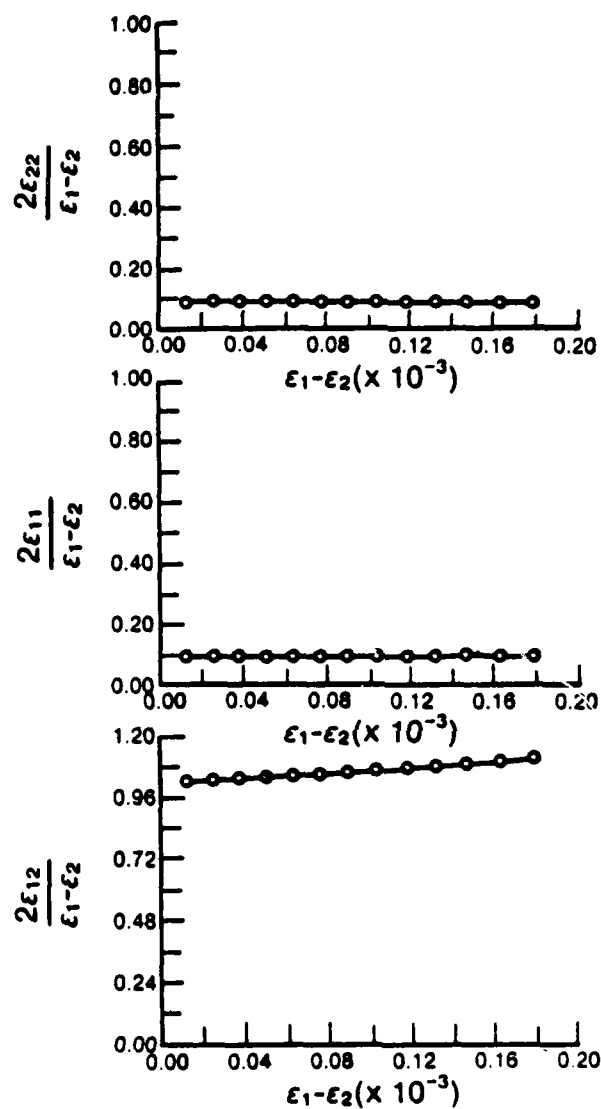


Figure G13. Medium 2: Compression with Constant Mean Stress $\sigma_0 = 1.0 \text{ Kg */cm}^2$. Normalized Element Stress Versus Applied Principal Strain Difference for All Elements Oriented 50° .

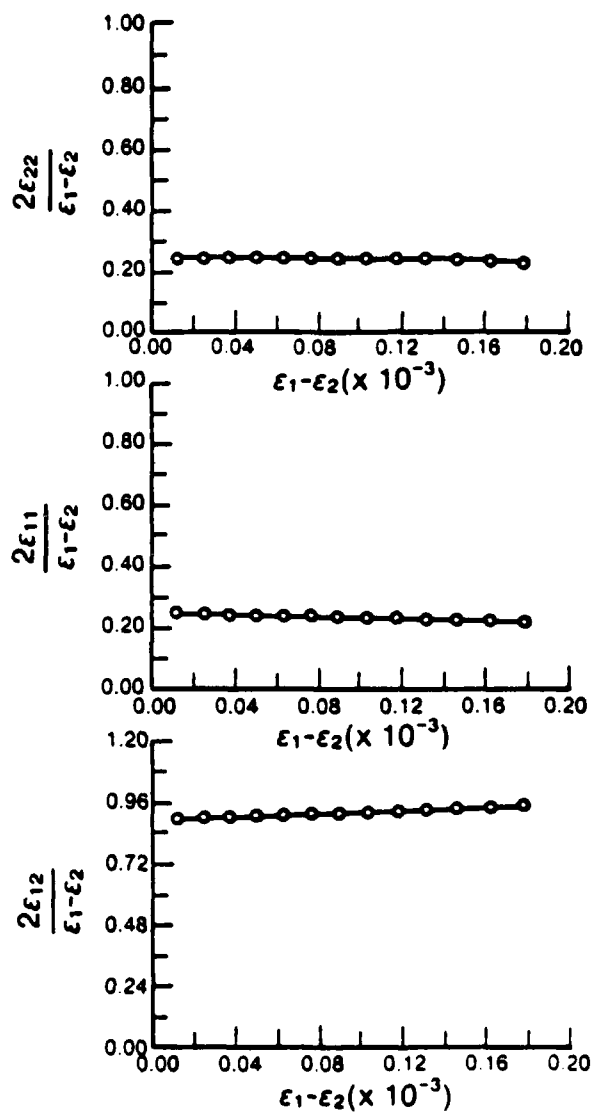


Figure G14. Medium 2: Compression with Constant Mean Stress $\sigma_0 = 1.0 \text{ Kg } ^*/\text{cm}^2$. Normalized Element Stress Versus Applied Principal Strain Difference for All Elements Oriented 60° .

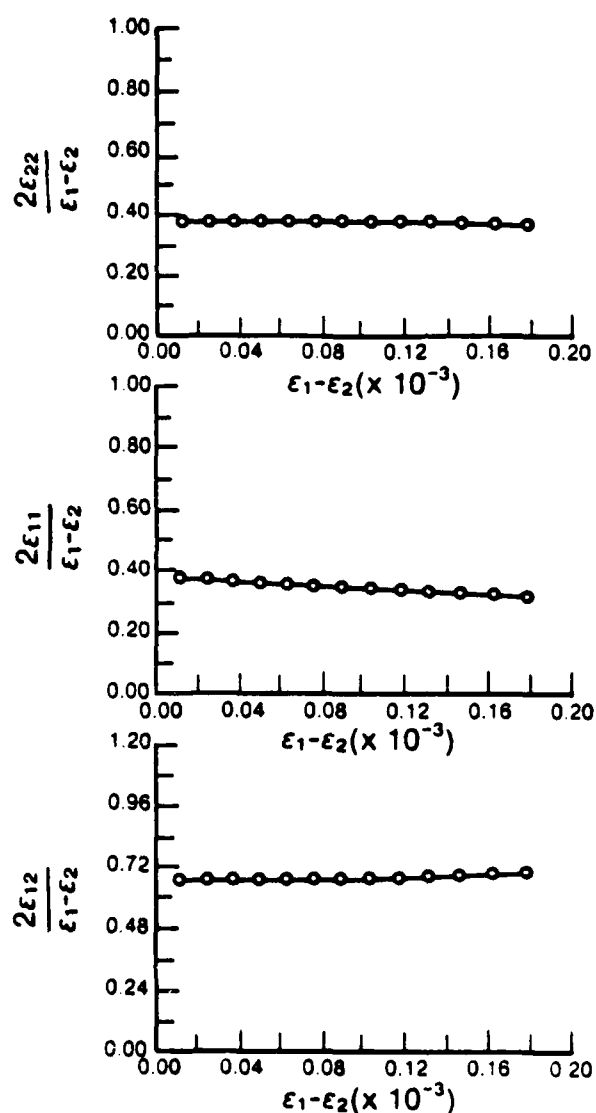


Figure G15. Medium 2: Compression with Constant Mean Stress $\sigma_o^o = 1.0 \text{ Kg}^*/\text{cm}^2$. Normalized Element Stress Versus Applied Principal Strain Difference for All Elements Oriented 70° .

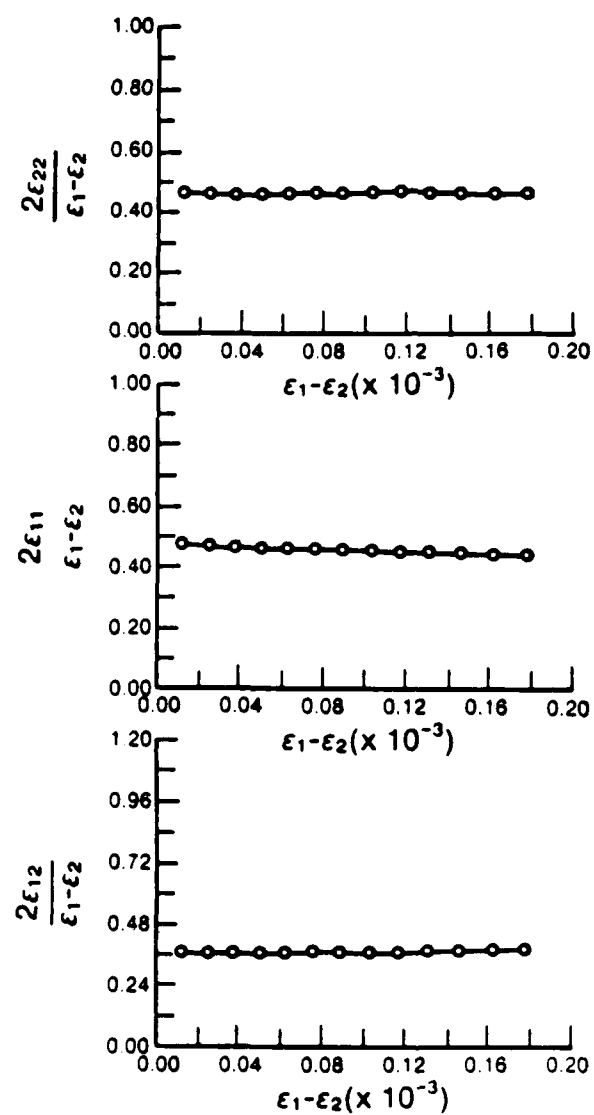


Figure G16. Medium 2: Compression with Constant Mean Stress $\sigma_0^0 = 1.0 \text{ Kg}^*/\text{cm}^2$. Normalized Element Stress Versus Applied Principal Strain Difference for All Elements Oriented 80° .

END

DATE

FILMED

5-88

DTIC